

TUNING EXCITED-STATE REACTIVITY TOWARD PROTON TRANSFER,  
ELECTRON TRANSFER, OR PROTON-COUPLED ELECTRON TRANSFER  
THROUGH ANCILLARY LIGAND EFFECTS FOR A SERIES OF RUTHENIUM  
(II) COMPLEXES

AN ABSTRACT

SUBMITTED ON THE 2ND DAY OF APRIL 2021

TO THE DEPARTMENT OF CHEMISTRY

IN PARTIAL FULFILLMENT OF THE REQUIREMENTS

OF THE SCHOOL OF SCIENCE AND ENGINEERING

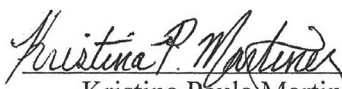
OF TULANE UNIVERSITY

FOR THE DEGREE

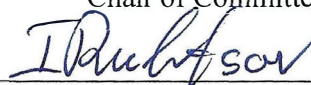
OF

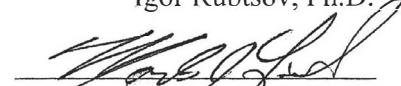
DOCTOR OF PHILOSOPHY

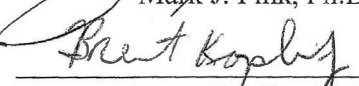
BY

  
\_\_\_\_\_  
Kristina Paula Martinez

APPROVED:   
\_\_\_\_\_  
Russell H. Schmehl, Ph.D.  
Chair of Committee

  
\_\_\_\_\_  
Igor Rubtsov, Ph.D.

  
\_\_\_\_\_  
Mark J. Fink, Ph.D.

  
\_\_\_\_\_  
Brent Koplitz, Ph.D.

## ABSTRACT

Inspired by nature, artificial photosynthesis seeks to take solar energy and convert it into storable fuels. Doing so requires the management of multiple redox and acid-base reactions. In natural photosynthesis, organisms couple proton transfer to electron transfer to reduce the overall driving force needed for reaction; this has made research on systems that exhibit proton-coupled electron transfer reactivity of particular interest to researchers in the area of solar fuels. Not only does coupling proton transfer to electron transfer reduce the free energy of reaction needed for the transfer of a redox process, but it also eliminates the generation of high energy intermediate species in multi-electron transfer events. These multi-electron transfer reactions are necessary to reduce protons to dihydrogen or reduce carbon dioxide to formate or carbon monoxide.

Incorporating light absorption into a proton-coupled electron transfer scheme has the added benefit of using light energy to initiate these reactions. For decades researchers have explored the reactivity of transition metal complex excited states for their photoinduced electron transfer reactions with organic substrates. Ruthenium polypyridyl complexes are well known for their long-lived metal-to-ligand charge transfer states capable of participating in electron transfer reactions that would otherwise be unfavorable from the ground-state molecules. More recently, these complexes have been explored for their proton-coupled electron transfer reactivity.

This work describes a series of projects aimed at investigating the excited state reactivity of ruthenium complexes with hydroxylated bipyridine ligands toward proton transfer, electron transfer, and proton-coupled electron transfer. The first chapter of this

dissertation will outline the background theoretical and thermochemical framework relevant to proton-coupled electron transfer reactions. Chapter 2 will describe in detail the synthesis and characterization of ruthenium chromophores explored in this work. Chapter 3 will provide a detailed account of the excited state proton transfer reactivity of ruthenium complexes with hydroxylated ligands. Chapter 4 systematically investigates the effect of functional group substitution on ancillary ligands on excited-state reactivity. Lastly, chapter 5 will provide a recent account of photoinduced proton-coupled electron transfer with 9,10-anthraquinone.

**TUNING EXCITED-STATE REACTIVITY TOWARD PROTON TRANSFER,  
ELECTRON TRANSFER, OR PROTON-COUPLED ELECTRON TRANSFER  
THROUGH ANCILLARY LIGAND EFFECTS FOR A SERIES OF RUTHENIUM  
(II) COMPLEXES**

A DISSERTATION

SUBMITTED ON THE 2ND DAY OF APRIL 2021

TO THE DEPARTMENT OF CHEMISTRY

IN PARTIAL FULFILLMENT OF THE REQUIREMENTS

OF THE SCHOOL OF SCIENCE AND ENGINEERING

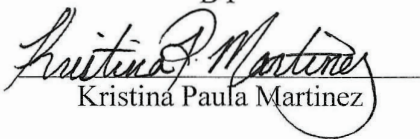
OF TULANE UNIVERSITY

FOR THE DEGREE

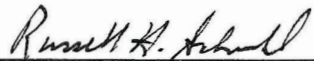
OF

DOCTOR OF PHILOSOPHY

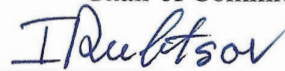
BY

  
Kristina Paula Martinez

APPROVED:



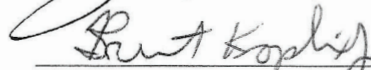
Russell H. Schmehl, Ph.D.  
Chair of Committee



Igor Rubtsov, Ph.D.



Mark J. Fink, Ph.D.



Brent Koplitz, Ph.D.



## ACKNOWLEDGEMENTS

I must first start by expressing gratitude for my research advisor and mentor, Dr. Russell Schmehl. I am grateful to have been given the opportunity to learn from an incredibly knowledgeable photochemist. I appreciate your patience and dedication over the years. I will look fondly upon my time as a researcher in your lab as I continue my career in the chemical sciences. I would also like to take the opportunity to acknowledge and thank my committee members, Dr. Mark Fink, Dr. Brent Koplitz, and Dr. Igor Rubtsov. Thank you to my collaborator at Villanova University, Dr. Jared Paul. Without the hard work and dedication of your laboratory, this dissertation would not be possible. It has been an absolute pleasure working with someone who has such a positive outlook and enthusiastic approach to research.

I would also like to shout out to my fellow Tulane chemistry graduate students. I can honestly say without the friendship of my fellow graduate students; graduate school would have been a lot more difficult. I am so thankful to have befriended people like Dr. Layla Qasim and Ross Zaenglein during my time at Tulane. Your positive vibes and reassurance lifted me up when the work had me feeling my most defeated.

To my fellow Schmehl group members, old and new, thank you! I am thankful to have had the opportunity to learn from Dr. Rebecca Dupre, Dr. Patricia Fontenot, and Dr. Aditya Kulkani in my early years of graduate school. You all helped build my foundation in research, and for that, I will be continuously thankful. I would also like to acknowledge Dr. Barry Pemberton; it was a privilege to work with you during my first few years of graduate school. Of course, I would be remiss not to acknowledge the current members of the Schmehl lab including, Fengqi Zhang, Shuangjie Zhao, Qingxin Chen, and Atahar

Rabby. You all are truly impressive scientists, and I look forward to seeing you all do great things in the field of photochemistry. Finally, to all of the undergraduates I have worked with during my time in graduate school, I am grateful to have been given the opportunity to work with you all and hope that you all go on to have fulfilling careers in the sciences.

To my church small group at Canal Street Church, you all are the best! You're so supportive and kind when I have needed it. You all have been so uplifting over the years, and your fellowship has inspired and encouraged me more than you know. To my friends Katie and Andrew, you all are the best. I love you guys so much. Katie, you have grounded me when I need it and have always been there when I have needed you. Andrew, your intellectual curiosity and dedication to logic and reasoning are an inspiration. You have encouraged me to be a better researcher.

I must also thank my truly wonderful and brilliant husband and best friend, Joshua Richardson. You have encouraged me every step of the way. Even when I did not believe that I could, you were there to remind me of who I am. You encouraged me to pursue this degree, listened to so many of my practice talks, and gave me invaluable feedback. I never thought I would be where I am today, and I know I would not be here without you. I am forever thankful for your support in my career pursuits. I am so excited to start a new adventure with you! Also, of course, thank you to our wonderful fur children, Q and Pascal, for always keeping my feet warm while I write.

To my family, my mother, Darlene, and my sister, Rebecca. I am so thankful for your love and support. You may not know what I do every day, but you know it is important to me and make it important to you. Thank you for your encouragement and your reminders

to take it easy from time to time. I would also like to acknowledge my late father, Vincent. Your curiosity about science influenced me more than you would ever know. You always encouraged my love of science, and for that, I am grateful.

## Table of Contents

ACKNOWLEDGEMENTS .....	ii
LIST OF FIGURES .....	viii
LIST OF TABLES .....	xix
Chapter 1: Role of Proton Coupled Electron Transfer and Proton Transfer in Solar Fuels Generation .....	1
1.1 Proton-Coupled Electron Transfer in Photosynthesis .....	1
1.2 Theoretical Models for Proton Coupled Electron Transfer Reactions .....	4
1.3 Redox Leveling and Thermodynamics of PCET Reactions .....	11
1.4 Combining Light Absorption with PCET and Applications to Solar Fuels .....	16
1.5 Conclusions .....	20
CHAPTER 1 REFERENCES .....	22
Chapter 2: Synthesis and Characterization of Ruthenium (II) Complexes and 4,4'-bipyridinium Quenchers .....	26
2.1 Introduction .....	26
2.2 Experimental .....	28
2.2.1 Spectroscopy .....	28
2.2.2 Electrochemistry .....	28
2.2.3 Time-Resolved Spectroscopy .....	29
2.3 Synthesis and Characterization .....	29
2.3.1 Materials .....	29
2.3.2 Synthesis of Ligands and Ruthenium Complexes .....	30
2.3.3 Synthesis of 4,4'-bipyridinium Quenchers .....	39
2.3.4 Electrospray Ionization Mass Spectrometry .....	40
2.3.5 <sup>1</sup> H-NMR and <sup>1</sup> H- <sup>1</sup> H COSY Assignments .....	45
2.4 Electrochemical and Photophysical Characterization .....	63
2.4.1 Electrochemical Characterization .....	63
2.4.2 UV-visible Absorption Properties .....	70
2.4.3 Excited-state Properties .....	72
2.5 Conclusions .....	81
CHAPTER 2 REFERENCES .....	83
Chapter 3: Excited-State Proton Transfer Reactions of [(bpy) <sub>2</sub> Ru(4,4'-dhbpy)] <sup>2+</sup> with pyridine bases .....	85

3.1	Proton Transfer Reactions of Transition Metal Complexes.....	85
3.2	Experimental .....	88
3.2.1	Materials .....	88
3.2.2	Transient Absorption Studies .....	88
3.2.3	Absorbance and Emission Spectroscopy .....	89
3.2.4	<sup>1</sup> H NMR Studies .....	89
3.3	Results and Discussion.....	89
3.3.1	Thermochemical Analysis of Proton Transfer Reactions.....	89
3.3.2	Proton-transfer Quenching Studies.....	103
3.3.3	Back Proton Transfer Reaction Dynamics .....	119
3.3.4	Free Energy Dependence for Proton Transfer Kinetics.....	122
3.4	Conclusion.....	126
CHAPTER 3 REFERENCES .....		127
Chapter 4: Excited-State Reactions with 4,4'-bipyridinium Quenchers .....		130
4.1	Introduction .....	130
4.2	Experimental .....	133
4.2.1	Materials .....	133
4.2.2	nsTA Spectroscopy.....	133
4.2.3	Electrochemistry.....	134
4.2.4	<sup>1</sup> H NMR Spectroscopy .....	134
4.2.5	UV-Vis Absorption Spectroscopy and Emission Spectroscopy.....	134
4.2.6	Preparation of Samples for KIE Studies.....	135
4.3	Results and Discussion.....	135
4.3.1	Acid-Base and Redox Chemistry of Ruthenium Complexes .....	135
4.3.2	Redox and Acid-Base Behavior of 4,4'-bipyridinium Quenchers .....	147
4.3.3	Thermochemical Analysis of ESPT, ESET, and ESPCET Reactions.....	153
4.3.4	Simulation of ET, PT, and PCET Product Spectra.....	161
4.3.5	ET, PT and PCET Quenching.....	176
4.3.6	Back Reaction Kinetics .....	198
4.3.7	Kinetic Isotope Effect Studies .....	200
4.3.8	Free Energy Relationship for ET, PT, and PCET Reactions.....	203
4.4	Conclusions .....	205

CHAPTER 4 REFERENCES .....	207
Chapter 5: Excited-State Proton-Coupled Electron Transfer with 9,10-Anthraquinone	
211	
5.1 Introduction .....	211
5.2 Experimental .....	214
5.2.1 Materials .....	214
5.2.2 Electrochemical Measurements .....	214
5.2.3 Nanosecond Transient Absorption Spectroscopy .....	214
5.2.4 Steady-State Emission Spectroscopy .....	215
5.2.5 UV-Visible Absorption Spectroscopy .....	215
5.3 Results and Discussion .....	215
5.3.1 Synthesis of Ligands and Complexes .....	215
5.3.2 Thermochemical Analysis .....	215
5.3.3 Simulation of ET, PT, and PCET Product Spectra .....	225
5.3.4 Quenching of Ruthenium(II) Excited States by AQ .....	228
5.4 Conclusions .....	232
CHAPTER 5 REFERENCES .....	234

## LIST OF FIGURES

<b>Figure 1.1</b> Simplified diagram of thylakoid membrane structures. Image reproduced from Thylakoid-Wikipedia by Somepics redistributed under CC BY-SA 4.0 license.....	3
<b>Figure 1.2</b> Potential energy surfaces showing categories of electron transfer reactions with respect to $\Delta G^\circ$ and $\lambda$ . Reprinted (adapted) with permission from J. Chem. Educ. 2019, 96, 11, 2450-2466. Copyright 2019 American Chemical Society.....	6
<b>Figure 1.3</b> Reactant (I) and Product (II) potential energy surfaces for vibronic states is shown. The open circles show the proton vibrational states associated with these points on the potential energy surfaces. The potential energy surfaces are on a collective solvent coordinate for both the proton and electron. Reprinted (adapted) with permission from J. Phys. Chem. B, Vol. 112, No. 45, 2008 Copyright 2008 American Chemical Society. ..	10
<b>Figure 1.4</b> Square scheme depicting stepwise reaction pathways (ETPT and PTET) and concerted path (diagonal).....	13
<b>Figure 1.5</b> Square scheme for a bimolecular PCET reaction.....	15
<b>Figure 1.6</b> Cascade of PCET reactions in PSII (a), classical D-A dyads (b), molecular triad featuring a ruthenium photosensitizer. Reprinted (adapted) with permission from <i>Journal of the American Chemical Society</i> 2017, 139 (38), 13308–13311. <a href="https://doi.org/10.1021/jacs.7b08761">https://doi.org/10.1021/jacs.7b08761</a> . Copyright (2017) American Chemical Society.....	20
<b>Figure 2.1</b> Experimental and calculated mass spectra of $[(bpy)_2Ru(4,4'-dhbpy)]^{2+}$ , calc. deviation 69 ppm.....	41
<b>Figure 2.2</b> Experimental and calculated mass spectra of $[(dpab)_2Ru(4,4'-dhbpy)]^{2+}$ , calc. deviation 46 ppm.....	41
<b>Figure 2.3</b> Experimental and calculated mass spectra of $[(dtb)_2Ru(4,4'-dhbpy)]^{2+}$ , calc. deviation 27 ppm.....	41
<b>Figure 2.4</b> Experimental and calculated mass spectra of $[(dtb)_2Ru(bpy)]^{2+}$ , calc. deviation 14 ppm .....	42
<b>Figure 2.5</b> Experimental and calculated mass spectra of $[(5-Clphen)_2Ru(4-OH-4'-OMebpy)]^{2+}$ , calc. deviation 801 ppm. ....	42
<b>Figure 2.6</b> Experimental and calculated mass spectra of $[5-Clphen)_2Ru(bpy)]^{2+}$ , calc. deviation 854 ppm.....	42
<b>Figure 2.7</b> Experimental and calculated mass spectra of $[(flpy)_2Ru(4,4'-dhbpy)]^{2+}$ , calc. deviation 14 ppm.....	43

<b>Figure 2.8</b> Experimental and calculated mass spectra $[(bpy)_2Ru(4-OHbpy)]^{2+}$ , calc. deviation 23 ppm.....	43
<b>Figure 2.9</b> Experimental and calculated mass spectra of $[(flpy)_2Ru(bpy)]^{2+}$ , calc. deviation 31 ppm.....	43
<b>Figure 2.10</b> Experimental and calculated mass spectra $[(bpy)_2Ru(4-OMebpy)]^{2+}$ , calc. deviation 20 ppm.....	44
<b>Figure 2.11</b> Experimental and calculated mass spectra of $[(bpy)_2Ru(4,4'-dmbpy)]^{2+}$ , calc deviation 6 ppm.....	44
<b>Figure 2.12</b> Experimental and calculated mass spectra for $[(bpy)_2Ru(4-OH-4'-OMebpy)]^{2+}$ , calc. deviation 21 ppm .....	44
<b>Figure 2.13</b> Experimental and calculated mass spectra of $[(dpab)_2Ru(bpy)]^{2+}$ , calc. deviation 35 ppm.....	45
<b>Figure 2.14</b> $^1H$ NMR of $[(dtb)_2Ru(4,4'-dhbpy)]^{2+}$ in $CD_3CN$ .....	46
<b>Figure 2.15</b> Aromatic region of the $^1H$ NMR of $[(dtb)_2Ru(4,4'-dhbpy)]^{2+}$ .....	46
<b>Figure 2.16</b> $^1H$ - $^1H$ COSY of $[(dtb)_2Ru(4,4'-dhbpy)]^{2+}$ in $CD_3CN$ .....	47
<b>Figure 2.17</b> $^1H$ NMR of $[(dtb)_2Ru(bpy)]^{2+}$ in $CD_3CN$ .....	49
<b>Figure 2.18</b> Aromatic region of $^1H$ NMR of $[(dtb)_2Ru(bpy)]^{2+}$ in $CD_3CN$ .....	49
<b>Figure 2.19</b> $^1H$ - $^1H$ COSY of $[(dtb)_2Ru(bpy)]^{2+}$ in $CD_3CN$ .....	50
<b>Figure 2.20</b> $^1H$ NMR spectrum of $[(flpy)_2Ru(bpy)]^{2+}$ in $CD_3CN$ .....	51
<b>Figure 2.21</b> Aromatic region of $^1H$ NMR of $[(flpy)_2Ru(bpy)]^{2+}$ .....	51
<b>Figure 2.22</b> $^1H$ - $^1H$ COSY of $[(flpy)_2Ru(bpy)]^{2+}$ .....	52
<b>Figure 2.23</b> $^1H$ NMR spectrum of $[(flpy)_2Ru(4,4'-(OH)_2bpy)]^{2+}$ in $CD_3CN$ .....	53
<b>Figure 2.24</b> Aromatic region of $^1H$ NMR of $[(flpy)_2Ru(4,4'-(OH)_2bpy)]^{2+}$ .....	53
<b>Figure 2.25</b> $^1H$ - $^1H$ COSY of $[(flpy)_2Ru(4,4'-(OH)_2bpy)]^{2+}$ in $CD_3CN$ .....	54
Figure 2.26 $^1H$ NMR of $[(dpab)_2Ru(4,4'-(OH)_2bpy)]^{2+}$ .....	55
<b>Figure 2.27</b> Aromatic region of $^1H$ NMR of $[(dpab)_2Ru(4,4'-(OH)_2bpy)]^{2+}$ in $CD_3CN$ ...	55
<b>Figure 2.28</b> $^1H$ - $^1H$ COSY spectrum of $[(dpab)_2Ru(4,4'-(OH)_2bpy)]^{2+}$ in $CD_3CN$ .....	56
<b>Figure 2.29</b> Aromatic region of $^1H$ NMR of $[(dpab)_2Ru(bpy)]^{2+}$ in $CD_3CN$ .....	57

<b>Figure 2.30</b> $^1\text{H-NMR}$ of $[(\text{dpab})_2\text{Ru}(\text{bpy})]^{2+}$ in $\text{CD}_3\text{CN}$ .....	57
<b>Figure 2.31</b> $^1\text{H-}^1\text{H}$ COSY of $[(\text{dpab})_2\text{Ru}(\text{bpy})]^{2+}$ in $\text{CD}_3\text{CN}$ .....	58
<b>Figure 2.32</b> $^1\text{H-NMR}$ of $[(\text{Cl-phen})_2\text{Ru}(\text{bpy})]^{2+}$ in $\text{CD}_3\text{CN}$ .....	59
<b>Figure 2.33</b> Aromatic region of $^1\text{H-NMR}$ of $[(\text{Cl-phen})_2\text{Ru}(\text{bpy})]^{2+}$ in $\text{CD}_3\text{CN}$ .....	59
<b>Figure 2.34</b> $^1\text{H-}^1\text{H}$ COSY of $[(\text{Cl-phen})_2\text{Ru}(\text{bpy})]^{2+}$ in $\text{CD}_3\text{CN}$ .....	60
<b>Figure 2.35</b> Aromatic region of $^1\text{H-NMR}$ of $[(\text{Cl-phen})_2\text{Ru}(4\text{-OH-}4'\text{-OMe-bpy})]^{2+}$ .....	61
<b>Figure 2.36</b> $^1\text{H-NMR}$ of $[(\text{Cl-phen})_2\text{Ru}(4\text{-OH-}4'\text{-OMe-bpy})]^{2+}$ .....	61
<b>Figure 2.37</b> $^1\text{H-}^1\text{H}$ COSY spectrum of $[(\text{Cl-phen})_2\text{Ru}(4\text{-OH-}4'\text{-OMe-bpy})]^{2+}$ .....	62
<b>Figure 2.38</b> Anodic and cathodic voltammograms of $[(\text{dpab})_2\text{Ru}(4,4'\text{-(OH)}_2\text{bpy})]^{2+}$ .....	65
<b>Figure 2.39</b> Anodic and cathodic voltammograms of $[(\text{dpab})_2\text{Ru}(4,4'\text{-(OH)}_2\text{-bpy})]^{2+}$ in the presence of 1 molar equivalent of TBAOH .....	65
<b>Figure 2.40</b> Anodic and cathodic voltammograms of $[(\text{dtb})_2\text{Ru}(4,4'\text{-(OH)}_2\text{-bpy})]^{2+}$ .....	65
<b>Figure 2.41</b> Anodic and cathodic voltammograms of $[(\text{flpy})_2\text{Ru}(4,4'\text{-(OH)}_2\text{-bpy})]^{2+}$ in the presence of 1 molar equivalent of TBAOH .....	66
<b>Figure 2.42</b> Anodic and cathodic voltammograms of $[(\text{flpy})_2\text{Ru}(4,4'\text{-(OH)}_2\text{-bpy})]^{2+}$ .....	66
<b>Figure 2.43</b> Anodic and cathodic voltammograms of $[(\text{dtb})_2\text{Ru}(4,4'\text{-(OH)}_2\text{-bpy})]^{2+}$ in the presence of 1 molar equivalent of TBAOH .....	66
<b>Figure 2.44</b> Anodic and cathodic voltammograms of $[(\text{Cl-phen})_2\text{Ru}(4\text{-(OH)-}4'\text{-(OMe)-bpy})]^{2+}$ .....	67
<b>Figure 2.45</b> Anodic and cathodic voltammograms of $[(\text{Cl-phen})_2\text{Ru}(\text{OH})\text{-}4'\text{-(OMe)-bpy})]^{2+}$ in the presence of 1 molar equivalent of TBAOH.....	67
<b>Figure 2.46</b> Anodic and cathodic voltammograms of $[(\text{bpy})_2\text{Ru}(4\text{-OHbpy})]^{2+}$ .....	67
<b>Figure 2.47</b> Anodic voltammogram of $[(\text{bpy})_2\text{Ru}(4\text{-OHbpy})]^{2+}$ in the presence of 11 molar equivalents of DABCO.....	68
<b>Figure 2.48</b> Anodic and cathodic voltammograms of $[(\text{dpab})_2\text{Ru}(\text{bpy})]^{2+}$ .....	68
<b>Figure 2.49</b> Anodic and cathodic voltammograms of $[(\text{dtb})_2\text{Ru}(\text{bpy})]^{2+}$ .....	68
<b>Figure 2.50</b> Anodic and cathodic voltammograms of $[(\text{flpy})_2\text{Ru}(\text{bpy})]^{2+}$ .....	69
<b>Figure 2.51</b> Anodic and cathodic voltammograms of $[(\text{Cl-phen})_2\text{Ru}(\text{bpy})]^{2+}$ .....	69

<b>Figure 2.52</b> Anodic and cathodic voltammograms of $[(bpy)_2Ru(4-OMebpy)]^{2+}$ .....	69
<b>Figure 2.53</b> UV-Visible absorption spectra of control complex series in acetonitrile.....	71
<b>Figure 2.54</b> UV-Visible absorption spectra of protonated complexes (left) and deprotonated complexes (right) in acetonitrile solution. ....	71
<b>Figure 2.55</b> Room temperature emission spectra for control complexes (left) and hydroxylated complexes (right) measured in acetonitrile solution.....	72
<b>Figure 2.56</b> 77 K Emission spectra of control complexes (left) and hydroxylated complexes (right) .....	73
<b>Figure 2.57</b> Emission energy vs. energy difference between oxidation and first reduction of complex taken from electrochemical measurements.....	74
<b>Figure 2.58</b> Emission spectrum of quantum yield reference, $[Ru(bpy)_3]^{2+}$ in acetonitrile .....	76
<b>Figure 2.59</b> Plot of $E_{0-0}$ at 77 K versus the natural log of the nonradiative decay rate constant ( $k_{nr}$ ) .....	78
<b>Figure 2.60</b> Transient absorption spectra of $[(bpy)_2Ru(4,4'-(OH)_2-bpy)]^{2+}$ (left) and $[(bpy)_2Ru(4,4'-(OMe)_2-bpy)]^{2+}$ (right) in acetonitrile .....	79
<b>Figure 2.61</b> Transient absorption spectra of $[(dpab)_2Ru(4,4'-(OH)_2-bpy)]^{2+}$ (left) and $[(dpab)_2Ru(bpy)]^{2+}$ (right) in acetonitrile.....	79
<b>Figure 2.62</b> Transient absorption spectra of $[(dtb)_2Ru(4,4'-(OH)_2-bpy)]^{2+}$ (left) and $[(dtb)_2Ru(bpy)]^{2+}$ (right) in acetonitrile .....	79
<b>Figure 2.63</b> Transient absorption spectra of $[(flpy)_2Ru(4,4'-(OH)_2-bpy)]^{2+}$ (left) and $[(flpy)_2Ru(bpy)]^{2+}$ (right) in acetonitrile.....	80
<b>Figure 2.64</b> Transient absorption spectra of $[(Cl-phen)_2Ru(4-(OH)-4'-(OMe)-bpy)]^{2+}$ (left) and $[(Cl-phen)_2Ru(bpy)]^{2+}$ (right) in acetonitrile.....	80
<b>Figure 2.65</b> Transient absorption spectra of $[(bpy)_2Ru(4-(OH)-bpy)]^{2+}$ (left) and $[(bpy)_2Ru(4-(OMe)-bpy)]^{2+}$ (right) in acetonitrile.....	80
<b>Figure 3.1</b> UV-Vis absorbance titration of $[(bpy)_2Ru(4-(OH)-4'-(OMe)bpy)]^{2+}$ with 4-aminopyridine in acetonitrile .....	90
<b>Figure 3.2</b> Linear fit of titration data to extract $K_{eq}$ for acid-base reaction between $[(bpy)_2Ru(4-(OH)-4'-(OMe)bpy)]^{2+}$ and 4-aminopyridine in acetonitrile .....	91
<b>Figure 3.3</b> Förster thermodynamic cycle .....	92

<b>Figure 3.4</b> Emission spectra of the protonated and monodeprotonated forms of $[(\text{bpy})_2\text{Ru}(4,4'-(\text{OH})_2\text{bpy})]^{2+}$ at $-42\text{ }^\circ\text{C}$ in acetonitrile.....	93
<b>Figure 3.5</b> Linear correlation between $\text{p}K_a$ 's in $\text{H}_2\text{O}$ and $\text{CH}_3\text{CN}$ for the pyridine series	94
<b>Figure 3.6</b> Structure of pyridine bases used along with $\text{p}K_a$ 's of the conjugate acid in both acetonitrile and water. Values in blue were determined by correlation with aqueous $\text{p}K_a$ data.....	95
<b>Figure 3.7</b> $^1\text{H}$ NMR spectra of $[(\text{bpy})_2\text{Ru}(4,4'-(\text{OH})_2\text{bpy})]^{2+}$ in the presence of increasing concentrations of pyridine- $\text{d}_5$ in $\text{CD}_3\text{CN}$ . .....	96
<b>Figure 3.8</b> The plot of observed chemical shift vs. the ration of concentrations of pyridine added and the initial concentration of $[\text{Ru}(\text{bpy})_2(4,4'-(\text{OH})_2\text{bpy})]^{2+}$ fit with a parabolic equation to extract $K_{\text{eq}}$ for H-bonding. ....	97
<b>Figure 3.9</b> $^1\text{H}$ NMR spectra of $[(\text{bpy})_2\text{Ru}(4,4'-(\text{OH})_2\text{bpy})]^{2+}$ in the presence of increasing concentrations of 2-picoline- $\text{d}_7$ .....	99
<b>Figure 3.10</b> $^1\text{H}$ NMR spectra of $[(\text{bpy})_2\text{Ru}(4,4'-(\text{OH})_2\text{bpy})]^{2+}$ in the presence of increasing concentrations of 4-picoline- $\text{d}_7$ .....	99
<b>Figure 3.11</b> The plot of observed chemical shift vs. the ration of concentrations of 2-picoline added and the initial concentration of $[\text{Ru}(\text{bpy})_2(4,4'-(\text{OH})_2\text{bpy})]^{2+}$ fit with a parabolic equation to extract $K_{\text{eq}}$ for H-bonding. ....	100
<b>Figure 3.12</b> The plot of observed chemical shift vs. the ration of concentrations of 4-picoline added and the initial concentration of $[\text{Ru}(\text{bpy})_2(4,4'-(\text{OH})_2\text{bpy})]^{2+}$ fit with a parabolic equation to extract $K_{\text{eq}}$ for H-bonding. ....	100
<b>Figure 3.13</b> Luminescence lifetimes (left) and steady-state emission spectra (right) of $[\text{Ru}(\text{bpy})_2(4,4'-(\text{OH})_2\text{bpy})]^{2+}$ in presence of varying concentrations of 3-methoxypyridine .....	103
<b>Figure 3.14</b> Luminescence lifetimes (left) and steady-state emission spectra (right) of $[\text{Ru}(\text{bpy})_2(4,4'-(\text{OH})_2\text{bpy})]^{2+}$ in presence of varying concentrations of 2-picoline .....	104
<b>Figure 3.15</b> Luminescence lifetimes (left) and steady-state emission spectra (right) of $[\text{Ru}(\text{bpy})_2(4,4'-(\text{OH})_2\text{bpy})]^{2+}$ in presence of varying concentrations of 4-bromo-2-picoline .....	104
<b>Figure 3.16</b> Luminescence lifetimes (left) and steady-state emission spectra (right) of $[\text{Ru}(\text{bpy})_2(4,4'-(\text{OH})_2\text{bpy})]^{2+}$ in presence of varying concentrations of 4-methoxypyridine .....	105

<b>Figure 3.17</b> Luminescence lifetimes (left) and steady-state emission spectra (right) of $[\text{Ru}(\text{bpy})_2(4,4'-(\text{OH})_2\text{bpy})]^{2+}$ in presence of varying concentrations of 4-phenylpyridine .....	105
<b>Figure 3.18</b> Luminescence lifetimes (left) and steady-state emission spectra (right) of $[\text{Ru}(\text{bpy})_2(4,4'-(\text{OH})_2\text{bpy})]^{2+}$ in presence of varying concentrations of 4-picoline .....	106
<b>Figure 3.19</b> Luminescence lifetimes (left) and steady-state emission spectra (right) of $[\text{Ru}(\text{bpy})_2(4,4'-(\text{OH})_2\text{bpy})]^{2+}$ in presence of varying concentrations of 2,4-lutidine .....	106
<b>Figure 3.20</b> Luminescence lifetimes (left) and steady-state emission spectra (right) of $[\text{Ru}(\text{bpy})_2(4,4'-(\text{OH})_2\text{bpy})]^{2+}$ in presence of varying concentrations of 2,6-lutidine .....	107
<b>Figure 3.21</b> Luminescence lifetimes (left) and steady-state emission spectra (right) of $[\text{Ru}(\text{bpy})_2(4,4'-(\text{OH})_2\text{bpy})]^{2+}$ in presence of varying concentrations of benzo[h]quinoline .....	107
<b>Figure 3.22</b> Luminescence lifetimes (left) and steady-state emission spectra (right) of $[\text{Ru}(\text{bpy})_2(4,4'-(\text{OH})_2\text{bpy})]^{2+}$ in presence of varying concentrations of 2,4,6-collidine .	108
<b>Figure 3.23</b> Luminescence lifetimes (left) and steady-state emission spectra (right) of $[\text{Ru}(\text{bpy})_2(4,4'-(\text{OH})_2\text{bpy})]^{2+}$ in presence of varying concentrations of isoquinoline.....	108
<b>Figure 3.24</b> Luminescence lifetimes (left) and steady-state emission spectra (right) of $[\text{Ru}(\text{bpy})_2(4,4'-(\text{OH})_2\text{bpy})]^{2+}$ in presence of varying concentrations of pyridine .....	109
<b>Figure 3.25</b> Luminescence lifetimes (left) and steady-state emission spectra (right) of $[\text{Ru}(\text{bpy})_2(4,4'-(\text{OH})_2\text{bpy})]^{2+}$ in presence of varying concentrations of quinoline .....	109
<b>Figure 3.26</b> Excited-state proton transfer reaction mechanism.....	111
<b>Figure 3.27</b> Plot of the ratio of the concentration of base added to the solution vs. the ratio of the $\phi_0/\phi$ with the modified Stern-Volmer approach (eq. 3.6).....	113
<b>Figure 3.28</b> Plot of the ratio of the concentration of base added to the solution vs. the ratio of the $\tau_0/\tau$ with the modified Stern-Volmer approach (eq. 3.6).....	114
<b>Figure 3.29</b> Difference spectrum generated using the UV-Visible absorption spectrum of $[\text{Ru}(\text{bpy})_2(4,4'-(\text{OH})_2\text{bpy})]^{2+}$ and $[\text{Ru}(\text{bpy})_2(4-(\text{O})-4'-(\text{OH})\text{bpy})]^+$ .....	118
<b>Figure 3.30</b> nsTA spectrum of the excited-state proton transfer products for the reaction between $[\text{Ru}(\text{bpy})_2(4,4'-(\text{OH})_2\text{bpy})]^{2+}$ and pyridine.....	119
<b>Figure 3.31</b> Back proton transfer kinetics monitored at 510 nm for reaction between the deprotonated ruthenium complex and benzo[h]quinoline .....	121
<b>Figure 3.32</b> Plot of the $\log(K_{\text{HB}})$ vs. $\Delta G_{\text{PT}}^*$ .....	123

<b>Figure 3.33</b> Linear free energy relationship for the ESPT reaction between $[\text{Ru}(\text{bpy})_2(4,4'-(\text{OH})_2\text{bpy})]^{2+}$ and substituted pyridine bases.....	125
<b>Figure 4.1</b> Hydroxylated complexes and bipyridinium quenchers .....	132
<b>Figure 4.2</b> Reactions used to calculate the equilibrium constant for the acid-base reaction between ruthenium complexes and pyridine/amine bases .....	137
<b>Figure 4.3</b> UV-Vis spectrophotometric titration spectra for $[(\text{Ru}(\text{flpy})_2(4,4'-(\text{OH})_2\text{bpy}))]^{2+}$ (top left), $[\text{Ru}(\text{Cl-phen})_2(4\text{-OH-4'-OMebpy})]^{2+}$ (top right), $[\text{Ru}(\text{dpab})_2(4,4'-(\text{OH})_2\text{bpy})]^{2+}$ (bottom left), and $[\text{Ru}(\text{dtb})_2(4,4'-(\text{OH})_2\text{bpy})]^{2+}$ (bottom right).....	138
<b>Figure 4.4</b> Linear fit of $[\text{RuO}^+][\text{BH}^+]/[\text{RuOH}]$ vs. $[\text{B}]_{\text{eq}}$ to determine $K_{\text{eq}}$ for acid-base reaction.....	140
<b>Figure 4.5</b> Thermodynamic cycle for oxidation and deprotonation of ruthenium complexes .....	141
<b>Figure 4.6</b> Plot of the difference in energy between the first reduction and oxidation potentials of complexes vs. $\text{p}K_{\text{a}}$ .....	143
<b>Figure 4.7</b> Low temperature emission spectra of protonated and deprotonated ruthenium complexes in acetonitrile solution .....	144
<b>Figure 4.8</b> Calculation of the excited state oxidation potential of ruthenium(II) complexes .....	145
<b>Figure 4.9</b> Reactions for determining the $\text{p}K_{\text{a}}$ of bipyridinium quenchers .....	148
<b>Figure 4.10</b> $^1\text{H}$ NMR spectra of $\text{MQ}^+$ (top) and $\text{BMQ}^+$ (bottom) with increasing concentration of $\text{Cl}_3\text{CCOOH}$ going from bottom to top of spectra in $\text{CD}_3\text{CN}$ .....	149
<b>Figure 4.11</b> Fit of $^1\text{H}$ NMR titration data with $\text{Cl}_3\text{CCOOH}$ to determine the $\text{p}K_{\text{a}}$ of quenchers $\text{MQ}^+$ (left) and $\text{BMQ}^+$ (right).....	151
<b>Figure 4.12</b> Cathodic voltammograms of $\text{MQ}^+$ (left) and $\text{HMQ}^{2+}$ (right) vs. $\text{Fc}^{+/0}$ .....	152
<b>Figure 4.13</b> Cathodic voltammograms of $\text{BMQ}^+$ (left) and $\text{HBMQ}^{2+}$ (right) vs. $\text{Fc}^{+/0}$ ..	152
<b>Figure 4.14</b> Cathodic voltammograms of $\text{BMQ}^+$ (left) and $\text{HBMQ}^{2+}$ (right) vs. $\text{Fc}^{+/0}$ ..	153
<b>Figure 4.15</b> Possible reactions between $[\text{Ru}(\text{LL})_2(4,4'-(\text{OH})_2\text{bpy})]^{2+*}$ and $\text{MQ}^+$ .....	154
<b>Figure 4.16</b> Free energies of reaction for each complex, for ESET, ESPT, and ESPCET with $\text{MQ}^+$ .....	161
<b>Figure 4.17</b> Absorption spectra of $\text{MQ}^+$ , $\text{HMQ}^{2+}$ , $\text{BMQ}^+$ , and $\text{HBMQ}^{2+}$ in acetonitrile	162

<b>Figure 4.18</b> Simulated spectra for ESPT for ruthenium complexes in acetonitrile .....	164
<b>Figure 4.19</b> Simulated spectra for ESET products for control complexes and their reaction with MQ <sup>+</sup> .....	168
<b>Figure 4.20</b> Simulated spectra for ESET products for control complexes and their reaction with BMQ <sup>+</sup> .....	169
<b>Figure 4.21</b> Simulated spectra for ESET products for hydroxylated complexes and their reaction with MQ <sup>+</sup> .....	170
<b>Figure 4.22</b> Simulated spectra for ESET products for hydroxylated complexes and their reaction with BMQ <sup>+</sup> .....	171
<b>Figure 4.23</b> Structure of 4-bromobenzenediazonium tetrafluoroborate.....	172
<b>Figure 4.24</b> Simulated spectra for ESPCET products for hydroxylated complexes and their reaction with MQ <sup>+</sup> .....	174
<b>Figure 4.25</b> Simulated spectra for ESPCET products for hydroxylated complexes and their reaction with BMQ <sup>+</sup> .....	175
<b>Figure 4.26</b> Luminescence lifetime quenching of [Ru(bpy) <sub>2</sub> (4,4'-(OMe) <sub>2</sub> bpy)] <sup>2+</sup> by MQ <sup>+</sup> (left) and the resulting Stern-Volmer plot (right) .....	176
<b>Figure 4.27</b> Luminescence lifetime quenching of [Ru(dpab) <sub>2</sub> (bpy)] <sup>2+</sup> by MQ <sup>+</sup> (left) and the resulting Stern-Volmer plot (right) .....	177
<b>Figure 4.28</b> Luminescence lifetime quenching of [Ru(dpab) <sub>2</sub> (bpy)] <sup>2+</sup> by BMQ <sup>+</sup> (left) and the resulting Stern-Volmer plot (right) .....	177
<b>Figure 4.29</b> Luminescence lifetime quenching of [Ru(Cl-phen) <sub>2</sub> (bpy)] <sup>2+</sup> by MQ <sup>+</sup> (left) and the resulting Stern-Volmer plot (right) .....	178
<b>Figure 4.30</b> Luminescence lifetime quenching of [Ru(Cl-phen) <sub>2</sub> (bpy)] <sup>2+</sup> by BMQ <sup>+</sup> (left) and the resulting Stern-Volmer plot (right) .....	178
<b>Figure 4.31</b> Luminescence lifetime quenching of [Ru(dtb) <sub>2</sub> (bpy)] <sup>2+</sup> by MQ <sup>+</sup> (left) and the resulting Stern-Volmer plot (right) .....	179
<b>Figure 4.32</b> Luminescence lifetime quenching of [Ru(dtb) <sub>2</sub> (bpy)] <sup>2+</sup> by BMQ <sup>+</sup> (left) and the resulting Stern-Volmer plot (right) .....	179
<b>Figure 4.33</b> Luminescence lifetime quenching of [Ru(flpy) <sub>2</sub> (bpy)] <sup>2+</sup> by MQ <sup>+</sup> (left) and the resulting Stern-Volmer plot (right) .....	180
<b>Figure 4.34</b> Luminescence lifetime quenching of [Ru(flpy) <sub>2</sub> (bpy)] <sup>2+</sup> by BMQ <sup>+</sup> (left) and the resulting Stern-Volmer plot (right) .....	180

<b>Figure 4.35</b> Luminescence lifetime quenching of $[\text{Ru}(\text{bpy})_2(4,4'-(\text{OH})_2\text{bpy})]^{2+}$ by $\text{MQ}^+$ (left) and the resulting Stern-Volmer plot (right) .....	181
<b>Figure 4.36</b> Luminescence lifetime quenching of $[\text{Ru}(\text{bpy})_2(4,4'-(\text{OH})_2\text{bpy})]^{2+}$ by $\text{BMQ}^+$ (left) and the resulting Stern-Volmer plot (right) .....	181
<b>Figure 4.37</b> Luminescence lifetime quenching of $[\text{Ru}(\text{dpab})_2(4,4'-(\text{OH})_2\text{bpy})]^{2+}$ by $\text{MQ}^+$ (left) and the resulting Stern-Volmer plot (right) .....	182
<b>Figure 4.38</b> Luminescence lifetime quenching of $[\text{Ru}(\text{dpab})_2(4,4'-(\text{OH})_2\text{bpy})]^{2+}$ by $\text{BMQ}^+$ (left) and the resulting Stern-Volmer plot (right).....	182
<b>Figure 4.39</b> Luminescence lifetime quenching of $[\text{Ru}(\text{Cl-phen})_2(4-(\text{OH})-4'-(\text{OMe})\text{bpy})]^{2+}$ by $\text{MQ}^+$ (left) and the resulting Stern-Volmer plot (right) .....	183
<b>Figure 4.40</b> Luminescence lifetime quenching of $[\text{Ru}(\text{Cl-phen})_2(4-(\text{OH})-4'-(\text{OMe})\text{bpy})]^{2+}$ by $\text{BMQ}^+$ (left) and the resulting Stern-Volmer plot (right) .....	183
<b>Figure 4.41</b> Luminescence lifetime quenching of $[\text{Ru}(\text{dtb})_2(4,4'-(\text{OH})_2\text{bpy})]^{2+}$ by $\text{BMQ}^+$ (left) and the resulting Stern-Volmer plot (right) .....	184
<b>Figure 4.42</b> Luminescence lifetime quenching of $[\text{Ru}(\text{dtb})_2(4,4'-(\text{OH})_2\text{bpy})]^{2+}$ by $\text{MQ}^+$ (left) and the resulting Stern-Volmer plot (right) .....	184
<b>Figure 4.43</b> Luminescence lifetime quenching of $[\text{Ru}(\text{flpy})_2(4,4'-(\text{OH})_2\text{bpy})]^{2+}$ by $\text{MQ}^+$ (left) and the resulting Stern-Volmer plot (right) .....	185
<b>Figure 4.44</b> Luminescence lifetime quenching of $[\text{Ru}(\text{flpy})_2(4,4'-(\text{OH})_2\text{bpy})]^{2+}$ by $\text{BMQ}^+$ (left) and the resulting Stern-Volmer plot (right) .....	185
<b>Figure 4.45</b> nsTA spectra of $[\text{Ru}(\text{bpy})_2(4,4'-(\text{OMe})_2\text{bpy})]^{2+}$ in the presence of 120 mM .....	188
<b>Figure 4.46</b> nsTA spectra $[\text{Ru}(\text{bpy})_2(4,4'-(\text{OH})_2\text{bpy})]^{2+}$ in the presence of 15 mM $\text{BMQ}^+$ .....	188
<b>Figure 4.47</b> nsTA spectra of $[\text{Ru}(\text{Cl-phen})_2(\text{bpy})]^{2+}$ in the presence of 200 mM $\text{MQ}^+$ (left) and $[\text{Ru}(\text{Cl-phen})_2(4-(\text{OH})-4'-(\text{OMe})\text{bpy})]^{2+}$ in the presence of 200 mM $\text{MQ}^+$ (right) .	189
<b>Figure 4.48</b> nsTA spectra of $[\text{Ru}(\text{Cl-phen})_2(\text{bpy})]^{2+}$ in the presence of 15 mM $\text{BMQ}^+$ (left) and $[\text{Ru}(\text{Cl-phen})_2(4-(\text{OH})-4'-(\text{OMe})\text{bpy})]^{2+}$ in the presence of 150 mM $\text{BMQ}^+$ (right)	189
<b>Figure 4.49</b> nsTA spectra of $[\text{Ru}(\text{dpab})_2(\text{bpy})]^{2+}$ in the presence of 150 mM $\text{MQ}^+$ (left) and $[\text{Ru}(\text{dpab})_2(4,4'-(\text{OH})_2\text{bpy})]^{2+}$ in the presence of 140 mM $\text{MQ}^+$ (right).....	190
<b>Figure 4.50</b> nsTA spectra of $[\text{Ru}(\text{dpab})_2(\text{bpy})]^{2+}$ in the presence of 150 mM $\text{BMQ}^+$ (left) and $[\text{Ru}(\text{dpab})_2(4,4'-(\text{OH})_2\text{bpy})]^{2+}$ in the presence of 200 mM $\text{BMQ}^+$ (right).....	190

<b>Figure 4.51</b> nsTA spectra of $\text{Ru}(\text{dtb})_2(\text{bpy})]^{2+}$ in the presence of 25 mM $\text{MQ}^+$ (left) and $[\text{Ru}(\text{dtb})_2(4,4'-(\text{OH})_2\text{bpy})]^{2+}$ in the presence of 50 mM $\text{MQ}^+$ (right).....	191
<b>Figure 4.52</b> nsTA spectra of $\text{Ru}(\text{dtb})_2(\text{bpy})]^{2+}$ in the presence of 100 mM $\text{BMQ}^+$ (left) and $[\text{Ru}(\text{dtb})_2(4,4'-(\text{OH})_2\text{bpy})]^{2+}$ in the presence of 200 mM $\text{BMQ}^+$ (right).....	191
<b>Figure 4.53</b> nsTA spectra of $\text{Ru}(\text{flpy})_2(\text{bpy})]^{2+}$ in the presence of 200 mM $\text{MQ}^+$ (left) and $[\text{Ru}(\text{flpy})_2(4,4'-(\text{OH})_2\text{bpy})]^{2+}$ in the presence of 200 mM $\text{MQ}^+$ (right).....	192
<b>Figure 4.54</b> nsTA spectra of $\text{Ru}(\text{flpy})_2(\text{bpy})]^{2+}$ in the presence of 200 mM $\text{BMQ}^+$ (left) and $[\text{Ru}(\text{flpy})_2(4,4'-(\text{OH})_2\text{bpy})]^{2+}$ in the presence of 150 mM $\text{MQ}^+$ (right).....	192
<b>Figure 4.55</b> Plot of the rate constant for PT vs. concentration of ruthenium(II) (left) and kinetics at 390 nm (right).....	195
<b>Figure 4.56</b> Back reaction kinetics at 460 nm for $[\text{Ru}(\text{bpy})_2(4,4'-(\text{OH})\text{bpy})]^{2+}$ (left) and $[\text{Ru}(\text{dtb})_2(4,4'-(\text{OH})_2\text{bpy})]^{2+}$ (right) in the presence of 200 mM $\text{MQ}^+$ .....	200
<b>Figure 4.57</b> Back reaction kinetics at 390 nm for $[\text{Ru}(\text{dpab})_2(4,4'-(\text{OH})_2\text{bpy})]^{2+}$ in the presence of 200 mM $\text{BMQ}^+$ .....	200
<b>Figure 4.58</b> Zone diagram relating the reaction mechanism to the free energy for PT and ET.....	204
<b>Figure 5.1</b> (a) Cyclic voltammetry of $[(\text{bpy})_2\text{Ru}(\text{OHbpy})]^{2+}$ in $\text{CH}_3\text{CN} / 0.1 \text{ M TBAPF}_6$ obtained at 0.1 V/s and (b) DPV of $[(\text{bpy})_2\text{Ru}(\text{OHbpy})]^{2+}$ in the presence of 0 – 11 mM DBU. Potentials vs. $\text{Fc}^+/\text{Fc}$ . .....	216
<b>Figure 5.2</b> Cyclic voltammetry of 3 mM AQ in $\text{CH}_3\text{CN} / 0.1 \text{ M TBAPF}_6$ obtained at 0.1 V/s in the presence of (a) 0 M and (b) 15 mM triflic acid). Potentials vs. $\text{Fc}^+/\text{Fc}$ .....	217
<b>Figure 5.3.</b> (a) UV-vis absorption spectrum of $[(\text{bpy})_2\text{Ru}(\text{OHbpy})]^{2+}$ in $\text{CH}_3\text{CN}$ (black) and in the presence of an excess of tetra-n-butylammonium hydroxide. (red) (b) the UV-vis absorption spectrum of $[(\text{bpy})_2\text{Ru}(4-(\text{OMe})\text{bpy})]^{2+}$ in $\text{CH}_3\text{CN}$ . .....	218
<b>Figure 5.4</b> Spectra from the titration of $[\text{Ru}(\text{bpy})_2(4-(\text{OH})\text{bpy})]^{2+}$ with 4-aminopyridine (left) and the linear fit of the concentrations calculated from the absorption spectra (right) .....	219
<b>Figure 5.5</b> (a) Luminescence spectra of $[(\text{bpy})_2\text{Ru}(4-\text{OHbpy})]^{2+}$ in $\text{CH}_3\text{CN}$ at room temperature. (b) Room temperature luminescence of $[(\text{bpy})_2\text{Ru}(4-(\text{OMe})\text{bpy})]^{2+}$ in $\text{CH}_3\text{CN}$ . Excitation wavelength : 450 nm. ....	220
<b>Figure 5.6</b> 77 K emission spectra in 1:1 methanol/ethanol solution for $[\text{Ru}(\text{bpy})_2(4-(\text{OH})\text{bpy})]^{2+}$ and $[\text{Ru}(\text{bpy})_2(4-(\text{O}^-)\text{bpy})]^{2+}$ .....	221
<b>Figure 5.7</b> Ground state reactions of $[\text{Ru}(\text{bpy})_2(4-(\text{OH})\text{bpy})]^{2+}$ ( $\text{Ru}(\text{II})-\text{OH}$ ) and AQ. ..	222

<b>Figure 5.8</b> Reactions of $[\text{Ru}(\text{bpy})_2(4\text{-(OH)bpy})]^{2+}$ ( $\text{Ru(II)-OH}^*$ ) (photoexcited) and AQ in $\text{CH}_3\text{CN}$ .....	223
<b>Figure 5.9</b> Possible excited state reactions between $[\text{Ru}(\text{bpy})_2(4\text{-(OH)bpy})]^{2+}$ ( $\text{Ru(II)-OH}$ ) and AQ (A) .....	224
<b>Figure 5.10</b> The difference absorption spectra generated from UV-Vis spectra and spectroelectrochemistry for ESET (left) and ESPT (right) with AQ .....	226
<b>Figure 5.11</b> TA of AQ in presence of i-prOH : spectrum of the HAQ radical. ....	227
<b>Figure 5.12</b> Simulated PCET product spectrum for the reaction of $[\text{Ru}(\text{bpy})_2(4\text{-(OH)bpy})]^{2+}$ with AQ.....	228
<b>Figure 5.13</b> Luminescence lifetime quenching of $[\text{Ru}(\text{bpy})_2(4\text{-(OMe)bpy})]^{2+}$ by AQ in acetonitrile.....	229
<b>Figure 5.14</b> Luminescence lifetime quenching of $[\text{Ru}(\text{bpy})_2(4\text{-(OH)bpy})]^{2+}$ by AQ in acetonitrile.....	229
<b>Figure 5.15</b> TA spectra of $[(\text{bpy})_2\text{Ru}(\text{OHbpy})]^{2+}$ in $\text{CH}_3\text{CN}$ solution at room temperature in the presence of (a) 0 M and (b) 2.6 mM AQ and 20 mM $\text{TBAPF}_6$ . ....	230
<b>Figure 5.16</b> TA spectra of $[(\text{bpy})_2\text{Ru}(4\text{-(OMe)bpy})]^{2+}$ in $\text{CH}_3\text{CN}$ at room temperature in the presence of (a) 0 and (b) 2.6 mM AQ and 20 mM $\text{TBAPF}_6$ .....	231

## LIST OF TABLES

<b>Table 2.1</b> Electrochemical potentials from cyclic voltammetric measurements presented here in V vs. $\text{Fc}^{+/0}$ . $E_{1/2}$ is used for reversible couples, while $E_p$ is used for irreversible couples. ....	70
<b>Table 2.2</b> Parameters from fitting of emission spectra at 77 K.....	75
<b>Table 2.3</b> Summary of photophysical properties of complexes.....	81
<b>Table 3.1</b> $\text{p}K_a$ 's of pyridine bases, equilibrium constants, and free energies.....	102
<b>Table 3.2</b> Summary of $K_{\text{HB}}$ and $k_q$ values from Stern-Volmer Quenching.....	117
<b>Table 3.3</b> Table of Back Reaction Rate Constants for Selected Bases .....	122
<b>Table 4.1</b> Summary of $\text{p}K_a$ for the ground state, excited state, and one-electron oxidized states. Reference compound $\text{p}K_a$ values are from ref. 14. ....	145
<b>Table 4.2</b> Summary of redox potentials, excited state energies and excited state redox potentials.....	146
<b>Table 4.3</b> Summary of redox potentials and $\text{p}K_a$ 's of quenchers .....	153
<b>Table 4.4</b> Calculated Gibbs free energy for ground state reactions given in kcal/mol ..	158
<b>Table 4.5</b> Calculated Gibbs free energy for excited state reactions given in kcal/mol ..	159
<b>Table 4.6</b> Summary of absorbance features for simulated ESPT products.....	165
<b>Table 4.7</b> Summary of absorbance features for simulated ESET products.....	167
<b>Table 4.8</b> Summary of quenching rate constants .....	186
<b>Table 4.9</b> Rate Dependence on the Concentration of Ru(II) for PT .....	194
<b>Table 4.10</b> Summary of PT rate constants for reaction following ESET.....	196
<b>Table 4.11</b> Summary of selected rate constants for back PCET .....	199
<b>Table 4.12</b> Summary of KIE Ratios .....	202
<b>Table 5.1</b> Summary of redox and excited state energies.....	221
<b>Table 5.2</b> Summary of Free Energies for ET, PT and PCET Reactions .....	225
<b>Table 5.3</b> Lifetimes of Ru(II) complexes and quenching rate constants with AQ.....	228

## Chapter 1: Role of Proton Coupled Electron Transfer and Proton Transfer in Solar Fuels Generation

### 1.1 Proton-Coupled Electron Transfer in Photosynthesis

Natural photosynthesis is a process by which photosynthetic organisms generate oxygen and carbohydrates through the oxidation of water and carbon dioxide reduction. The reactions of photosynthesis in bulk are carried out in structures embedded in the chloroplast's thylakoid membrane of photosynthetic organisms. These photosynthetic components include photosystem II (PSII), the cytochrome  $b_6$  complex, photosystem I (PSI), and ATP Synthase. PSII is responsible for the photoinduced oxidation of water, where electrons collected from this oxidative process are used to supply PSI for the reduction of  $\text{NADP}^+$  to NADPH.<sup>1</sup> Ultimately, reduction of carbon dioxide via the Calvin Cycle occurs in the chloroplast stroma using NADPH generated in PSI.<sup>2</sup> In a publication by Moore and Brudvig, they break down photosynthesis into five phases: initial absorption of light, energy transfer from antennas to the reaction center, charge separation, stabilization of charge-separated species, and synthesis of stable chemical products.<sup>1</sup>

In photosynthesis, the four-electron, four-proton water oxidation process is carried out in PSII. Initially, light is absorbed through antenna systems and transferred via chlorophyll-binding proteins to the reaction center. Here,  $\text{P}_{680}$  is excited and begins the cascade of electron transfer events that ultimately result in a spatially separated electron-hole pair, whereby the hole resides on the  $\text{P}_{680}$  chromophore and the electron on plastoquinone-A ( $\text{Q}_A$ ). From here, the electron is further shuttled away from  $\text{P}_{680}^+$  via plastoquinone-B ( $\text{Q}_B$ ), which is reduced to plastoquinol after absorption of a second photon of light and transfer of a second electron; the overall reduction includes two protons as well. The reduced  $\text{Q}_B$

shuttles electrons to the cytochrome  $b_{f6}$  complex, where electrons are moved to plastocyanin (a protein), which will donate its electrons to PSI. Along with this, the  $P_{680}^+$  is reduced by a tyrosine residue, referred to as  $Y_z$ , thereby resetting the system for photon absorption.

$P_{680}$  is the driving force behind the removal of electrons from water at the oxygen-evolving complex (OEC) in PSII, with a standard reduction potential of 1.2 V vs. a standard hydrogen electron (SHE) reference. This is more than enough energy to drive the oxidation of water to  $O_2$ , which occurs at a standard reduction potential of 0.82 V vs. SHE at pH 7. The OEC is comprised of a tetramanganese cluster with calcium. Because each  $P_{680}^+$  serves as a single-electron oxidant, it takes four absorption events to oxidize fully one water molecule. The four sequential light absorption events that provide the oxidizing equivalents to remove electrons from water are known as the Kok cycle. It consists of four states labeled  $S_0$  to  $S_4$ . The generation of  $S_1$  through  $S_4$  is light-induced, and the regeneration of  $S_0$  from  $S_4$  occurs spontaneously in the dark. <sup>3</sup>

Before activation of the OEC,  $P_{680}^+$  oxidizes  $Y_z$  to  $Y_z^{\bullet+}$ . Ultimately,  $Y_z^+$  will serve to oxidize the OEC by one electron. It was suggested that oxidation of  $Y_z$  by  $P_{680}^+$  must occur in conjunction with the phenol's deprotonation by a neighboring histidine residue, His190. This so-called multi-site proton-coupled electron transfer (MS-PCET) reaction was interrogated by removing the His190 residue, which resulted in photosynthesis becoming inoperable.<sup>4,5</sup> This MS-PCET reaction provides a pathway for reducing  $P_{680}^+$  with a larger driving force than in the absence of His190, a whopping free energy of -8.4 kcal/mol for MS-PCET compared to +1.6 kcal/mol for electron transfer (ET) alone.<sup>1</sup> Figure 1.1 shows a simplified route for the reactions of photosynthesis described above. <sup>6</sup>

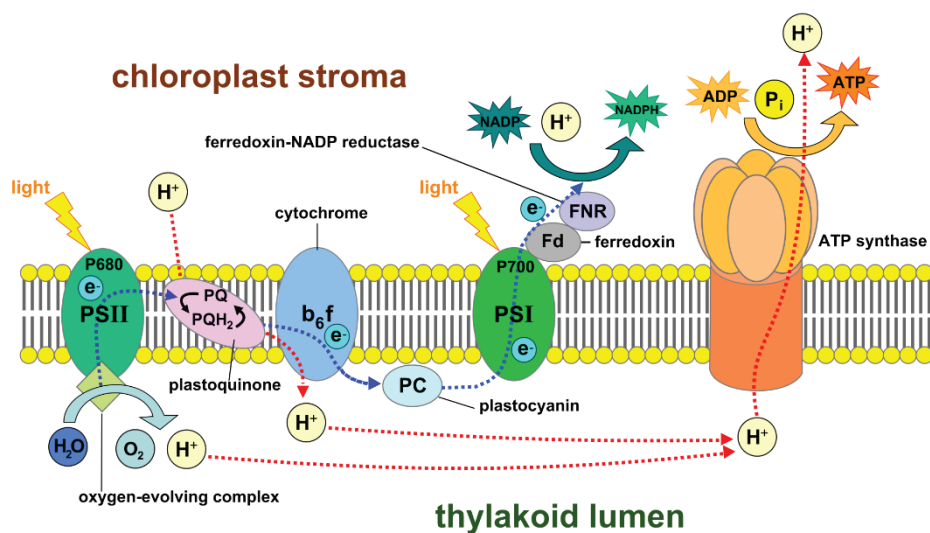


**Figure 1.1** Simplified diagram of thylakoid membrane structures. Image reproduced from Thylakoid-Wikipedia by Somepics redistributed under CC BY-SA 4.0 license.

The example of proton-coupled electron transfer in the water oxidation reaction of photosynthesis highlights the thermodynamic advantage created by avoiding charge build-up on reactive intermediates in schemes involving the management of multiple protons and electrons. Developing a greater understanding of the role of proton-coupled electron transfer (PCET) reactions is pivotal to realizing light to chemical energy conversion or the generation of solar fuels. Invoking theoretical, computational studies and studying molecular systems that utilize PCET reaction pathways are crucial to accomplishing artificial photosynthesis for the generation of solar fuels.

## 1.2 Theoretical Models for Proton Coupled Electron Transfer Reactions

The exploitation of PCET for artificial photosynthesis requires a detailed understanding of the factors, both kinetic and thermodynamic, that govern these reactions. Over the past 40 years, researchers have made great strides to develop a theoretical understanding of proton-coupled electron transfer. This theoretical work has been aided by the experimental efforts of many in the field.<sup>7-15</sup> A well-respected theoretical framework of PCET reactions has been developed extensively by Hammes-Schiffer and colleagues.<sup>13,16-21</sup> In this model, an understanding of how electron transfer and proton transfer can co-occur is established, building from Marcus theory of electron transfer.

In the work of Hammes-Schiffer, systems in which both adiabatic and nonadiabatic proton motion are considered. For the intent of this body of research, the most relevant model will be discussed in detail, that is, the nonadiabatic regime for proton-coupled electron transfer. References are listed that provide a complete picture of the theory developed by Hammes-Schiffer and coworkers. In the case of nonadiabatic proton-coupled electron transfer, the vibronic coupling between the reactant and product potential energy surfaces is considered to be much less than the Boltzmann constant and temperature product  $k_B T$ , or thermal energy. This situation is found by Hammes-Schiffer's work to be generally true for systems that exhibit concerted proton and electron transfer (CEPT). For adiabatic electron transfer reactions, the coupling of reactant and product states is very strong, and a different approach must be taken to model kinetics for these reactions.

To begin, a review of Marcus theory for electron transfer is necessary. Marcus theory provides a way to understand the relationship between the nuclear and electronic factors

that influence the rate of electron transfer processes. Marcus theory predicts a parabolic dependence of the natural log of the rate constant for an electron transfer ( $\ln k_{ET}$ ) reaction on the Gibbs free energy,  $\Delta G^\circ$ , or driving force for the reaction. The semiclassical Marcus expression for this relationship is given in equation 1.1.<sup>22-25</sup>

$$k_{ET} = \frac{2\pi}{\hbar} \frac{H_{DA}^2}{\sqrt{4\pi k_B T}} \exp \left[ -\frac{(\Delta G^\circ + \lambda)^2}{4\lambda k_B T} \right] \quad (1.1)$$

In the expression above,  $H_{DA}$  is the electronic coupling factor governed by the extent of wavefunction overlap between the donor and acceptor species,  $k_B$  is the Boltzmann constant,  $T$  is the temperature, and  $\lambda$  is the combined term for both inner sphere and outer-sphere reorganization energies. Inner sphere reorganization energy is a result of the changes in bond length and bond angles in response to the changing charge distribution during the electron transfer process. Outer sphere reorganization is related to the change in the solvent dielectric due to the change in charge distribution. These values can be computed using the expressions shown in equations 1.2-1.4. In equation 1.2,  $\lambda_i$  is the inner sphere reorganization energy which is summed over all bonds,  $j$ , involved,  $\lambda_o$  is the outer sphere reorganization energy. In equation 1.3,  $n$  is the number of bonds involved,  $d_p$  and  $d_r$  are the reactant and product equilibrium bond lengths, and  $f$  is the force constant. In equation 1.4,  $\epsilon_{op}$  is the optical dielectric constant for the solvent,  $\epsilon_s$  is the static dielectric constant for the solvent,  $R$  is the donor and acceptor distance,  $r_D$  and  $r_A$  are the donor and acceptor radii.<sup>23</sup>

$$\lambda = \lambda_i + \lambda_o \quad (1.2)$$

$$\lambda_i = n \left[ \frac{1}{2} \sum_j f_j (d_p - d_r)^2 \right] \quad (1.3)$$

$$\lambda_o = \frac{e^2}{4\pi\epsilon_0} \left( \frac{1}{2r_D} - \frac{1}{2r_A} + \frac{1}{R} \right) \left( \frac{1}{\epsilon_{op}} - \frac{1}{\epsilon_s} \right) \quad (1.4)$$

The Marcus expression can be evoked to better understand the nature of an electron transfer reaction. Typically, for a series of homologous compounds, the electron transfer

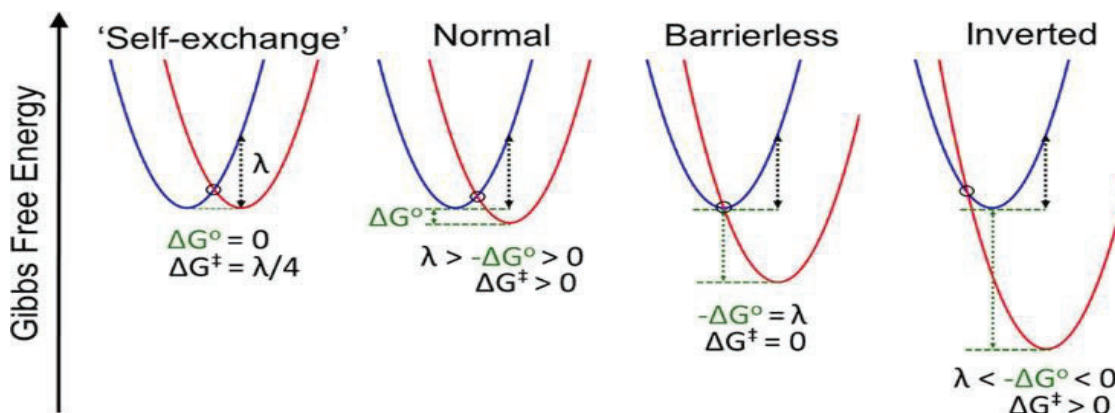


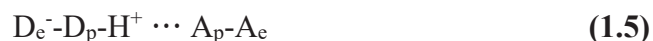
**Figure 1.2** Potential energy surfaces showing categories of electron transfer reactions with respect to  $\Delta G^\circ$  and  $\lambda$ . Reprinted (adapted) with permission from J. Chem. Educ. 2019, 96, 11, 2450-2466. Copyright 2019 American Chemical Society.

rate constants can be measured and interpreted regarding the driving force and fitting of the data with equation 1.1. From this fitting, the individual reactions can be interpreted in terms of the barrier to reaction. Although the rate is expected to increase with increasing driving force, at a certain point, the increase in driving force will lead to a reduction in the rate of electron transfer. This region is referred to as the inverted region.

Preceding the inverted region are the normal and activationless regions. What governs which regime the reaction lies in is the magnitude of the driving force in relation to the reorganization energy. For the normal region, it is expected that  $-\Delta G^\circ$  is less than  $\lambda$ , while in the barrierless region,  $-\Delta G^\circ$  is equal to  $\lambda$  and in the inverted region,  $-\Delta G^\circ$  is greater than  $\lambda$ ; this is expressed in the potential energy surface shown in figure 1.2. It can be understood that when the reaction is barrierless, the crossing point between the reaction and product surfaces occurs at the potential energy minimum for the reactants, leading to an activation

energy,  $\Delta G^\ddagger$ , of zero. In contrast,  $\Delta G^\ddagger$  will be greater than zero for both normal and inverted reactions.

While Marcus theory provides a context for understanding how driving force influences the dynamics of an electron transfer reaction, it does not allow for the understanding of how the transfer of proton can coincide with the transfer of an electron. Hammes-Schiffer and coworkers' theoretical framework provides a means of reconciling electron transfer coupled to proton transfer. Before introducing these theoretical concepts, it is essential to define the types of coupled proton and electron transfer reactions. There are four states of the bimolecular system represented in equations 1.5-1.8 Equation 1.5 shows the initial state of the system, with the electron and proton residing on the donor, 1.6 shows proton transfer only between D and A, 1.7 depicts electron transfer from the donor to the acceptor, and finally 1.8 shows the electron and proton transferred to the acceptor.<sup>20</sup> Different sites can be involved in ET/PT processes on the donor and acceptor, indicated as  $D_e$  and  $D_p$  as well as  $A_e$  and  $A_p$ .



In the literature encompassing the body of work considered under the umbrella of proton-coupled electron transfer, there are two categories of reaction that the four-state model describes, these include concerted processes—CEPT and hydrogen atom transfer (HAT)—and sequential processes in which either an electron transfer occurs before proton

transfer (ETPT) or a proton is transferred before the electron transfer (PTET). The theoretical model reviewed here refers to reactions that are considered CEPT in nature. HAT reactions are not included in this interpretation as typically they are strongly adiabatic, and implicit assumptions made in this model do not apply. What distinguishes a CEPT reaction from a HAT reaction is the orbital origination of the transferring electron and proton; in HAT, both the electron and proton will generally originate from the same orbital or bond, causing a substantial degree of vibronic coupling between the electron and proton. Unlike HAT reactions, in CEPT, the electron and proton originate from different sites on the donor molecule or maybe from independent species in solution, as is the case for multi-site proton-coupled electron transfer (MS-PCET).

In reconciling proton motion in conjunction with electron motion, vibronic states must be considered to incorporate the hydrogen ion's nuclear motion. In this theory, proton motion and electron motion are described by vibronic coupling between donor and acceptor states, rather than electronic coupling in the case of ET theory. Traditionally, electronic transitions can be described in terms of the Born-Oppenheimer approximation, whereby the electronic and nuclear wavefunctions can be factored out from one another. In this approximation, when the electronic coupling matrix element,  $H_{DA}$ , become zero, a transition is considered to be forbidden.<sup>26</sup> From experimental work, this is not the case; even though a transition can be regarded as electronically forbidden, it may still occur because electronic and nuclear wavefunctions cannot always be considered separable from one another. This inability to fully separate electronic and nuclear wavefunctions demonstrates the phenomenon of vibronic coupling. With proton-coupled electron transfer reactions, the degree of vibronic coupling is of pivotal importance. For CEPT reactions,

Hammes-Schiffer and coworkers have derived a rate expression that describes these vibronically coupled, weakly nonadiabatic transfers of electrons and protons. In a 2015 Perspective for the *Journal of the American Chemical Society*, Hammes-Schiffer describes vibronic coupling as a "product of the electronic coupling and the overlap integral of the reactant and product vibrational wavefunctions."<sup>18</sup>

Considering the criteria above for describing a vibronically coupled system in which PCET is likely to occur, the rate constant expression for this category of reaction is shown in equation 1.9:

$$k^{EPT} = \sum_{\mu} P_{\mu} \sum_{\nu} \frac{|V^{el} S_{\mu\nu}|^2}{\hbar} \sqrt{\frac{\pi}{\lambda k_B T}} \exp \left[ \frac{(\Delta G_{\mu\nu}^0 + \lambda)^2}{4\lambda k_B T} \right] \quad (1.9)$$

Here,  $P_{\mu}$  describes the Boltzmann probability for the reactant state,  $\mu$ ,  $V^{el}$  is the electronic coupling,  $S_{\mu\nu}$  is the overlap between the reactant and product vibrational wavefunctions for all states  $\mu$  and  $\nu$ , and  $\Delta G_{\mu\nu}^0$  is the free energy for the reaction for each of the combinations of  $\mu$  and  $\nu$ .<sup>18,27</sup> This expression shares similarities with the above semiclassical Marcus expression for nonadiabatic electron transfer. Still, in this case, the electronic coupling matrix element,  $H_{DA}$ , is replaced by the product  $V^{el} S_{\mu\nu}$ , which describes the electronic coupling and the vibrational overlap, and therefore, vibronic coupling for the system. The

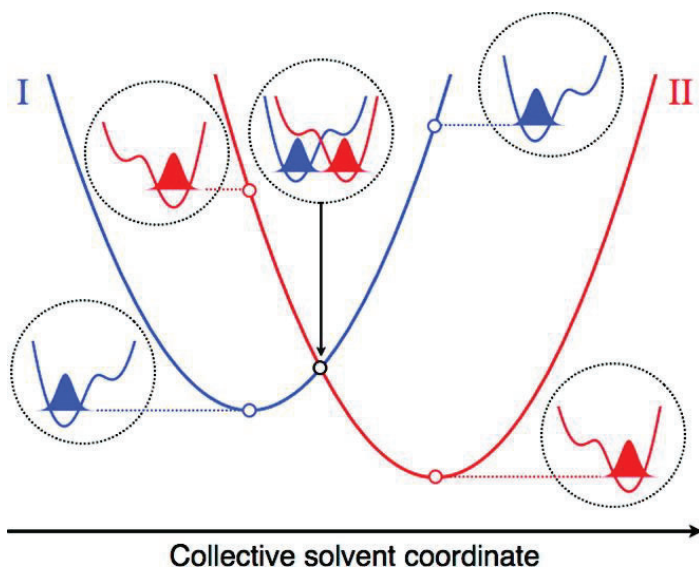


**Figure 1.3** Reactant (I) and Product (II) potential energy surfaces for vibronic states is shown. The open circles show the proton vibrational states associated with these points on the potential energy surfaces. The potential energy surfaces are on a collective solvent coordinate for both the proton and electron. Reprinted (adapted) with permission from J. Phys. Chem. B, Vol. 112, No. 45, 2008 Copyright 2008 American Chemical Society.

transition from the reactant to product potential energy surfaces is mediated through solvent fluctuations. Figure 1.3 shows the reactant and product energy surfaces as a function of the collective solvent coordinate. The equation expressed in equation 1.8 is like the modified Marcus equation derived for nonadiabatic electron transfer by Bixon and Jortner. Hammes-Schiffer notes in her work that the major difference is that in PCET among other differences, proton motion is coupled to solvent fluctuations, occurs at higher frequency.<sup>18</sup>

With this framework in mind, the development of systems for which proton-coupled electron transfer is an operable mechanism can be accomplished. Knowing the influence of vibrational wavefunction overlap on the overall reaction rate can help one formulate an

understanding of how to design a system for which the rate of electron-proton transfer is competitive with the rate of electron transfer.

It is important to emphasize one final criterion that affects the observation of PCET, which is the distance dependence for the vibrational wavefunction overlap. The term  $S_{\mu\nu}$ , or Huang-Rhys factor, can be described in terms of the donor and acceptor distance,  $r$ , as shown in equation 1.10, where  $\beta$  is an attenuation factor, and  $r_0$  is the equilibrium donor and acceptor distance.<sup>27,28</sup>

$$S_{\mu\nu}(r) = S_{\mu\nu}(r_0) \exp \left[ -\frac{\beta}{2}(r - r_0) \right] \quad (1.10)$$

Given the above considerations, to exploit a proton-coupled electron transfer pathway, a system needs to have a reasonable degree of overlap between the donor and acceptor, provided through intermolecular hydrogen bonding interactions. The distance dependence can influence whether PCET is competitive with ET.

### 1.3 Redox Leveling and Thermodynamics of PCET Reactions

The free energy for the reaction,  $\Delta G^\circ$ , is fundamental in the equations from the previous section that describe both electron and proton-coupled electron transfer dynamics. Given the possibility of electron transfer occurring over PCET, the relative free energies for the reactions must be considered. The free energy for electron transfer can be calculated from the donor's oxidation potential,  $D^{+/0}$ , and the reduction potential of the acceptor,  $A^{-/0}$ . The summation of the donor and acceptor redox potentials can be taken as the minimum energy required for an electron transfer reaction. These values are readily obtained experimentally from electrochemical measurements.

In generating the oxidized donor,  $D^+$ , and reduced acceptor,  $A^-$ , there is energetic consideration to make in solvating the charged species generated from electron transfer. Meyer et al. generalize this effect by considering the charged species' solvation through a Born solvation model. In this model, for redox couple,  $Ox_2^{(n+2)+}/Red_2^{(n+1)+}$  ( $E_2^{\circ'}$ ) and  $Ox_1^{(n+1)+}/Red_1^{n+}$  ( $E_1^{\circ'}$ ):

$$\Delta E^{\circ'} = E_2^{\circ'} - E_1^{\circ'} = \left(\frac{2e^2}{rD_s}\right) + I'_{n+1} - I'_n = \left(\frac{2e^2}{rD_s}\right) + \Delta I' \quad (1.11)$$

in equation 1.11, where the energy for the redox process is changed by the addition of the charging term; in other words, the term is associated with the change in charge for each species generated through the redox reaction.<sup>27</sup> The charging term is dependent on  $e$ , the elementary charge,  $D_s$ , the static dielectric constant, and  $r$ , the spherical radius of the Ox/Red couple. The term  $I$  is the ionizing energy for promoting an electron to the surface of the spherical complex.<sup>27</sup> The charging term becomes consequential when looking at reactions in a solvent with low dielectric constants. Therefore, to reduce the charging term, having a system with no net change in the redox species' charge becomes essential. A system in which this is feasible is one that undergoes a proton transfer along with electron transfer. When this occurs, the change in charge on the products generated from the PCET reaction is zero, and the charging term reduces to zero. This effect has been termed "redox potential leveling". Redox potential leveling is an important thermodynamic implication of proton-coupled electron transfer reactions. It demonstrates the ability of a system to undergo multiple redox/proton transfer events without generating high-energy intermediate species. This is of great importance to the development of systems for artificial photosynthesis, as the generation of solar fuels necessarily requires the transfer of multiple

electrons and protons. This redox potential leveling effect is thought to help allow the multiple electron and proton transfers in oxygen evolution during photosynthesis.<sup>2</sup> The issue with charge build-up in a system is that if the redox process occurs first, then the proton transfer process is in kinetic competition with back electron transfer. If the kinetics for back electron transfer are fast relative to proton transfer, then reduction of charge will occur in a nonproductive back reaction. From a thermodynamic perspective, reducing charge reduces the free energy for the reaction, making electron-proton transfer reactions generally more thermodynamically favorable over ET or PT transfer reactions.

When exploring systems that are capable of PCET, thermodynamic considerations must be made. Proton-coupled electron transfer reaction thermodynamics can be defined by the constituent stepwise reaction free energies. For instance, the free energy for proton transfer, followed by electron transfer or the free energy for electron transfer followed by proton transfer can be calculated. The sum of the free energies for each set of processes (PTET or ETPT) will be equivalent as defined by Hess' Law.<sup>29</sup> The total free energy for an electron/proton transfer is path independent. Square schemes have been used as a convenient way to represent the three available reaction paths— CEPT, ETPT, or PTET— as shown in figure 1.4.

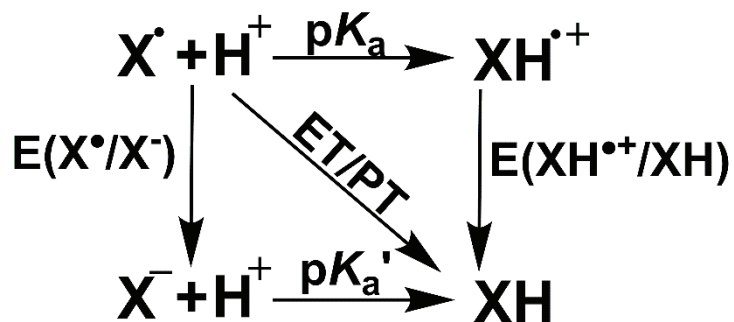


**Figure 1.4** Square scheme depicting stepwise reaction pathways (ETPT and PTET) and concerted path (diagonal).

In the square scheme, the free energy for ET can be calculated from the  $E_{1/2}$  values obtained from electrochemical measurements, while  $pK_a$ 's can be readily measured through titration versus pH (for aqueous systems) or with respect to a reference compound with a known  $pK_a$  value in the nonaqueous solvent of interest. These values can be readily expressed in terms of free energy using the following equations:<sup>29,30</sup>

$$\Delta G_{PT}^{\circ} = -RT \ln(K_a) = 2.303RT pK_a = -(1.37 \text{ kcal mol}^{-1}) pK_a \text{ (at 298 K)} \quad (1.12)$$

$$\Delta G_{ET}^{\circ} = -nFE^{\circ} = -(23.06 \text{ kcal mol}^{-1} \text{ V}^{-1}) E^{\circ} \quad (1.13)$$

$$\Delta G(H^+/e^-) = 2.3RT pK_a(XH) + FE(X^{\bullet}/X^+) = FE(XH^{\bullet+}/XH) + 2.3RT pK_a(XH^{\bullet+}) \quad (1.14)$$

In addition to determining the free energy for ET and PT reactions, these values can be used to calculate the bond dissociation free energy (BDFE) for the homolytic bond cleavage of a hydrogen atom from a compound of interest. Equation 1.14 shows the calculation of a BDFE in terms of measurable values,  $pK_a$  and  $E^{\circ}$ . It is important to note that this is a free energy for H-atom loss and therefore includes the entropy for generating radical ions through a PCET reaction. In equation 1.15, the additional term,  $C_{g,sol}$ , describes the free energy for reduction of a proton to an H-atom. This value has been measured in a variety of solvents, including acetonitrile.<sup>30</sup>

$$\text{BDFE}_{\text{sol}}(X-H) = 1.37 pK_a + 23.06 E^{\circ} + C_{g,sol} \quad (1.15)$$

Equations 1.9-1.12 describe the thermochemical parameters for a single reactant in a bimolecular PCET reaction. In order to calculate the free energy for PCET, ET, and PT between two species the  $pK_a$  values for the two species in both oxidation states represented in the square scheme plus the reduction potentials for each compound and their respective

conjugate acids must be known. Figure 1.5 shows a square scheme for a bimolecular PCET reaction. Equation 1.16 shows the calculation of the free energy for PCET for the reaction in figure 1.5.

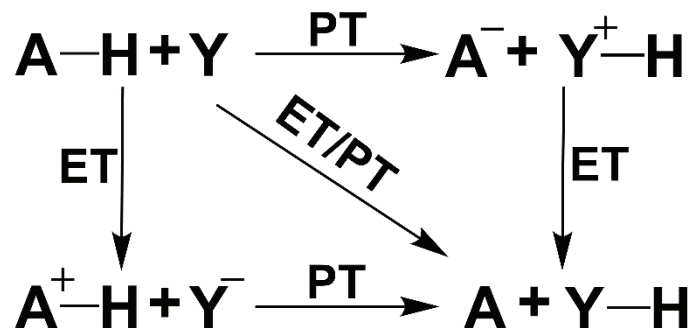


**Figure 1.5** Square scheme for a bimolecular PCET reaction

$$\begin{aligned}
 \Delta G(H^{+}/e^{-}) &= 2.3RT(pK_a(AH) - pK_a(YH^{+})) + F(E(A^{\bullet}/A^{-}) - E(YH^{+}/YH^{\bullet})) = \\
 &F(E(AH^{\bullet+}/AH) - E(Y/Y^{\bullet-})) + 2.3RT(pK_a(AH^{\bullet+}) - pK_a(YH^{\bullet})) \quad (1.16)
 \end{aligned}$$

Understanding the thermochemical landscape for ET, PT, and PCET reactions, allows one to formulate an idea of what the most thermodynamically favored reaction pathway will be. This information can serve to corroborate experimental findings that indicate a specific reaction pathway. In terms of reaction free energy, ignoring any activation barrier that may be present, the most thermodynamically favored pathway will always be the PCET pathway over ET or PT.<sup>29</sup> This is due to the fact that energy of the product state is necessarily downhill from any intermediate species that will be formed in a stepwise reaction. This can be proven out by taking a system for which the values of  $E^{\circ}$  and  $pK_a$  are known and calculating the relative free energies of reaction for the stepwise and concerted processes. Bearing in mind this information, though thermochemical calculations are of

extreme importance in understanding the viability of a bimolecular reaction involving PCET, they alone cannot provide a verification of reaction mechanism. Thus, further experiments to probe the kinetics of reaction or possibly observe intermediate species formed in a reaction must be undertaken to fully elucidate the reaction mechanism.

#### **1.4 Combining Light Absorption with PCET and Applications to Solar Fuels**

In a scheme for developing solar fuels, or storable liquid fuels that are produced using photons as energy, PCET reactions become of extreme value for reducing the total energy required for the process. In an ideal system for solar fuels production, water splitting driven by light absorption processes would provide electrons and protons for the reduction of carbon dioxide. While this can be done electrochemically, light absorption has an advantage by making use of excited state energy to generate the potential energy source for driving forward these energy intensive redox processes. Coupling light absorption with PCET would allow for excited-state energy to be funneled into a catalyst without building up charge, leaving the system primed for secondary redox chemistry, a requirement for the oxidation of water or reduction of carbon dioxide.

The concept of incorporating light absorption into PCET reactions is not a new endeavor.<sup>1,3,31-34</sup> Researchers have investigated systems utilizing transition metal complexes as light absorbers that participate in PCET reactions. A recent review highlights several of these systems.<sup>35</sup> With an understanding of the thermodynamic requirements for a PCET reaction to occur, understanding the basics of light absorption processes will provide a firm foundation for the development of systems in which light absorption is brought together PCET reactions that drive forward multi-electron, multi-proton transfer reactions for the generation of liquid fuels.

For many studies related to artificial photosynthesis, transition metal complexes are of interest due to their broad absorbance in the visible region of the electromagnetic spectrum. This region is of particular interest given that it overlaps with the solar spectrum. Complexes of ruthenium, iridium, and rhenium have been investigated for their reactivity toward PCET.<sup>34,36–38</sup>

This work will focus on the photoinduced reactions of ruthenium (II) complexes, and thus a brief description of ruthenium (II) properties is appropriate. The ruthenium (II) cation is  $d^6$  metal that is low spin, despite the nature of the ligand field because of a larger degree of octahedral field splitting. This makes the ground state a  $(t_{2g})^6$  configuration. The most well studied ruthenium complex for its excited-state properties is ruthenium (II) tris(2,2'-bipyridine),  $[\text{Ru}(\text{bpy})_3]^{2+}$ .<sup>39,40</sup> This complex has three chelating diimine ligands which serve as good  $\sigma$  donors through the lone pair on the nitrogen, while the delocalized aromatic orbitals act as good  $\pi$ -donor and  $\pi^*$ -acceptors. The complex is of lowered symmetry from an octahedral point group ( $O_h$ ), because the chelating 2-2'-bipyridine ligands form a propellor like structure around the metal center. This propellor structure reduces the symmetry from octahedral to  $D_3$ .<sup>41</sup>

Upon absorption of a photon, the initial singlet metal-to-ligand charge transfer ( $^1\text{MLCT}$ ) state is formed. Rapid inner system crossing aided by a high degree of spin-orbit coupling due to the nature of the heavy ruthenium metal center, proceeds to generate the triplet state, ( $^3\text{MLCT}$ ) in which the spin orientation of the electron is no longer paired with the electron now in the singly occupied metal  $t_{2g}$  orbital. The nature of the  $^3\text{MLCT}$  is one of  $d \rightarrow \pi^*$ , promoting an electron from the highest occupied molecular orbital (HOMO), a metal  $t_{2g}$  orbital, to the lowest unoccupied molecular orbital on the ligand, a  $\pi^*$  antibonding

orbital. Because this  $^3\text{MLCT}$  state is no longer spin-paired with the ground state, the transition is spin forbidden resulting in slow relaxation to the ground state on the order of nanoseconds to microseconds. The intersystem crossing efficiency from the singlet excited state to the triplet state is considered to be nearly 100%. Relaxation of the electron back to the singlet ground state occurs through a combination of radiative and nonradiative processes.<sup>41</sup>

Spectroscopic features of  $[\text{Ru}(\text{LL})_3]^{2+}$  (LL=diimine ligand) complexes show strong absorbance in the ultraviolet corresponding to ligand-centered  $\pi \rightarrow \pi^*$  transitions, the absorbance between 420 and 500 nm corresponds to the MLCT state of the complex.<sup>41</sup> Due to the lowest energy excited-state being a triplet, the emission band of the triplet state is substantially shifted to lower energy versus the corresponding absorption band.

Ruthenium complexes containing polypyridyl ligands are of interest for photoinduced electron transfer and proton-coupled electron transfer reactions due to their low metal centered oxidation potentials (1.26 V vs SCE in aqueous solution), their long-lived excited-states (around 600 ns), and excited-state energy (2.12 eV). Taking the difference in the Ru (III/II) potential and the Ru(II)\* energy gives a total potential energy for reduction of a substrate by ruthenium of about -0.86 V vs. SCE.<sup>41</sup> This energy can be used to drive reactions without the need of additional thermal energy. As such, these complexes have been investigated for their potential role in photoinduced PCET reactions for solar fuels generation.

Important to natural photosynthesis is the generation of long-lived, charge-separated species. This is accomplished in PSII through a series of electron and proton transfer reactions involving the  $\text{Y}_z$ -His190 pair as well as  $\text{Q}_B$ . In a *Journal of the American*

*Chemical Society* communication, Pannwitz and Wenger exemplify the complex generation of long-lived, charge separated species aided by PCET in a molecular triad consisting of a ruthenium metal center as the primary light absorber. Figure 1.6 shows the comparison between PSII, “classical” donor acceptor dyads, and the molecular triad presented in their work.<sup>42</sup>

The molecular triad incorporates a ruthenium polypyridyl core as the photosensitizer, which upon excitation serves to reduce the pendant 4,4'-bipyridinium, which is protonated upon reduction. To diminish back electron transfer, a phenol serves to reduce the Ru<sup>III</sup> back to Ru<sup>II</sup>, while releasing a proton. Without the PCET reactions at the phenol and 4,4'-bipyridinium, back reaction to reform Ru(II), would not allow for efficient and long-lived charge separation. Utilizing PCET allows for no net charge buildup in the system, which allows for storage of 1.2 eV of light energy.<sup>42</sup> This system can be seen as model for the development of charge separated states that can be used to drive productive reactions to generate solar fuels.

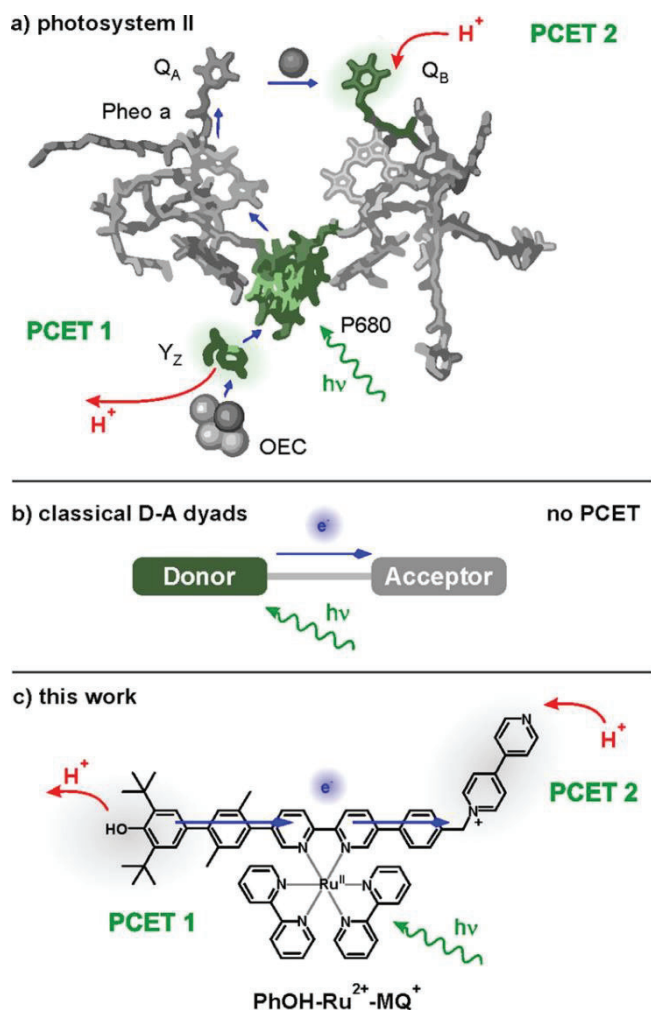


**Figure 1.6** Cascade of PCET reactions in PSII (a), classical D-A dyads (b), molecular triad featuring a ruthenium photosensitizer. Reprinted (adapted) with permission from *Journal of the American Chemical Society* 2017, 139 (38), 13308–13311. <https://doi.org/10.1021/jacs.7b08761>. Copyright (2017) American Chemical Society.

## 1.5 Conclusions

In summary, the above section has outlined experimental criteria for proton-coupled electron transfer reactions and their applicability to both natural and artificial photosynthetic schemes. PCET reactions are pivotal to the viability of natural photosynthesis, as proven through studies in which the proton accepting His190 was replaced phenylalanine, and oxygen evolution from photosynthetic algae ceased to occur.

In addition, in natural photosynthesis, PCET is essential for lowering the free energy for water oxidation.

Using natural photosynthesis as a model for designing systems that produce usable fuels, whether they be hydrogen, in the case of hydrogen evolution reactions, or reduced carbon dioxide products (formic acid, methanol, methane), PCET provides a means for reducing the free energy for these reactions, as well as stabilizing reactive intermediates, generating the possibility of executing multiple redox reactions that are necessary for solar fuels production.

A theoretical understanding of PCET reaction dynamics, as well as a procedure for mapping the thermodynamics for PCET reactions provides insight into designing systems that utilize PCET. Incorporation of long-lived excited states furthers the development of artificial photosynthetic schemes.

With the overview of PCET reactivity from this chapter, the following chapters will explore reactions of proton transfer, electron transfer and proton-coupled electron transfer originating from ruthenium (II) excited-states. Chapter 2 will provide an experimental background on the synthesis and characterization of complexes reported on in subsequent chapters. Chapter 3 will serve to provide an understanding of photoinduced proton transfer reactions and the influence of hydrogen bonding, an important aspect of PCET reactions. Chapter 4 will outline a series of ruthenium complexes with substituted diimine ligands and their reactivity with two organic compounds that can accept a proton and an electron. Lastly, Chapter 5 will discuss the use of a neutral substrate, 9,10-anthraquinone, and its reactivity with a ruthenium (II) complex capable of acting as one-electron, one-proton donor.

## CHAPTER 1 REFERENCES

- (1) Moore, G. F.; Brudvig, G. W. Energy Conversion in Photosynthesis: A Paradigm for Solar Fuel Production. *Annu. Rev. Condens. Matter Phys.* **2011**, *2* (1), 303–327. <https://doi.org/10.1146/annurev-conmatphys-062910-140503>.
- (2) Gagliardi, C. J.; Vannucci, A. K.; Concepcion, J. J.; Chen, Z.; Meyer, T. J. The Role of Proton Coupled Electron Transfer in Water Oxidation. *Energy Environ. Sci.* **2012**, *5* (7), 7704. <https://doi.org/10.1039/c2ee03311a>.
- (3) Gagliardi, C. J.; Westlake, B. C.; Kent, C. A.; Paul, J. J.; Papanikolas, J. M.; Meyer, T. J. Integrating Proton Coupled Electron Transfer (PCET) and Excited States. *Coord. Chem. Rev.* **2010**, *254* (21–22), 2459–2471. <https://doi.org/10.1016/j.ccr.2010.03.001>.
- (4) Debus, R. J.; Barry, B. A.; Babcock, G. T.; McIntosh, L. Site-Directed Mutagenesis Identifies a Tyrosine Radical Involved in the Photosynthetic Oxygen-Evolving System. *Proc. Natl. Acad. Sci. U. S. A.* **1988**, *85* (2), 427–430.
- (5) Roffey, R. A.; Kramer, D. M.; Govindjee; Sayre, R. T. Lumenal Side Histidine Mutations in the D1 Protein of Photosystem II Affect Donor Side Electron Transfer in *Chlamydomonas Reinhardtii*. *Biochim. Biophys. Acta BBA - Bioenerg.* **1994**, *1185* (3), 257–270. [https://doi.org/10.1016/0005-2728\(94\)90240-2](https://doi.org/10.1016/0005-2728(94)90240-2).
- (6) Wikipedia contributors. *Thylakoid* — *Wikipedia, The Free Encyclopedia*; 2021. [https://upload.wikimedia.org/wikipedia/commons/4/49/Thylakoid\\_membrane\\_3.svg](https://upload.wikimedia.org/wikipedia/commons/4/49/Thylakoid_membrane_3.svg) (Accessed April 6, 2021)
- (7) Cukier, R. I. A Theory That Connects Proton-Coupled Electron-Transfer and Hydrogen-Atom Transfer Reactions. *J. Phys. Chem. B* **2002**, *106* (7), 1746–1757. <https://doi.org/10.1021/jp012396m>.
- (8) Damrauer, N. H.; Hodgkiss, J. M.; Rosenthal, J.; Nocera, D. G. Observation of Proton-Coupled Electron Transfer by Transient Absorption Spectroscopy in a Hydrogen-Bonded, Porphyrin Donor–Acceptor Assembly. *J. Phys. Chem. B* **2004**, *108* (20), 6315–6321. <https://doi.org/10.1021/jp049296b>.
- (9) Deng, Y.; Roberts, J. A.; Peng, S.-M.; Chang, C. K.; Nocera, D. G. The Amidinium–Carboxylate Salt Bridge as a Proton-Coupled Interface to Electron Transfer Pathways. *Angew. Chem. Int. Ed. Engl.* **1997**, *36* (19), 2124–2127. <https://doi.org/10.1002/anie.199721241>.
- (10) Hodgkiss, J. M.; Damrauer, N. H.; Pressé, S.; Rosenthal, J.; Nocera, D. G. Electron Transfer Driven by Proton Fluctuations in a Hydrogen-Bonded Donor–Acceptor Assembly. *J. Phys. Chem. B* **2006**, *110* (38), 18853–18858. <https://doi.org/10.1021/jp056703q>.

- (11) Roberts, J. A.; Kirby, J. P.; Wall, S. T.; Nocera, D. G. Electron Transfer within Ruthenium(H) Polypyridyl-(Salt Bridge)- Dimethylaniline Acceptor-- Donor complexes. 11.
- (12) Roberts, J. A.; Kirby, J. P.; Nocera, D. G. Photoinduced Electron Transfer within a Donor-Acceptor Pair Juxtaposed by a Salt Bridge. *J. Am. Chem. Soc.* **1995**, *117* (30), 8051–8052. <https://doi.org/10.1021/ja00135a038>.
- (13) Soudackov, A.; Hammes-Schiffer, S. Theoretical Study of Photoinduced Proton-Coupled Electron Transfer through Asymmetric Salt Bridges. *J. Am. Chem. Soc.* **1999**, *121* (45), 10598–10607. <https://doi.org/10.1021/ja992380y>.
- (14) Turro, C.; Chang, C. K.; Leroi, G. E.; Cukier, R. I.; Nocera, D. G. Photoinduced Electron Transfer Mediated by a Hydrogen-Bonded Interface. *J. Am. Chem. Soc.* **1992**, *114* (10), 4013–4015. <https://doi.org/10.1021/ja00036a081>.
- (15) Young, E. R.; Rosenthal, J.; Hodgkiss, J. M.; Nocera, D. G. Comparative PCET Study of a Donor–Acceptor Pair Linked by Ionized and Nonionized Asymmetric Hydrogen-Bonded Interfaces. *J. Am. Chem. Soc.* **2009**, *131* (22), 7678–7684. <https://doi.org/10.1021/ja809777j>.
- (16) Hammes-Schiffer, S. Theoretical Perspectives on Proton-Coupled Electron Transfer Reactions. *Acc. Chem. Res.* **2001**, *34* (4), 273–281.
- (17) Hammes-Schiffer, S. Theory of Proton-Coupled Electron Transfer in Energy Conversion Processes. *Acc. Chem. Res.* **2009**, *42* (12), 1881–1889. <https://doi.org/10.1021/ar9001284>.
- (18) Hammes-Schiffer, S. Proton-Coupled Electron Transfer: Moving Together and Charging Forward. *J. Am. Chem. Soc.* **2015**, *137* (28), 8860–8871. <https://doi.org/10.1021/jacs.5b04087>.
- (19) Hammes-Schiffer, S.; Hatcher, E.; Ishikita, H.; Skone, J. H.; Soudackov, A. V. Theoretical Studies of Proton-Coupled Electron Transfer: Models and Concepts Relevant to Bioenergetics. *Coord. Chem. Rev.* **2008**, *252* (3), 384–394. <https://doi.org/10.1016/j.ccr.2007.07.019>.
- (20) Hammes-Schiffer, S.; Soudackov, A. V. Proton-Coupled Electron Transfer in Solution, Proteins, and Electrochemistry †. *J. Phys. Chem. B* **2008**, *112* (45), 14108–14123. <https://doi.org/10.1021/jp805876e>.
- (21) Hammes-Schiffer, S.; Stuchebrukhov, A. A. Theory of Coupled Electron and Proton Transfer Reactions. *Chem. Rev.* **2010**, *110* (12), 6939–6960. <https://doi.org/10.1021/cr1001436>.
- (22) Kavarnos, G. J.; Turro, N. J. Photosensitization by Reversible Electron Transfer: Theories, Experimental Evidence, and Examples. *Chem. Rev.* **1986**, *86* (2), 401–449.

- (23) Piechota, E. J.; Meyer, G. J. Introduction to Electron Transfer: Theoretical Foundations and Pedagogical Examples. *J. Chem. Educ.* **2019**, *96* (11), 2450–2466. <https://doi.org/10.1021/acs.jchemed.9b00489>.
- (24) Marcus, R. A.; Sutin, N. Electron Transfers in Chemistry and Biology. *Biochim. Biophys. Acta BBA-Rev. Bioenerg.* **1985**, *811* (3), 265–322.
- (25) Sutin, N.; Creutz, C. Electron-Transfer Reactions of Excited States. *J. Chem. Educ.* **1983**, *60* (10), 809. <https://doi.org/10.1021/ed060p809>.
- (26) Barltrop, J. A.; Coyle, J. D. *Principles of Photochemistry*; John Wiley & Sons, 1978.
- (27) Weinberg, D. R.; Gagliardi, C. J.; Hull, J. F.; Murphy, C. F.; Kent, C. A.; Westlake, B. C.; Paul, A.; Ess, D. H.; McCafferty, D. G.; Meyer, T. J. Proton-Coupled Electron Transfer. *Chem. Rev.* **2012**, *112* (7), 4016–4093. <https://doi.org/10.1021/cr200177j>.
- (28) Tyburski, R.; Liu, T.; Glover, S. D.; Hammarström, L. Proton-Coupled Electron Transfer Guidelines, Fair and Square. *J. Am. Chem. Soc.* **2021**. <https://doi.org/10.1021/jacs.0c09106>.
- (29) Mayer, J. M. PROTON-COUPLED ELECTRON TRANSFER: A Reaction Chemist's View. *Annu. Rev. Phys. Chem.* **2004**, *55* (1), 363–390. <https://doi.org/10.1146/annurev.physchem.55.091602.094446>.
- (30) Warren, J. J.; Tronic, T. A.; Mayer, J. M. Thermochemistry of Proton-Coupled Electron Transfer Reagents and its Implications <https://pubs.acs.org/doi/pdf/10.1021/cr100085k> (accessed Jan 23, 2021). <https://doi.org/10.1021/cr100085k>.
- (31) Wenger, O. S. Proton-Coupled Electron Transfer with Photoexcited Metal Complexes. *Acc. Chem. Res.* **2013**, *46* (Copyright (C) 2018 American Chemical Society (ACS). All Rights Reserved.), 1517–1526. <https://doi.org/10.1021/ar300289x>.
- (32) Wenger, O. S. Proton-Coupled Electron Transfer with Photoexcited Ruthenium(II), Rhenium(I), and Iridium(III) Complexes. *Coord. Chem. Rev.* **2015**, *282–283*, 150–158. <https://doi.org/10.1016/j.ccr.2014.03.025>.
- (33) Freys, J. C.; Bernardinelli, G.; Wenger, O. S. Proton-Coupled Electron Transfer from a Luminescent Excited State. *Chem. Commun.* **2008**, No. 36, 4267. <https://doi.org/10.1039/b806175k>.
- (34) Concepcion, J. J.; Brennaman, M. K.; Deyton, J. R.; Lebedeva, N. V.; Forbes, M. D. E.; Papanikolas, J. M.; Meyer, T. J. Excited-State Quenching by Proton-Coupled Electron Transfer. *J. Am. Chem. Soc.* **2007**, *129* (22), 6968–6969. <https://doi.org/10.1021/ja069049g>.

- (35) Lennox, J. C.; Kurtz, D. A.; Huang, T.; Dempsey, J. L. Excited-State Proton-Coupled Electron Transfer: Different Avenues for Promoting Proton/Electron Movement with Solar Photons. *ACS Energy Lett.* **2017**, *2* (5), 1246–1256. <https://doi.org/10.1021/acsenerylett.7b00063>.
- (36) Bronner, C.; Wenger, O. S. Proton-Coupled Electron Transfer between 4-Cyanophenol and Photoexcited Rhenium(I) Complexes with Different Protonatable Sites. *Inorg. Chem.* **2012**, *51* (15), 8275–8283. <https://doi.org/10.1021/ic300834c>.
- (37) Pannwitz, A.; Wenger, O. S. Proton Coupled Electron Transfer from the Excited State of a Ruthenium(II) Pyridylimidazole Complex. *Phys. Chem. Chem. Phys.* **2016**, *18* (16), 11374–11382. <https://doi.org/10.1039/C6CP00437G>.
- (38) Freys, J. C.; Bernardinelli, G.; Wenger, O. S. Proton-Coupled Electron Transfer from a Luminescent Excited State. *Chem. Commun.* **2008**, No. 36, 4267–4269. <https://doi.org/10.1039/B806175K>.
- (39) Kalyanasundaram, K. Photophysics, Photochemistry and Solar Energy Conversion with Tris(Bipyridyl)Ruthenium(II) and Its Analogues. *Coord. Chem. Rev.* **1982**, *46*, 159–244. [https://doi.org/10.1016/0010-8545\(82\)85003-0](https://doi.org/10.1016/0010-8545(82)85003-0).
- (40) Wang, X.; Del Guerso, A.; Schmehl, R. H. Photophysical Behavior of Transition Metal Complexes Having Interacting Ligand Localized and Metal-to-Ligand Charge Transfer States. *J. Photochem. Photobiol. C Photochem. Rev.* **2004**, *5* (1), 55–77. <https://doi.org/10.1016/j.jphotochemrev.2004.01.002>.
- (41) Campagna, S.; Puntoriero, F.; Nastasi, F.; Bergamini, G.; Balzani, V. Photochemistry and Photophysics of Coordination Compounds: Ruthenium. In *Photochemistry and Photophysics of Coordination Compounds I*; Balzani, V., Campagna, S., Eds.; Topics in Current Chemistry; Springer: Berlin, Heidelberg, 2007; pp 117–214. [https://doi.org/10.1007/128\\_2007\\_133](https://doi.org/10.1007/128_2007_133).
- (42) Pannwitz, A.; Wenger, O. S. Photoinduced Electron Transfer Coupled to Donor Deprotonation and Acceptor Protonation in a Molecular Triad Mimicking Photosystem II. *J. Am. Chem. Soc.* **2017**, *139* (38), 13308–13311. <https://doi.org/10.1021/jacs.7b08761>.

## Chapter 2: Synthesis and Characterization of Ruthenium (II) Complexes and 4,4'-bipyridinium Quenchers

### 2.1 Introduction

Ruthenium (II) complexes bearing hydroxylated diimine ligands have been explored for their change in acid-base behavior upon photoexcitation. (refs). In addition to their acid-base chemistry, reports of a complex,  $[(\text{bpy})_2\text{Ru}(5,6\text{-dihydroxy-1,10-phenanthroline})]^{2+}$  undergoing a proton-coupled electron transfer reaction were commented on in a review article on photoinduced proton-coupled electron transfer by Meyer.<sup>1</sup> A detailed follow-up on the PCET reactivity for this complex was never reported. Characterization of ruthenium complexes bearing hydroxylated 2,2'-bipyridine ligands have been reported on for their unique acid-base reactivity.<sup>2</sup>

These reports served as inspiration for the investigation of photoinduced electron and proton transfer in hydroxylated bipyridine ruthenium complexes with substituted ancillary ligands. The incorporation of electron-withdrawing groups (EWG) or electron-donating groups (EDG) provide a method of altering the photophysical, electrochemical as well as acid-base behavior of these complexes. Exploring a series of structurally related complexes and their reactivity toward photoinduced proton-coupled electron transfer could provide greater insight into designing a system for photoinduced PCET that can be incorporated into an artificial photosynthetic scheme.

The complexes investigated here have similar spectroscopic properties to  $[\text{Ru}(\text{bpy})_3]^{2+}$ . They exhibit strong MLCT absorbance between 400 and 500 nm, and emission with

maxima between 600 and 700 nm.<sup>3</sup> The ruthenium (III/II) reduction potentials scale with the electronic effects of the ancillary ligands.

The use of 4,4'-bipyridinium quenchers allows for the facile characterization of intermediate species formed during laser flash photolysis studies with  $[(LL)_2Ru(4,4'\text{-dhhbpy})]^{2+}$  complexes since these quenchers have distinct blue colors in their one electron reduced forms. Transient absorption spectroscopy and electrochemical studies allow the exploration of the effect of driving force on reaction mechanism.

The synthesis and characterization of Ru(II) complexes of 4,4'-dihydroxy-2,2'-bipyridine complexes with the following ancillary ligands: 2,2'-bipyridine, 4,4'-di-tert-butyl-2,2'-bipyridine, 4,4'-bis(dipropylamido)-2,2'-bipyridine, and 4,4'-bis(trifluoromethyl)-2,2'-bipyridine is discussed in this chapter. Also included in this series are the complexes  $[(5\text{-chloro-1,10-phenanthroline})_2Ru(4\text{-hydroxy-4'-methoxy-2,2'-bipyridine})]^{2+}$ ,  $[(2,2'\text{-bipyridine})_2Ru(4,4'\text{-dimethoxy-2,2'-bipyridine})]^{2+}$ , and  $[(2,2'\text{-bipyridine})_2Ru(4\text{-methoxy-4'-hydroxy-2,2'-bipyridine})]^{2+}$ . In addition control complexes of the type  $[(LL)_2Ru(2,2'\text{-bipyridine})]^{2+}$  where LL is : 2,2'-bipyridine, 4,4'-di-tert-butyl-2,2'-bipyridine, 4,4'-bis(dipropylamido)-2,2'-bipyridine, and 4,4'-bis(trifluoromethyl)-2,2'-bipyridine were synthesized. Synthesis and characterization of the quenchers *N*-methyl-4,4'-bipyridinium and *N*-benzyl-4,4'-bipyridinium are also included in this section. Careful purification of the complexes and quenchers is important to the proper characterization of photoinduced reactions between the complexes and quenchers.

Initial characterization of the transition metal complexes was done using <sup>1</sup>H NMR, COSY, and ESI-MS. Following this, photophysical and electrochemical properties were measured for these complexes. For complexes bearing pendant hydroxyl groups, additional

photophysical and electrochemical characterization was conducted for the monodeprotonated complexes.

## 2.2 Experimental

### 2.2.1 Spectroscopy

$^1\text{H}$  NMR spectra and gradient COSY spectra were collected on a Bruker 300 MHz Spectrometer. For an internal reference, the solvent residual peak of acetonitrile was used. (ref) For electrospray ionization mass spectrometry (ESI-MS), data was collected on a Bruker micro-TOF mass spectrometer. UV-Vis absorption spectra were collected on either an HP 8452 Diode Array spectrophotometer, or an Ocean Optics HR2000+ES. For UV-Visible absorption spectra, a 1 cm pathlength,  $l$ , was used. Emission spectra were collected using a PTI Quantmaster spectrophotometer equipped with a red sensitive Hamamatsu R928 PMT detector or using an Ocean Optics HR2000+ES CCD detector. Unless otherwise stated, absorption and emission spectra were collected in  $\text{N}_2$  or Ar degassed acetonitrile solution.

### 2.2.2 Electrochemistry

Cyclic voltammograms and differential pulse voltammograms were obtained using a CH Instruments 630 electrochemical workstation. Experiments were conducted using a standard three-electrode set-up with a glassy carbon working electrode, platinum wire counter electrode, and either an Ag/AgCl reference or silver wire pseudo reference. For measurements made with silver wire pseudo reference, ferrocene was used as an internal reference. All electrochemical measurements were made in acetonitrile that was dried over  $\text{CaH}_2$  and distilled prior to use. Tetrabutylammonium hexafluorophosphate, used as supporting electrolyte, was recrystallized from hot ethanol, and dried in vacuo prior to use.

For cathodic voltammograms, solutions were deaerated with Argon to displace O<sub>2</sub> prior to measurement.

### 2.2.3 Time-Resolved Spectroscopy

Transient absorption spectroscopy on the nanosecond to microsecond time scale was conducted using a Quantel Brilliant B Q-Switched Nd:YAG laser-pumped OPO (Opotek) for visible light excitation with 2-3 ns pulses. Unless otherwise stated, 450 nm light was used as the excitation wavelength. Either a 1 cm x 1 cm cuvette or 0.2 cm x 1 cm cuvette was used for measurements. Unless otherwise stated, solutions were deaerated prior to photolysis studies with N<sub>2</sub> gas for 10-15 minutes. Data acquisition was accomplished using an Applied Photophysics LKS 80 laser flash photolysis system equipped with a 150 W pulsed Xenon arc lamp as the probe light source, a single grating monochromator, a Hamamatsu R928 PMT detector, and an Agilent Infiniium oscilloscope. Data were acquired with linear oversampling.

## 2.3 Synthesis and Characterization

### 2.3.1 Materials

4,4'-di-tert-butyl-2,2'-bipyridine (dtb), 2,2'-bipyridine (bpy), and benzyl chloride were purchased from Sigma Aldrich. 5-chloro-1,10-phenanthroline (Cl-phen) and 4,4'-bipyridine (4,4'-bpy) were purchased from Alfa Aesar. Ammonium hexafluorophosphate was purchased from Oakwood Chemicals. Ruthenium (III) trichloride hydrate was purchased from Pressure chemical, [Ru(p-cymene)Cl]<sub>2</sub>Cl<sub>2</sub> was obtained from Strem Chemical. [Ru(bpy)<sub>3</sub>]<sup>2+</sup> was previously prepared in our lab following literature procedure.<sup>4</sup> Potassium tetrakis(pentafluorophenyl)borate was purchased from TCI Chemicals. Acetonitrile was purchased from Fisher Scientific. 2-bromo-4-methoxypyridine,

tetrakis(triphenylphosphine)palladium(0), 2-pyridinboronic acid *N*-phenyl-diethanolamine ester, and copper(I) iodide were purchased from Oakwood Chemical. Amine-free *N,N*-dimethylformamide was purchased from Alfa Aesar. Methanol was purchased from Fisher Scientific. Diethyl ether was purchased from VWR. Alumina used for column chromatography was purchased from Alfa Aesar, alumina plates for preparative TLC were purchased from Analtech. Deuterated solvents for NMR and kinetic isotope studies were purchased from Cambridge Isotope Laboratories. HPLC-grade acetonitrile for ESI-MS was purchased from Fisher Scientific.

### 2.3.2 Synthesis of Ligands and Ruthenium Complexes

In this section, the synthesis of each compound is reported. The analysis of mass spectra and <sup>1</sup>H NMR spectra will be done in subsequent sections.

**4,4'-dihydroxy-2,2'-bipyridine(4,4'-(OH)<sub>2</sub>bpy):** This ligand was prepared as previously reported and provided by our collaborator at Villanova University, Jared Paul.<sup>5</sup>

**4,4'-bis(trifluoromethyl)-2,2'-bipyridine (flpy):** This ligand was synthesized as previously reported and provided through our collaboration with Jared Paul at Villanova University.<sup>6</sup>

**4,4'-dipropylamido-2,2'-bipyridine (dpab):** This ligand was synthesized as previously reported, starting from 4,4'-dicarboxy-2,2'-bipyridine that was previously synthesized in our laboratory.<sup>7</sup>

**4-hydroxy-4'-methoxy-2,2'-bipyridine (4-OH-4'-OMe-bpy):** This ligand was synthesized as previously reported, and provided by our collaborator at Villanova University, Jared Paul.<sup>8</sup>

**4-methoxy-2,2'-bipyridine (OMebpy):** This ligand was synthesized by Kaitlyn Benson from the Paul Group at Villanova University. 15 mL of THF was added to a 100 mL round bottom flask containing 715 mg 2-pyridineboronic acid N-phenyl-diethanolamine ester (1.7 mmol), 76 mg copper(I) iodide (0.4 mmol), 275 mg anhydrous potassium carbonate (2.0 mmol), and 115 mg tetrakis(triphenylphosphine) palladium(0) (10 mol%). To the flask, 190 mg 2-bromo-4-methoxypyridine (1.01 mmol) and 0.04 mL of deionized water was added to the solution and refluxed overnight under argon. The solution was cooled to room temperature and quenched by 40 mL of a saturated aqueous EDTA solution. The THF was removed under reduced pressure. The product was extracted with 50 mL x3 DCM and dried over sodium sulfate. The DCM was removed under reduced pressure. The crude product was isolated by a silica column with a gradient mobile phase of 100 mL 10% ethyl acetate/ 5% triethylamine in hexanes which was then switched to 400 mL 30% ethyl acetate/ 5% triethylamine in hexanes. The collected fractions were monitored by TLC with a mobile phase 30% ethyl acetate/ 5% triethylamine in hexanes. The solvent system was removed under vacuum, affording a light pink solid. Yield: 0.0911 g (0.49 mmol), 49%.  $^1\text{H NMR}$  (300 MHz,  $\text{CDCl}_3$ )  $\delta$ 8.675 (d, 1H,  $J=3.9$ )  $\delta$ 8.486 (q, 1H,  $J=6.0$ )  $\delta$ 8.396 (d, 1H,  $J=7.5$ )  $\delta$ 7.976 (d, 1H,  $J=2.7$ )  $\delta$ 7.813 (td, 1H,  $J=7.8$ , 1.8)  $\delta$ 7.312 (dd, 1H,  $J=7.8$ , 6.6)  $\delta$ 6.849 (dd, 1H,  $J=5.1$ , 2.4)  $\delta$ 3.957 (t, 3H,  $J=5.4$ ).

**4-hydroxy-2,2'-bipyridine (4-OH-bpy):** This ligand was synthesized by Kaitlyn Benson from the Paul group at Villanova University. 1.0 mL of 48% aqueous HBr solution was added to a 100 mL round bottom flask containing 176 mg 4-methoxy-2,2'-bipyridine (0.95 mmol) in 25 mL glacial acetic acid. The solution was refluxed overnight open to the

atmosphere. The solution was cooled to room temperature and the product was collected by vacuum filtration to afford a white solid. Yield: 0.3175 g (0.95 mmol), 100%.

**[(bpy)<sub>2</sub>(4,4'-(OH)<sub>2</sub>-bpy)ruthenium (II)](PF<sub>6</sub>)<sub>2</sub> ([Ru(bpy)<sub>2</sub>(4,4'-(OH)<sub>2</sub>bpy)](PF<sub>6</sub>)<sub>2</sub>)** : This complex was synthesized as previously reported, and provided by our collaborator at Villanova University, Jared Paul.<sup>2</sup>

**[(bpy)<sub>2</sub>(4,4'-(OMe)<sub>2</sub>-bpy) ruthenium (II)](PF<sub>6</sub>)<sub>2</sub> ([Ru(bpy)<sub>2</sub>(4,4'-(OMe)<sub>2</sub>bpy)](PF<sub>6</sub>)<sub>2</sub>)** : This complex was synthesized as previously reported, and provided by our collaborator at Villanova University, Jared Paul.<sup>2</sup>

**[(p-cymene)Ruthenium (II) (4,4'-(OH)<sub>2</sub>bpy)chloro]Chloride:** [(p-cymene)Ru(4,4'-dhbpy)Cl]Cl was prepared via modification of a previously reported synthesis for an analogous compound.<sup>9</sup> [(p-cymene)RuCl<sub>2</sub>]<sub>2</sub> (0.327 g, 0.53 mmol) and 4,4'-dihydroxy-2,2'-bipyridine (0.201 g, 1.06 mmol) were added to 20 mL acetonitrile and degassed for 20 minutes prior to refluxing for 4 hours under nitrogen atmosphere. During reflux a yellow precipitate formed. Upon cooling, the solution was filtered, and the product was rinsed several times with acetonitrile. The crude product was then dissolved in methanol and the solution was filtered to remove any undissolved material. The product was reprecipitated using diethyl ether. The yield was 0.479 g (90.7%) and was used without further purification.

**[(p-cymene)Ruthenium (II) (bpy)Cl]Cl. [(p-cymene)Ru(bpy)Cl]Cl:** was prepared in the same manner as above using 2,2'-bipyridine (0.259 g, 1.66 mmol) in place of 4,4'-dihydroxybipyridine and [(p-cymene)RuCl<sub>2</sub>]<sub>2</sub> (0.507 g, 0.827 mmol). The product yield was 0.50 g (65%).

**$[(dpab)_2(4,4'-(OH)_2-bpy) Ruthenium (II)](PF_6)_2$**  ( $[(dpab)_2Ru(4,4'-(OH)_2bpy)](PF_6)_2$ ): [(p-cymene)Ru(4,4'-(OH)<sub>2</sub>bpy)Cl]Cl (0.100 g, 0.201 mmol) and 4,4'-bis(dipropylamido)-2,2'-bipyridine (0.132 g, 0.404 mmol) were dissolved in 5 mL amine-free N,N-dimethylformamide (dried over 3 Å molecular sieves). The mixture was degassed for 20 minutes prior to refluxing for 4 hours under nitrogen atmosphere. Once cooled, excess acetone was added, and the mixture was cooled in the freezer overnight. The precipitated product,  $[(dpab)_2Ru(4,4'-dhbpy)]Cl_2$  was collected on a fine fritted filter. The complex was precipitated as the hexafluorophosphate salt by addition of a molar excess of aqueous ammonium hexafluorophosphate to an aqueous solution of the product.  $[(dpab)_2Ru(4,4'-dhbpy)](PF_6)_2$  was purified to remove the predominant impurity  $[Ru(dpab)_3](PF_6)_2$  using column chromatography. The crude product was added to a neutral alumina column with an eluent of 5% methanol in dichloromethane. The desired product remained unmovable with this eluent mixture, but the  $[Ru(dpab)_3](PF_6)_2$  was quickly removed from the column. A secondary eluent mixture was added, 1:1 H<sub>2</sub>O and acetonitrile. The desired product was successfully removed from the column yielding 0.070 g (28%). The product was characterized by <sup>1</sup>HNMR, COSY, and ESI-MS. <sup>1</sup>HNMR (300 MHz, CD<sub>3</sub>CN, residual internal (CD<sub>2</sub>H)CN δ= 1.94 ppm ) δ 8.91 (s, 4H), 7.98 (d, J = 5.9 Hz, 2H), 7.82 (d, J = 6.0 Hz, 2H), 7.74 (d, J = 5.8 Hz, 2H), 7.70 – 7.59 (m, 6H), 7.52 (s, 2H), 7.17 (d, J = 6.4 Hz, 2H), 6.72 (d, J = 6.5 Hz, 2H), 3.37 (m, J = 14.4, 6.8 Hz, 9H), 1.62 (m, J = 7.5 Hz, 8H), 0.95 (q, J = 7.1 Hz, 12H). ESI-MS m/z: [C<sub>46</sub>H<sub>52</sub>N<sub>10</sub>O<sub>6</sub>Ru]<sub>2</sub><sup>+</sup> Calcd 471.1558; Found 471.1342.

**$[(dpab)_2(bpy)ruthenium (II)](PF_6)_2$**  ( $[(dpab)_2Ru(bpy)](PF_6)_2$ ) ∴ The above synthesis was repeated using the aforementioned procedure for  $[(dpab)_2Ru(4,4'-(OH)_2-$

bpy)](PF<sub>6</sub>)<sub>2</sub> using [(p-cymene)Ru(bpy)Cl]Cl (0.152 g, 0.329 mmol) and 4,4'-bis(dipropylamido)-2,2'-bipyridine (0.214 g, 0.656 mmol). For this complex, no column was used to treat the product. As the presence of [Ru(dpab)<sub>3</sub>](PF<sub>6</sub>)<sub>2</sub> in trace amounts had no effect on subsequent experiments. The yield was 0.091 g (23%). The product was characterized by <sup>1</sup>H NMR, COSY, and ESI-MS. <sup>1</sup>H NMR (300 MHz, CD<sub>3</sub>CN, residual internal (CD<sub>2</sub>H)CN δ = 1.94 ppm ) δ 8.95 (t, J = 1.9 Hz, 4H), 8.54 (dd, J = 8.1, 1.2 Hz, 2H), 8.12 (td, J = 7.9, 1.5 Hz, 2H), 7.88 (t, J = 5.5 Hz, 4H), 7.72 (ddt, J = 7.9, 4.1, 1.9 Hz, 6H), 7.53 (d, J = 5.1 Hz, 4H), 7.44 (ddd, J = 7.2, 5.6, 1.3 Hz, 2H), 3.40 (dtd, J = 7.7, 6.1, 2.1 Hz, 8H), 1.66 (hd, J = 7.3, 2.2 Hz, 8H), 0.98 (td, J = 7.4, 2.1 Hz, 12H). ESI-MS m/z: [C<sub>46</sub>H<sub>52</sub>N<sub>10</sub>O<sub>4</sub>Ru]<sup>2+</sup> Calcd 455.1609; Found 455.1770.

**[(dtb)<sub>2</sub>(4,4'-(OH)<sub>2</sub>bpy)ruthenium (II)](PF<sub>6</sub>)<sub>2</sub> ([[(dtb)Ru(4,4'-(OH)-<sub>2</sub>bpy)](PF<sub>6</sub>)<sub>2</sub>)** : Ru(dtb)<sub>2</sub>Cl<sub>2</sub> was synthesized according to a modification of a literature procedure.<sup>10</sup> 231 mg (.33 mmol) of Ru(dtb)<sub>2</sub>Cl<sub>2</sub> and 78 mg of 4,4'-dihydroxy-2,2'-bipyridine were refluxed for one hour in 50/50 ethanol and water solution. The reaction was cooled, and ethanol removed by evaporation. The chloride salt was not isolated, but rather excess aqueous ammonium hexafluorophosphate was added to precipitate out the product. The resulting product was then purified by column chromatography on neutral alumina to remove trace amounts of [Ru(dtb)<sub>3</sub>]<sup>2+</sup>. The crude product was added to an alumina column with an eluent of 5% methanol in dichloromethane. The desired product remained unmovable with this eluent mixture, but the [Ru(dtb)<sub>3</sub>](PF<sub>6</sub>)<sub>2</sub> was quickly removed from the column. A secondary eluent mixture was added, 1:1 H<sub>2</sub>O and acetonitrile. The yield of pure product was 92.4 mg (25%). <sup>1</sup>H NMR (300 MHz, Acetonitrile-d<sub>3</sub>) δ 8.44 (dd, J = 4.6, 2.0 Hz, 2H), 7.82 (d, J = 6.0 Hz, 1H), 7.67 (d, J = 2.7

Hz, 1H), 7.56 (d, J = 6.0 Hz, 1H), 7.45 (dd, J = 6.1, 2.0 Hz, 1H), 7.33 (dd, J = 6.1, 2.0 Hz, 1H), 7.01 (d, J = 6.5 Hz, 1H), 6.55 (dd, J = 6.5, 2.4 Hz, 1H), 1.97 (p, J = 2.5 Hz, 3H), 1.42 (s, 6H), 1.40 (s, 12H). ESI-MS m/z: [C<sub>46</sub>H<sub>56</sub>N<sub>6</sub>O<sub>2</sub>Ru]<sup>2+</sup> Calcd 413.1755; Found 413.1867. **[(dtb)<sub>2</sub>(bpy)ruthenium (II)](PF<sub>6</sub>)<sub>2</sub> ((dtb)<sub>2</sub>Ru(bpy)](PF<sub>6</sub>)<sub>2</sub>** : 252 mg (0.55 mmol) of [Ru(p-cymene)(bpy)Cl]Cl and 275 mg (1.02 mmol) of 4,4'-di-tert-butyl-2,2'-bipyridine (dtb) were refluxed in 5 mL of amine-free DMF under argon gas for four hours. The reaction mixture was cooled to room temperature and diethyl ether was added to precipitate out the product. The crude product was dissolved in water and precipitated out using a saturated solution of NH<sub>4</sub>PF<sub>6</sub>. The resulting precipitate was collected by vacuum filtration over a fine fritted glass filter and rinsed with additional diethyl ether. The product was checked for purity by <sup>1</sup>H NMR and ESI-MS, and needed no further purification. The yield was 224 mg (51%). <sup>1</sup>H NMR (300 MHz, Acetonitrile-d<sub>3</sub>) δ 8.54 – 8.42 (m, 6H), 8.03 (ddd, J = 9.2, 6.1, 1.5 Hz, 2H), 7.74 – 7.63 (m, 2H), 7.62 – 7.50 (m, 4H), 7.45 – 7.32 (m, 6H), 1.42 – 1.34 (m, 36H). ESI-MS m/z: [C<sub>46</sub>H<sub>56</sub>N<sub>6</sub>Ru]<sup>2+</sup> Calcd 397.1806; Found 397.1862.

**[(flpy)<sub>2</sub>(4,4'-(OH)<sub>2</sub>-bpy)ruthenium (II)](PF<sub>6</sub>)<sub>2</sub> ((flpy)<sub>2</sub>Ru(4,4'-(OH)<sub>2</sub>bpy)](PF<sub>6</sub>)<sub>2</sub>** : 126 mg (0.26 mmol) of [Ru(p-cymene)(4,4'-(OH)<sub>2</sub>bpy)Cl]Cl and 148 mg (0.51 mmol) of 4,4'-bis(trifluoromethyl)-2,2'-bipyridine were refluxed in 5 mL of amine-free DMF under argon gas for four hours. The reaction mixture was cooled to room temperature and diethyl ether was added to precipitate out the product. The resulting precipitate was collected by vacuum filtration over a fine fritted glass filter and rinsed with additional diethyl ether. The hexafluorophosphate salt was obtained by taking the pure chloride salt in aqueous solution and adding excess ammonium hexafluorophosphate. The

yield was 129 mg (43%). Purification was accomplished by preparative TLC on alumina using a 1:1 acetonitrile/ toluene mixture. The lower band was removed and verified as the product by ESI-MS.  $^1\text{H}$  NMR (300 MHz, Acetonitrile- $d_3$ )  $\delta$  8.97 – 8.88 (m, 2H), 8.12 (d,  $J$  = 5.9 Hz, 1H), 7.99 (d,  $J$  = 5.9 Hz, 1H), 7.84 – 7.78 (m, 1H), 7.77 – 7.72 (m, 1H), 7.66 (dd,  $J$  = 6.0, 1.9 Hz, 1H), 7.21 (d,  $J$  = 6.4 Hz, 1H), 6.79 (dd,  $J$  = 6.6, 2.2 Hz, 1H). ESI-MS  $m/z$ :  $[\text{C}_{34}\text{H}_{20}\text{F}_{12}\text{N}_6\text{O}_2\text{Ru}]^{2+}$  Calcd 437.0309; Found 437.0249.

**$[(\text{flpy})_2(\text{bpy})\text{ruthenium (II)}](\text{PF}_6)_2$  ( $[(\text{flpy})_2\text{Ru}(\text{bpy})](\text{PF}_6)_2$ )** : 108 mg (0.52mmol) of  $\text{RuCl}_3 \cdot x\text{H}_2\text{O}$ , 233 mg (0.80 mmol) of 4,4'-bis(trifluoromethyl)-2,2'-bipyridine, and 10 mg of LiCl were refluxed in amine-free DMF under argon gas for four hours. The reaction was cooled to room temperature and excess diethyl ether was added to precipitate out the product,  $\text{Ru}(\text{flpy})_2\text{Cl}_2$ . The resulting yield of this reaction was 128 mg. This product and 35 mg (0.22 mmol) of 2,2'-bipyridine were refluxed for four hours in 50/50 ethanol and deionized water under argon gas. The reaction mixture was cool to room temperature and ethanol removed by evaporation. Excess aqueous ammonium hexafluorophosphate was added to the aqueous solution of the crude product, and the resulting hexafluorophosphate salt precipitated from solution. The product needed no further purification as confirmed by  $^1\text{H}$ NMR and ESI-MS. The yield was 76 mg (54 %).  $^1\text{H}$  NMR (300 MHz, Acetonitrile- $d_3$ )  $\delta$  8.97 (d,  $J$  = 2.2 Hz, 2H), 8.56 (d,  $J$  = 8.1 Hz, 1H), 8.15 (td,  $J$  = 7.9, 1.5 Hz, 1H), 8.00 (t,  $J$  = 6.4 Hz, 4H), 7.72 (ddd,  $J$  = 7.5, 4.7, 1.7 Hz, 3H), 7.46 (ddd,  $J$  = 7.3, 5.6, 1.3 Hz, 1H). ESI-MS  $m/z$ :  $[\text{C}_{34}\text{H}_{20}\text{F}_{12}\text{N}_6\text{Ru}]^{2+}$  Calcd 421.0300; Found 421.0431.

**$[\text{Cl-phen}]_2(4-(\text{OH})-4'-(\text{OMe})\text{-bpy})\text{ruthenium (II) }](\text{PF}_6)_2$  ( $[(\text{Cl-phen})_2\text{Ru}(4-(\text{OH})-4'-(\text{OMe})\text{bpy})](\text{PF}_6)_2$ )** : 205 mg (0.99 mmol) of  $\text{RuCl}_3 \cdot x\text{H}_2\text{O}$ , 330 mg (1.54 mmol)

of 5-chloro-1,10-phenanthroline, and 30 mg LiCl were refluxed in amine-free DMF under argon gas for four hours. The reaction was cooled to room temperature and excess H<sub>2</sub>O was added to induce precipitation of the product. The resulting precipitate was collected by vacuum filtration on a fine fritted filter and rinsed with excess water to remove any residual [Ru(5-Clphen)<sub>3</sub>]<sup>2+</sup>. The product was dried in vacuo and weighed, yielding 472 mg (xx%). 223 mg (0.37 mmol) of Ru(5-Clphen)<sub>2</sub>Cl<sub>2</sub> and 79 mg (.42 mmol) of 4,4'-dihydroxy-2,2'-bipyridine were refluxed in 50/50 water/ethanol under argon gas for twelve hours. The reaction was cooled to room temperature and ethanol removed by evaporation. The product was precipitated from aqueous solution by the addition of excess ammonium hexafluorophosphate. The resulting product yield was 635 mg (xx%). A small portion, less than 20 mg of the complex, was purified by preparative TLC on alumina using 1:1 acetonitrile/toluene as the eluent. The resulting mass of the product was less than 5 mg. <sup>1</sup>H NMR (400 MHz, Acetonitrile-d<sub>3</sub>) δ 8.88 – 8.82 (m, 1H), 8.77 – 8.69 (m, 1H), 8.55 (d, J = 8.4 Hz, 1H), 8.47 – 8.20 (m, 6H), 8.01 – 7.75 (m, 5H), 7.72 – 7.46 (m, 4H), 7.33 (ddd, J = 8.5, 6.6, 3.8 Hz, 1H), 6.95 (d, J = 8.1 Hz, 1H), 6.76 (dt, J = 4.4, 1.8 Hz, 1H), 6.47 (s, 1H), 3.91 (d, J = 1.2 Hz, 3H). ESI-MS m/z: [C<sub>35</sub>H<sub>24</sub>Cl<sub>2</sub>N<sub>6</sub>O<sub>2</sub>Ru]<sup>2+</sup> Calcd 366.0187; Found 365.7256.

**[(Cl-phen)<sub>2</sub>(bpy)ruthenium (II)](PF<sub>6</sub>)<sub>2</sub> ([Cl-phen)<sub>2</sub>Ru(bpy)](PF<sub>6</sub>)<sub>2</sub> : 222 mg (0.37 mmol) of Ru(5-Clphen)<sub>2</sub>Cl<sub>2</sub> and 61 mg (0.39 mmol) of 2,2'-bipyridine were refluxed in 50:50 ethanol/water for 12 hours. The reaction was cooled to room temperature and ethanol removed by evaporation. The complex was precipitated from solution by addition of excess aqueous ammonium hexafluorophosphate. The precipitate was collected by vacuum filtration on a fine-fritted glass filter and rinsed several times with diethyl ether.**

The yield of the product was 182 mg. A portion of the complex was purified by preparative TLC on neutral alumina using 70:30 acetonitrile/ toluene mixture as the eluent. The resulting bands were collected and analyzed by ESI-MS, and it was determined that the top band on the plate was the desired complex.  $^1\text{H}$  NMR (400 MHz, Acetonitrile- $d_3$ )  $\delta$  8.90 – 8.78 (m, 1H), 8.78 – 8.71 (m, 1H), 8.62 (d,  $J$  = 7.4 Hz, 1H), 8.57 – 8.32 (m, 8H), 8.21 (dd,  $J$  = 5.6, 3.2 Hz, 1H), 8.14 (td,  $J$  = 11.0, 10.2, 6.1 Hz, 1H), 7.99 (ddtd,  $J$  = 35.8, 17.6, 9.8, 9.0, 5.6 Hz, 5H), 7.84 (dt,  $J$  = 8.1, 4.4 Hz, 2H), 7.74 (dtd,  $J$  = 25.6, 8.6, 5.1 Hz, 3H), 7.61 (dq,  $J$  = 9.8, 4.7 Hz, 2H), 7.51 (ddd,  $J$  = 21.0, 9.6, 5.2 Hz, 2H), 7.44 – 7.37 (m, 1H), 7.35 (s, 1H), 7.29 – 7.13 (m, 2H), 2.10 (s, 18H). ESI-MS  $m/z$ :  $[\text{C}_{34}\text{H}_{22}\text{Cl}_2\text{N}_6\text{Ru}]^{2+}$  Calcd 343.0159; Found 343.3089.

**$[(\text{bpy})_2\text{Ru}(4\text{-hydroxy-2,2'-bipyridine})](\text{PF}_6)_2$  ( $[(\text{bpy})_2\text{Ru}(4\text{-OHbpy})](\text{PF}_6)_2$ ) :**

This complex was synthesized by Kaitlyn Benson from the Paul group at Villanova University.  $\text{Ru}(\text{bpy})_2\text{Cl}_2$  was synthesized as previously reported.<sup>10</sup> A round bottom flask containing 30 mL 1:1 EtOH:H<sub>2</sub>O was degassed for 30 min by bubbling argon through it. To the flask, 0.3142 g  $\text{Ru}(\text{bpy})_2\text{Cl}_2$  (0.649 mmol) and 0.1736 g 4-OHbpy·2Br<sup>-</sup> (0.6451 mmol) were added to the solution and refluxed overnight under argon. The solution was cooled to room temperature, followed by filtration to remove any insoluble, unreacted ligand. Two drops of HCl were added to ensure protonation of the complex, followed by the addition of a saturated 10 mL solution of  $\text{NH}_4\text{PF}_6$  in water, affording a red-orange precipitate. The solid was collected and rinsed with water. Yield: 0.2445 g (0.279 mmol), 43.2%.  $^1\text{H}$  NMR (300MHz, CD<sub>3</sub>CN)  $\delta$ 8.501 (d, 5H,  $J$ =7.8)  $\delta$ 8.420 (d, 1H,  $J$ =8.1)  $\delta$ 8.059 (dd, 5H,  $J$ =14.1, 8.4)  $\delta$ 7.919 (d, 1H,  $J$ =3.0)  $\delta$ 7.802 (dd, 2H,  $J$ =13.5, 5.4)  $\delta$ 7.738 (t, 3H,  $J$ =5.1)  $\delta$ 7.453- 7.361 (m, 5H)  $\delta$ 6.891 (dd, 1H,  $J$ =6.3, 2.4). Anal. Calc. for

$\text{RuC}_{30}\text{N}_6\text{OH}_{24}\text{P}_2\text{F}_{12}$ : C, 41.15; N, 9.60; H, 2.76%. Found: C, 40.64; N, 9.44; H, 2.88%.  
ESI-MS  $m/z$ :  $[\text{C}_{30}\text{H}_{24}\text{N}_6\text{ORu}]^{2+}$  Calcd 293.0526; Found 293.0526.

**$[(\text{bpy})_2\text{Ru}(4\text{-methoxy-2,2'-bipyridine})](\text{PF}_6)_2$** : This complex was synthesized by Kaitlyn Benson from the Paul group at Villanova University. A round bottom flask containing 30 mL ethylene glycol was degassed for 30 min by bubbling argon through it. To the flask, 0.4849 g (1.00 mmol)  $\text{Ru}(\text{bpy})_2\text{Cl}_2$ , and 0.1922 g (1.03 mmol) 4-(OMe)bpy were added and the solution was refluxed for 3 hours under argon. The solution was cooled to room temperature, followed by filtration to remove insoluble, unreacted ligand. The solution was diluted to 180 mL with water and the product was precipitated with the addition of a saturated 10 mL solution of  $\text{NH}_4\text{PF}_6$  in water, affording the product as a bright orange precipitate. The solid was collected and rinsed with water. Yield: 0.6469 g (0.7272 mmol), 72%.  $^1\text{H}$  NMR (300 MHz,  $\text{CD}_3\text{CN}$ )  $\delta$ 8.537- 8.494 (m, 5H)  $\delta$ 8.096- 8.025 (m, 6H)  $\delta$ 7.785 (t, 2H,  $J=3.9$ )  $\delta$ 7.738 (d, 3H,  $J=5.7$ ).  $\delta$ 7.471 (d, 1H,  $J=6.3$ )  $\delta$ 7.444 (q, 2H,  $J=1.2$ )  $\delta$ 7.395 (t, 3H,  $J=6.6$ )  $\delta$ 6.977 (dd, 1H,  $J=6.3, 2.4$ )  $\delta$ 4.010 (s, 3H). Anal. Calc. for  $\text{RuC}_{31}\text{N}_6\text{OH}_{26}\text{P}_2\text{F}_{12}$ : C, 41.86; N, 9.45; H, 2.95%. Found: C, 42.15; N, 9.52; H, 3.02%.  
ESI-MS  $m/z$ :  $[\text{C}_{31}\text{H}_{26}\text{N}_6\text{ORu}]^{2+}$  Calcd 300.0604; Found 300.0663.

### 2.3.3 Synthesis of 4,4'-bipyridinium Quenchers

***N*-methyl-4,4'-bipyridinium hexafluorophosphate**: was synthesized as previously reported.<sup>11</sup> 4,4'-bipyridine was refluxed in the presence of one equivalent of methyl iodide in dichloromethane overnight. The product precipitated out as a yellow powder. The iodide salt was isolated, and iodide exchanged for the hexafluorophosphate anion by dissolving the iodide salt in water and precipitating out the  $\text{PF}_6$  salt by addition of saturated aqueous  $\text{NH}_4\text{PF}_6$ . The isolated  $\text{PF}_6$  salt was then recrystallized from hot ethanol twice and dried in

vacuo overnight. The resulting white powder was used without further purification.  $^1\text{H}$  NMR (400 MHz, Acetonitrile- $d_3$ )  $\delta$  8.93 – 8.80 (m, 2H), 8.71 (d,  $J$  = 6.5 Hz, 2H), 8.30 (d,  $J$  = 6.3 Hz, 2H), 7.86 – 7.73 (m, 2H), 4.32 (s, 3H).

***N*-benzyl-4,4'-bipyridinium hexafluorophosphate:** 4,4'-bipyridine (5.04 g, 0.0323 mol) and benzyl bromide (3.8 mL, 0.032 mol) were dissolved in toluene and refluxed for 12 hours under an argon atmosphere. A yellow precipitate was isolated by filtration and washed with diethyl ether. The crude product, *N*-benzyl-4,4'-bipyridinium bromide ( $\text{BMQ}^+$ ), was dissolved in water and precipitated out as a hexafluorophosphate salt by the addition of a molar excess of aqueous ammonium hexafluorophosphate.  $\text{BMQ}^+$  was purified by recrystallization from hot ethanol. The product was collected and dried in vacuo to yield 5.38 g (51.5 %). The compound was characterized by  $^1\text{H}$  NMR.  $^1\text{H}$  NMR (300 MHz, Acetonitrile- $d_3$ )  $\delta$  8.84 (m, 4H), 8.35 – 8.25 (m, 2H), 7.83 – 7.74 (m, 2H), 7.49 (s, 5H), 5.76 (s, 2H).

### 2.3.4 Electrospray Ionization Mass Spectrometry

Electrospray ionization mass spectrometry was used to characterize the complexes by their exact mass. Due to the fact that electrospray ionization is a soft ionization technique, the resulting mass spectra represent on the molecular ion peak, with no subsequent fragmentation of the complexes. Because of the abundance of many isotopes of ruthenium, the mass spectra contain a weighted distribution of peaks based on the natural abundance of each of the ruthenium isotopes. Also contributing to the unique isotope patterns for each complex are the isotopes of carbon, nitrogen, hydrogen, fluorine, chlorine, and oxygen. The mass spectra are shown in figures 2.1 through 2.10 below and include

both the experimentally measured exact masses of the complexes, as well as the exact masses obtained computationally. Note, the instrument used for obtaining mass spectra of the complexes is not a high-resolution instrument.

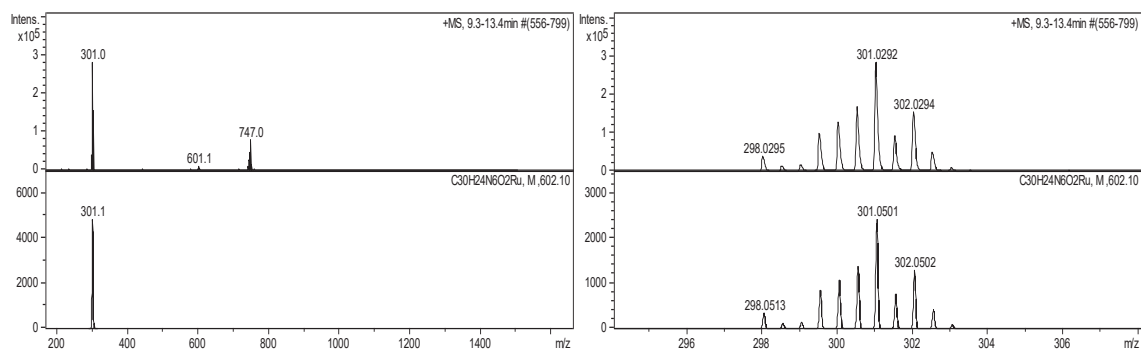


**Figure 2.1** Experimental and calculated mass spectra of  $[(bpy)_2Ru(4,4'-dhbpy)]^{2+}$ , calc. deviation 69 ppm.

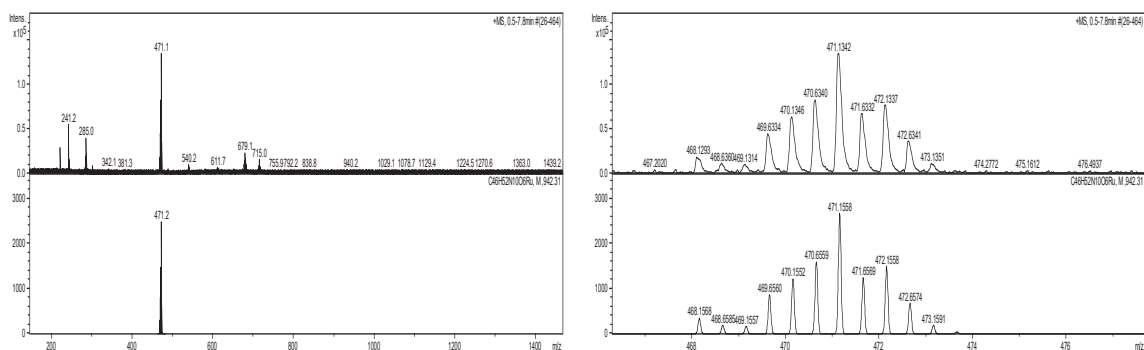


**Figure 2.2** Experimental and calculated mass spectra of  $[(dpab)_2Ru(4,4'-dhbpy)]^{2+}$ , calc. deviation 46 ppm

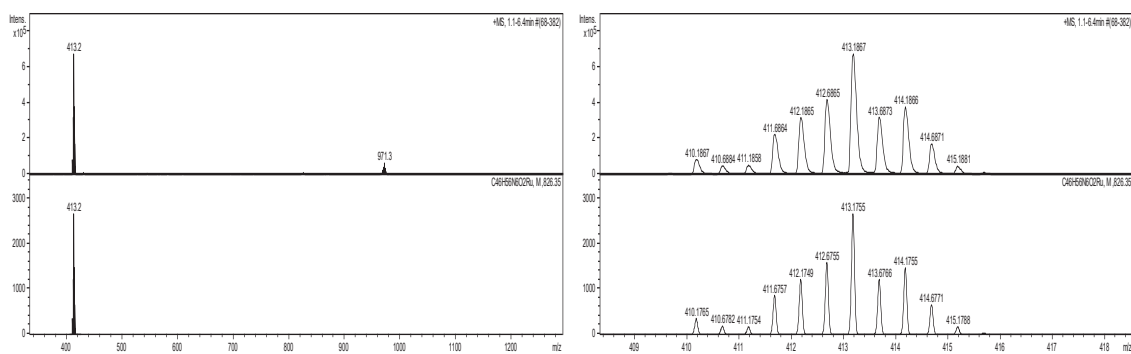


**Figure 2.3** Experimental and calculated mass spectra of  $[(dtb)_2Ru(4,4'-dhbpy)]^{2+}$ , calc. deviation 27 ppm

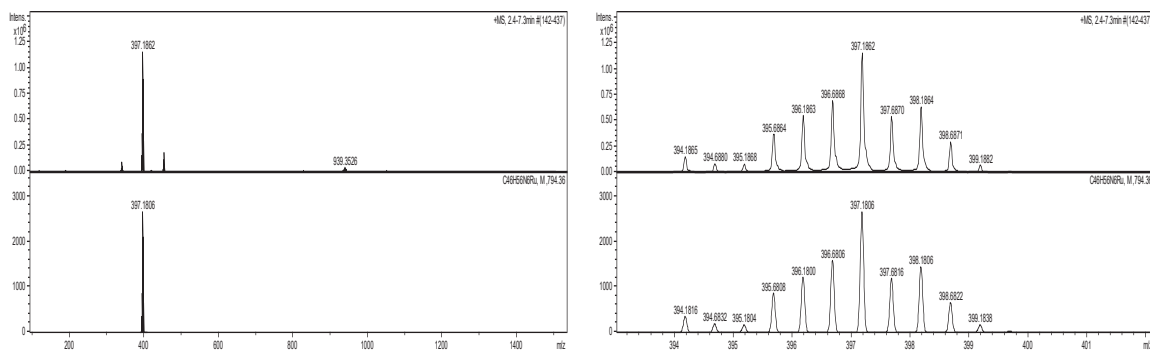


**Figure 2.4** Experimental and calculated mass spectra of  $[(dtb)_2Ru(bpy)]^{2+}$ , calc. deviation 14 ppm

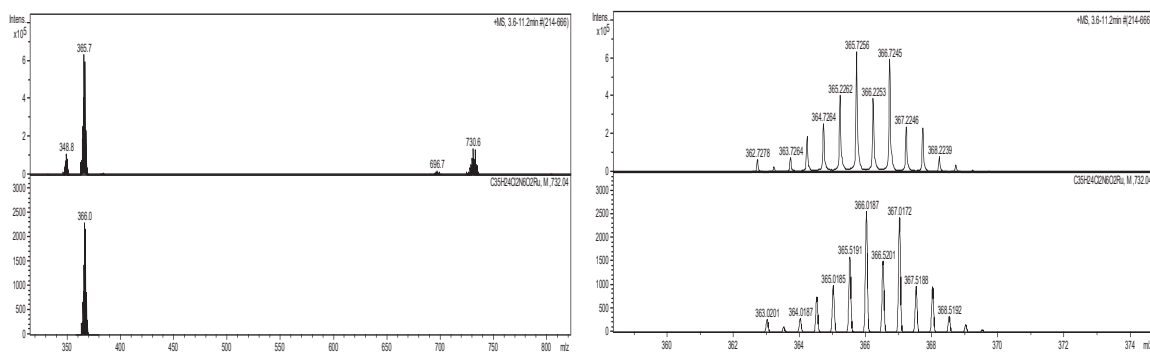


**Figure 2.5** Experimental and calculated mass spectra of  $[(5-Clphen)_2Ru(4-OH-4'-OMebpy)]^{2+}$ , calc. deviation 801 ppm.

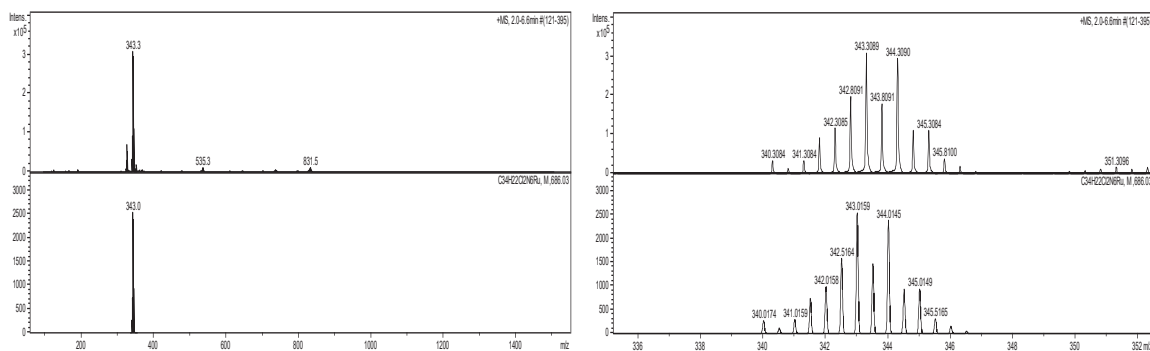


**Figure 2.6** Experimental and calculated mass spectra of  $[5-Clphen)_2Ru(bpy)]^{2+}$ , calc. deviation 854 ppm.

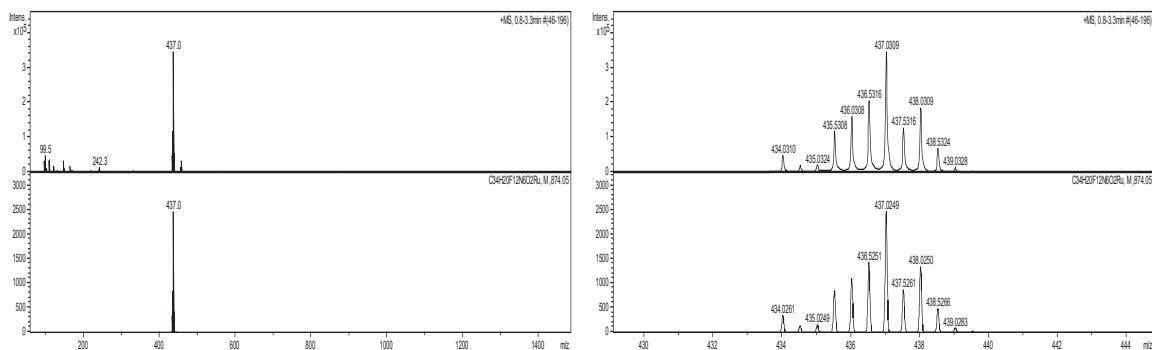


**Figure 2.7** Experimental and calculated mass spectra of  $[(\text{flpy})_2\text{Ru}(4,4'\text{-dhbpy})]^{2+}$ , calc. deviation 14 ppm

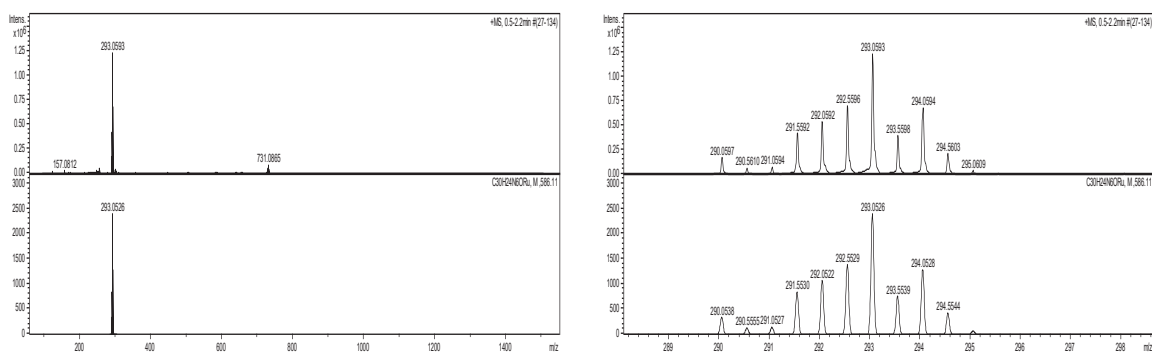


**Figure 2.8** Experimental and calculated mass spectra  $[(\text{bpy})_2\text{Ru}(4\text{-OHbpy})]^{2+}$ , calc. deviation 23 ppm.

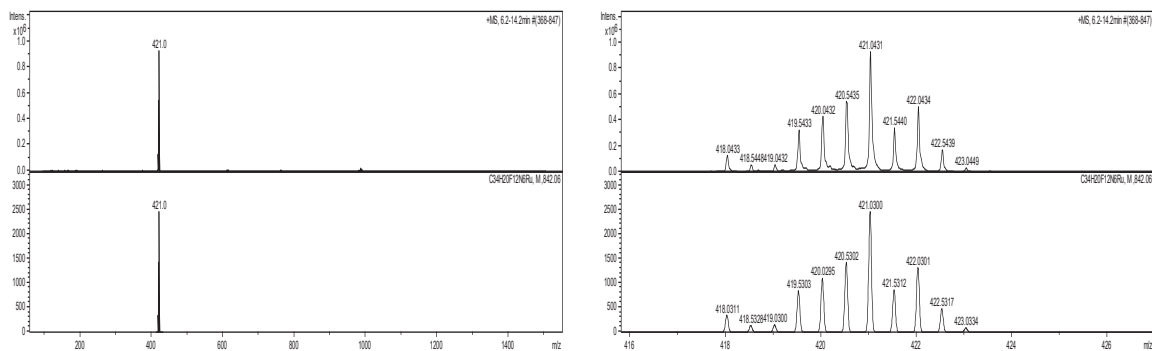


**Figure 2.9** Experimental and calculated mass spectra of  $[(\text{flpy})_2\text{Ru}(\text{bpy})]^{2+}$ , calc. deviation 31 ppm.

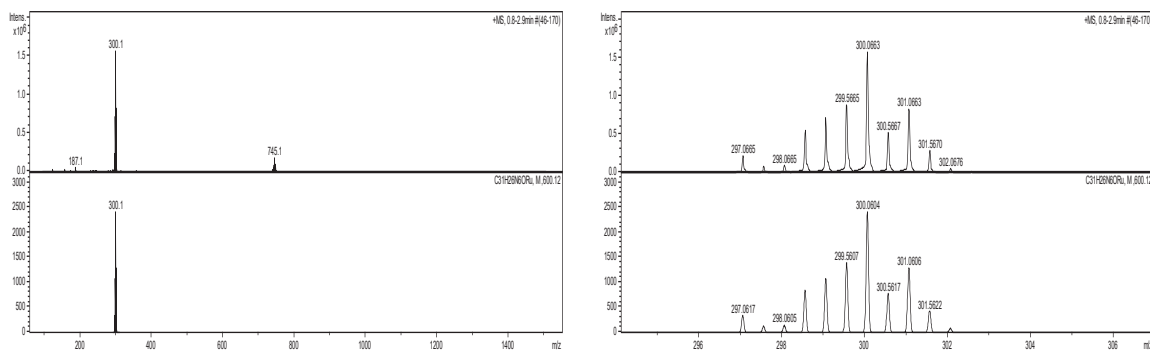


**Figure 2.10** Experimental and calculated mass spectra  $[(bpy)_2Ru(4-OMebpy)]^{2+}$ , calc. deviation 20 ppm

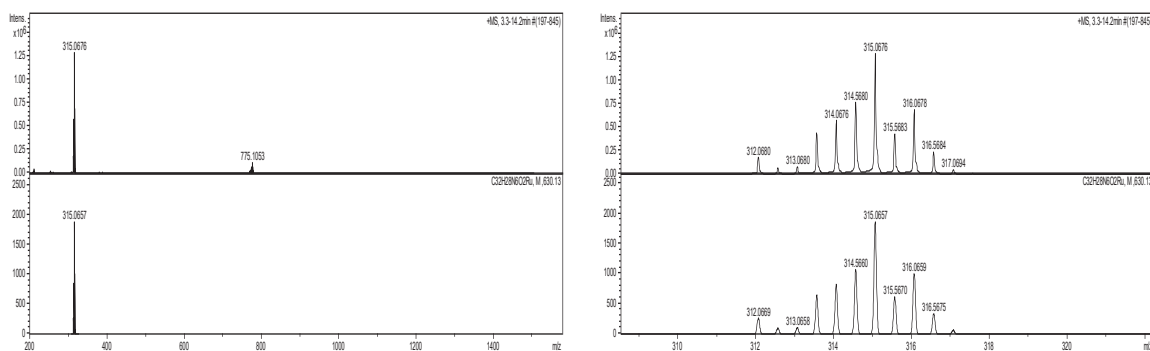


**Figure 2.11** Experimental and calculated mass spectra of  $[(bpy)_2Ru(4,4'-dmbpy)]^{2+}$ , calc deviation 6 ppm

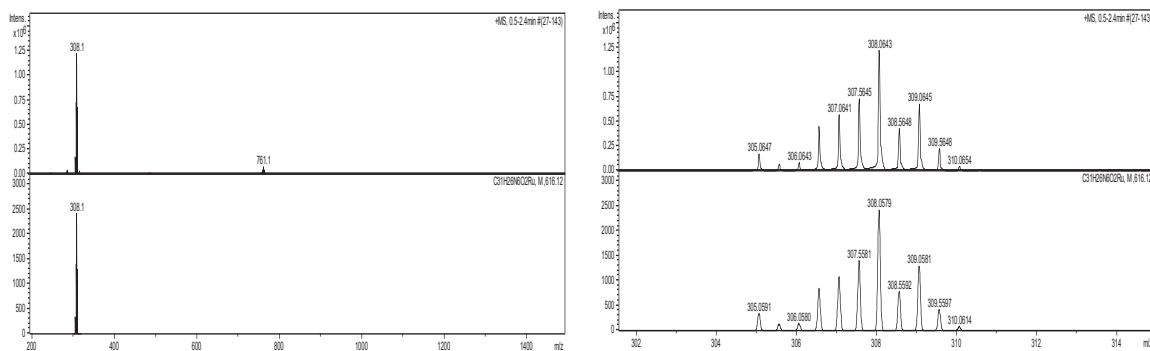


**Figure 2.12** Experimental and calculated mass spectra for  $[(bpy)_2Ru(4-OH-4'-OMebpy)]^{2+}$ , calc. deviation 21 ppm

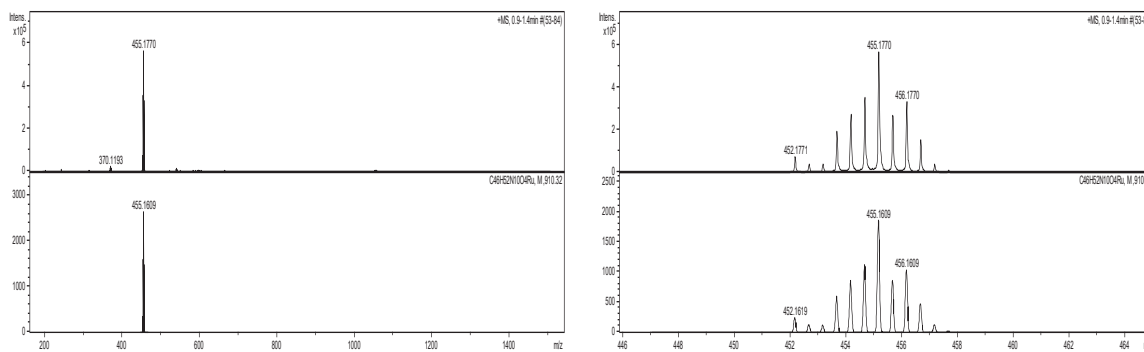


**Figure 2.13** Experimental and calculated mass spectra of  $[(dpab)_2Ru(bpy)]^{2+}$ , calc. deviation 35 ppm

### 2.3.5 $^1H$ NMR and $^1H$ - $^1H$ COSY Assignments

In addition to ESI-MS,  $^1H$ NMR and COSY spectra were used to help characterize the complexes and bipyridinium quenchers. For bis-heteroleptic complexes, the aromatic region will be composed of three sets of three protons when each ligand is a symmetric substituted or unsubstituted 2,2'-bipyridine. When the ligands are asymmetric, a greater number of peaks are observed in the NMR spectrum. For tris-chelate ruthenium complexes, proton chemical shifts are influenced by the ligands being trans to one another. For many complexes, this trans effect will be observed by producing nondegenerate chemical shifts for chemically identical ligands. For the complexes  $[(bpy)_2Ru(4,4'-dhbpy)]^{2+}$  and  $[(bpy)_2Ru(4,4'-dmbpy)]^{2+}$ , the NMR's have been reported in the literature for these complexes.  $[(bpy)_2Ru(4-OHbpy)]^{2+}$  and  $[(bpy)_2Ru(4-OMebpy)]^{2+}$  were synthesized and characterized by collaborators at Villanova University. The mass spectra were presented for all complexes to ensure that trace impurities (those which are below the threshold of detection by  $^1H$ NMR and elemental analysis) were not present that would interfere with subsequent photophysical studies. Below are reported the  $^1H$ NMR and COSY spectra

obtained for compounds synthesized for this work. In all cases, the residual solvent peak was used as an internal reference.<sup>12</sup>

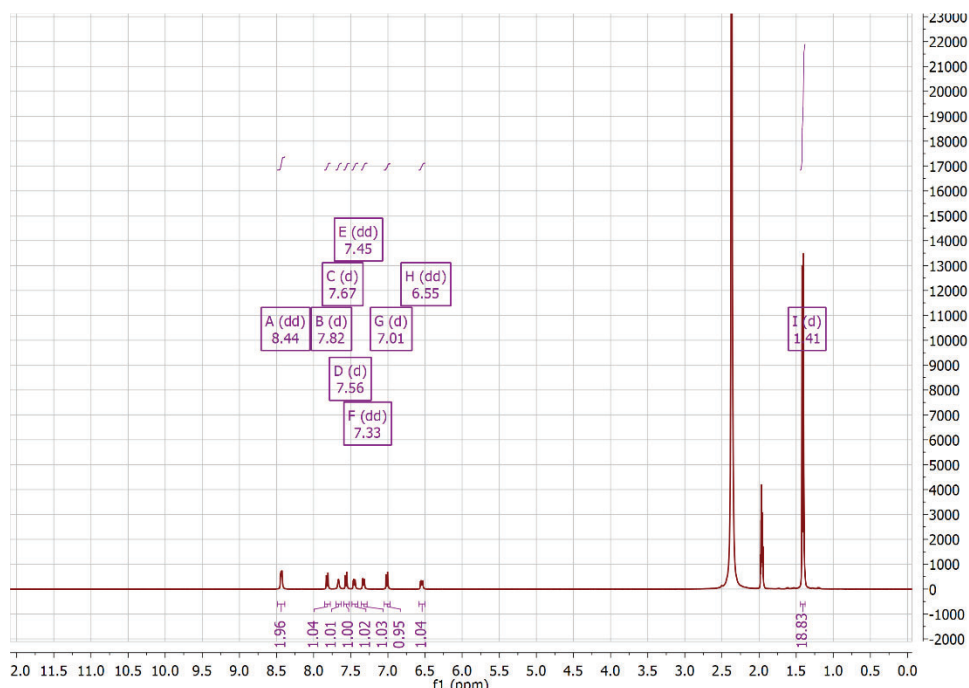


Figure 2.14  $^1\text{H}$ NMR of  $[(\text{dtb})_2\text{Ru}(4,4'\text{-dhbpy})]^{2+}$  in  $\text{CD}_3\text{CN}$

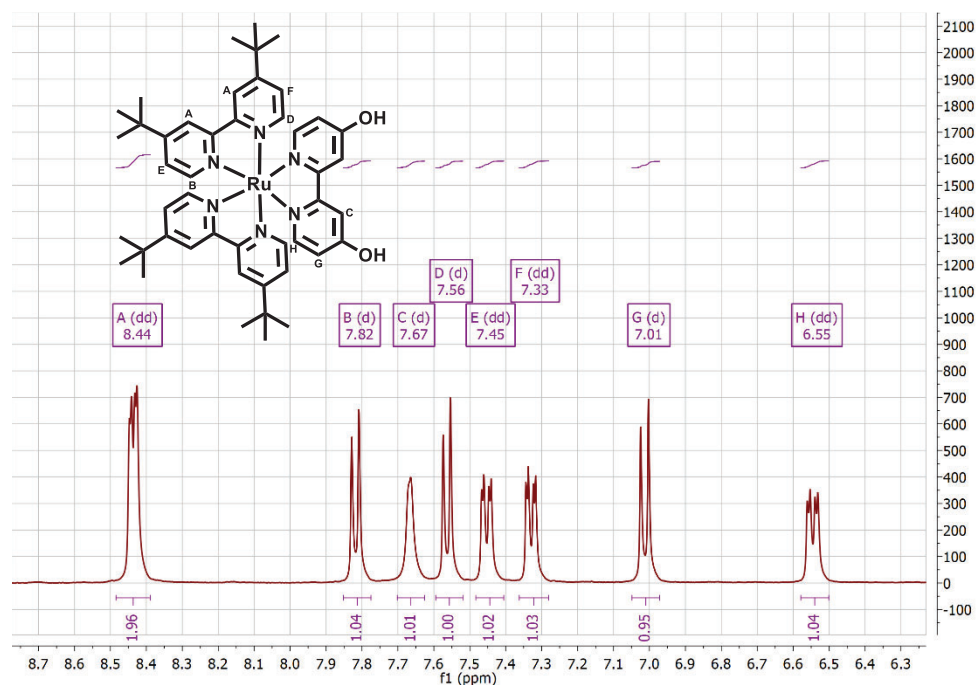
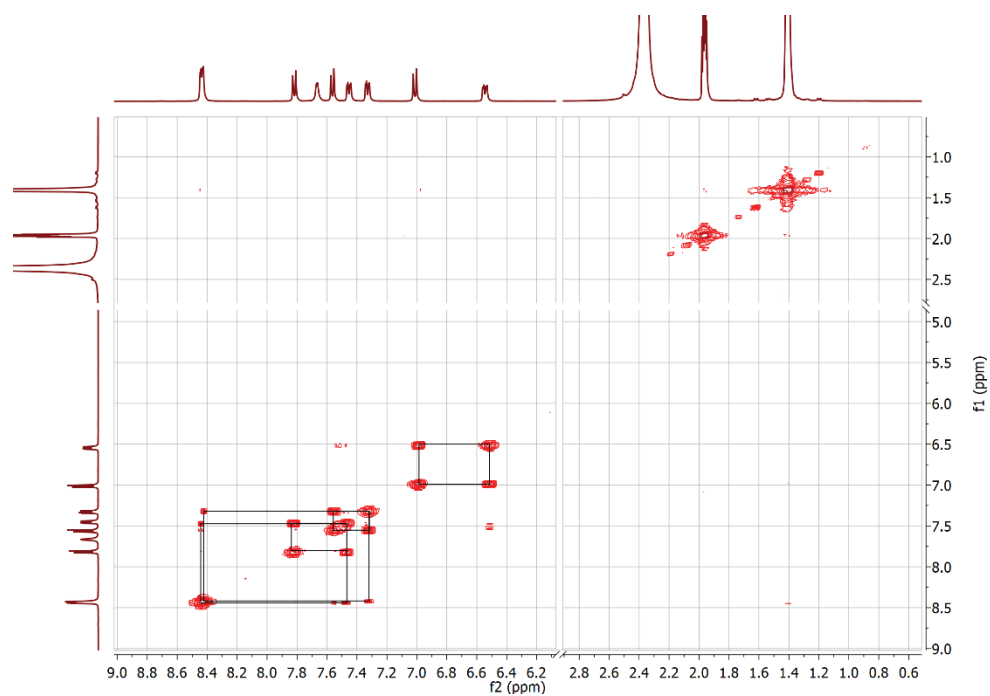


Figure 2.15 Aromatic region of the  $^1\text{H}$ NMR of  $[(\text{dtb})_2\text{Ru}(4,4'\text{-dhbpy})]^{2+}$



**Figure 2.16**  $^1\text{H}$ - $^1\text{H}$  COSY of  $[(\text{dtb})_2\text{Ru}(4,4'\text{-dhbpy})]^{2+}$  in  $\text{CD}_3\text{CN}$

In the  $^1\text{H-NMR}$  spectrum of  $[(\text{dtb})_2\text{Ru}(4,4'\text{-dhbpy})]^{2+}$  the cross-ring coupling between aromatic protons can help aid in the assignment of chemical shifts. For the complex, there are three aromatic protons for each unique pyridine ring on the molecule that will be coupled with one another. The assignments are listed with letters A-F. The use of  $^1\text{H-}^1\text{H}$  correlation spectroscopy allows for the determination of which aromatic peaks belong to the same ring. The coupling constants are expected based on the degree of cross ring coupling. For protons A, it can be expected to have a small coupling constant between 1-2 Hz as it coupled with proton F. For proton D, coupling constant for J-coupling with proton F is expected to be between 5-6 Hz. And for proton F, because it couples to both A and D, the peak is split into a doublet of doublets with a 5-6 Hz coupling constant and a 1-2 Hz coupling constant corresponding to coupling with D and A, respectively. The same coupling pattern can be seen for the other 6 unique protons, as the substitution on the pyridine ring is the same. The assignments of protons are labeled in figure 2.14.

For the corresponding control complex,  $[(\text{dtb})_2\text{Ru}(\text{bpy})]^{2+}$  the coupling is more complex, as there is an additional proton on the unsubstituted rings of the 2,2'-bipyridine. The resulting  $^1\text{H-NMR}$  shows several overlapping peaks, for which assignment is made difficult as the coupling constants cannot be elucidated from the spectrum. An attempt at making assignments can be made using the homonuclear COSY spectrum, but again, assignment is convoluted by the nature of the overlapping peaks. For characterization, the integration is in line with what is expected for the complex. The  $^1\text{H-NMR}$  and COSY spectra are shown in figures 2.16-2.18 below.

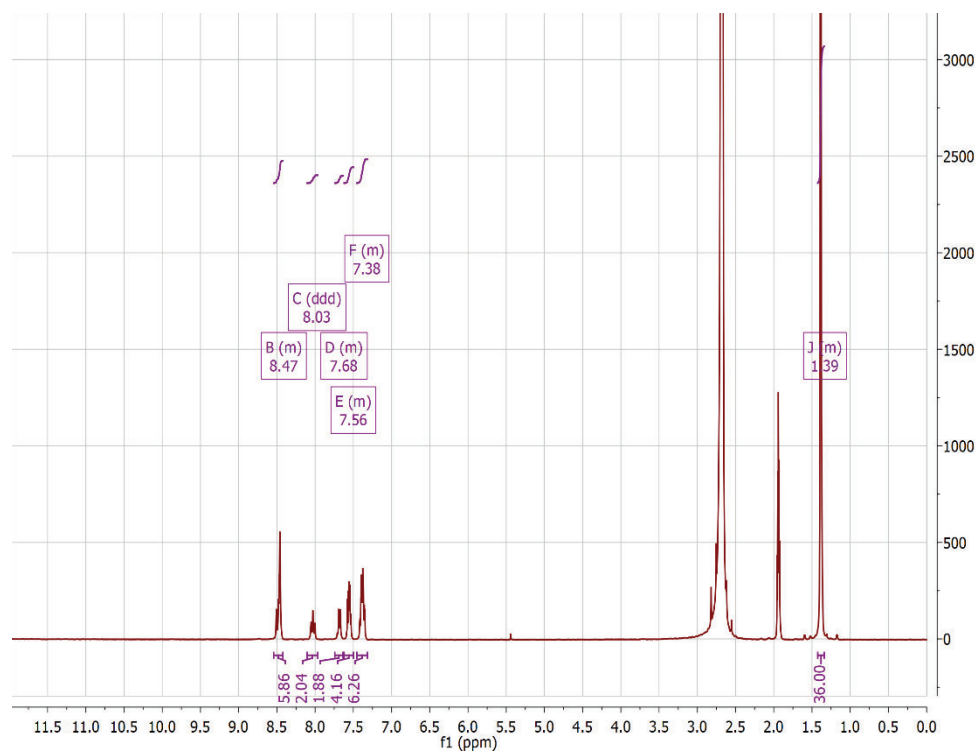


Figure 2.17  $^1\text{H NMR}$  of  $[(\text{dtb})_2\text{Ru}(\text{bpy})]^{2+}$  in  $\text{CD}_3\text{CN}$

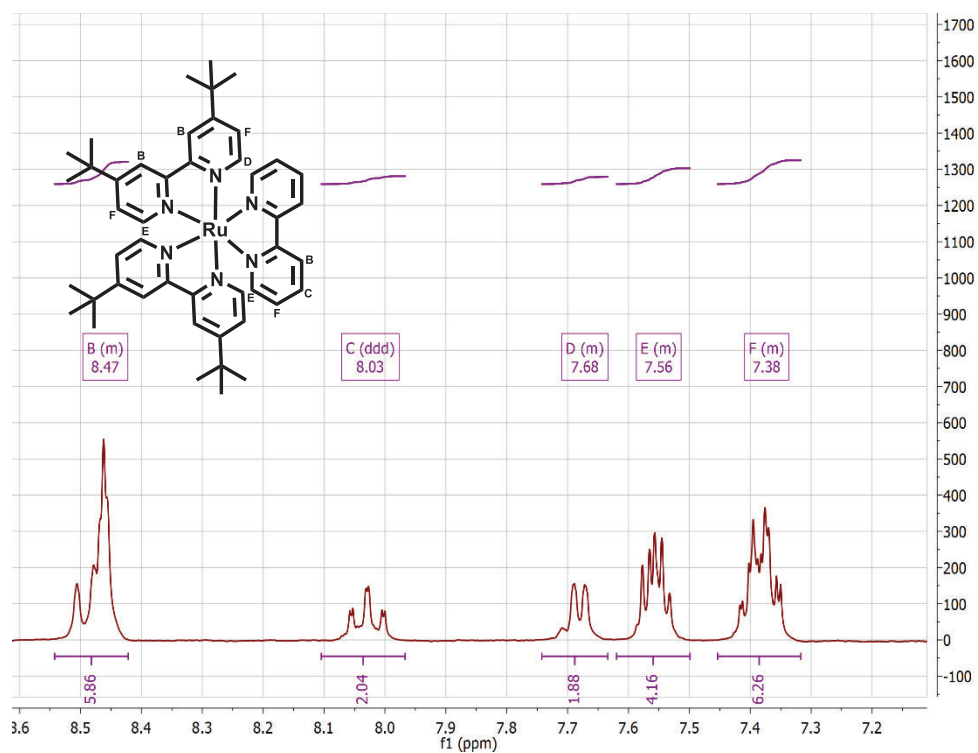
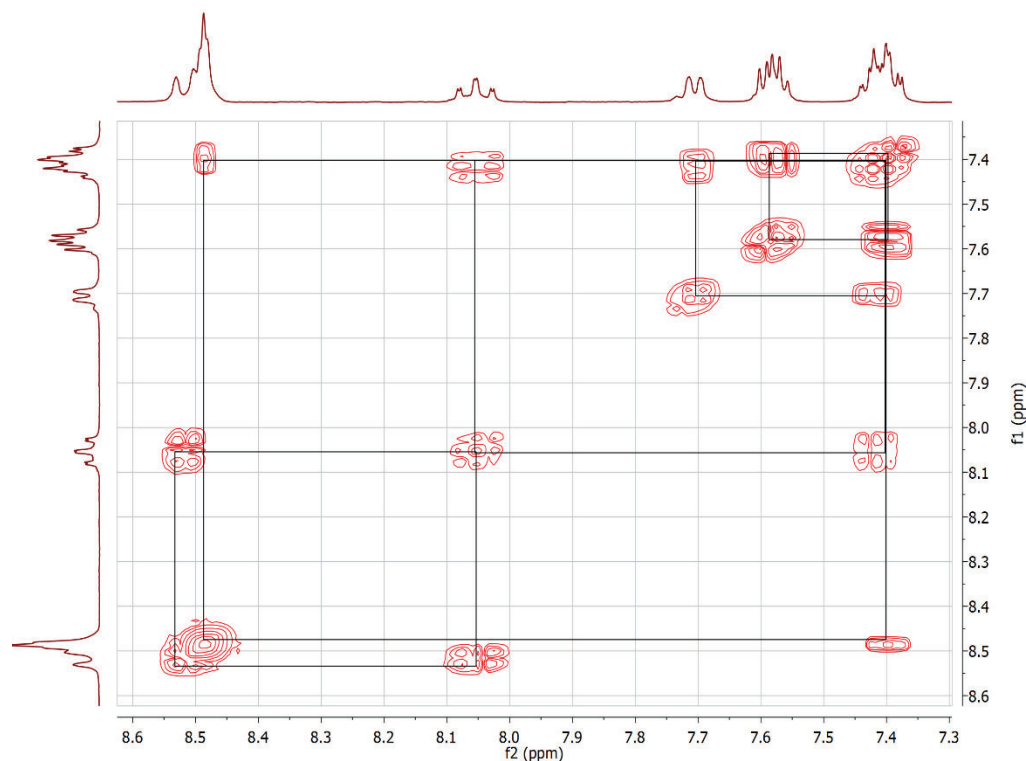
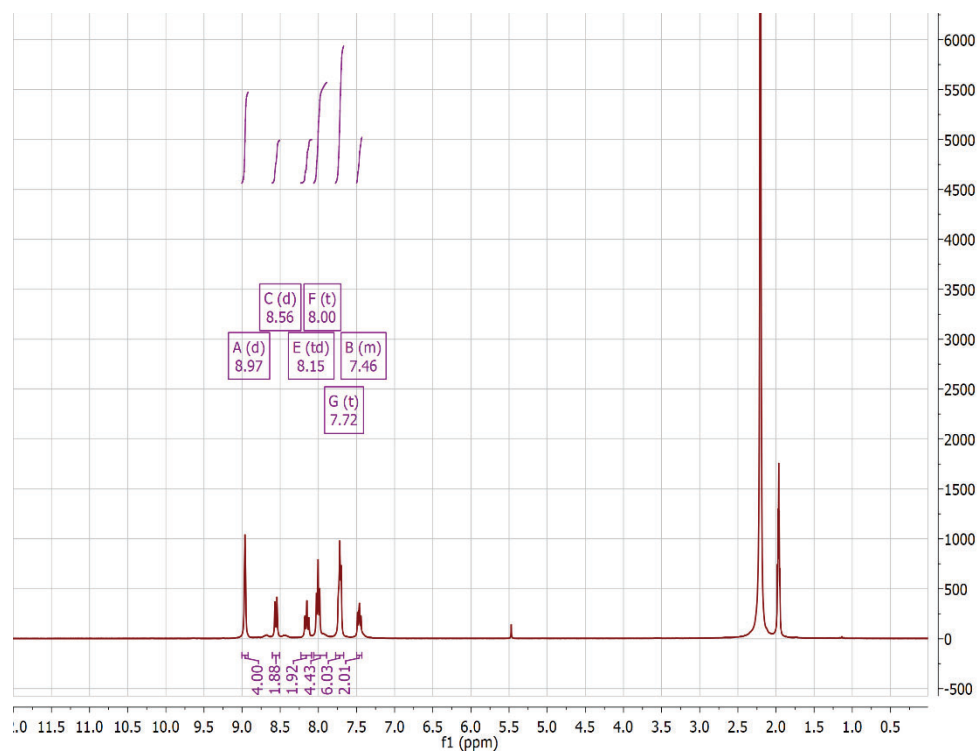


Figure 2.18 Aromatic region of  $^1\text{H NMR}$  of  $[(\text{dtb})_2\text{Ru}(\text{bpy})]^{2+}$  in  $\text{CD}_3\text{CN}$



**Figure 2.19**  $^1\text{H}$ - $^1\text{H}$  COSY of  $[(\text{dtb})_2\text{Ru}(\text{bpy})]^{2+}$  in  $\text{CD}_3\text{CN}$

As with the previous control complex,  $[(\text{flpy})_2\text{Ru}(\text{bpy})]^{2+}$  shows a substantial degree of peak overlap in the aromatic region. COSY was useful in distinguishing what protons were coupled to each other and the assignments of protons can be seen in figure 2.20. The  $^1\text{H}$ NMR and COSY spectra are shown in figures 2.19-2.21. The coupling constants are reported for several of the peaks as follows, A ( $J=2.2$  Hz), C ( $J=8.1$  Hz), E ( $J=7.9, 1.5$  Hz), F ( $J=6.4$  Hz), and G ( $J=6.0$  Hz). Due to the structural similarities between  $[(\text{dtb})_2\text{Ru}(\text{bpy})]^{2+}$  and  $[(\text{flpy})_2\text{Ru}(\text{bpy})]^{2+}$  the splitting of the aromatic protons is expected to be the same for this complex. Likewise, the same can be said of the  $[(\text{flpy})_2\text{Ru}(4,4'-(\text{OH})_2\text{-bpy})]^{2+}$  complex as well as the dpab complexes.



**Figure 2.20**  $^1\text{H}$ NMR spectrum of  $[(\text{fipy})_2\text{Ru}(\text{bpy})]^{2+}$  in  $\text{CD}_3\text{CN}$

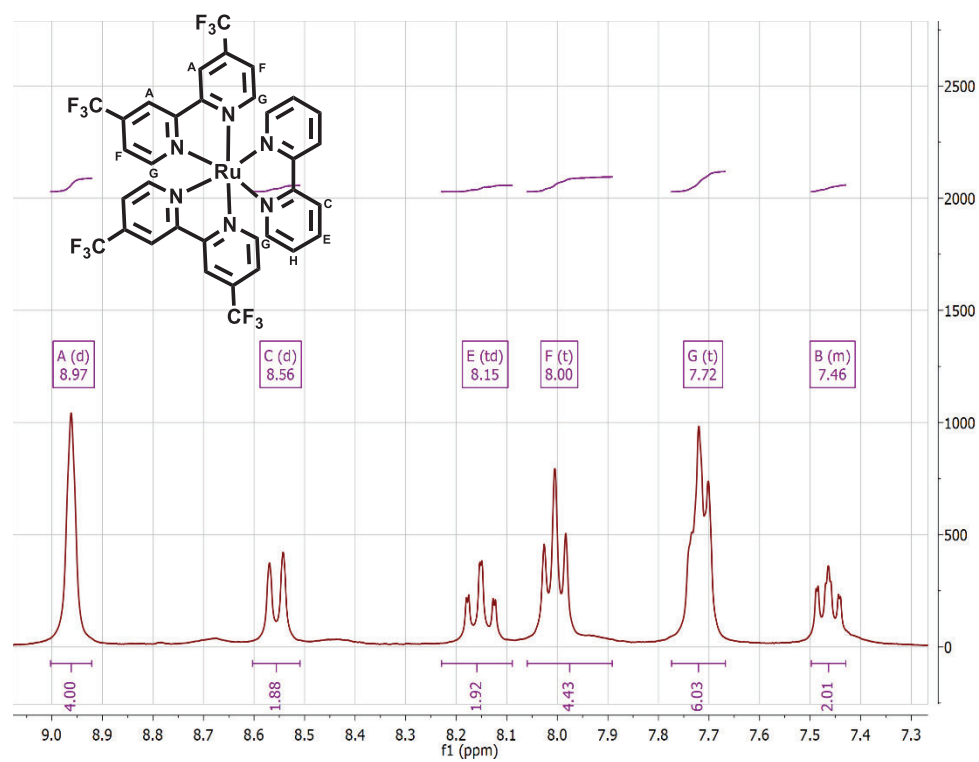


**Figure 2.21** Aromatic region of  $^1\text{H}$ NMR of  $[(\text{fipy})_2\text{Ru}(\text{bpy})]^{2+}$

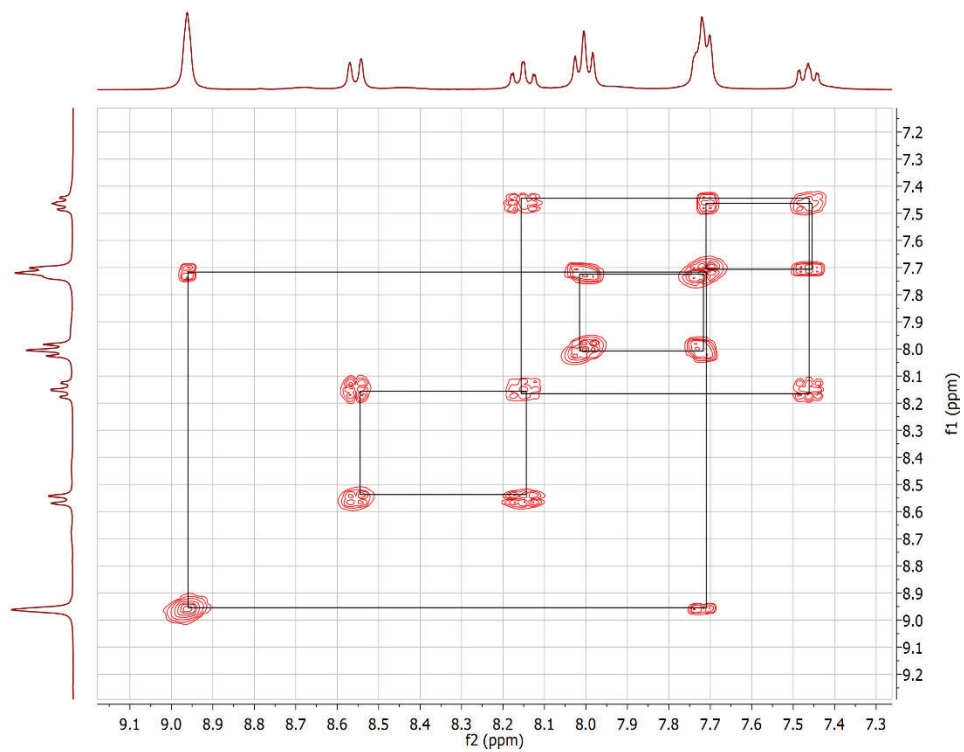


**Figure 2.22**  $^1\text{H}$ - $^1\text{H}$  COSY of  $[(\text{flpy})_2\text{Ru}(\text{bpy})]^{2+}$

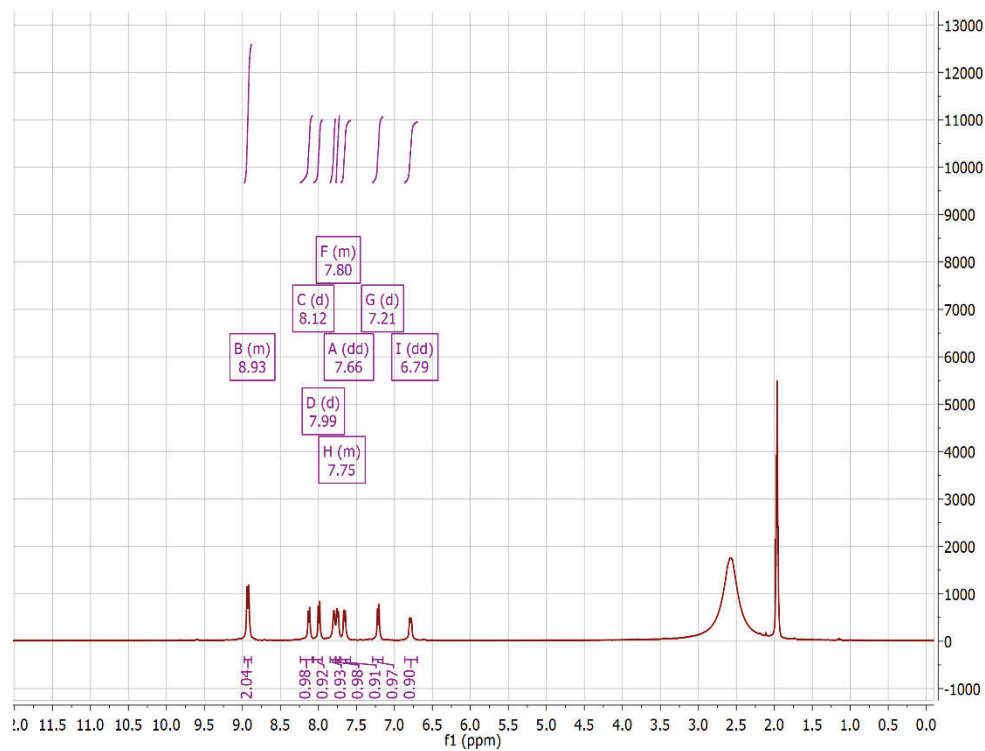


**Figure 2.23**  $^1\text{H}$ NMR spectrum of  $[(\text{fipy})_2\text{Ru}(4,4'\text{-(OH)}_2\text{bpy})]^{2+}$  in  $\text{CD}_3\text{CN}$

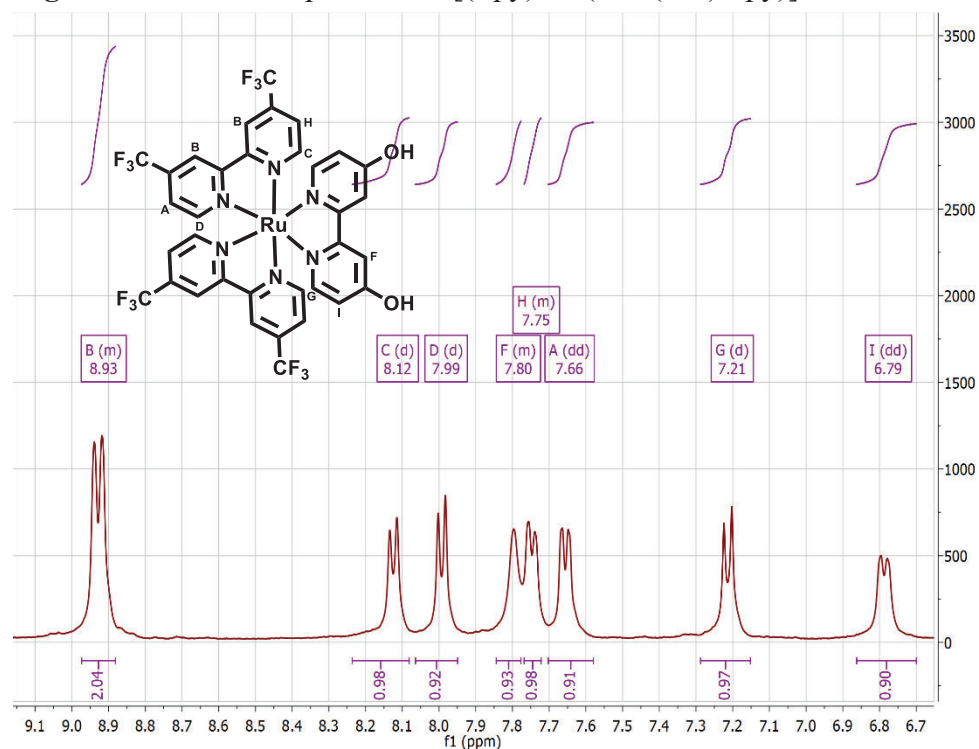


**Figure 2.24** Aromatic region of  $^1\text{H}$ NMR of  $[(\text{fipy})_2\text{Ru}(4,4'\text{-(OH)}_2\text{bpy})]^{2+}$

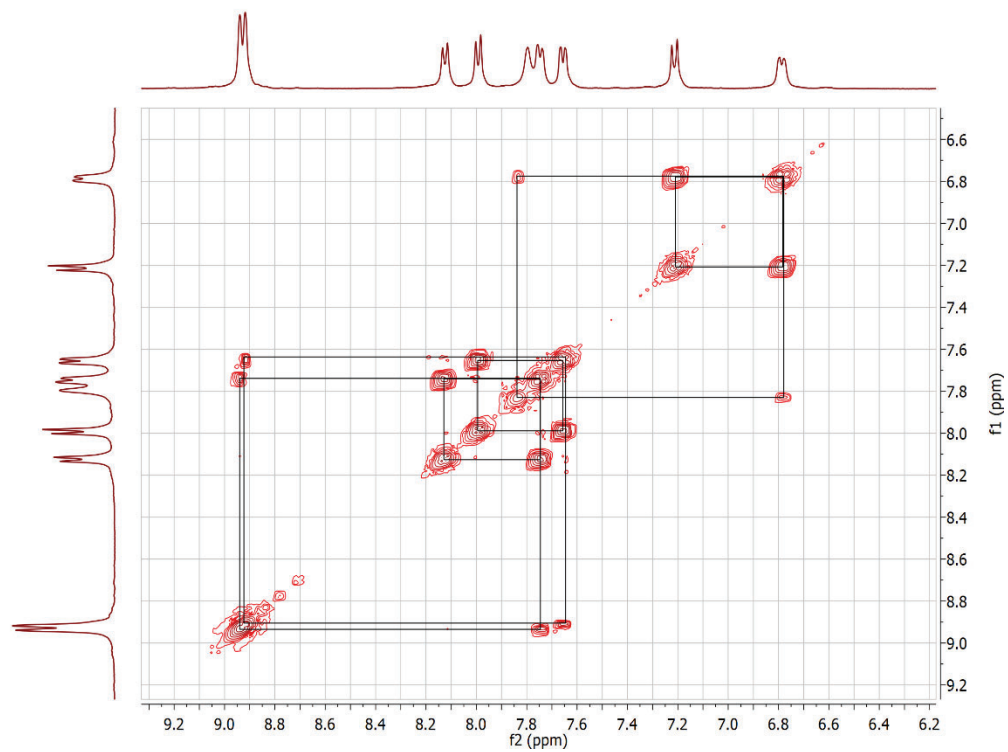


**Figure 2.25**  $^1\text{H}$ - $^1\text{H}$  COSY of  $[(\text{flpy})_2\text{Ru}(4,4'\text{-(OH)}_2\text{bpy})]^{2+}$  in  $\text{CD}_3\text{CN}$

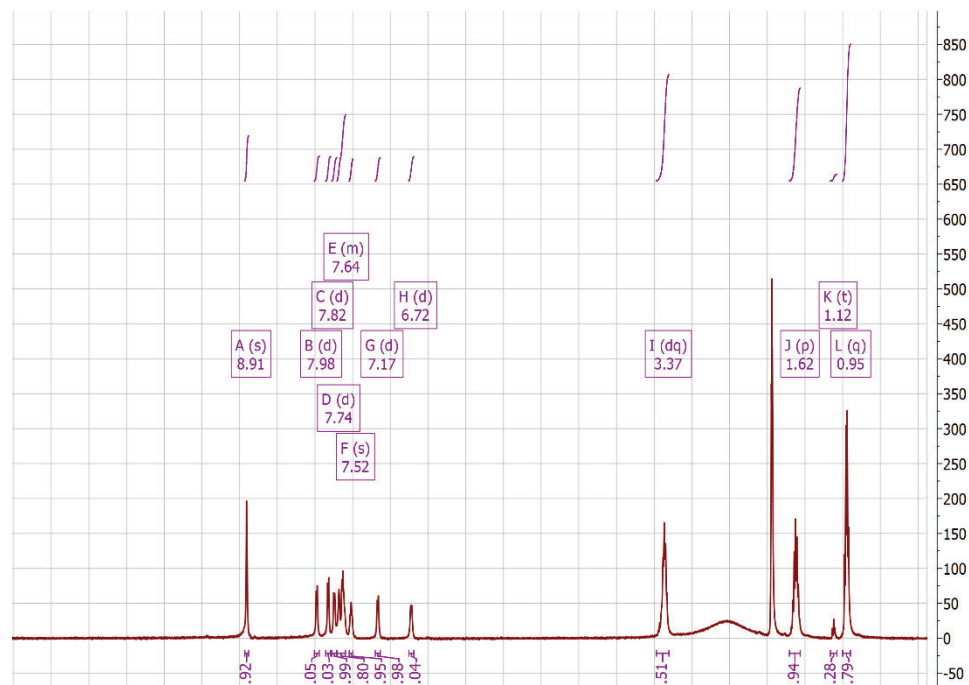


Figure 2.26  $^1\text{H NMR}$  of  $[(\text{dpab})_2\text{Ru}(4,4'\text{-(OH)}_2\text{bpy})]^{2+}$

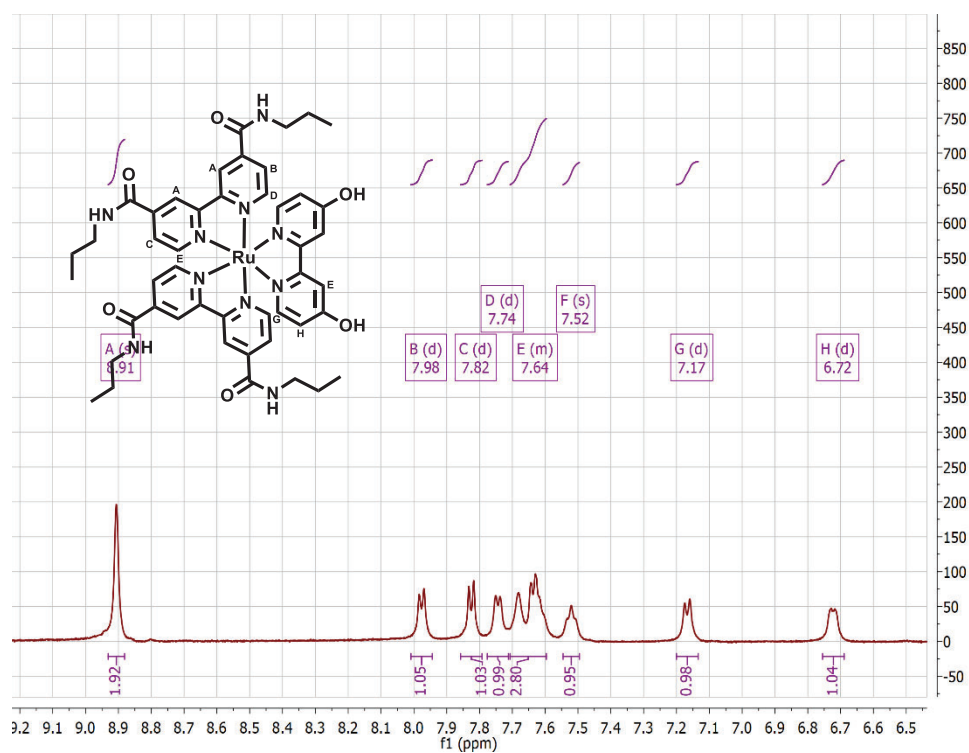
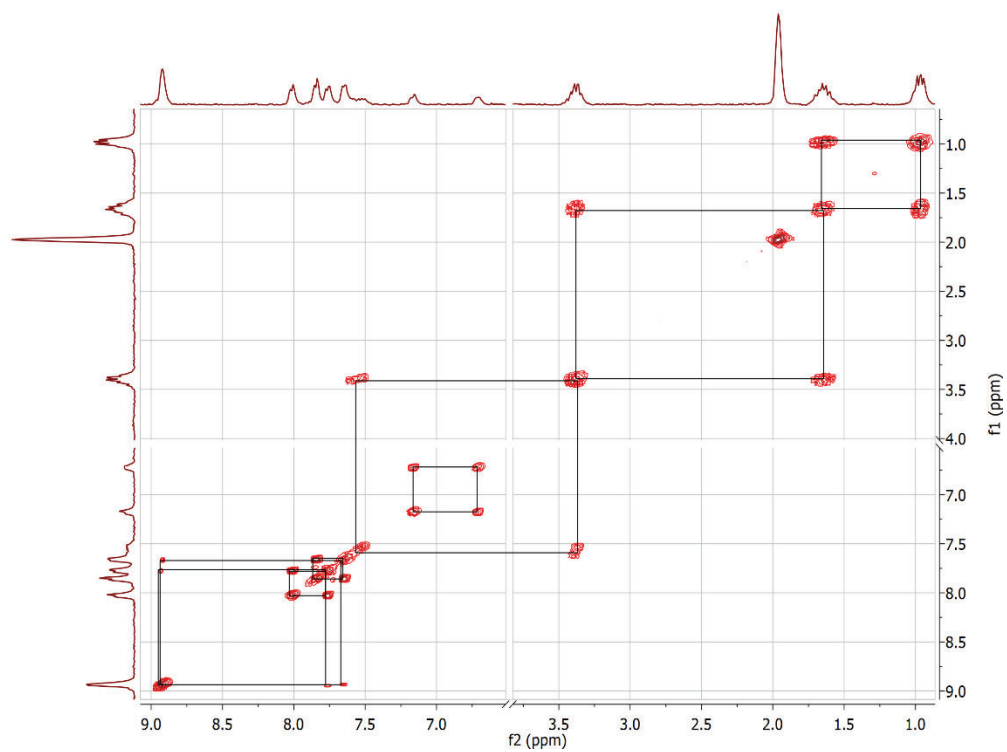


Figure 2.27 Aromatic region of  $^1\text{H NMR}$  of  $[(\text{dpab})_2\text{Ru}(4,4'\text{-(OH)}_2\text{bpy})]^{2+}$  in  $\text{CD}_3\text{CN}$



**Figure 2.28**  $^1\text{H}$ - $^1\text{H}$  COSY spectrum of  $[(\text{dpab})_2\text{Ru}(4,4'\text{-(OH)}_2\text{bpy})]^{2+}$  in  $\text{CD}_3\text{CN}$

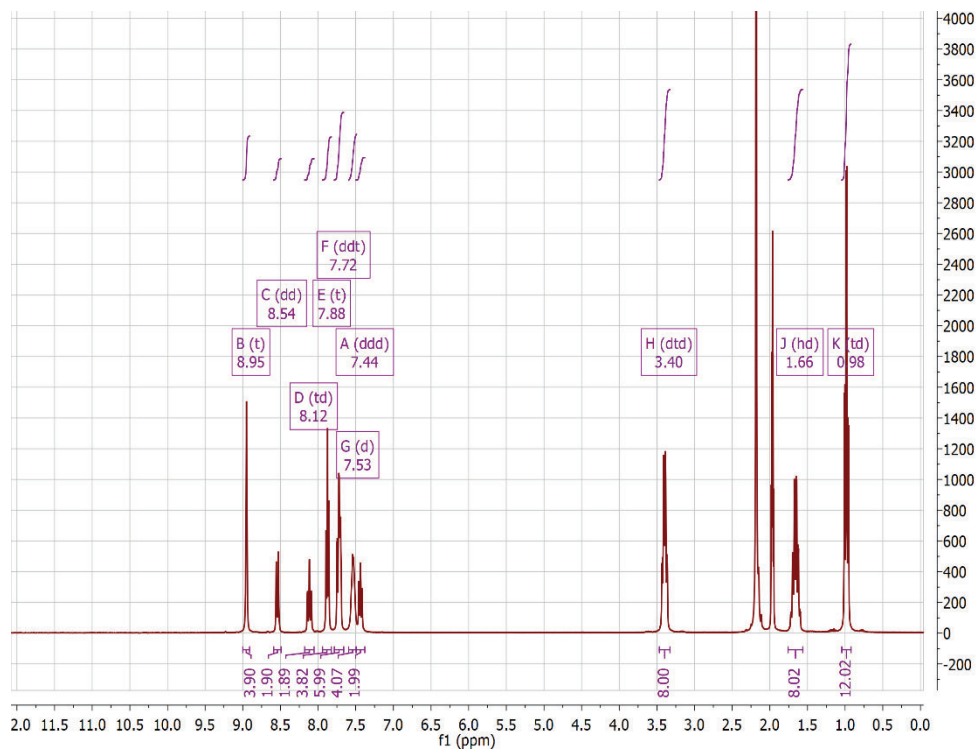


Figure 2.30  $^1\text{H NMR}$  of  $[(\text{dpab})_2\text{Ru}(\text{bpy})]^{2+}$  in  $\text{CD}_3\text{CN}$

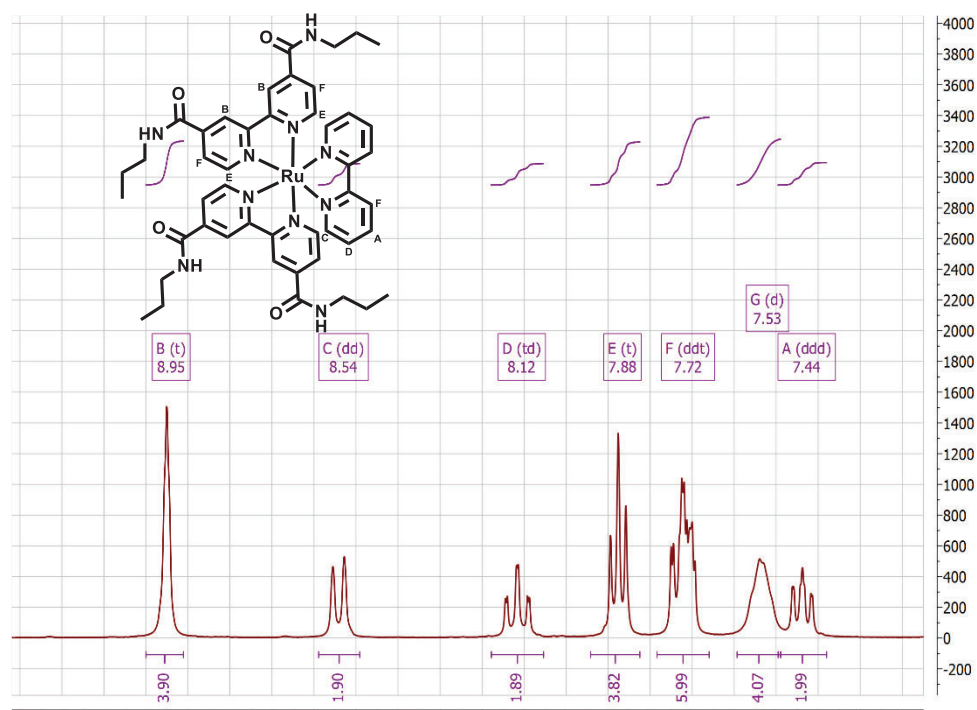
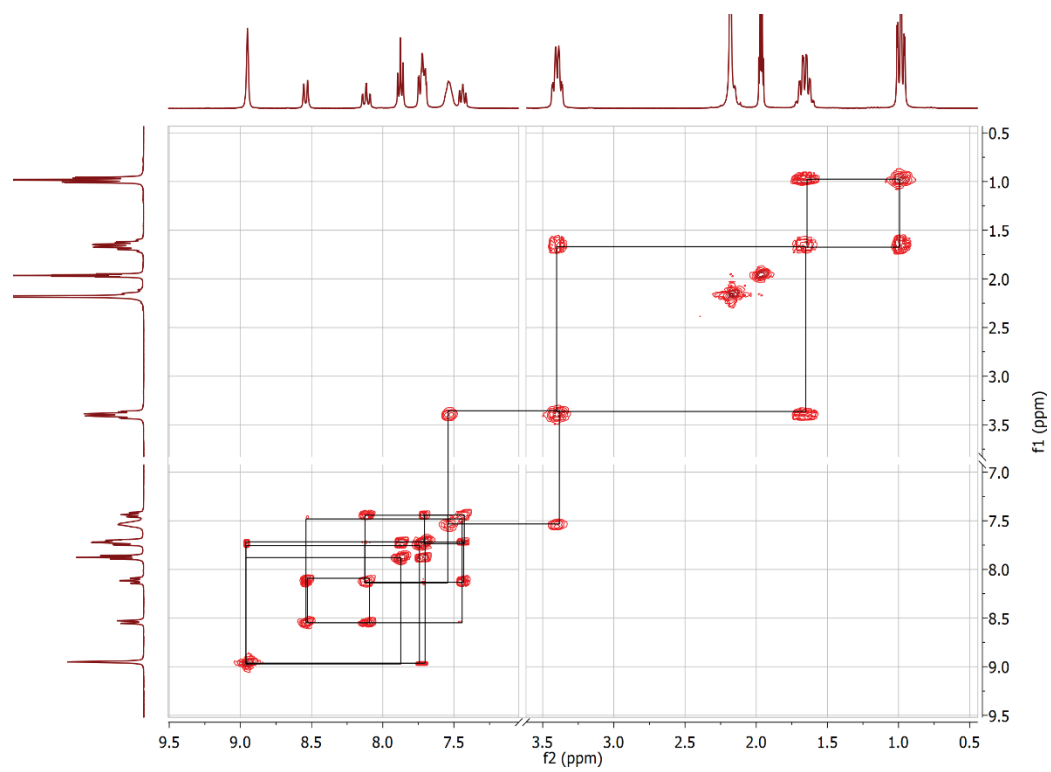


Figure 2.29 Aromatic region of  $^1\text{H NMR}$  of  $[(\text{dpab})_2\text{Ru}(\text{bpy})]^{2+}$  in  $\text{CD}_3\text{CN}$



**Figure 2.31**  $^1\text{H}$ - $^1\text{H}$  COSY of  $[(\text{dpab})_2\text{Ru}(\text{bpy})]^{2+}$  in  $\text{CD}_3\text{CN}$

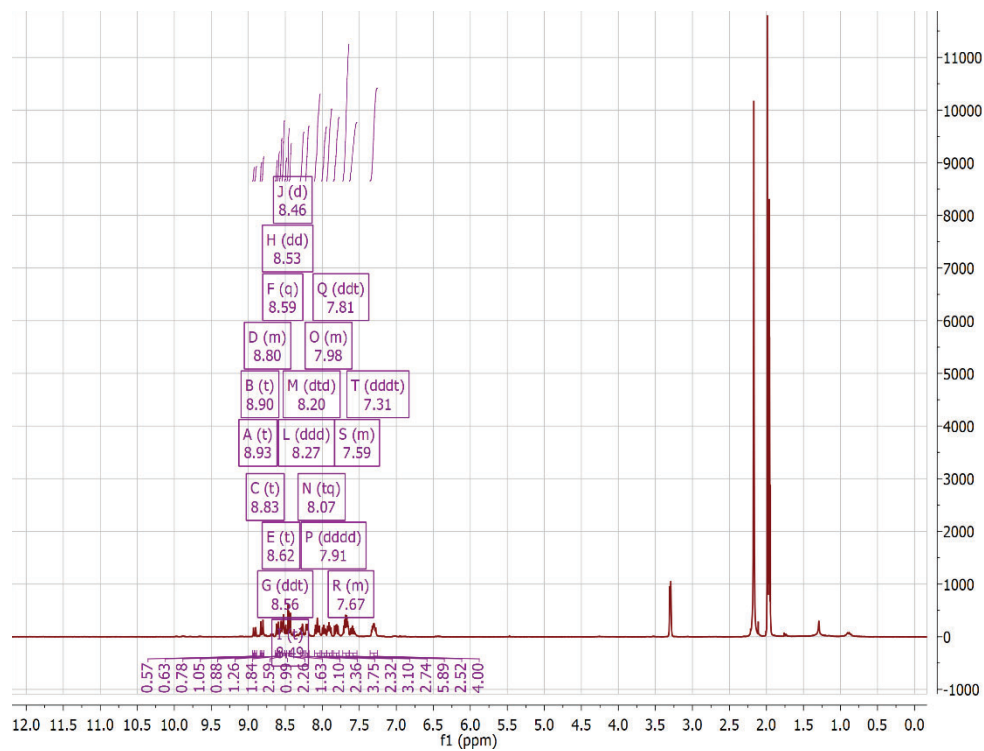


Figure 2.32  $^1\text{H NMR}$  of  $[(\text{Cl-phen})_2\text{Ru}(\text{bpy})]^{2+}$  in  $\text{CD}_3\text{CN}$

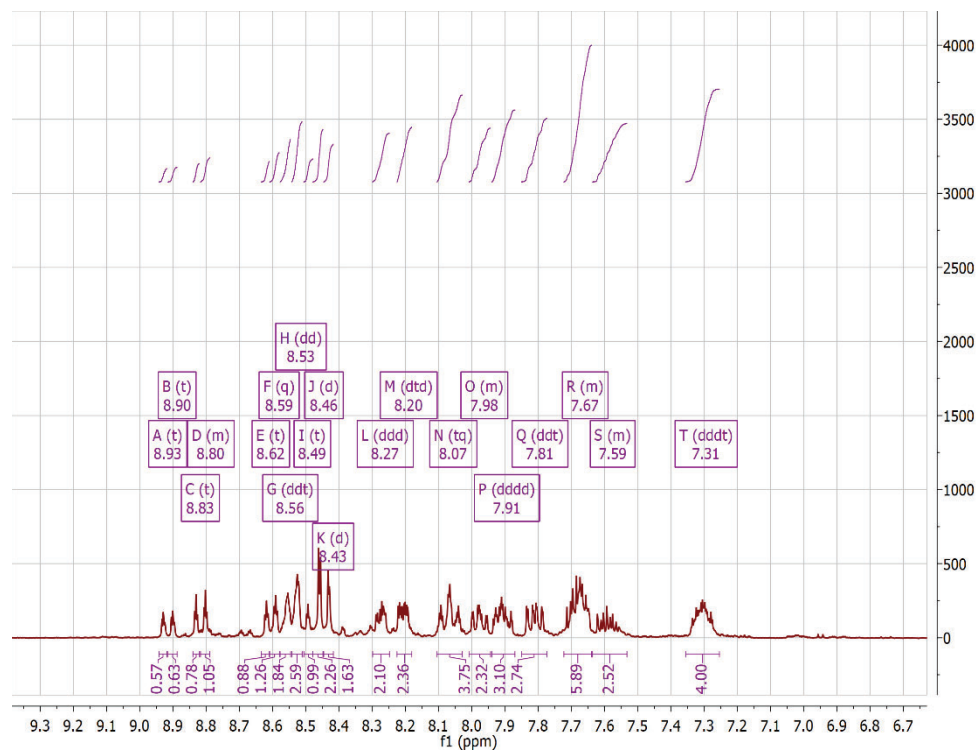
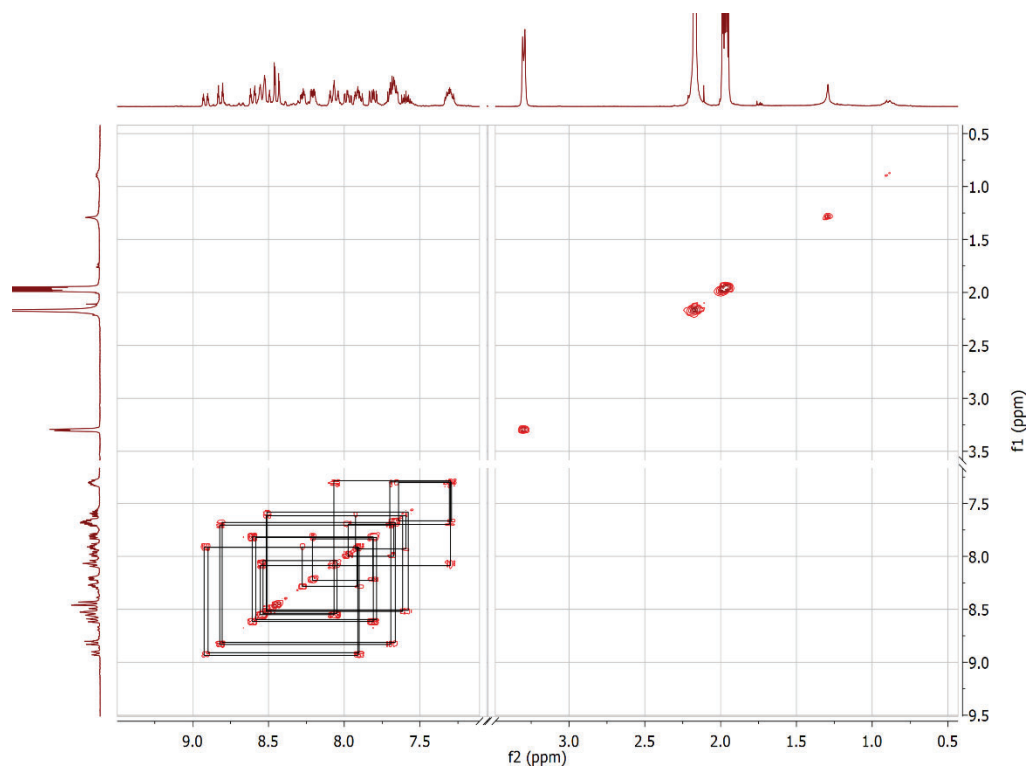


Figure 2.33 Aromatic region of  $^1\text{H NMR}$  of  $[(\text{Cl-phen})_2\text{Ru}(\text{bpy})]^{2+}$  in  $\text{CD}_3\text{CN}$



**Figure 2.34** <sup>1</sup>H-<sup>1</sup>H COSY of [(Cl-phen)<sub>2</sub>Ru(bpy)]<sup>2+</sup> in CD<sub>3</sub>CN

The degree of overlap of the aromatic peaks for the isomers of the complex [Ru(Cl-phen)<sub>2</sub>(bpy)]<sup>2+</sup> make definitive assignment of the peaks difficult. Although assignment is precluded by complex overlaying peaks, the integration is consistent with the desired product. ESI-MS further confirms the presence of one ruthenium complex.

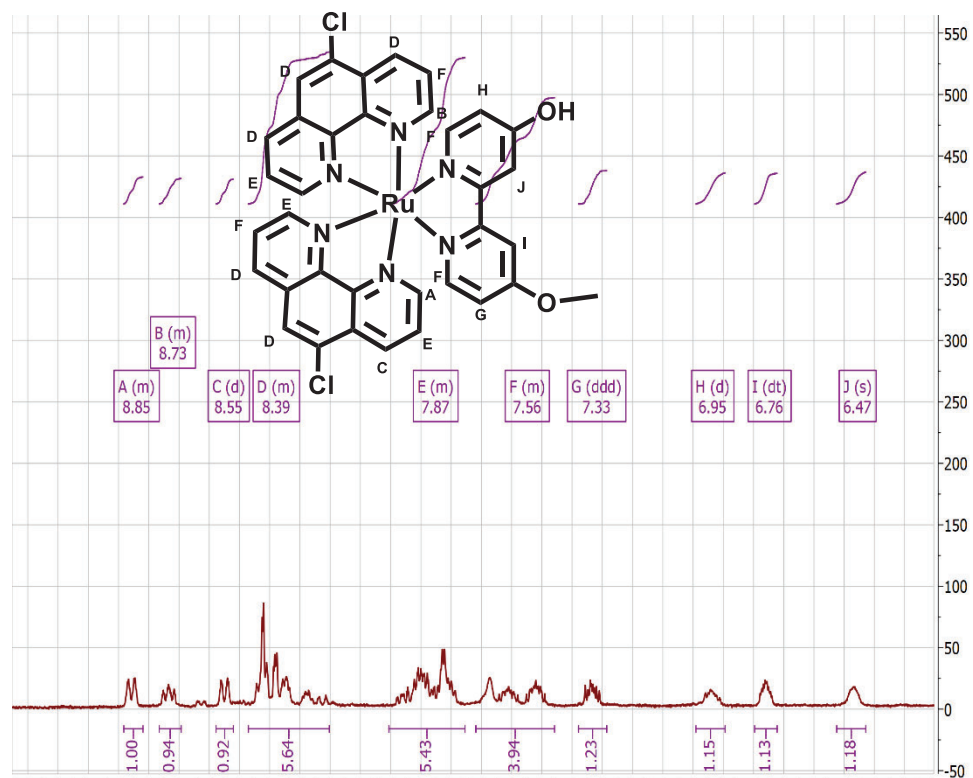


Figure 2.35 Aromatic region of  $^1\text{H NMR}$  of  $[(\text{Cl-phen})_2\text{Ru}(4\text{-OH-4'-OMe-bpy})]^{2+}$

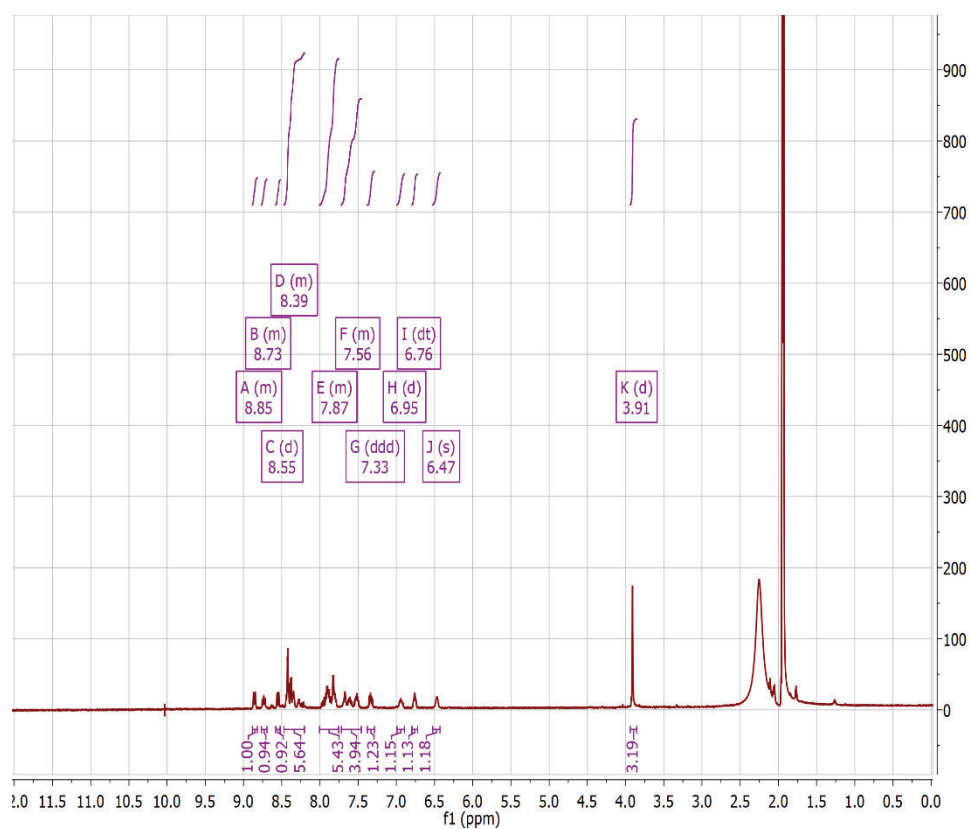
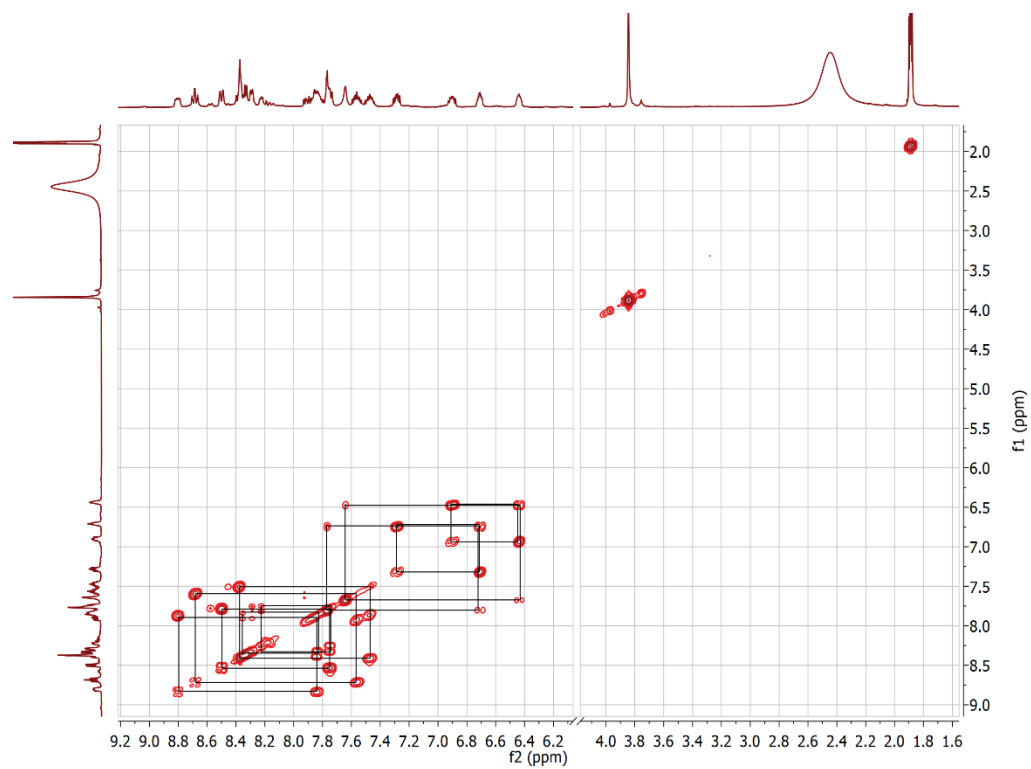


Figure 2.36  $^1\text{H NMR}$  of  $[(\text{Cl-phen})_2\text{Ru}(4\text{-OH-4'-OMe-bpy})]^{2+}$



**Figure 2.37**  $^1\text{H}$ - $^1\text{H}$  COSY spectrum of  $[(\text{Cl-phen})_2\text{Ru}(4\text{-OH-4'-OMe-bpy})]^{2+}$

## 2.4 Electrochemical and Photophysical Characterization

### 2.4.1 Electrochemical Characterization

For all complexes, cyclic voltammetric measurements were made in acetonitrile with 0.1 M tetrabutylammonium hexafluorophosphate as supporting electrolyte. All voltammograms are referenced to the  $\text{Fc}^{+/0}$  redox couple and are reported as such in Table 2.1, for voltammograms where ferrocene was used as an internal reference, the  $\text{Fc}^{+/0}$  redox couple is shown in the voltammogram with the  $E_{1/2}$  value at 0 V. The scan rate for all measurements was 0.1 V/sec. For complexes bearing hydroxylated bipyridine ligands, cyclic voltammetric measurements were made in the presence of one molar equivalent of tetrabutylammonium hydroxide to determine the reduction potentials of the deprotonated complexes. For ruthenium diimine complexes, it is expected that in the anodic voltammograms, there should be a single reversible oxidation corresponding to the Ru(III/II) couple. In cathodic voltammograms, there should be observed three reversible reductions corresponding to the one-electron reduction of each of the diimine ligands. Incorporation of the hydroxy functional groups on the 2,2'-bipyridine ligands creates irreversibility in the cathodic voltammograms relative to the corresponding 2,2'-bipyridine control complexes. Incorporation of electron donating and electron withdrawing groups affects the ability to observe reversible diimine based reductions for some complexes.<sup>13</sup>

For the series of complexes, incorporation of electron donating groups shifts the Ru(III/II) potential to more negative relative to the parent  $[(\text{bpy})_2\text{Ru}(4,4'-(\text{OH})_2\text{-bpy})]^{2+}$  complex, while incorporation of electron withdrawing groups (flpy, dpab) shifts the Ru(III/II) potential to more positive values, corresponding to a more difficult oxidation of the metal center.

In the anodic voltammograms for the deprotonated complexes, the oxidation of the ruthenium metal center is irreversible. In some of the voltammograms, there can be seen a small residual current from the protonated complex. For all deprotonated complexes, the cathodic peak potential was used as an estimate for the Ru(III/II) couple which is important for thermochemical analysis of PCET systems that will be discussed in subsequent chapters.

For the complexes,  $[(\text{bpy})_2\text{Ru}(4,4'-(\text{OH})_2\text{-bpy})]^{2+}$  and  $[(\text{bpy})_2\text{Ru}(4,4'-(\text{OMe})_2\text{-bpy})]^{2+}$ , the electrochemistry has been reported in the literature.<sup>2</sup> In addition, the complex  $[(\text{bpy})_2\text{Ru}(4-(\text{OH})-4'-(\text{OMe})\text{-bpy})]^{2+}$  was not investigated for its electrochemical behavior as it was used only for the assessment of the  $\text{p}K_{\text{a}}$  of  $[(\text{bpy})_2\text{Ru}(4,4'-(\text{OH})_2\text{-bpy})]^{2+}$ .

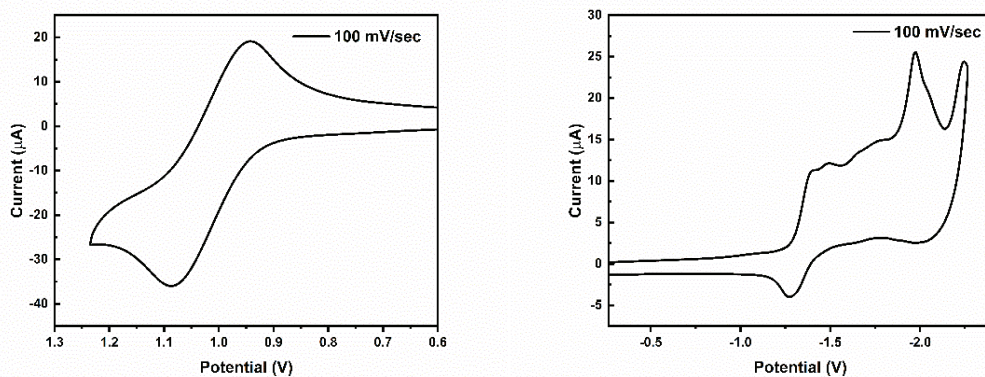


**Figure 2.38** Anodic and cathodic voltammograms of  $[(dpab)_2Ru(4,4'-(OH)_2bpy)]^{2+}$

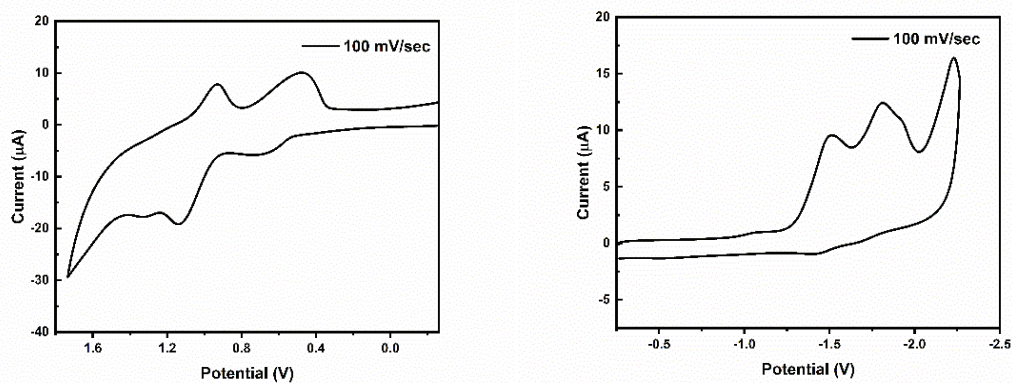


**Figure 2.39** Anodic and cathodic voltammograms of  $[(dpab)_2Ru(4,4'-(OH)_2-bpy)]^{2+}$  in the presence of 1 molar equivalent of TBAOH

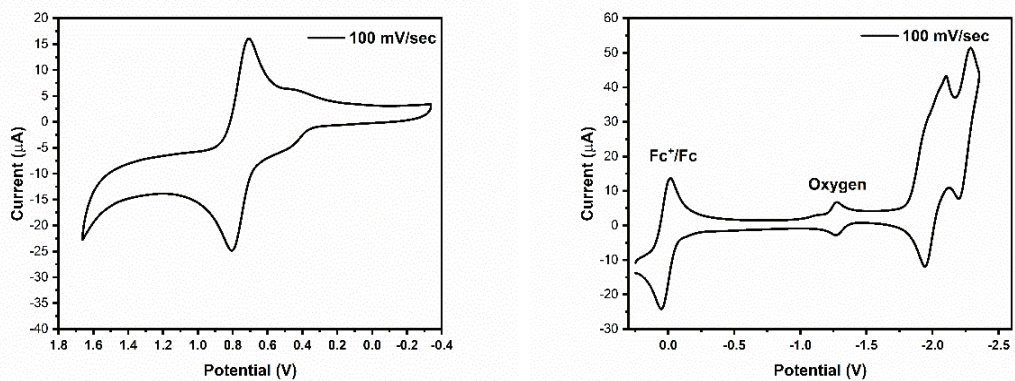


**Figure 2.40** Anodic and cathodic voltammograms of  $[(dtb)_2Ru(4,4'-(OH)_2-bpy)]^{2+}$

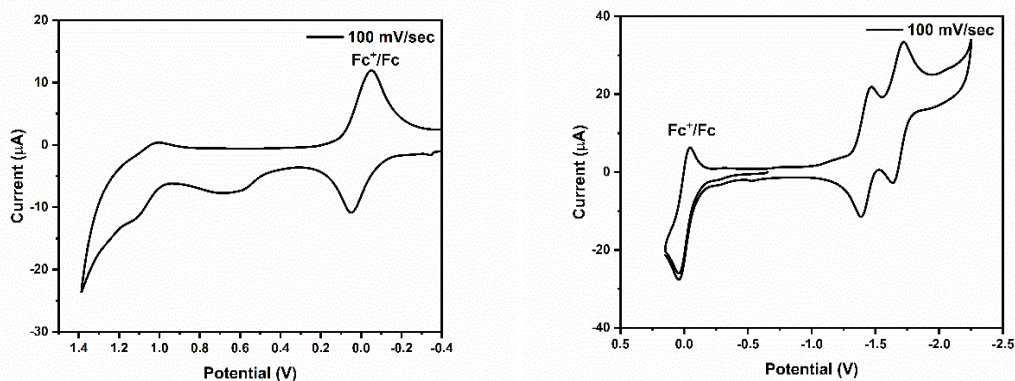


**Figure 2.41** Anodic and cathodic voltammograms of  $[(\text{flpy})_2\text{Ru}(4,4'\text{-(OH)}_2\text{-bpy})]^{2+}$  in the presence of 1 molar equivalent of TBAOH

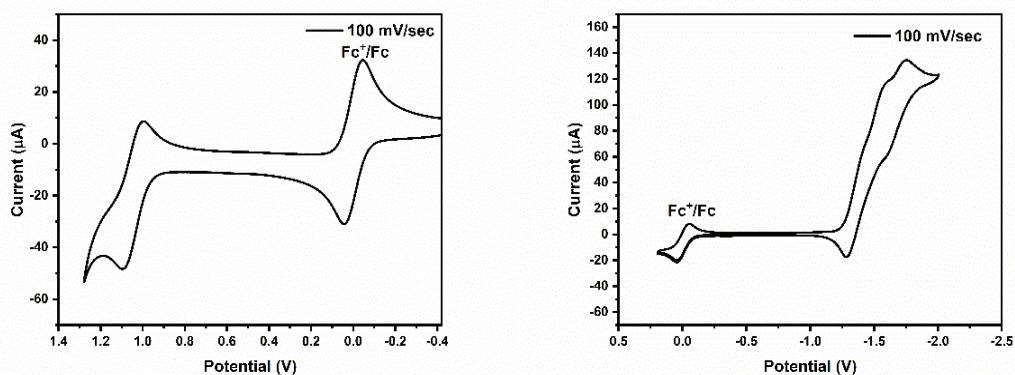


**Figure 2.42** Anodic and cathodic voltammograms of  $[(\text{flpy})_2\text{Ru}(4,4'\text{-(OH)}_2\text{-bpy})]^{2+}$  in the presence of 1 molar equivalent of TBAOH

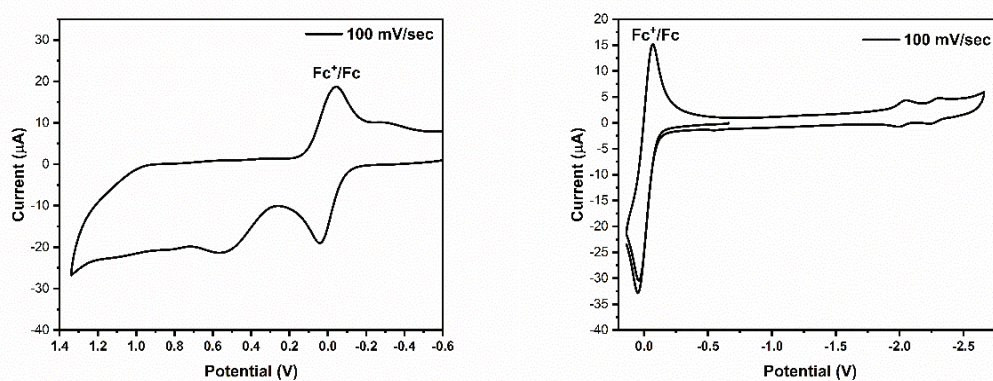


**Figure 2.43** Anodic and cathodic voltammograms of  $[(\text{dtb})_2\text{Ru}(4,4'\text{-(OH)}_2\text{-bpy})]^{2+}$  in the presence of 1 molar equivalent of TBAOH

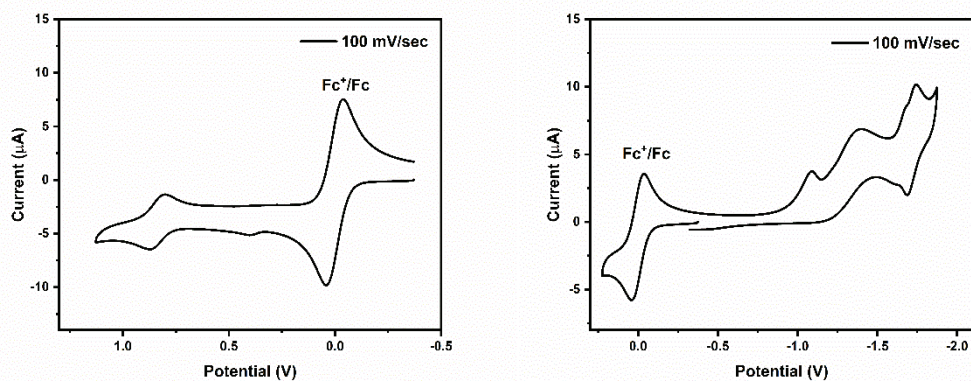


**Figure 2.44** Anodic and cathodic voltammograms of  $[(Cl-phen)_2Ru(4-(OH)-4'-(OMe)-bpy)]^{2+}$

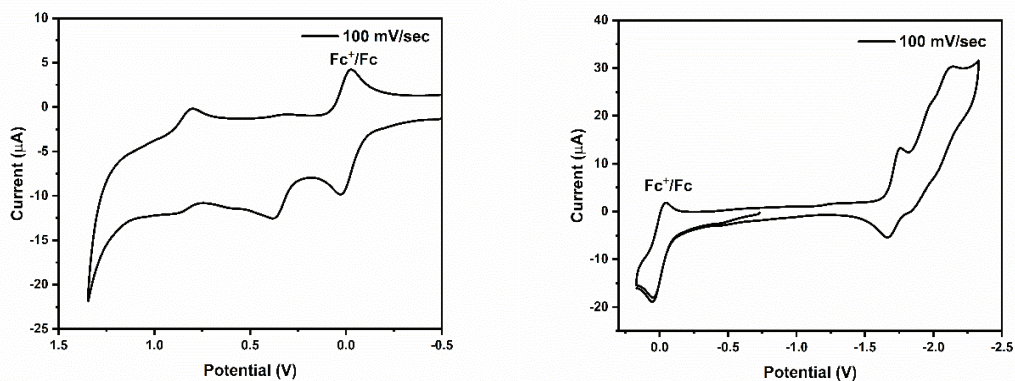


**Figure 2.45** Anodic and cathodic voltammograms of  $[(Cl-phen)_2Ru(OH)-4'-(OMe)-bpy]^{2+}$  in the presence of 1 molar equivalent of TBAOH

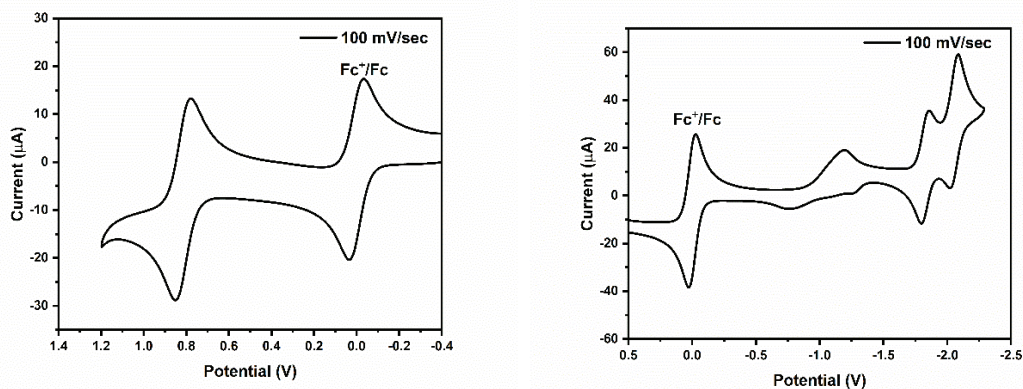


**Figure 2.46** Anodic and cathodic voltammograms of  $[(bpy)_2Ru(4-OHbpy)]^{2+}$

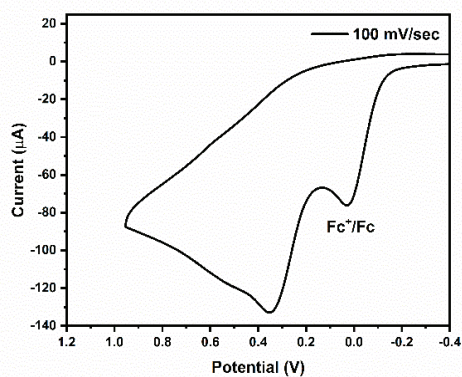


**Figure 2.47** Anodic voltammogram of  $[(bpy)_2Ru(4-OHbpy)]^{2+}$  in the presence of 11 molar equivalents of DABCO

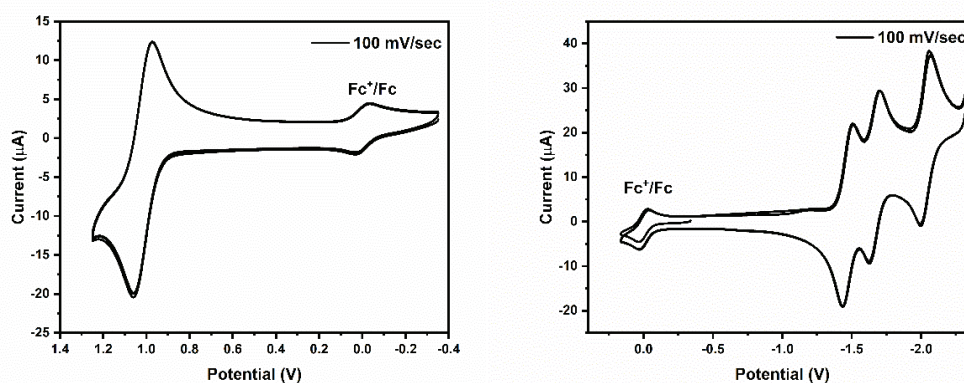


**Figure 2.48** Anodic and cathodic voltammograms of  $[(dpab)_2Ru(bpy)]^{2+}$

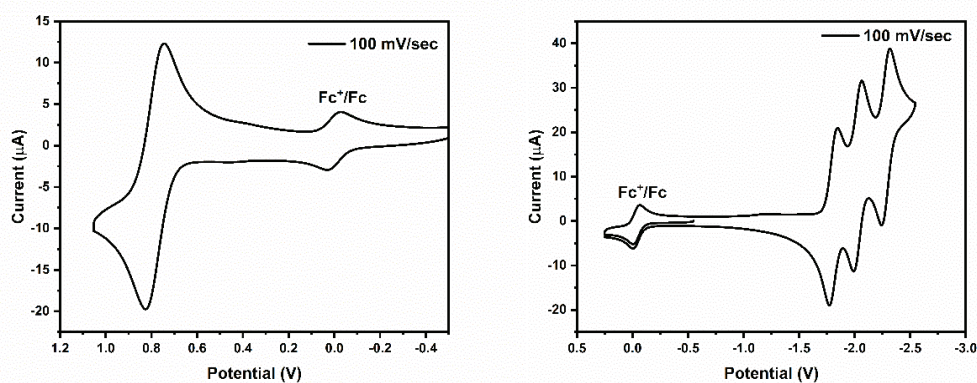


**Figure 2.49** Anodic and cathodic voltammograms of  $[(dtb)_2Ru(bpy)]^{2+}$

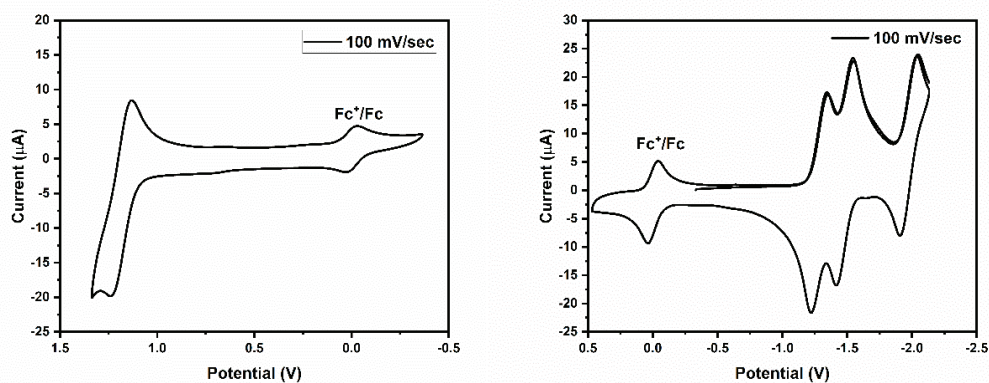


Figure 2.50 Anodic and cathodic voltammograms of  $[(\text{flpy})_2\text{Ru}(\text{bpy})]^{2+}$

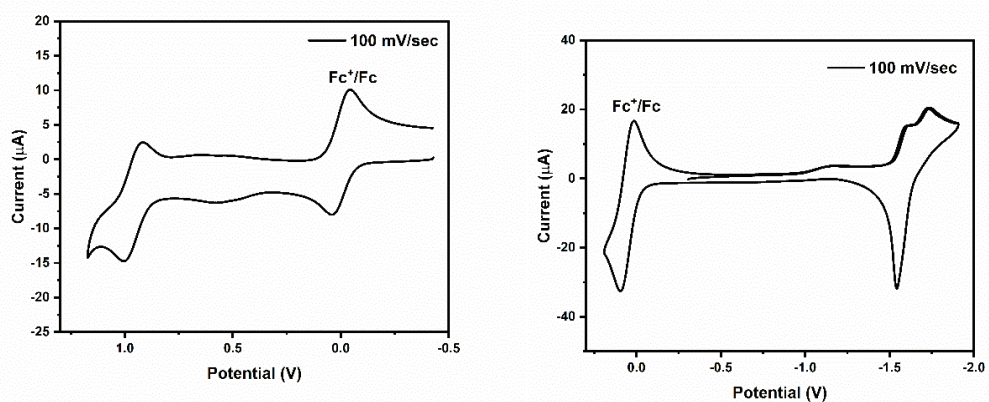


Figure 2.51 Anodic and cathodic voltammograms of  $[(\text{Cl-phen})_2\text{Ru}(\text{bpy})]^{2+}$

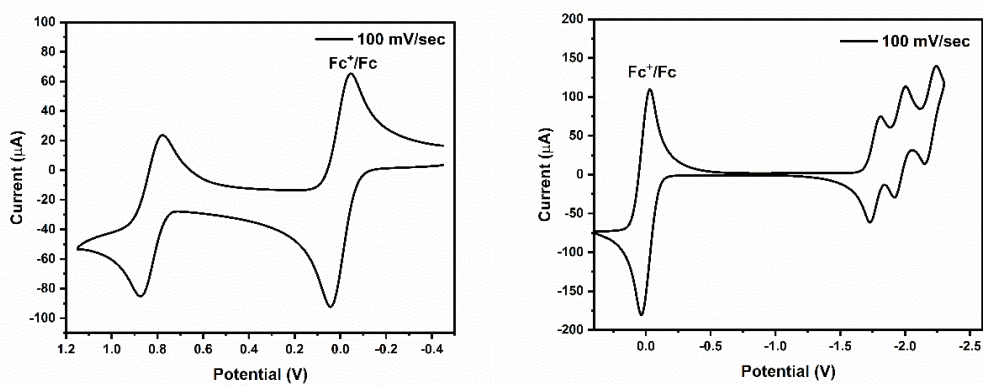


Figure 2.52 Anodic and cathodic voltammograms of  $[(\text{bpy})_2\text{Ru}(4\text{-OMebpy})]^{2+}$

**Table 2.1** Electrochemical potentials from cyclic voltammetric measurements presented here in V vs.  $\text{Fc}^{+/0}$ .  $E_{1/2}$  is used for reversible couples, while  $E_p$  is used for irreversible couples.

	$\text{Ru}^{\text{III/II}} (E_{1/2})$	$\text{Ru}^{\text{III/II}} (E_{p,a})$ deprotonated	1 <sup>st</sup> Reduction ( $E_{1/2}$ )
$[(\text{NN})_2\text{Ru}(4,4'-(\text{OH})_2\text{-bpy})]^{2+}$			
bpy	0.85	0.26	-1.71
dpab	0.93	0.63	-1.51
flpy	1.05	0.66	-1.34
dtb	0.65	0.56	-2.03
$[(\text{Cl-phen})_2\text{Ru}(4-(\text{OH})-4'-(\text{OMe})\text{-bpy})]^{2+}$	0.85	0.382	-1.71
$[(\text{bpy})_2\text{Ru}(4\text{-OHbpy})]^{2+}$	0.82	0.55	-1.83
$[(\text{NN})_2\text{Ru}(\text{bpy})]^{2+}$			
dpab	1.02		-1.47
flpy	1.19		-1.28
dtb	0.79		-1.81
Cl-phen	0.96		-1.57
$[(\text{bpy})_2\text{Ru}(4,4'-(\text{OMe})_2\text{bpy})]^{2+}$	0.87		-1.68
$[(\text{bpy})_2\text{Ru}(4\text{-OMebpy})]^{2+}$	0.83		-1.77

#### 2.4.2 UV-visible Absorption Properties

The absorption spectra for the protonated complexes and deprotonated complexes are shown in figure 2.49. The absorption spectra of control complexes are shown in figure 2.50. The lowest energy absorbance shown in these figures is the metal-to-ligand charge

transfer transition (MLCT) from a  $\text{Ru}^{\text{II}}$   $d\pi$  orbital to a ligand based  $\pi^*$  orbital. This is in line with ruthenium diimine complexes analogous to those reported here.<sup>3</sup>

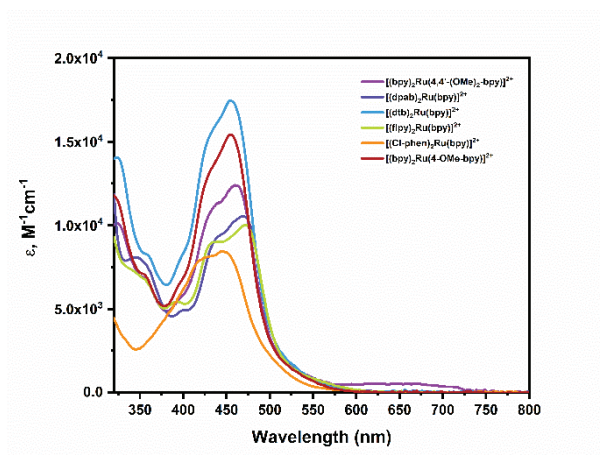


**Figure 2.53** UV-Visible absorption spectra of control complex series in acetonitrile

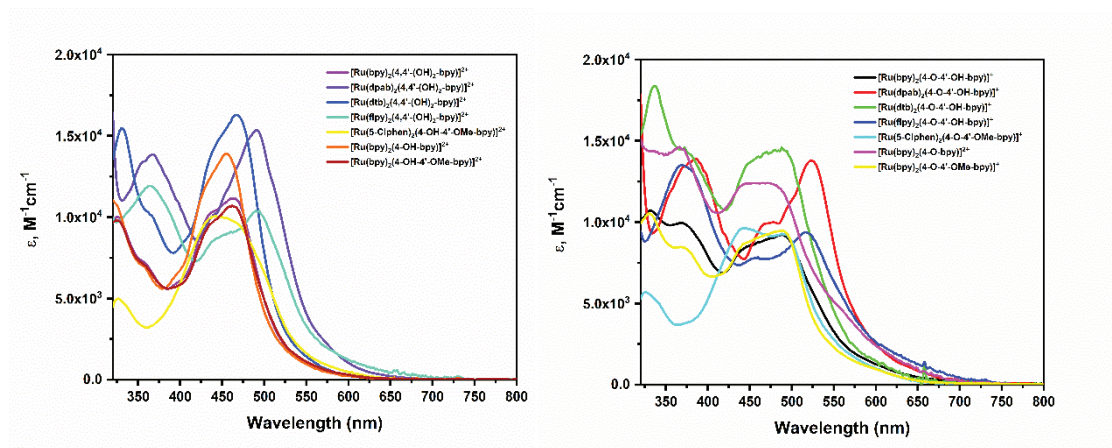


**Figure 2.54** UV-Visible absorption spectra of protonated complexes (left) and deprotonated complexes (right) in acetonitrile solution.

The MLCT band shows two maxima likely arising from the heteroleptic nature of the complexes. The energy of the MLCT correlates to the relative electron donating and withdrawing ability of the functional groups on the ancillary ligands. When electron withdrawing groups are incorporated on the spectator ligands, the MLCT energy shifts to longer wavelength, making the MLCT lower in energy. The opposite effect is expected for

those complexes with ancillary ligands bearing electron donating groups. For the deprotonated complexes, the absorption spectra for the monodeprotonated complexes are shown for complexes bearing two hydroxy groups. Upon deprotonation, all of the absorption spectra red shift to longer wavelength (lower energy). This is an expected transition as increasing the electron density on the hydroxylated bipyridine ligand enables a more facile charge transfer to the spectator ligands. This observation parallels the decrease in the oxidation potential for the Ru<sup>III/II</sup> couple upon deprotonation that is observed for the complexes. The control complexes show the same trend in absorption as seen for the hydroxylated complexes, that is when more electron withdrawing groups are incorporated on the complex, the MLCT shifts to lower energy.

### 2.4.3 Excited-state Properties

The room temperature emission spectra are shown for the complexes in acetonitrile in Figure 2.51. For the hydroxylated complexes, room temperature emission is only observed from the dtb complex. In order to know the energy of the <sup>3</sup>MLCT state, 77 K emission spectra were collected in 1:1 methanol and ethanol solution.

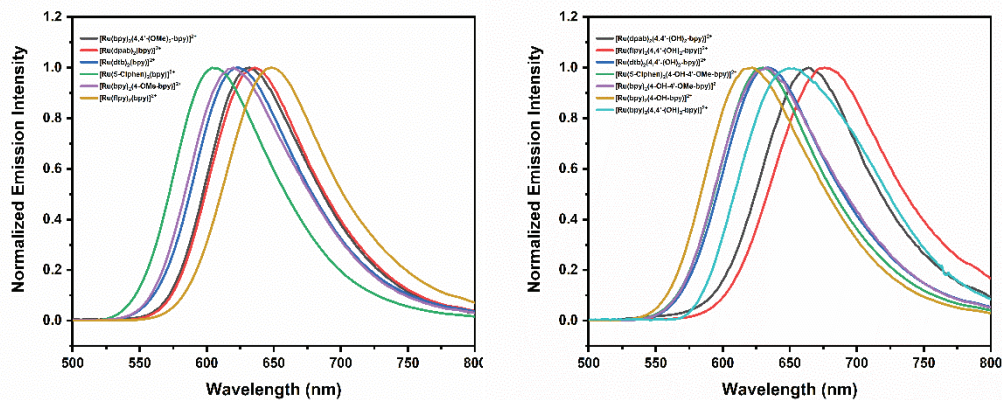


**Figure 2.55** Room temperature emission spectra for control complexes (left) and hydroxylated complexes (right) measured in acetonitrile solution.

The emission spectra collected at 77 K were analyzed using a Franck-Condon fitting routine.<sup>14</sup> The analysis of 77 K emission spectra allow for the extraction of the  $E_{0,0}$  value which corresponds to the transition from the zeroth ground-state vibrational mode to the zeroth excited-state vibrational mode,  $v=0$  to  $v'=0$  and the Huang-Rhys factor,  $S_m$  which describes the extent of nuclear distortion incurred on going from the ground state to the excited state. In addition, the vibrational spacing between acceptor modes,  $\hbar\omega_m$  and the bandwidth at half max,  $\Delta\tilde{\nu}_{1/2}$  can be extracted from the fit. The equation used for fitting data is shown in equation 2.1.

$$I(\tilde{\nu}) = \sum_m^N \left[ \left( \frac{E_0 - m\hbar\omega_m}{E_0} \right) \left( \frac{S_m^m}{m!} \right) \exp \left[ -4 \ln(2) \left( \frac{\tilde{\nu} - E_0 + m\hbar\omega_m}{\tilde{\nu}_{1/2}} \right)^2 \right] \right] \quad (2.1)$$

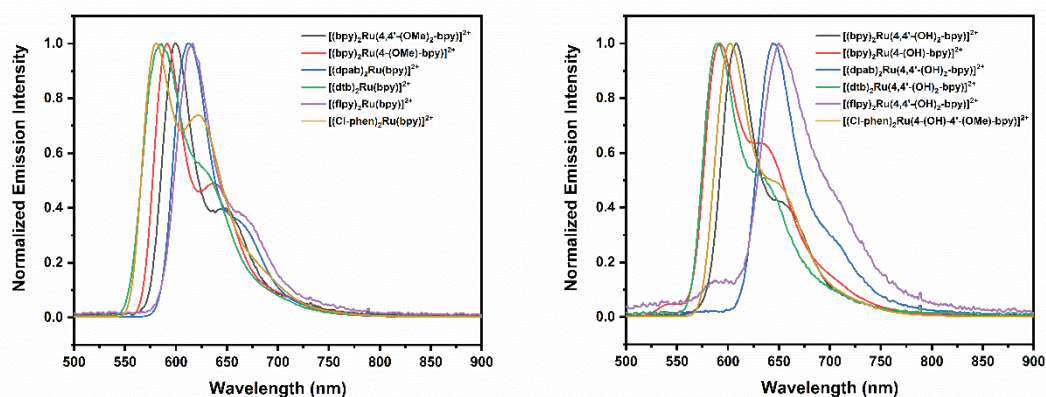


**Figure 2.56** 77 K Emission spectra of control complexes (left) and hydroxylated complexes (right)

Table 2.2 summarizes the extracted parameters from the Franck-Condon analysis of the 77 K emission spectra. The complexes in this series have a relatively high Huang-

Rhys factor relative to  $[\text{Ru}(\text{bpy})_3]^{2+}$ . This is indicative of a high degree of nuclear distortion present in these complexes.

Taking the difference in the  $\text{Ru}^{\text{III/II}}$  potential and the first reduction potential and plotting this against the  $E_{0-0}$  emission energy obtained from the fitting of the 77 K emission spectra reveals a linear correlation between the two quantities. This is in line with the assignment of the excited-state as a metal-to-ligand charge transfer state. The linear plot can be seen in figure 2.57.

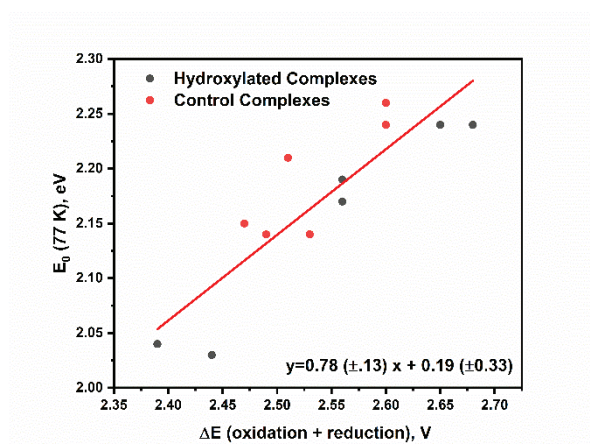


**Figure 2.57** Emission energy vs. energy difference between oxidation and first reduction of complex taken from electrochemical measurements

**Table 2.2** Parameters from fitting of emission spectra at 77 K

	$E_0, \text{ cm}^{-1}$ (eV)	$\hbar\omega, \text{ cm}^{-1}$	$S_m$	$\tilde{\nu}_{1/2}, \text{ cm}^{-1}$
<b>[(NN)<sub>2</sub>Ru(4,4'-(OH)<sub>2</sub>-bpy)]<sup>2+</sup></b>				
bpy	17,524 (2.17)	1084	1.14	957
dpab	16,381 (2.03)	832	1.09	858
flpy	16,427 (2.04)	1034	1.12	1124
dtb	18,076 (2.24)	1166	1.22	1028
<b>[(Cl-phen)<sub>2</sub>Ru(4-(OH)-4'-(OMe)-bpy)]<sup>2+</sup></b>	17,685 (2.19)	1110	1.20	996
<b>[(bpy)<sub>2</sub>Ru(4-OHbpy)]<sup>2+</sup></b>	18,047 (2.24)	1212	1.29	1085
<b>[(NN)<sub>2</sub>Ru(bpy)]<sup>2+</sup></b>				
dpab	17,252 (2.14)	900	1.12	890
flpy	17,303 (2.15)	1048	1.12	973
dtb	18,245 (2.26)	1137	1.20	1125
Cl-phen	18,335 (2.27)	1197	1.35	1040
<b>[(bpy)<sub>2</sub>Ru(4,4'-(OMe)<sub>2</sub>bpy)]<sup>2+</sup></b>	17,799 (2.21)	1159	1.15	942
<b>[(bpy)<sub>2</sub>Ru(4-OMebpy)]<sup>2+</sup></b>	18,050 (2.24)	1185	1.21	945

Emission quantum yields were measured from each of the complexes studied in this work. The values obtained for quantum yields of emission ( $\phi_{em}$ ) along with other photophysical properties for the complexes are shown in Table 2.3. The emission quantum yields were measured with reference to  $[\text{Ru}(\text{bpy})_3]^{2+}$ . This is a well-established method for determining quantum yields of emission.<sup>15</sup> For these measurements, each sample was absorbance-matched at the excitation wavelength to the reference complex,  $[\text{Ru}(\text{bpy})_3]^{2+}$ . The samples were all deaerated with argon gas for 10 minutes prior to measurement. For

calculation of the quantum yield of emission, the ratio of the integrated area under the emission spectrum was taken as a ratio of the quantum yields (figure 2.58). Knowing the quantum yield of the reference complex then allows for the extraction of the quantum yield of the unknown chromophore. Equation 2.2 shows the expression for the relative quantum yield for emission. In this equation,  $\phi_{em}$  is the emission quantum yield,  $\phi_r$  is the emission quantum yield of the reference compound,  $A_r$  is the absorbance at the excitation wavelength of the reference compound,  $A$  is the absorbance at the excitation wavelength for the compound being measured,  $\eta$  and  $\eta_r$  are the refractive indices for the solvent for the reference compound and sample being measured. The emission spectrum of the reference,  $[\text{Ru}(\text{bpy})_3]^{2+}$ , is shown in figure 2.58.

$$\phi_{em} = \phi_r \frac{I}{I_r} \frac{A_r}{A} \frac{\eta^2}{\eta_r^2} \quad (2.2)$$

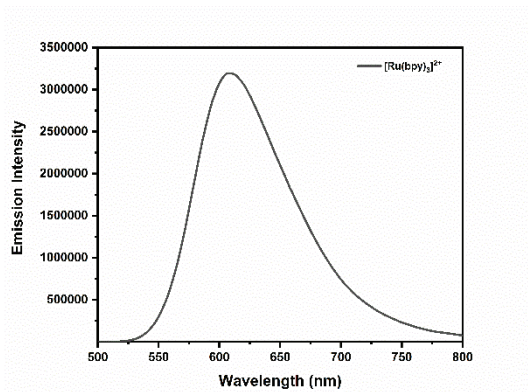


**Figure 2.58** Emission spectrum of quantum yield reference,  $[\text{Ru}(\text{bpy})_3]^{2+}$  in acetonitrile

The emission quantum yield is influenced by the radiative and nonradiative decay rate constants. Knowing the excited-state lifetime,  $\tau_0$ , and  $\phi_{em}$  allows for the calculation of the nonradiative decay rate constants for each complex. Equation 2.3 shows the excited-state lifetime expression as the reciprocal of the sum of the radiative,  $k_r$ , and nonradiative,

$k_{nr}$ , decay rate constants. Equation 2.4 shows the expression emission quantum yield in terms of the radiative and nonradiative decay rate constants.

Excited-state lifetimes were measured by nanosecond transient absorption and time-resolved emission. The decay for the absorbance and emission were fit using a single exponential decay equation, indicating the presence of only one emitting or excited state. The excited-state lifetimes along with other photophysical properties of the complexes explored here are shown in Table 2.3.

$$\tau_0 = \frac{1}{k_r + k_{nr}} \quad (2.3)$$

$$\phi_{em} = \frac{k_r}{k_r + k_{nr}} \quad (2.4)$$

Figure 2.59 shows the relationship between the natural log of the nonradiative decay constant and the emission energy,  $E_{0-0}$ , as extracted from the Franck-Condon analysis of the 77 K emission spectra. Although the points in Figure 2.59 appear scattered, they follow a relatively linear trend, as predicted by the energy gap law.<sup>16,17</sup> As the energy gap

increases between the ground and excited-state potential energy surfaces, the rate of nonradiative decay slows exponentially.

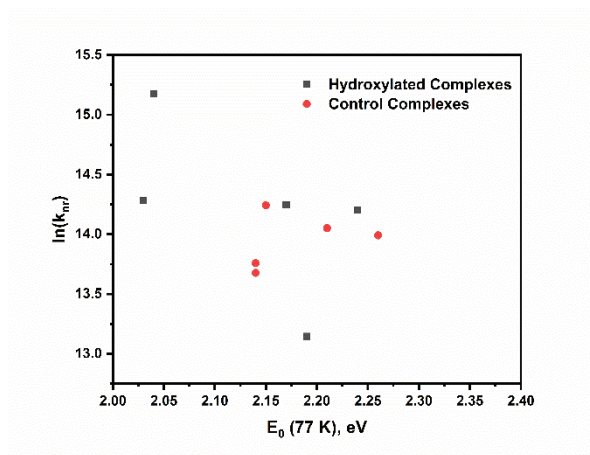


**Figure 2.59** Plot of  $E_{0-0}$  at 77 K versus the natural log of the nonradiative decay rate constant ( $k_{nr}$ )

Transient absorption spectra of all complexes are shown in Figures 2.60 through 2.65. The transient spectra are difference absorption spectra where the absorbance from the ground state appears as a negative absorbance, or bleach, and the absorbance of the charge transfer excited state are shown as positive absorption. For all complexes, positive, long-wavelength absorption is observed. This absorption is due to an instrumental effect from overcorrection of subtracted emission; therefore, it is not assigned to any electronic transition from the excited state. The positive absorbance between 350-400 nm reflects the absorbance of the transiently reduced diimine ligand.

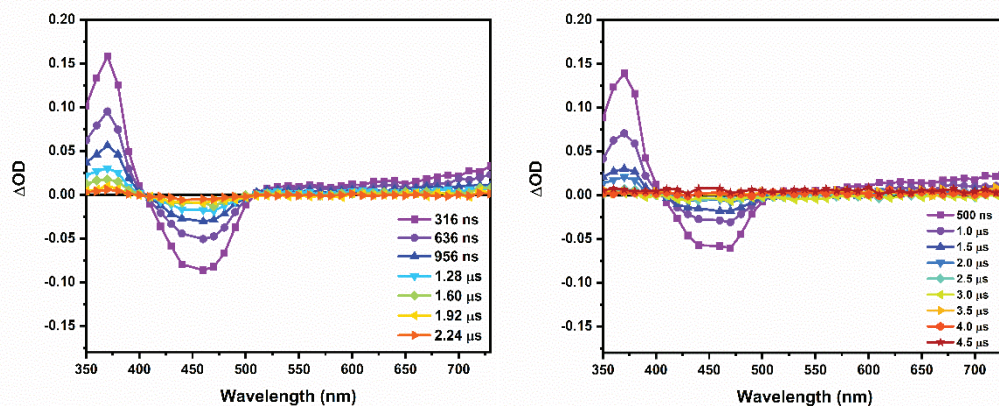


**Figure 2.60** Transient absorption spectra of  $[(bpy)_2Ru(4,4'-(OH)_2-bpy)]^{2+}$  (left) and  $[(bpy)_2Ru(4,4'-(OMe)_2-bpy)]^{2+}$  (right) in acetonitrile

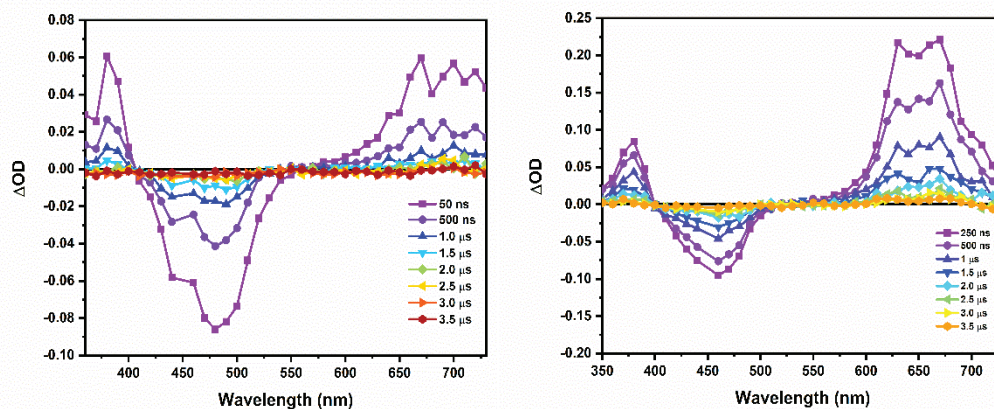


**Figure 2.61** Transient absorption spectra of  $[(dpab)_2Ru(4,4'-(OH)_2-bpy)]^{2+}$  (left) and  $[(dpab)_2Ru(bpy)]^{2+}$  (right) in acetonitrile

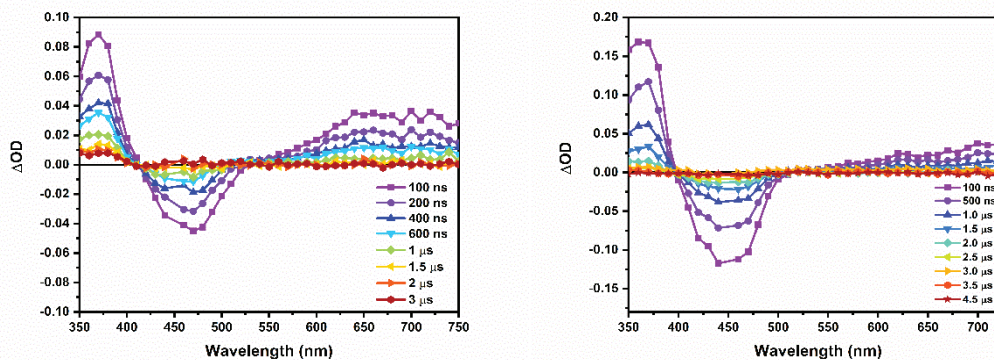


**Figure 2.62** Transient absorption spectra of  $[(dtb)_2Ru(4,4'-(OH)_2-bpy)]^{2+}$  (left) and  $[(dtb)_2Ru(bpy)]^{2+}$  (right) in acetonitrile

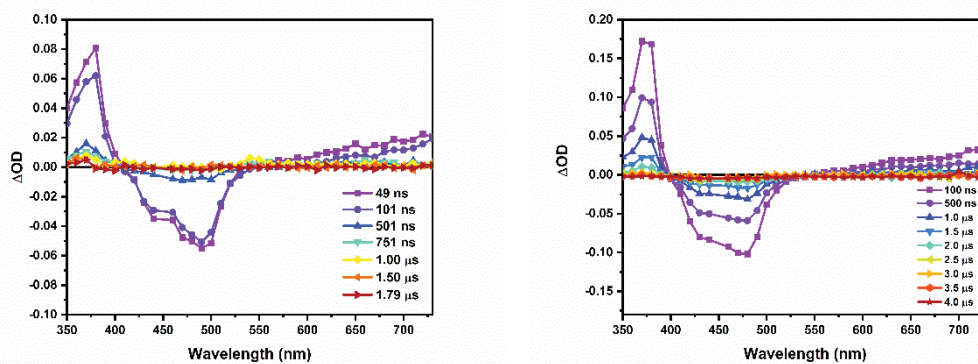


**Figure 2.63** Transient absorption spectra of  $[(\text{flpy})_2\text{Ru}(4,4'\text{-(OH)}_2\text{-bpy})]^{2+}$  (left) and  $[(\text{flpy})_2\text{Ru}(\text{bpy})]^{2+}$  (right) in acetonitrile

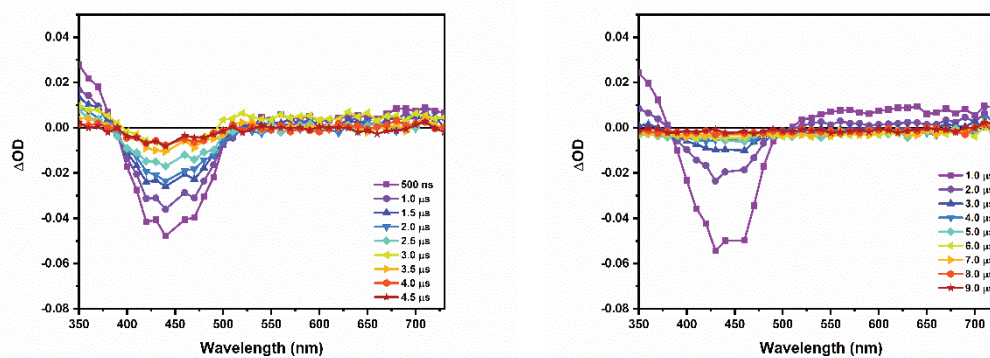


**Figure 2.64** Transient absorption spectra of  $[(\text{Cl-phen})_2\text{Ru}(4\text{-(OH)-4'-(OMe)-bpy})]^{2+}$  (left) and  $[(\text{Cl-phen})_2\text{Ru}(\text{bpy})]^{2+}$  (right) in acetonitrile

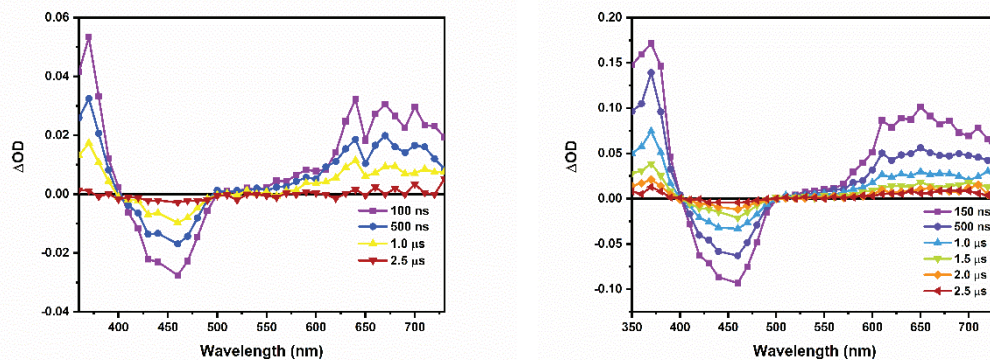


**Figure 2.65** Transient absorption spectra of  $[(\text{bpy})_2\text{Ru}(4\text{-(OH)-bpy})]^{2+}$  (left) and  $[(\text{bpy})_2\text{Ru}(4\text{-(OMe)-bpy})]^{2+}$  (right) in acetonitrile

**Table 2.3** Summary of photophysical properties of complexes

	$\lambda_{\max}$ , nm ( $\epsilon$ , M <sup>-1</sup> cm <sup>-1</sup> )	$E_{em}$ , 298 K, nm (eV)	$E_{em}$ , 77 K, nm (eV)	$\tau_0$ (ns)	$\phi_{em}$	ln ( $k_{nr}$ )
<b>[(NN)<sub>2</sub>Ru(4,4'-(OH)<sub>2</sub>-bpy)]<sup>2+</sup></b>						
bpy	454 (13,900)	651 (1.90)	571 (2.17)	640	0.014	14.2
dpab	490 (15,360)	664 (1.87)	610 (2.03)	615	0.017	14.3
flpy	492 (10,300)	676 (1.83)	609 (2.04)	256	0.005	15.2
dtb	466 (16,200)	634 (1.96)	553 (2.24)	660	0.030	14.2
<b>[(Cl-phen)<sub>2</sub>Ru(4-(OH)-4'-(OMe)-bpy)]<sup>2+</sup></b>	442 (10,070)	630 (1.97)	565 (2.19)	1900	0.028	13.1
<b>[(bpy)<sub>2</sub>Ru(4-OHbpy)]<sup>2+</sup></b>	454 (13,900)	622 (1.99)	554 (2.24)	820		
<b>[(NN)<sub>2</sub>Ru(bpy)]<sup>2+</sup></b>						
dpab	468 (10,500)	636 (1.95)	580 (2.14)	1040	0.095	13.7
flpy	472 (10,000)	648 (1.91)	578 (2.14)	629	0.036	14.2
dtb	454 (17,460)	624 (1.99)	548 (2.26)	790	0.059	14.0
Cl-phen	446 (8500)	605 (2.05)	545 (2.27)	1000	0.056	13.8
<b>[(bpy)<sub>2</sub>Ru(4,4'-(OMe)<sub>2</sub>bpy)]<sup>2+</sup></b>	460 (12,300)	631 (1.96)	562 (2.21)	750	0.051	14.1
<b>[(bpy)<sub>2</sub>Ru(4-OMebpy)]<sup>2+</sup></b>	454 (15,400)	620 (2.00)	554 (2.24)	910		

## 2.5 Conclusions

The synthesis and characterization of hydroxylated complexes and control complexes were explored in this chapter. The complex synthesis was informed by a variety of reported literature procedures. Several variations of hydroxylated ligands were synthesized by our collaborators at Villanova University.

The complexes incorporating electron donating and withdrawing groups show systematic change in redox properties and photophysical properties that align with expectations for MLCT complexes based on the energy gap law. The ease of synthetic modification of these complexes by incorporating electron donating and withdrawing groups on ancillary ligands is extremely convenient for studying the effect of changing free energy for PT and ET reactions on the observed reaction mechanism for interaction with a proton/electron accepting quencher. The implications of the variation in free energy on proton-coupled electron transfer reactivity will be the subject of chapter 4 and 5.

In addition, chapter 3 will explore the excited-state acid-base chemistry of  $[(\text{bpy})_2\text{Ru}(4,4'\text{-(OH)}_2\text{-bpy})]^{2+}$  with a series of pyridine bases. Knowing the photophysical properties of this complex allow for calculation of  $\text{p}K_{\text{a}}$  and  $\text{p}K_{\text{a}}^*$  values for the complex that will be detailed further in chapter 3.

## CHAPTER 2 REFERENCES

- (1) Gagliardi, C. J.; Westlake, B. C.; Kent, C. A.; Paul, J. J.; Papanikolas, J. M.; Meyer, T. J. Integrating Proton Coupled Electron Transfer (PCET) and Excited States. *Coordination Chemistry Reviews* **2010**, *254* (21–22), 2459–2471. <https://doi.org/10.1016/j.ccr.2010.03.001>.
- (2) Klein, S.; Dougherty, W. G.; Kassel, W. S.; Dudley, T. J.; Paul, J. J. Structural, Electronic, and Acid/Base Properties of [Ru(Bpy)<sub>2</sub>(Bpy(OH)<sub>2</sub>)]<sup>2+</sup> (Bpy = 2,2'-Bipyridine, Bpy(OH)<sub>2</sub> = 4,4'-Dihydroxy-2,2'-Bipyridine). *Inorg. Chem.* **2011**, *50* (7), 2754–2763. <https://doi.org/10.1021/ic1017054>.
- (3) Kalyanasundaram, K. Photophysics, Photochemistry and Solar Energy Conversion with Tris (Bipyridyl) Ruthenium (II) and Its Analogues. *Coordination Chemistry Reviews* **1982**, *46*, 159–244.
- (4) Broomhead, J. A.; Young, C. G.; Hood, P. 29. Tris(2,2'-Bipyridine)Ruthenium(II) Dichloride Hexahydrate. In *Inorganic Syntheses*; John Wiley & Sons, Ltd, 1982; pp 127–128. <https://doi.org/10.1002/9780470132524.ch29>.
- (5) Hong, Y.-R.; Gorman, C. B. Synthetic Approaches to an Isostructural Series of Redox-Active, Metal Tris(Bipyridine) Core Dendrimers. *J. Org. Chem.* **2003**, *68* (23), 9019–9025. <https://doi.org/10.1021/jo0351116>.
- (6) Lennox, J. C.; Dempsey, J. L. Influence of Proton Acceptors on the Proton-Coupled Electron Transfer Reaction Kinetics of a Ruthenium–Tyrosine Complex. *J. Phys. Chem. B* **2017**, *121* (46), 10530–10542. <https://doi.org/10.1021/acs.jpcc.7b06443>.
- (7) Nandi, M.; Santra, S.; Akhuli, B.; Ghosh, P. Threading of Various ‘U’ Shaped Bidentate Axles into a Heteroditopic Macrocyclic Wheel via Ni<sup>III</sup>/Cu<sup>II</sup> Templatation. *Dalton Trans.* **2017**, *46* (23), 7421–7433. <https://doi.org/10.1039/C7DT00699C>.
- (8) Sand, H.; Weberskirch, R. Bipyridine-Functionalized Amphiphilic Block Copolymers as Support Materials for the Aerobic Oxidation of Primary Alcohols in Aqueous Media. *RSC Adv.* **2015**, *5* (48), 38235–38242. <https://doi.org/10.1039/C5RA05715A>.
- (9) Freedman, D. A.; Evju, J. K.; Pomije, M. K.; Mann, K. R. Convenient Synthesis of Tris-Heteroleptic Ruthenium(II) Polypyridyl Complexes. *Inorg. Chem.* **2001**, *40* (22), 5711–5715. <https://doi.org/10.1021/ic010603r>.
- (10) Ji, Z.; Huang\*, S. D.; Guadalupe\*, A. R. Synthesis, X-Ray Structures, Spectroscopic and Electrochemical Properties of Ruthenium(II) Complexes Containing 2,2'-Bipyrimidine. *Inorganica Chimica Acta* **2000**, *305* (2), 127–134. [https://doi.org/10.1016/S0020-1693\(00\)00123-7](https://doi.org/10.1016/S0020-1693(00)00123-7).

- (11) Gao, Y.; Sun, Z.-Y.; Huang, Z.-H.; Chen, P.-G.; Chen, Y.-X.; Zhao, Y.-F.; Li, Y.-M. Covalent Bond or Noncovalent Bond: A Supramolecular Strategy for the Construction of Chemically Synthesized Vaccines. *Chemistry – A European Journal* **2014**, *20* (42), 13541–13546. <https://doi.org/10.1002/chem.201404013>.
- (12) Fulmer, G. R.; Miller, A. J. M.; Sherden, N. H.; Gottlieb, H. E.; Nudelman, A.; Stoltz, B. M.; Bercaw, J. E.; Goldberg, K. I. NMR Chemical Shifts of Trace Impurities: Common Laboratory Solvents, Organics, and Gases in Deuterated Solvents Relevant to the Organometallic Chemist. *Organometallics* **2010**, *29* (9), 2176–2179. <https://doi.org/10.1021/om100106e>.
- (13) Juris, A.; Balzani, V.; Barigelletti, F.; Campagna, S.; Belser, P.; von Zelewsky, A. Ru(II) Polypyridine Complexes: Photophysics, Photochemistry, Electrochemistry, and Chemiluminescence. *Coordination Chemistry Reviews* **1988**, *84*, 85–277. [https://doi.org/10.1016/0010-8545\(88\)80032-8](https://doi.org/10.1016/0010-8545(88)80032-8).
- (14) Claude, J. P.; Meyer, T. J. Temperature Dependence of Nonradiative Decay. *J. Phys. Chem.* **1995**, *99* (1), 51–54. <https://doi.org/10.1021/j100001a010>.
- (15) *Handbook of Photochemistry*, 3rd ed.; 2006.
- (16) Brouwer, A. M. Standards for photoluminescence quantum yield measurements in solution (IUPAC Technical Report). *Pure and Applied Chemistry* **2011**, *83* (12), 2213–2228. <https://doi.org/10.1351/PAC-REP-10-09-31>.
- (17) Caspar, J. V.; Kober, E. M.; Sullivan, B. P.; Meyer, T. J. Application of the Energy Gap Law to the Decay of Charge-Transfer Excited States. *J. Am. Chem. Soc.* **1982**, *104* (2), 630–632. <https://doi.org/10.1021/ja00366a051>.

### Chapter 3: Excited-State Proton Transfer Reactions of [(bpy)<sub>2</sub>Ru(4,4'-dhbpy)]<sup>2+</sup> with pyridine bases

#### 3.1 Proton Transfer Reactions of Transition Metal Complexes

It is well known that some protic molecules, upon photoexcitation, experience enhanced acidity or basicity. Early reports from Demas and coworkers on transition metal complexes suggest the presence of an excited-state acid-base equilibrium.<sup>1,2</sup> An equilibrium can be established due to the enhanced excited-state lifetime of the <sup>3</sup>MLCT state of the ruthenium polypyridyl complexes studied. For complexes of the type [Ru(bpy)<sub>2</sub>(CN)<sub>2</sub>] protonation of the cyano groups (one or both) in the ground-state, followed by excitation yields emission solely from the deprotonated complex, implying that [Ru(bpy)<sub>2</sub>(CNH)<sub>2</sub>]<sup>2+\*</sup> and [Ru(bpy)<sub>2</sub>(CN)(CNH)]<sup>+\*</sup> are more acidic in their excited-states.

Additional examples of excited-state acid-base chemistry of transition metal complexes include the well-studied series of heteroleptic ruthenium complexes bearing carboxylated bipyridyl ligands, [(LL)<sub>2</sub>Ru(dcbpy)]<sup>2+</sup> (dcbpy = 4,4'-dicarboxy-2,2'-bipyridine).<sup>3</sup> Here, on photoexcitation, the anion radical is localized on the dcbpy ligand, thus increasing the basicity of the carboxylate groups. Recent work on dcbpy complexes shows that if LL is sufficiently electron withdrawing, the carboxylic acid moiety becomes more acidic in the excited state of these chromophores, indicating that the nature of the CT is an essential factor influencing the pK<sub>a</sub><sup>\*</sup>.

Complexes bearing hydroxylated diimine ligands have been studied since the 1970s when Giordano and coworkers published work on the excited-state proton transfer

reactions of Ru(bpy)<sub>2</sub>(4,7-dihydroxy-1,10-phenanthroline) complexes.<sup>4,5</sup> Here it was observed that on excitation, the chromophores become much more acidic, due to the charge-transfer being localized on the ancillary ligands. Further studies have been conducted on complexes of Ru(LL)<sub>2</sub>(4,4'-dihbpy) (4,4'-dihbpy=4,4'-dihydroxy-2,2'-bipyridine). The structural and electrochemical assessment has been published.<sup>6-8</sup> Early work indicates that the excited state is localized on the spectator ligand when LL=bpy.

More recently, work has been done on ruthenium complexes with hydroxylated bipyridine ligands to interpret the mechanism for excited-state quenching via electron and proton transfer.<sup>6-11</sup> The conclusions drawn so far indicate that for a chromophore-quencher pair, excited-state deactivation occurs primarily through an outer sphere electron transfer process followed by ground-state acid-base chemistry to yield a net H-atom transfer product.<sup>7</sup>

Lymer and coworkers have demonstrated the role of hydrogen bond interactions between ruthenium complexes with bipyrazine ligands and proton donors on excited-state processes, namely proton-coupled electron transfer.<sup>12,13</sup> Their studies support the idea that there is the potential for a pre-associated complex through hydrogen bond interactions that influences the mechanism for electron/proton transfer.

In the past, proton transfer reactions had been viewed in light of a transition-state theory approach, for which the product and reactant surfaces would be strongly interacting. This model has become less popular in recent years because it neglects the quantum nature of the proton itself.<sup>14</sup> In reconciling this failure to incorporate the probability of proton tunneling through the reaction barrier, Bell proposed a correction to this model.<sup>15</sup> Despite

the fact that this model is more detailed, it does not fit for all experimental examples of proton transfer.

Studies by Hynes and colleagues has created a theoretical framework for nonadiabatic proton transfer similar to theoretical models for PCET developed by Hammes-Schiffer and coworkers.<sup>16-18</sup> In this model, like with that of PCET, for weakly hydrogen-bonding donor and acceptor systems, the proton transfer is considered to be nonadiabatic and is dominated by solvent fluctuations that facilitate proton tunneling through the electronic barrier. This is the weakly interacting regime discussed in Chapter 1 for PCET reactions. This theoretical model includes considerations for normal and inverted regions in the free energy dependence of proton transfer

Exploring the free energy dependence of the rate constant for proton transfer can help to elucidate details about the reactant and product states in the proton transfer reaction, which can in turn be incorporated into systems for which both proton and electron transfer are possible.

The work presented herein was conducted to assess the excited-state proton transfer (ESPT) chemistry of  $\text{Ru}(\text{bpy})_2(4,4'\text{-dhbpy})$  with a series of pyridine bases. A primary goal of this work is to understand the factors governing the rate of proton transfer. This work was carried out in an aprotic environment,  $\text{CH}_3\text{CN}$ , providing the ability to track the protons, with little ambiguity. Using a series of pyridine bases as proton acceptors allows for the evaluation of a free energy relationship for the proton transfer reaction.

## 3.2 Experimental

### 3.2.1 Materials

All experiments were conducted in acetonitrile (Fisher) that was dried and distilled from CaH<sub>2</sub>. Pyridine (Sigma Aldrich), 2-picoline (TCI), 2,6-lutidine (TCI), quinoline (TCI) were all treated with decolorizing carbon and dried over 3 Å molecular sieves. 2,6-di-tert-butylpyridine and 7,8-benzoquinoline were used as received from TCI. 2-methoxypyridine (Alfa Aesar), 3-methoxypyridine, 4-methoxy-2methylpyridine (Ambeed), 2,6-dimethoxypyridine (Synthonix), 4-picoline (Sigma Aldrich), 2,4,6-collidine (Alfa Aesar), 4-methoxypyridine (TCI), 3,4-lutidine (Alfa Aesar), 2,4-lutidine (Alfa Aesar), quinoline (Alfa Aesar), 4-phenylpyridine (Alfa Aesar), 4-bromo-2-methoxypyridine (TCI) were all used without further purification. Isoquinoline (TCI) was purified through recrystallization of the isoquinolinium dihydrogen phosphate salt. from methanol. The free base was regenerated dilute sodium hydroxide solution. The Isoquinoline was extracted from the aqueous solution into dichloromethane and dried over anhydrous MgSO<sub>4</sub> (Fisher). Potassium tetrakis(pentafluorophenyl)borate was purchased from Alfa Aesar. 4-aminopyridine (Sigma Aldrich) was recrystallized according to literature procedure before use.<sup>19</sup> Deuterated bases and deuterated acetonitrile were purchased from Cambridge isotope laboratories and used as received. Sodium tetrakis(bis-(trifluoromethyl)phenyl)borate (NaBARF<sub>24</sub>) was synthesized according to literature procedure.<sup>20</sup>

### 3.2.2 Transient Absorption Studies

Visible nanosecond transient absorption studies (nsTA) were done using an Applied Photophysics LKS 60 Laser Flash Photolysis system with laser excitation

provided by a Quantel Brilliant B Q-switched laser with second and third harmonic attachments and an OPO (OPOTEK) for visible light generation. Data were recorded using an Agilent Infinium digitizer. Laser excitation (approximated 12 mJ/pulse) of the sample was generated at 450 nm. For emission lifetimes, a longpass filter at 535 nm was used to filter out excitation light.

### 3.2.3 Absorbance and Emission Spectroscopy

Absorption spectra were collected using an Ocean Optics UV-visible source and HR2000 spectrometer. Emission spectra were collected on a PTI Quantamaster with a photomultiplier detector.

### 3.2.4 $^1\text{H}$ NMR Studies

$^1\text{H}$ NMR studies were conducted on a Varian 400 MHz NMR.

## 3.3 Results and Discussion

### 3.3.1 Thermochemical Analysis of Proton Transfer Reactions

The  $\text{p}K_{\text{a}}$  (17.3) and  $\text{p}K_{\text{a}}^*$  (15.2) of the hydroxylated complex have been previously assigned.<sup>7</sup> Evaluation of the ground-state  $\text{p}K_{\text{a}}$  was done using a monohydroxylated compound,  $[(\text{bpy})_2\text{Ru}(4\text{-(OH)}-4'\text{-(OMe)}\text{-bpy})]^{2+}$ , as the  $\Delta\text{p}K_{\text{a}}$  between the two hydroxy groups of  $[(\text{bpy})_2\text{Ru}(4,4'\text{-(OH)}_2\text{bpy})]^{2+}$  is  $<3$ , thereby not allowing for the clean spectroscopic assessment of the  $\text{p}K_{\text{a}}$  of the first acidic proton in an aprotic solvent for the dihydroxy complex. The complex used for determining the  $\text{p}K_{\text{a}}$  of  $[(\text{bpy})_2\text{Ru}(4,4'\text{-(OH)}_2\text{bpy})]^{2+}$  has very similar spectroscopic features and electronic properties for the ligand 4-(OH)-4'(OMe)-bpy compared to the 4,4'-(OH)<sub>2</sub>bpy ligand. This justifies the use of this complex as a convenient way to assess the  $\text{p}K_{\text{a}}$  of the complex studied in this work.

Measurement of the  $pK_a$  was achieved using a photometric titration technique with 4-aminopyridine ( $pK_a=17.63$ ) as the reference compound.<sup>21</sup> Figure 3.1 shows the resulting UV-Vis absorbance spectra from the titration, and Figure 3.2 shows the fit of the data to assess the equilibrium constant. Using equation 3.1, the  $pK_a$  of the ruthenium complex can be calculated from the measured equilibrium constant and the reported  $pK_a$  of the conjugate acid of 4-aminopyridine. The  $pK_a$  was determined to be  $17.7 \pm 0.0197$ .

$$pK_a(RuOH) = pK_a(BH^+) - \log(K_{eq}) \quad (3.1)$$

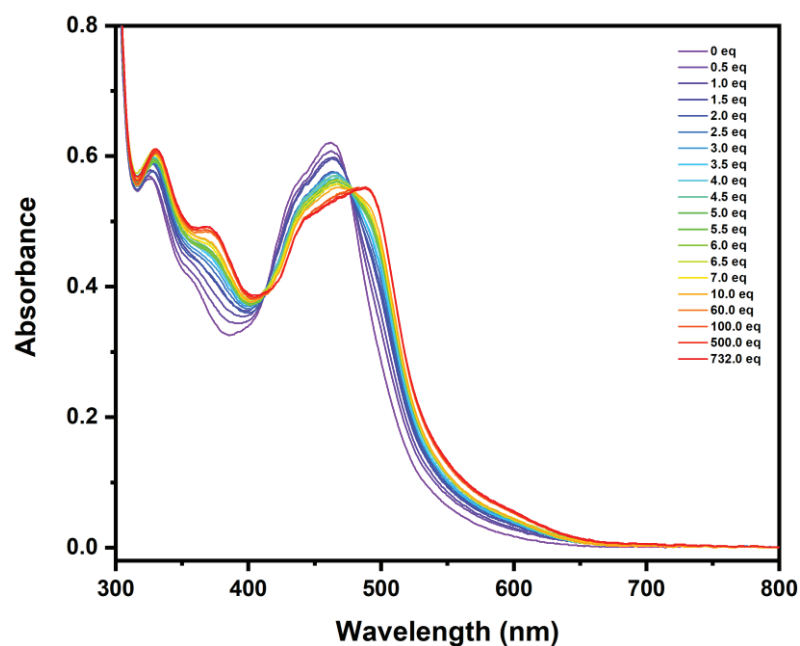


**Figure 3.1** UV-Vis absorbance titration of  $[(bpy)_2Ru(4-(OH)-4'-(OMe)bpy)]^{2+}$  with 4-aminopyridine in acetonitrile

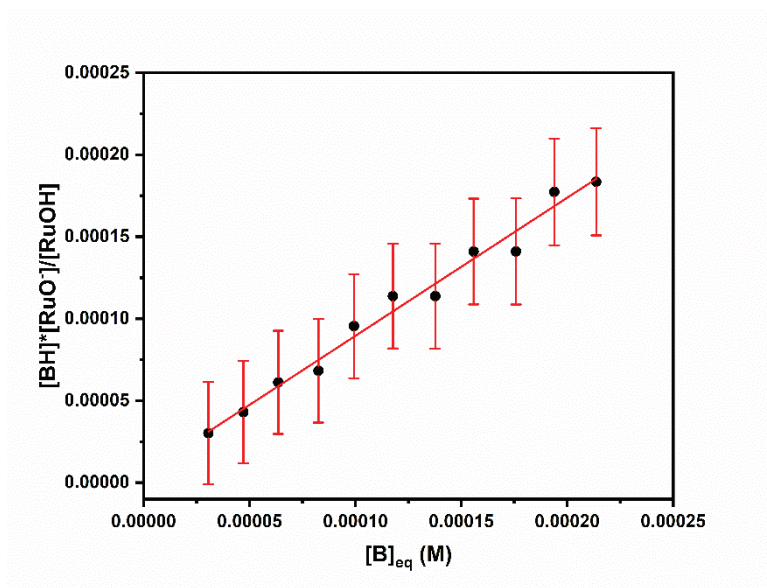


**Figure 3.2** Linear fit of titration data to extract  $K_{eq}$  for acid-base reaction between  $[(bpy)_2Ru(4-(OH)-4'-(OMe)bpy)]^{2+}$  and 4-aminopyridine in acetonitrile

The excited-state acidity was calculated using a Förster equation (equation 3.2) at  $-42^\circ\text{C}$ , as the chromophore exhibits no detectable emission in its monodeprotonated form at room temperature.<sup>15</sup> Figure 3.3 shows a depiction of the Förster thermodynamic cycle in terms of  $\Delta G$ .

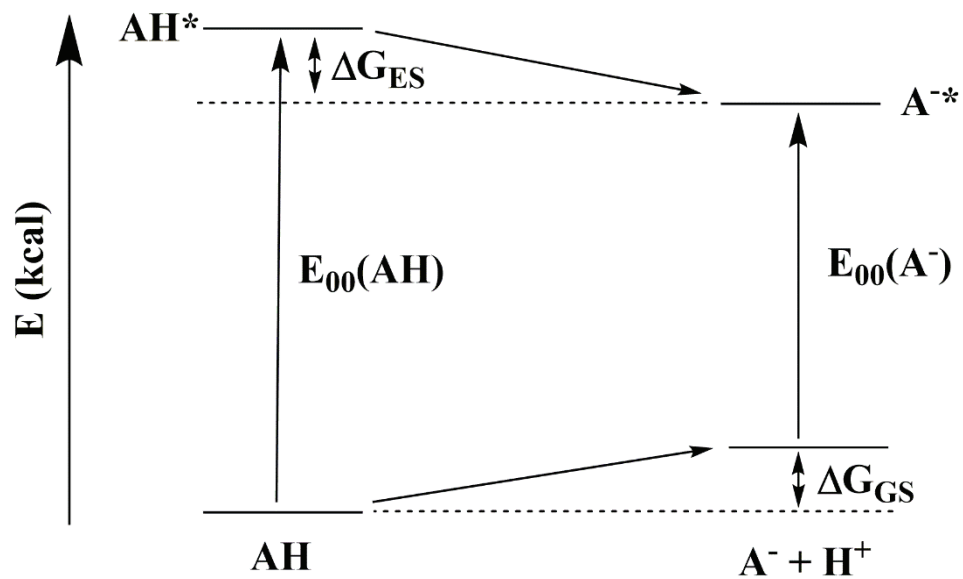


**Figure 3.3** Förster thermodynamic cycle

The cycle used implies that the change in entropy going from the ground to excited state is negligible and therefore, the enthalpy can be approximated by the Gibbs free energy.

$$pK_a^* = pK_a - \frac{E_0(AH) - E_0(A^-)}{2.303RT} \quad (3.2)$$

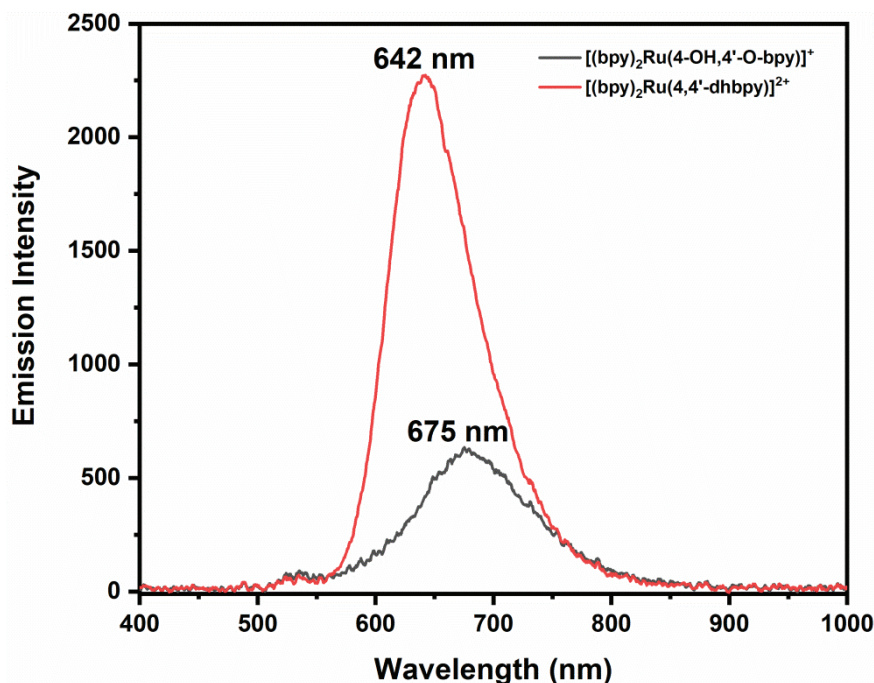


**Figure 3.4** Emission spectra of the protonated and monodeprotonated forms of  $[(bpy)_2Ru(4,4'-(OH)_2bpy)]^{2+}$  at  $-42\text{ }^\circ\text{C}$  in acetonitrile

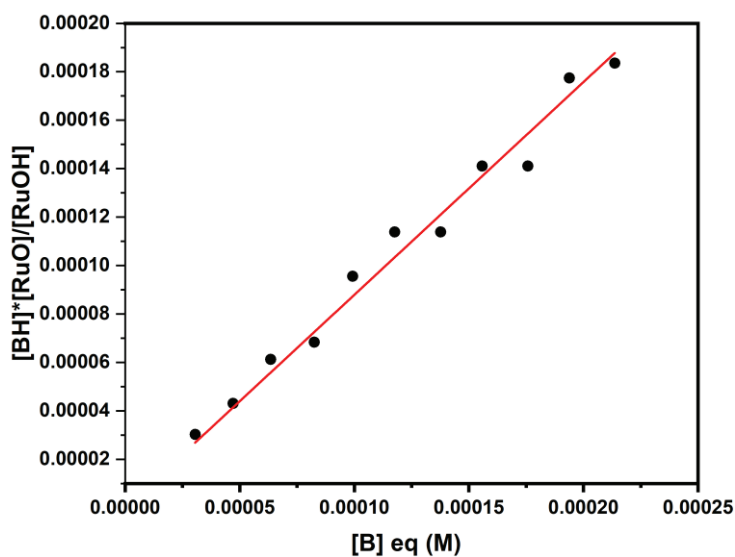
Unfortunately, the Förster cycle does introduce a degree of error in assuming that the enthalpy and free energy are equivalent. Normally, one could measure the excited state  $pK_a$  through emission titration experiments, pending the excited state of the deprotonated complex is emissive. In employing the Förster cycle here, we acknowledge that the free energy terms may be off, albeit in a consistent and systematic way. The emission spectra at  $-42\text{ }^\circ\text{C}$  are shown in figure 3.4. The  $pK_a^*$  was determined to be 15.3.

For analysis of the excited-state proton transfer reactivity of this complex, a series of structurally related bases that will not undergo protonation by the ground state of the chromophore were selected to investigate excited-state proton transfer over a range of  $pK_a$ 's. A series of substituted pyridines with  $pK_a$  values for the conjugate acid ranging from 10.8 to 14.1 in acetonitrile were used for these studies.<sup>21,22</sup> The structures of these bases are depicted in figure 3.6. For some of the bases, the  $pK_a$  of the conjugate acid in acetonitrile

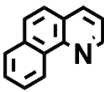
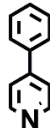
was not reported. In order to determine the  $pK_a$  of these bases, aqueous titration was used and the resulting  $pK_a$  in water was correlated to the  $pK_a$  in acetonitrile based on the reported  $pK_a$ 's of other pyridine compounds in this series. The correlation fit is shown in figure 3.5. Table 3.1 lists the  $pK_a$  values for the conjugate acid of pyridine compounds used in this work. The linear least squares fit provided equation 3.3.

$$pK_a(CH_3CN) = 0.77(\pm 0.05) * pK_a(H_2O) - 4.4(\pm 0.7) \quad (3.3)$$

Before embarking on a study of the excited-state proton transfer reaction between the selected pyridine bases and  $[(bpy)_2Ru(4,4'-(OH)_2-bpy)]^{2+}$ , the equilibrium constant for ground-state proton transfer was evaluated to ensure that no deprotonation would occur prior to photoexcitation. Table 3.1 shows the  $K_{eq}$  values for proton transfer with each base, as calculated by equation 3.2. The calculated equilibrium constant for excited-state proton transfer is also shown in table 3.1, using equation 3.2 and the  $pK_a^*$  value instead of the ground-state  $pK_a$ .



**Figure 3.5** Linear correlation between  $pK_a$ 's in  $H_2O$  and  $CH_3CN$  for the pyridine series

	$pK_a$ (H <sub>2</sub> O)	$pK_a$ (CH <sub>3</sub> CN)		$pK_a$ (H <sub>2</sub> O)	$pK_a$ (CH <sub>3</sub> CN)
	4.25	10.84		5.94	13.69
	4.38	11.83		5.95	13.32
	4.77	12.03		6.19	14.39
	4.97	11.96		6.59	13.81
	5.23	12.53		6.62	14.61
	5.37	12.69		6.67	14.13
	5.45	13.11		7.27	15.17
				7.33	14.98

**Figure 3.6** Structure of pyridine bases used along with  $pK_a$ 's of the conjugate acid in both acetonitrile and water. Values in blue were determined by correlation with aqueous  $pK_a$  data.

In addition to investigation ground-state proton transfer equilibria, the equilibrium constants for H-bonding between selected bases and the ruthenium complex were assessed. The ground-state equilibrium constant for hydrogen bonding was assessed by <sup>1</sup>HNMR titration with pyridine-d<sub>5</sub>, 4-picoline-d<sub>7</sub>, and 2-picoline-d<sub>7</sub>. A shift in the aromatic protons associated with the hydroxylated bipyridine rings was observed and used to quantify the ground-state equilibrium constant for this process.

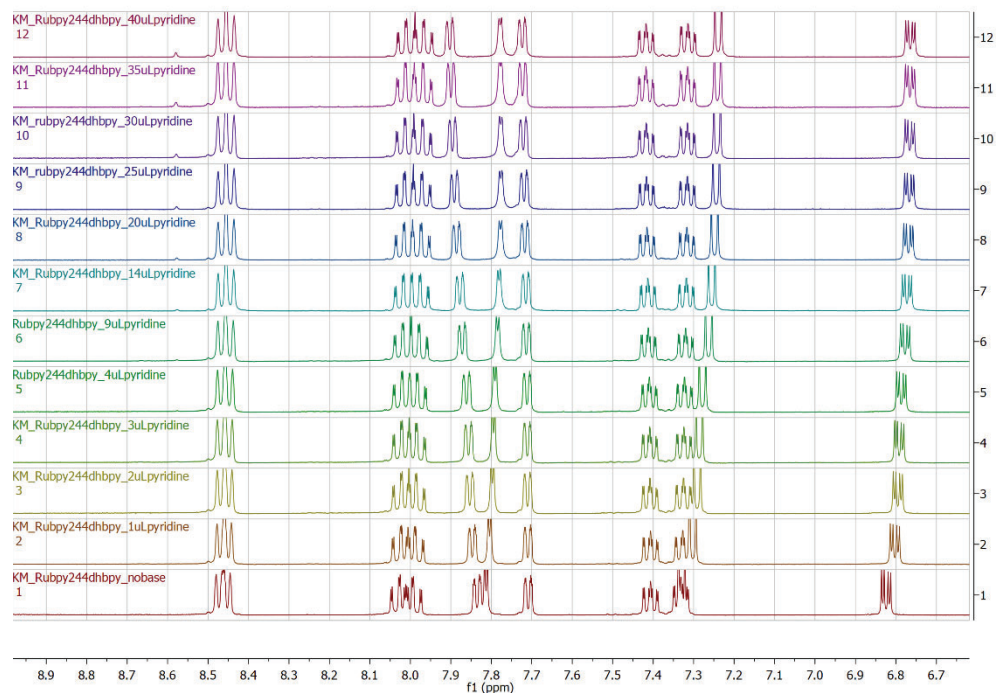


**Figure 3.7**  $^1\text{H}$ NMR spectra of  $[(\text{bpy})_2\text{Ru}(4,4'\text{-(OH)}_2\text{bpy})]^{2+}$  in the presence of increasing concentrations of pyridine- $\text{d}_5$  in  $\text{CD}_3\text{CN}$ .

The  $^1\text{H}$ NMR spectra from the titrations are shown in figures 3.7-3.12. A selected aromatic proton associated with hydroxylated bipyridine ligand was used to monitor the extent of hydrogen bonding. The chemical shift was plotted versus the ratio of the concentration of base added to the initial concentration of ruthenium. The data was then fit according to equations 3.4a and 3.4b.<sup>23</sup> In these equations,  $\delta_{\text{obs}}$  is the observed chemical shift in the presence of base,  $\delta_{\text{RuOH}}$  is the chemical shift of free ruthenium complex,  $\Delta\delta$  is the maximum change in chemical shift between the free chromophore and the hydrogen bonded chromophore,  $[B]_0$  is the concentration of base added to solution,  $[\text{RuOH}]_0$  is the initial concentration of ruthenium complex, lastly,  $K_{\text{eq}}$  is the equilibrium constant for hydrogen bond formation. From the fit of the data obtained, the equilibrium constants for hydrogen bonding were assessed for each base and are shown in Table 3.1. It is important to note

that the concentration of base used was below the concentration needed to appreciably deprotonate the complex according to the calculated  $K_{eq}$  values for proton transfer.

$$\delta_{obs} = \delta_{RuOH} - \frac{\Delta\delta * \left( b - \sqrt{b^2 - 4 * \frac{[B]_0}{[RuOH]_0}} \right)}{2} \quad (3.4a)$$

$$b = 1 + \frac{[B]_0}{[RuOH]_0} + \frac{1}{K_{eq}[RuOH]_0} \quad (3.4b)$$

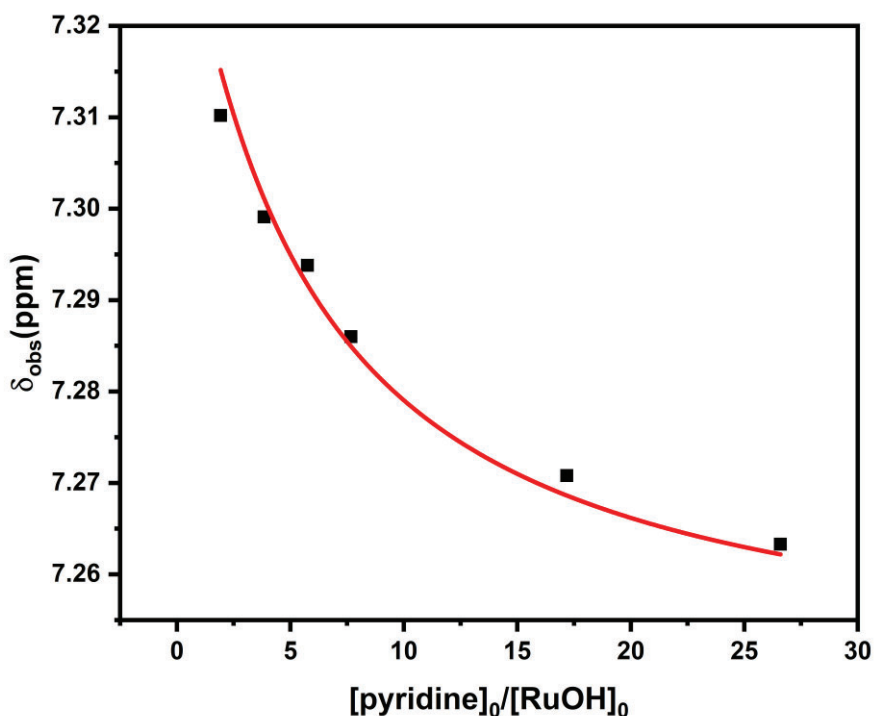


**Figure 3.8** The plot of observed chemical shift vs. the ratio of concentrations of pyridine added and the initial concentration of  $[Ru(bpy)_2(4,4'-(OH)_2bpy)]^{2+}$  fit with a parabolic equation to extract  $K_{eq}$  for H-bonding.

Although equilibrium constants for ground state hydrogen bond formation could be obtained for 2-picoline, 4-picoline, and pyridine, the remaining bases used for ESPT studies could not be assessed for their ground state equilibrium constant as they were not commercially available in their perdeuterated forms. Several attempts were made to

synthesize perdeuterated bases by pressure reaction, microwave reaction, and through the N-oxide of the pyridine base, but ultimately resulted in only partial deuteration of the bases, which is not suitable for use in  $^1\text{H}$ NMR experiments.  $^1\text{H}$ NMR was used as the primary tool for investigating hydrogen bond equilibria due to the fact that upon addition of base, no spectroscopic changes were detectable by UV-Vis spectroscopy. A correlation can be made for the H-bonding equilibrium constant with the  $\text{p}K_{\text{a}}$  of the base, and the expected equilibrium constant for H-bonding with other bases, solely based on the  $\text{p}K_{\text{a}}$ , and excluding other steric factors, can be made.

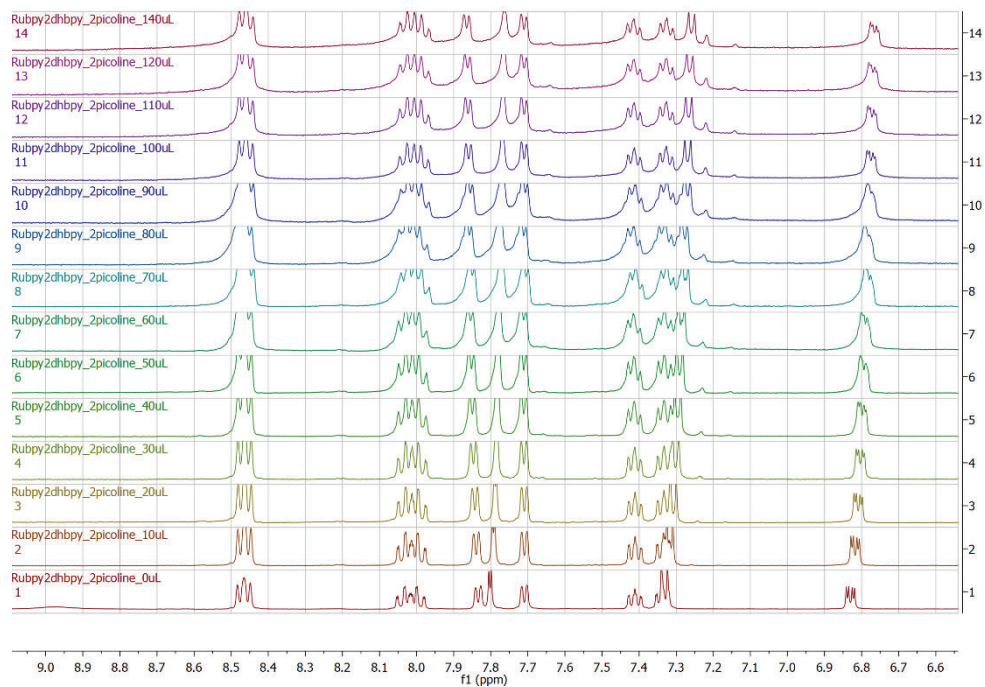


**Figure 3.9** <sup>1</sup>H NMR spectra of  $[(bpy)_2Ru(4,4'-(OH)_2bpy)]^{2+}$  in the presence of increasing concentrations of 2-picoline-d<sub>7</sub>

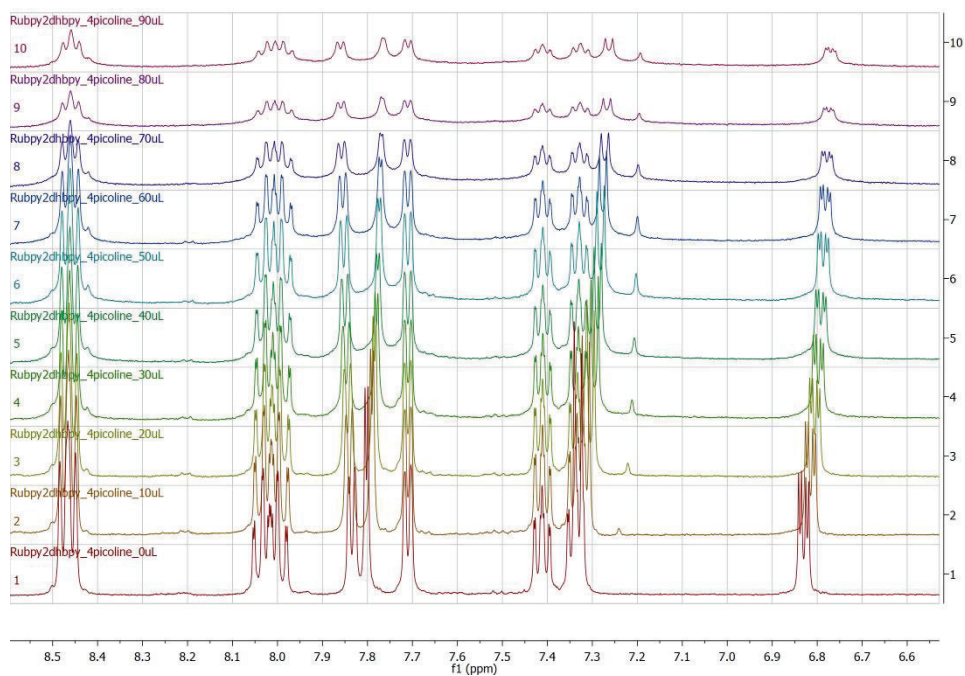


**Figure 3.10** <sup>1</sup>H NMR spectra of  $[(bpy)_2Ru(4,4'-(OH)_2bpy)]^{2+}$  in the presence of increasing concentrations of 4-picoline-d<sub>7</sub>

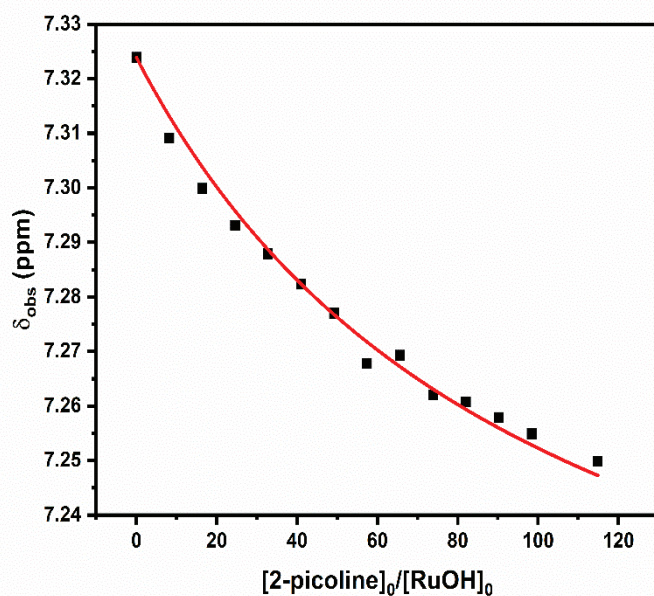


**Figure 3.11** The plot of observed chemical shift vs. the ratio of concentrations of 2-picoline added and the initial concentration of  $[\text{Ru}(\text{bpy})_2(4,4'\text{-(OH)}_2\text{bpy})]^{2+}$  fit with a parabolic equation to extract  $K_{\text{eq}}$  for H-bonding.

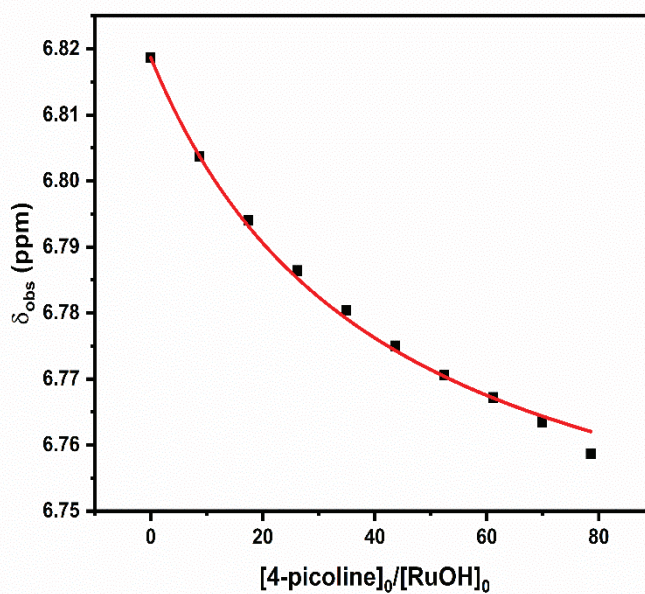


**Figure 3.12** The plot of observed chemical shift vs. the ratio of concentrations of 4-picoline added and the initial concentration of  $[\text{Ru}(\text{bpy})_2(4,4'\text{-(OH)}_2\text{bpy})]^{2+}$  fit with a parabolic equation to extract  $K_{\text{eq}}$  for H-bonding.

From the  $pK_a$  values, the free energy for excited-state and ground-state proton transfer can be calculated. The trend follows that as the  $pK_a$  of the conjugate acid of the pyridine base increases, the free energy for proton transfer will become smaller, indicating the ESPT reaction is more exergonic (but is still endergonic). Knowing the free energy for proton transfer will allow for the analysis of the rate dependence on free energy, which will be discussed in further detail in section 3.3.3.

**Table 3.1**  $pK_a$ 's of pyridine bases, equilibrium constants, and free energies

	$pK_a$	$K_{PT}$	Err.	$K_{PT}^*$	Err.	$K_{HB}$	$\Delta G(PT)$ (kcal/mol)	$\Delta G(PT^*)$ (kcal/mol)
<i>benzo[h]quinoline</i>	10.84	1.35E-07	$\pm 6E-9$	3.5E-05	$\pm 2E-06$		$9.4 \pm 0.1$	$6.1 \pm 0.1$
<i>4-bromo-2-methylpyridine</i>	11.83	1.32E-06	$\pm 6E-8$	3.4E-04	$\pm 2E-05$		$8.06 \pm 0.09$	$4.8 \pm 0.1$
<i>3-methoxypyridine</i>	12.03	2.09E-06	$\pm 9E-8$	5.4E-04	$\pm 2E-05$		$7.78 \pm 0.09$	$4.5 \pm 0.1$
<i>quinoline</i>	11.96	1.78E-06	$\pm 8E-8$	4.57E-04	$\pm 2E-06$		$7.88 \pm 0.09$	$4.58 \pm 0.1$
<i>pyridine</i>	12.53	6.6E-06	$\pm 3E-7$	1.70E-03	$\pm 8E-05$	30	$7.1 \pm 0.1$	$3.79 \pm 0.06$
<i>Isoquinoline</i>	12.69	9.6E-06	$\pm 4E-7$	2.5E-03	$\pm 1E-04$		$6.9 \pm 0.1$	$3.6 \pm 0.1$
<i>4-phenylpyridine</i>	13.11	2.5E-05	$\pm 1E-6$	6.5E-03	$\pm 3E-04$		$6.3 \pm 0.1$	$3.0 \pm 0.1$
<i>4-picoline</i>	13.69	9.6E-05	$\pm 4E-6$	2.5E-02	$\pm 1E-03$	68	$5.5 \pm 0.1$	$2.2 \pm 0.1$
<i>2-picoline</i>	13.32	4.1E-05	$\pm 2E-6$	1.05E-02	$\pm 5E-04$	27	$6.0 \pm 0.1$	$2.71 \pm 0.05$
<i>3,4-lutidine</i>	14.39	4.79E-04	$\pm 2E-6$	1.23E-01	$\pm 6E-03$		$4.55 \pm 0.06$	$1.25 \pm 0.04$
<i>4-methoxypyridine</i>	13.81	1.26E-04	$\pm 6E-6$	3.2E-02	$\pm 2E-03$		$5.34 \pm 0.07$	$2.0 \pm 0.1$
<i>2,4-lutidine</i>	14.61	7.9E-04	$\pm 4E-5$	2.0E-01	$\pm 1E-02$		$4.2 \pm 0.1$	$0.95 \pm 0.03$
<i>2,6-lutidine</i>	14.13	2.6E-04	$\pm 1E-5$	6.8E-02	$\pm 3E-03$		$4.9 \pm 0.1$	$1.6 \pm 0.1$
<i>4-methoxy-2-methylpyridine</i>	15.17	2.9E-03	$\pm 1E-4$	7.4E-01	$\pm 3E-02$		$3.5 \pm 0.1$	$0.18 \pm 0.03$
<i>2,4,6-collidine</i>	14.98	1.86E-03	$\pm 8E-5$	4.8E-01	$\pm 2E-02$		$3.74 \pm 0.06$	$0.44 \pm 0.03$

### 3.3.2 Proton-transfer Quenching Studies

Stern-Volmer quenching studies by both steady-state emission and time-resolved emission were undertaken to evaluate the rate of excited-state proton transfer for the complex  $[\text{Ru}(\text{bpy})_2(4,4'-(\text{OH})_2\text{bpy})]^{2+}$  and a series of substituted pyridines. The resulting emission spectra and luminescence lifetime decays are shown in figures 3.13-3.26. It should be noted that the luminescence lifetime decays were fit with a single exponential function, thus indicating the presence of only one emitting species.

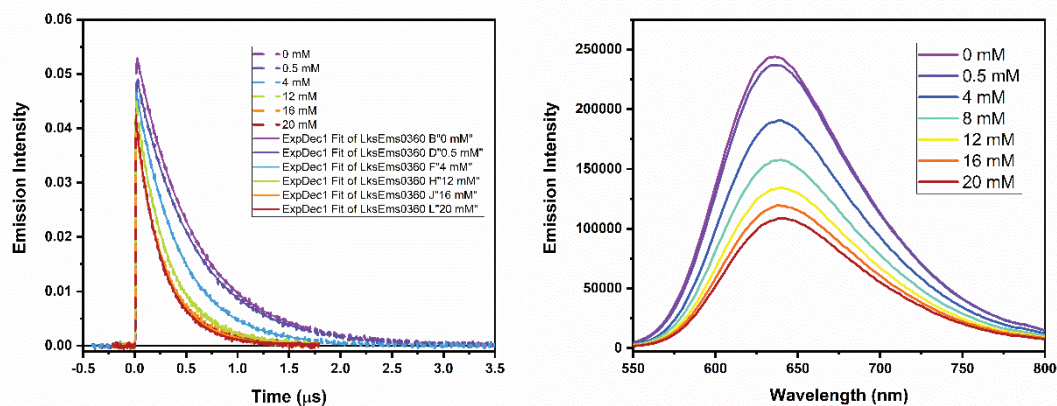


**Figure 3.13** Luminescence lifetimes (left) and steady-state emission spectra (right) of  $[\text{Ru}(\text{bpy})_2(4,4'-(\text{OH})_2\text{bpy})]^{2+}$  in presence of varying concentrations of 3-methoxypyridine

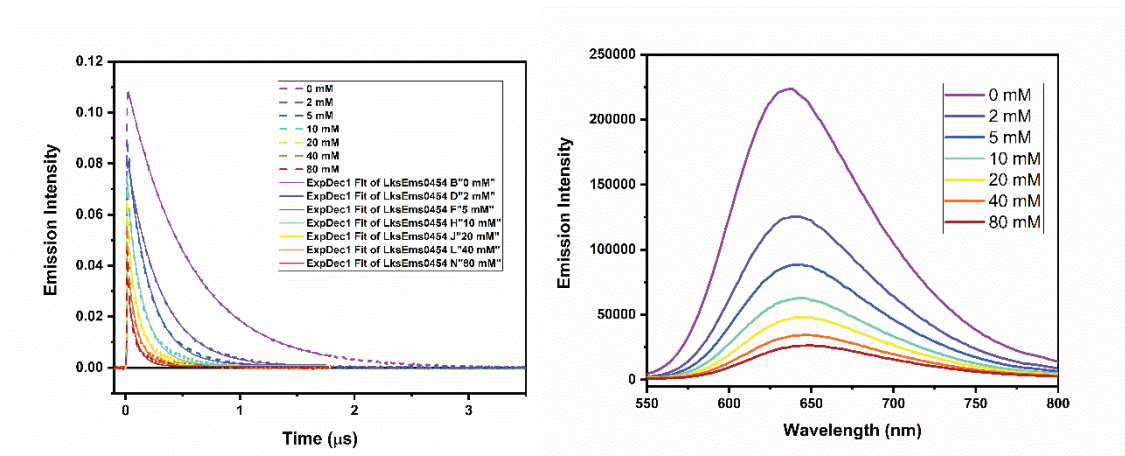


**Figure 3.14** Luminescence lifetimes (left) and steady-state emission spectra (right) of  $[\text{Ru}(\text{bpy})_2(4,4'-(\text{OH})_2\text{bpy})]^{2+}$  in presence of varying concentrations of 2-picoline

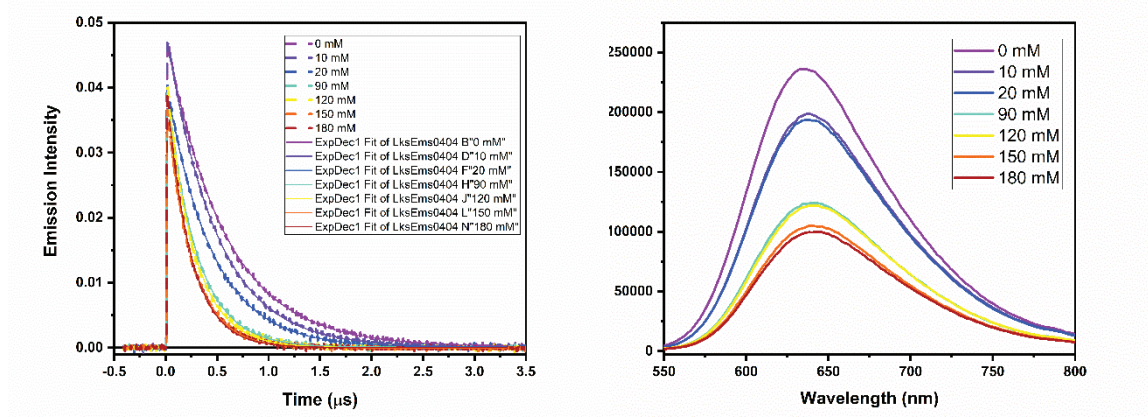


**Figure 3.15** Luminescence lifetimes (left) and steady-state emission spectra (right) of  $[\text{Ru}(\text{bpy})_2(4,4'-(\text{OH})_2\text{bpy})]^{2+}$  in presence of varying concentrations of 4-bromo-2-picoline

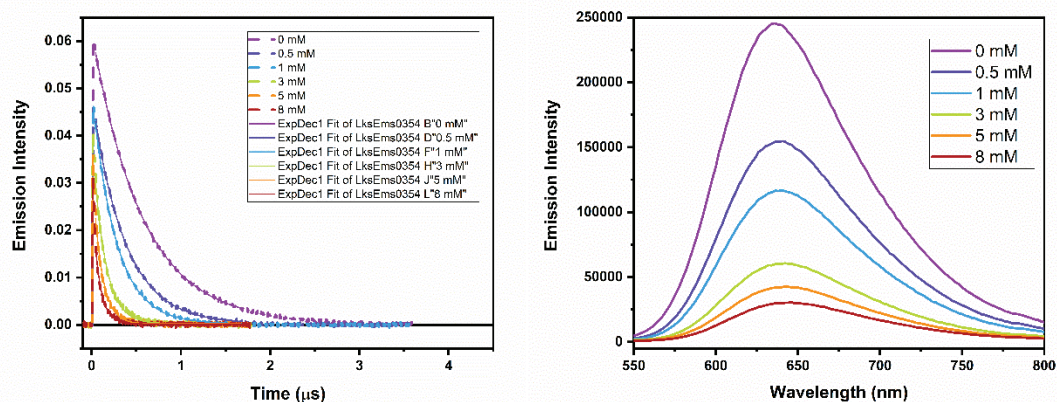


**Figure 3.16** Luminescence lifetimes (left) and steady-state emission spectra (right) of  $[\text{Ru}(\text{bpy})_2(4,4'-(\text{OH})_2\text{bpy})]^{2+}$  in presence of varying concentrations of 4-methoxypyridine

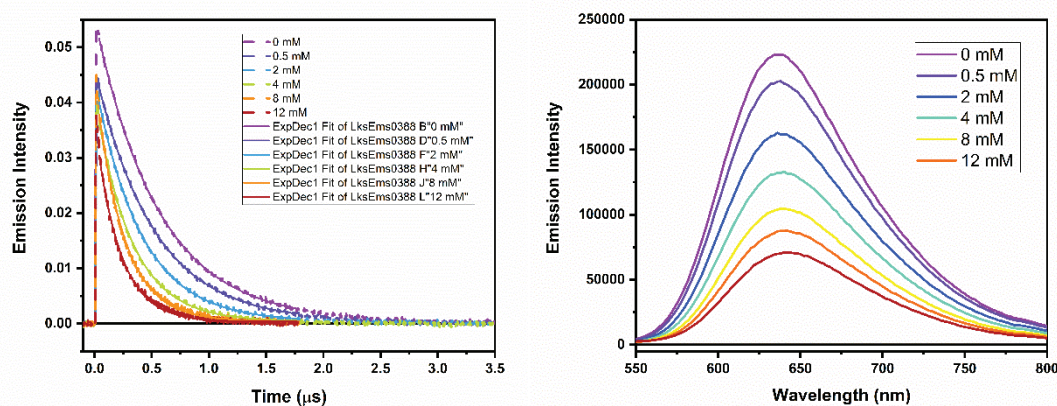


**Figure 3.17** Luminescence lifetimes (left) and steady-state emission spectra (right) of  $[\text{Ru}(\text{bpy})_2(4,4'-(\text{OH})_2\text{bpy})]^{2+}$  in presence of varying concentrations of 4-phenylpyridine

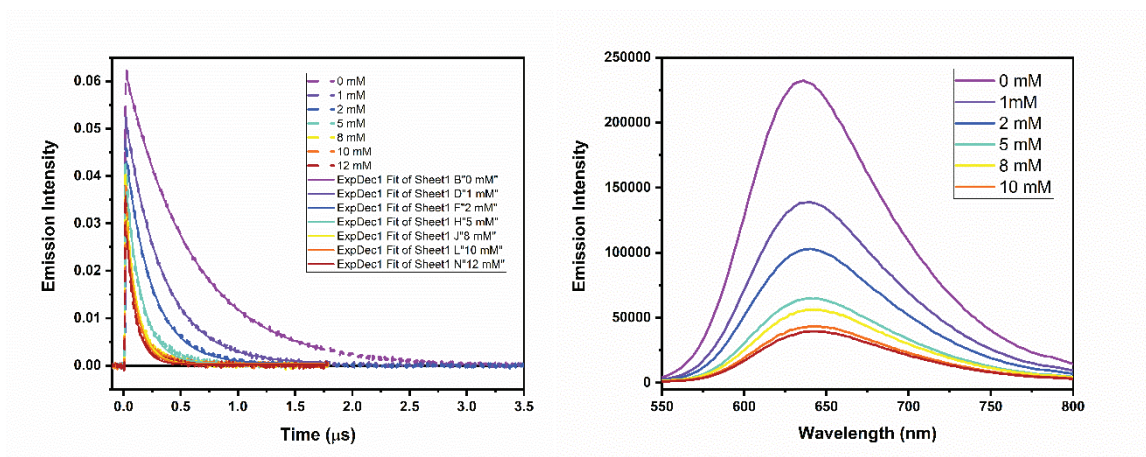


**Figure 3.18** Luminescence lifetimes (left) and steady-state emission spectra (right) of  $[\text{Ru}(\text{bpy})_2(4,4'-(\text{OH})_2\text{bpy})]^{2+}$  in presence of varying concentrations of 4-picoline

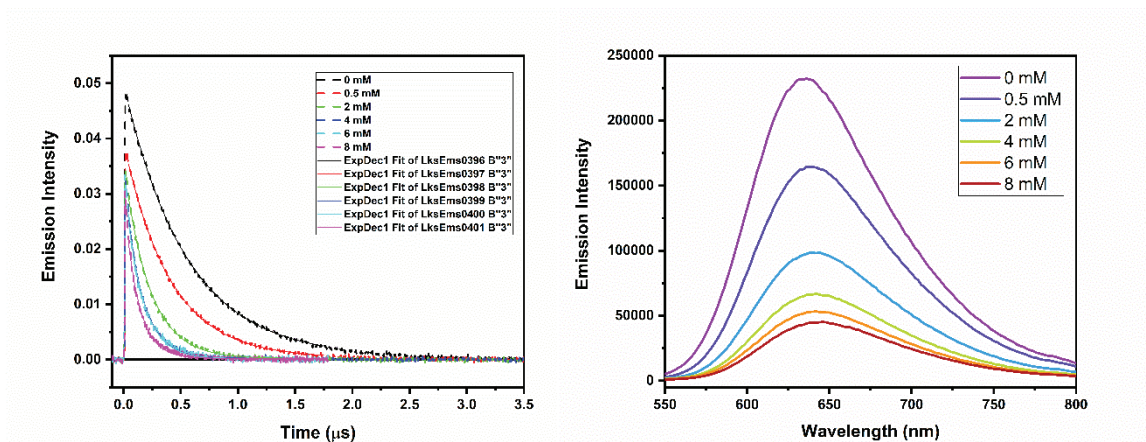


**Figure 3.19** Luminescence lifetimes (left) and steady-state emission spectra (right) of  $[\text{Ru}(\text{bpy})_2(4,4'-(\text{OH})_2\text{bpy})]^{2+}$  in presence of varying concentrations of 2,4-lutidine

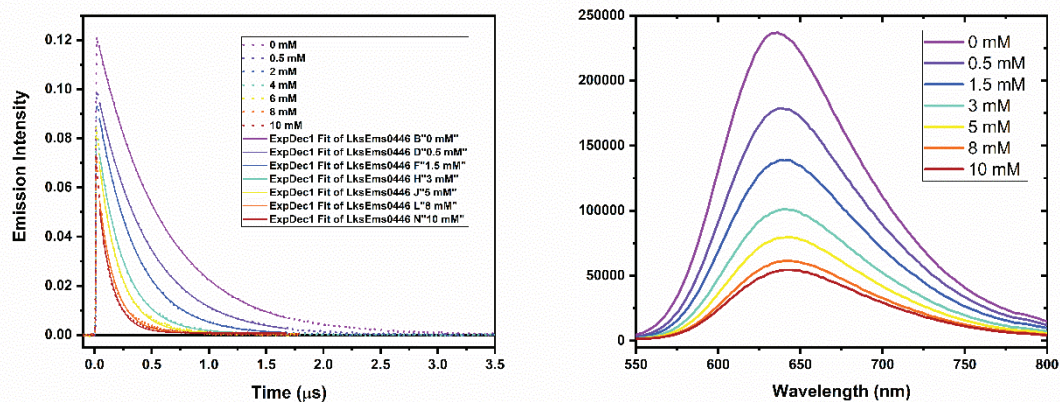


**Figure 3.20** Luminescence lifetimes (left) and steady-state emission spectra (right) of  $[\text{Ru}(\text{bpy})_2(4,4'-(\text{OH})_2\text{bpy})]^{2+}$  in presence of varying concentrations of 2,6-lutidine

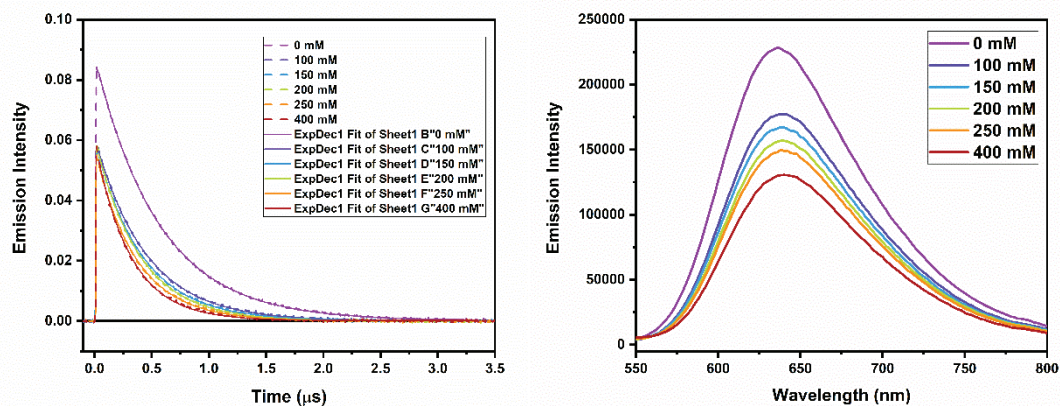


**Figure 3.21** Luminescence lifetimes (left) and steady-state emission spectra (right) of  $[\text{Ru}(\text{bpy})_2(4,4'-(\text{OH})_2\text{bpy})]^{2+}$  in presence of varying concentrations of benzo[h]quinoline

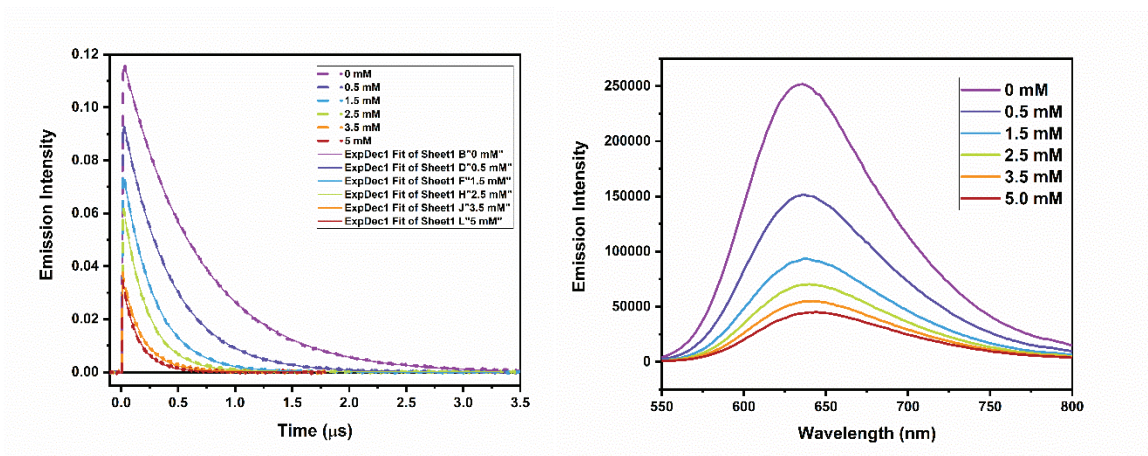


**Figure 3.22** Luminescence lifetimes (left) and steady-state emission spectra (right) of  $[\text{Ru}(\text{bpy})_2(4,4'-(\text{OH})_2\text{bpy})]^{2+}$  in presence of varying concentrations of 2,4,6-collidine

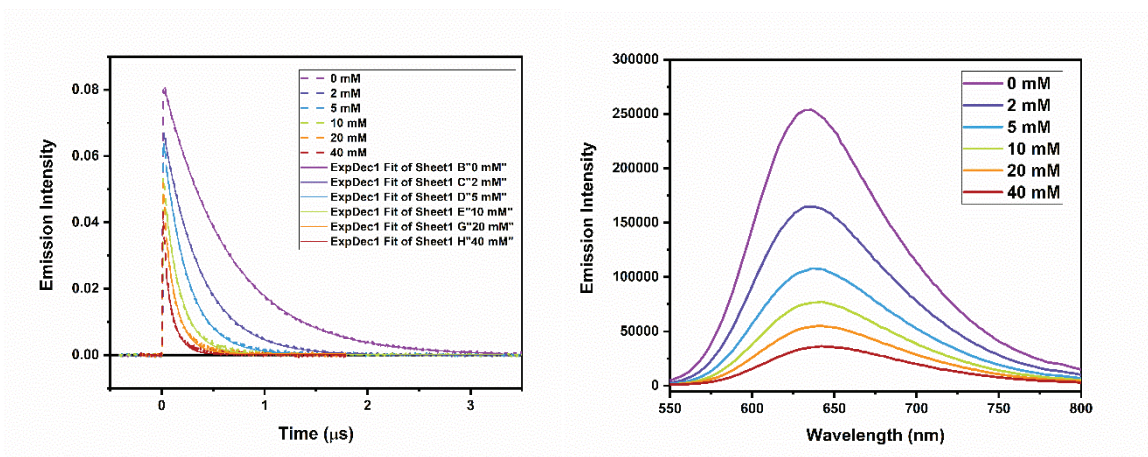


**Figure 3.23** Luminescence lifetimes (left) and steady-state emission spectra (right) of  $[\text{Ru}(\text{bpy})_2(4,4'-(\text{OH})_2\text{bpy})]^{2+}$  in presence of varying concentrations of isoquinoline

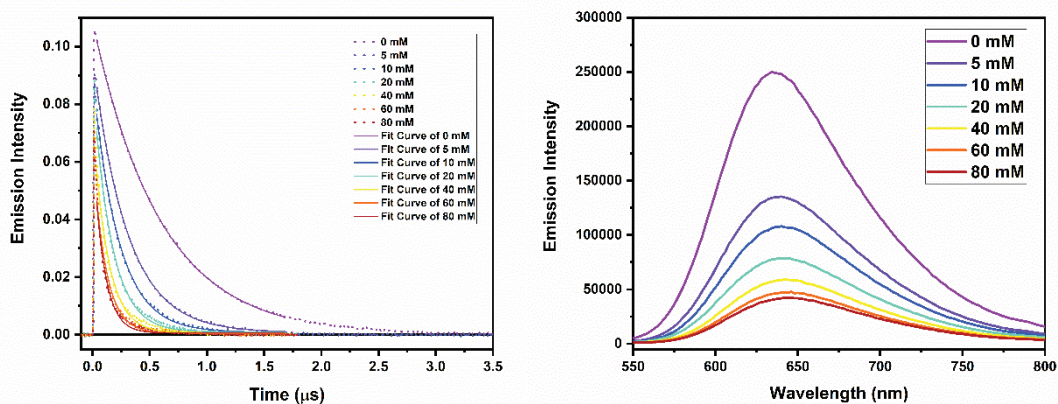


**Figure 3.24** Luminescence lifetimes (left) and steady-state emission spectra (right) of  $[\text{Ru}(\text{bpy})_2(4,4'-(\text{OH})_2\text{bpy})]^{2+}$  in presence of varying concentrations of pyridine

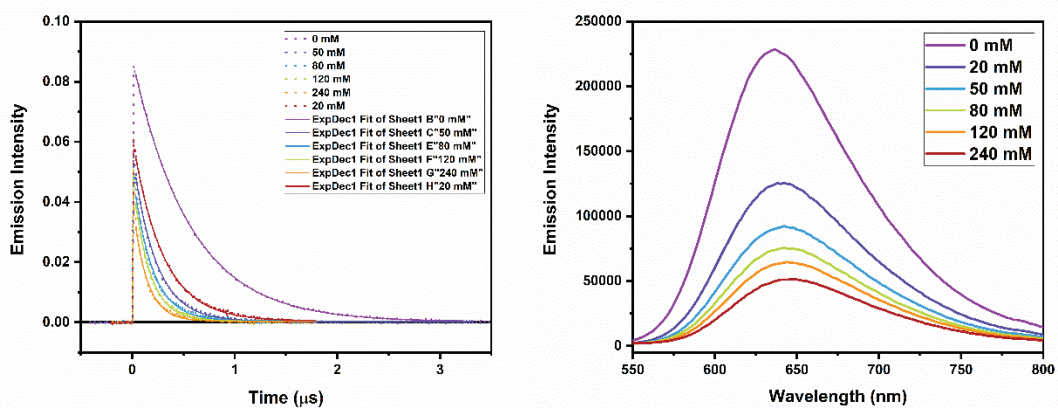


**Figure 3.25** Luminescence lifetimes (left) and steady-state emission spectra (right) of  $[\text{Ru}(\text{bpy})_2(4,4'-(\text{OH})_2\text{bpy})]^{2+}$  in presence of varying concentrations of quinoline

Before embarking on a discussion of the quenching mechanism, one thing must be addressed. For the preliminary proton transfer experiments that were conducted, the hexafluorophosphate salt of the complex was used. The data it produced for the steady-state emission studies showed, for some bases, a large static quenching component. At first glance, this might seem reasonable, given the nature of the hydrogen-bonding ground state adduct. When bases such as 4-picoline were used, immediate precipitation of the complex and base occurred from acetonitrile solution. An attempt was made to obtain crystals of this precipitate, but unfortunately only powders were obtained. As such, a decision was made to attempt using a more soluble salt of the complex, namely the tetrakis(bis(trifluoromethyl)phenyl)borate salt. Using this salt allowed for the collection of data with a wider range of bases. Results from quenching studies with pyridines show a downward curvature in the Stern-Volmer quenching plots for all bases. This is in contrast to the observations made with the  $\text{PF}_6^-$  salt. One possible reason for the discrepancy is that the  $\text{PF}_6^-$  ion may participate in the acid-base reaction, yielding HF and  $\text{PF}_5$ . Though this is speculative, the studies using the  $\text{BArF}_{24}$  salt seem to be consistent throughout the series of bases and is therefore the more suitable choice of complex to study for these reactions, as the bulky  $\text{BArF}_{24}$  counterion should likely not participate in acid base chemistry.

In a typical Stern-Volmer plot for dynamic bimolecular quenching, the fit of the ratio  $\phi_0/\phi$ , or  $\tau_0/\tau$ , versus the concentration of quencher results in a linear regression with a y-intercept of 1.<sup>24</sup> This relationship can be seen in the Stern-Volmer equation, equation 3.5. In this equation,  $\tau_0$  is the lifetime of the chromophore in the absence of quencher,  $\tau$  is the lifetime in the presence of quencher,  $k_q$  is the quenching rate constant, and  $[Q]$  is the concentration of added quencher. This same phenomenon was exhibited for all other bases

in the series. This downward curvature has been observed by others for quenching mechanisms that involve an excited-state pre-equilibrium process prior to the excited-state electron, or proton transfer event. For this equilibrium process to be observable in quenching studies, the equilibrium must be rapid or at least competitive with excited-state deactivation through radiative or nonradiative processes. Figures 3.27 and 3.28 show the resultant Stern-Volmer plots for the quenching reactions with base.

$$\frac{\tau_0}{\tau} = 1 + \tau_0 k_q [Q] \quad (3.5)$$

Lymar and coworkers have shown the impact of hydrogen bonding interactions on the kinetics of excited-state quenching. The detailed derivation of fitting models for quenching of systems in which hydrogen bonding takes place between the chromophore, quencher, and the solvent has been explored. Here, the results of these derivations are applied to fit the data collected where Stern-Volmer plots show a deviation in linearity, namely a downward curvature.<sup>12</sup> The equilibria for the excited-state proton transfer reaction are shown in figure 3.26. This scheme indicates that diffusion of the two species together

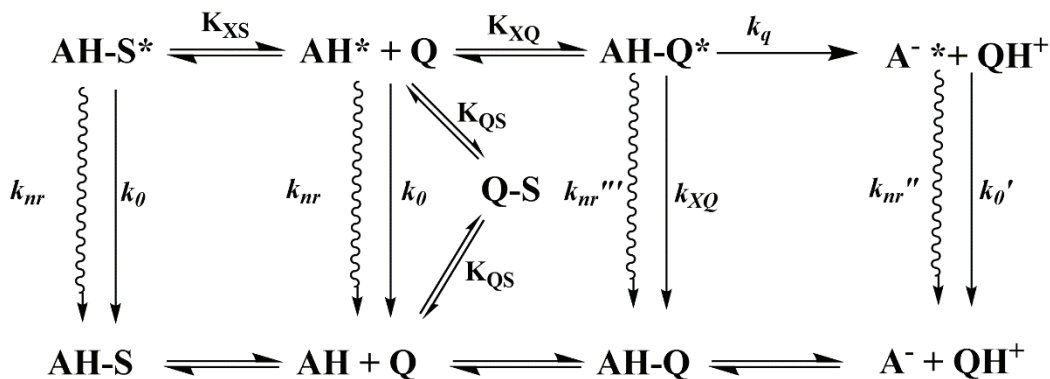


**Figure 3.26** Excited-state proton transfer reaction mechanism

is incorporated into the equilibrium for hydrogen-bond formation between the proton donating chromophore and the proton accepting base.

$$\frac{\tau_0}{\tau} = \frac{\varphi_0}{\varphi} = 1 + \frac{\tau_0 k_q^{app} K_{XQ}^{app} [Q]}{1 + K_{XQ}^{app} [Q]} \quad (3.6)$$

$$k_q^{app} = k_{XQ} + k_q - k_0 \quad (3.7)$$

$$K_{HB}^{app} = \frac{(1 + K_{XQ})}{(1 + K_{XS})(1 + K_{QS})} \quad (3.8)$$

Equation 3.6 was used as the fitting function for the data. In this equation,  $\tau_0$  is the lifetime of the chromophore in the absence of base,  $\tau$  is the observed lifetime in the presence of base,  $\varphi_0$  is the emission quantum yield in the absence of base,  $\varphi$  is the emission quantum yield in the presence of base,  $k_q^{app}$  is the apparent quenching rate constant that is defined by the relationship in equation 3.7,  $K_{XQ}^{app}$  is the apparent equilibrium constant for hydrogen bonding between the chromophore and base which is defined by equation 3.8, and  $[Q]$  is the concentration of base. In equation 3.6,  $k_{XQ}$  is the rate constant for the decay of the hydrogen-bonded chromophore to base,  $K_{XQ}$  is the equilibrium constant for the formation of the excited-state hydrogen-bonded adduct to base,  $K_{XS}$  is the equilibrium constant for the formation of the excited-state hydrogen bonded adduct to solvent, and  $K_{QS}$  is the equilibrium constant for formation of the hydrogen bonded adduct between the base and solvent. In equation 3.7, the quenching rate constant extracted from the fit of the quenching data is taken as the sum of rate constants for decay of the excited hydrogen-bonded adduct between the chromophore and base and the quenching rate constant for the proton transfer reaction less the rate of decay for the free chromophore. In equation 3.8 the equilibrium constant observed is a function of the hydrogen bonding equilibria between

solvent and base ( $K_{QS}$ ), chromophore and base ( $K_{XQ}$ ), and solvent and chromophore ( $K_{XS}$ ).

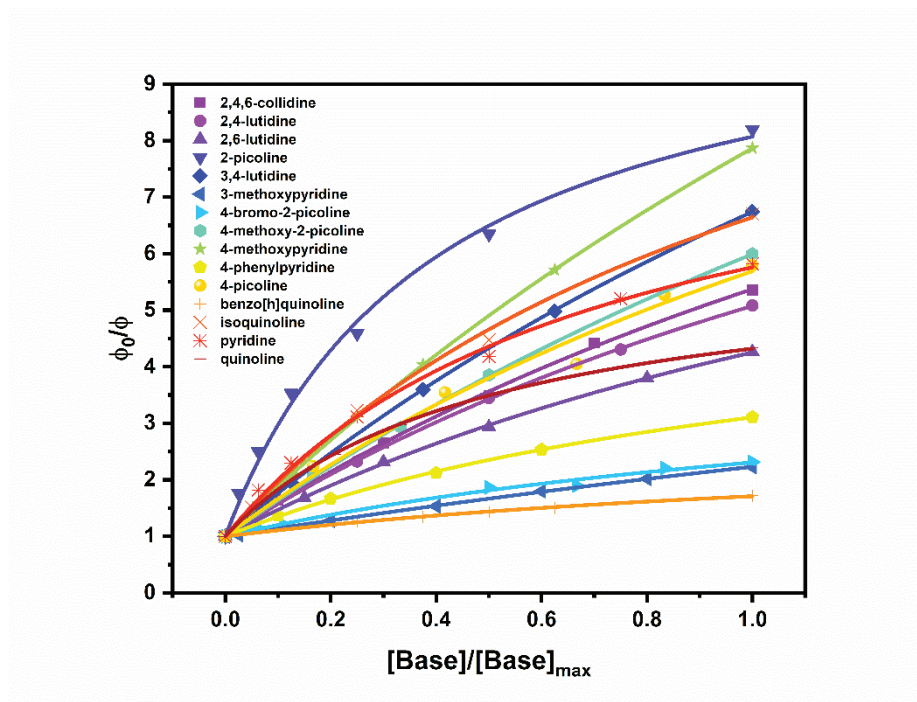


**Figure 3.27** Plot of the ratio of the concentration of base added to the solution vs. the ratio of the  $\phi_0/\phi$  with the modified Stern-Volmer approach (eq. 3.6)

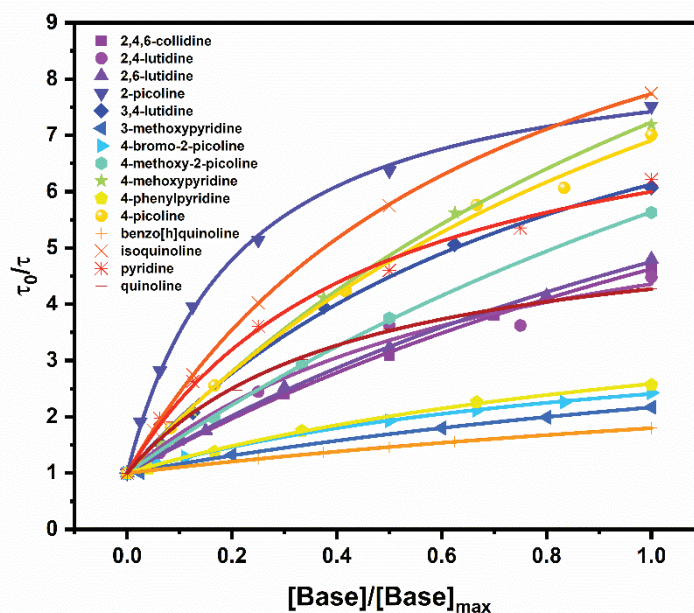


**Figure 3.28** Plot of the ratio of the concentration of base added to the solution vs. the ratio of the  $\tau_0/\tau$  with the modified Stern-Volmer approach (eq. 3.6)

Here it is important to point out that isolation of an equilibrium constant for a hydrogen-bond equilibrium in the excited-state is complicated by the hydrogen bonding interaction between the hydroxyl group on the chromophore and solvent, acetonitrile. Solvent hydrogen bonding to the bases chosen for these experiments is unlikely, and an equilibrium constant for this process can be estimated using the system developed by Ingold which uses  $\alpha$  and  $\beta$  constants that indicate the ability for a particular species to either accept or donate a hydrogen bond. Because acetonitrile is a poor H-bond donor, this equilibrium can be considered to contribute negligibly to the overall excited-state HB equilibrium constant. However, in the case of  $[\text{Ru}(\text{bpy})_2(4,4'-(\text{OH})_2\text{bpy})]^{2+}$ , the phenol-like proton can be assumed a decent hydrogen bond donor and acetonitrile is a better HB acceptor than donor such that extraction of the equilibrium constant for hydrogen bonding between  $[\text{Ru}(\text{bpy})_2(4,4'-(\text{OH})_2\text{bpy})]^{2+*}$  and base from the  $K^{\text{app}}$  is not currently possible. In

addition, we can assume that the excited state lifetime of the hydrogen-bonded chromophore to base is the same as the free chromophore. This assumption is based on the fact that hydrogen bonding interactions are relatively weak. In addition, no evidence for multi-exponential kinetics exists in the luminescence lifetime quenching studies conducted here, further indicating that hydrogen bonding does not affect the lifetime of the chromophore to any appreciable extent. With that said, this makes the  $k_q^{\text{app}}=k_q$ .

Steady-state luminescence quenching measurements were made in addition to time-resolved measurements. When generating the Stern-Volmer plots for these experiments, it became obvious that there was a discrepancy between the  $\tau_0/\tau$  and  $\phi_0/\phi$  plots in the degree of quenching and in the values of  $K_{\text{HB}}^{\text{app}}$  and  $k_q$ . Upon further investigation of the luminescence lifetime quenching data, it was revealed that the emission intensity at  $t=0$  s shows a decrease upon increasing concentration of base. This trend is linearly dependent on the base concentration. Unfortunately, the data for the emission intensity at  $t=0$  s assumes a decent degree of error due to the nature of how the experiments were conducted, i.e., consistency of chromophore concentration in samples and laser intensity. Although quantitative analysis is prohibited by the quality of the data, it is proof positive that static quenching plays a role in the mechanism for proton transfer. An attempt was made to incorporate a static quenching component into the model for fitting the steady-state Stern-Volmer plots, but unfortunately this yielded unreasonable values for some of the ground-state equilibrium constants. In order to reduce the extent of error in these measurements, iterative experiments would need to be completed to yield reasonable values for the ground-state equilibrium constant for hydrogen bonding. We do know, however, based on  $^1\text{H}$ NMR experiments, that hydrogen bonding is present in the ground-state (table 3.1), so

there is no doubt a ground state chromophore/base complex is formed. This serves to further validate the explanation for the discrepancy between the luminescence lifetime quenching studies and steady-state quenching studies. With that said, the analysis of the quenching dynamics will be made using only the luminescence lifetime quenching studies, to eliminate the complication of static quenching as a component in the data.

In figures 3.27 and 3.28, there are a few things to note. First, the efficiency of quenching is lower for less basic pyridines. In addition, for those bases with reduced quenching efficiency, the degree of the plateau effect is also smaller. This could just be due to the fact that for these bases, both the efficiency of forming a hydrogen-bonded pair and the rate constant for the full proton transfer event is lower.

**Table 3.2** Summary of  $K_{HB}$  and  $k_q$  values from Stern-Volmer Quenching

	$pK_a$ (CH3 CN)	$K_{HB}$	$\Delta G_{PT}$ (kcal/mol)	$\Delta G_{PT}^*$ (kcal/mol)	$\log(K_{HB})$	$k_q$	$\log(k_q)$
<i>benzo[h]quinoline</i>	10.84	0. 95	$9.4 \pm 0.1$	$6.1 \pm 0.1$	- 0.022	5.26E +06	6.72
<i>4-bromo-2-methylpyridine</i>	11.23	5	$8.06 \pm 0.09$	$4.8 \pm 0.1$	0.70	5.33E +06	6.73
<i>3-methoxypyridine</i>	11.74	23	$7.78 \pm 0.09$	$4.5 \pm 0.1$	1.36	6.62E +06	6.82
<i>quinoline</i>	11.96	10	$7.88 \pm 0.09$	$4.58 \pm 0.1$	1.0	8.21E +06	6.91
<i>pyridine</i>	12.53	27	$7.1 \pm 0.1$	$3.79 \pm 0.06$	1.43	1.23E +07	7.09
<i>Isoquinoline</i>	12.69	36	$6.9 \pm 0.1$	$3.6 \pm 0.1$	1.56	1.76E +07	7.25
<i>4-phenylpyridine</i>	12.62	63	$6.3 \pm 0.1$	$3.0 \pm 0.1$	1.79	6.64E +06	6.82
<i>4-picoline</i>	13.26	62	$5.5 \pm 0.1$	$2.2 \pm 0.1$	1.79	2.36E +07	7.37
<i>2-picoline</i>	13.32	60	$6.0 \pm 0.1$	$2.71 \pm 0.05$	1.78	1.40E +07	7.15
<i>3,4-lutidine</i>	14.39	13 9	$4.55 \pm 0.06$	$1.25 \pm 0.04$	2.14	1.69E +07	7.23
<i>4-methoxypyridine</i>	14.1	79	$5.34 \pm 0.07$	$2.0 \pm 0.1$	1.90	2.88E +07	7.46
<i>2,4-lutidine</i>	14.61	17 0	$4.2 \pm 0.1$	$0.95 \pm 0.03$	2.23	1.06E +07	7.03
<i>2,6-lutidine</i>	14.13	48	$4.9 \pm 0.1$	$1.6 \pm 0.1$	1.68	2.00E +07	7.30
<i>4-methoxy-2-methylpyridine</i>	14.98	69	$3.5 \pm 0.1$	$0.18 \pm 0.03$	1.84	2.81E +07	7.45
<i>2,4,6-collidine</i>	14.98	90	$3.74 \pm 0.06$	$0.44 \pm 0.03$	1.95	1.78E +07	7.25

Transient absorption (figure 3.30) studies show that for all bases, full proton transfer occurs. This is corroborated by the observation of absorption in the visible region with a maximum at 510 nm that is consistent with the difference spectrum generated using the absorbance spectra of the protonated ruthenium and mono-deprotonated ruthenium

complexes. The difference spectrum can be used to sufficiently model the spectrum for the observed proton transfer products, as the protonated forms of all pyridine bases used in this study do not absorb in the visible region, figure 3.29.

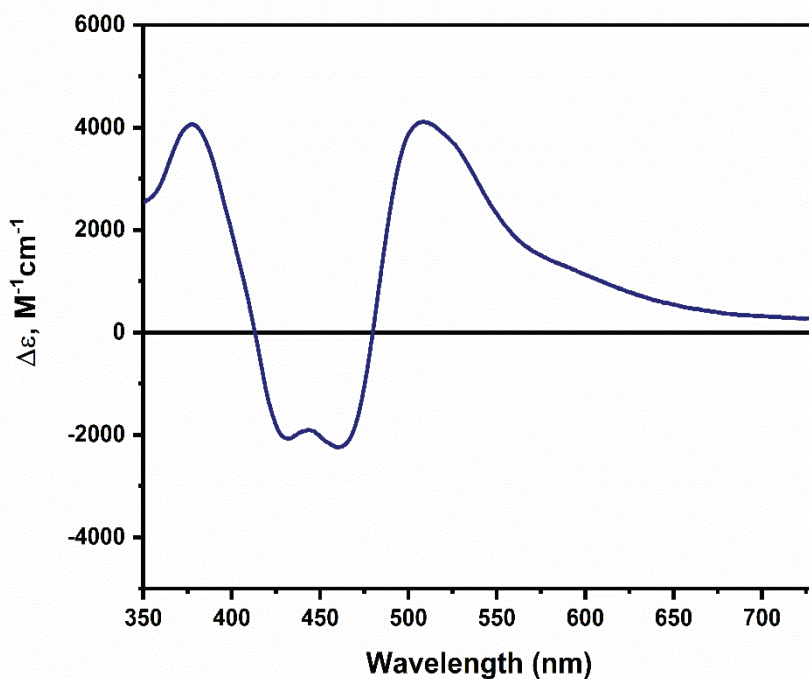


**Figure 3.29** Difference spectrum generated using the UV-Visible absorption spectrum of  $[\text{Ru}(\text{bpy})_2(4,4'-(\text{OH})_2\text{bpy})]^{2+}$  and  $[\text{Ru}(\text{bpy})_2(4-(\text{O})-4'-(\text{OH})\text{bpy})]^+$

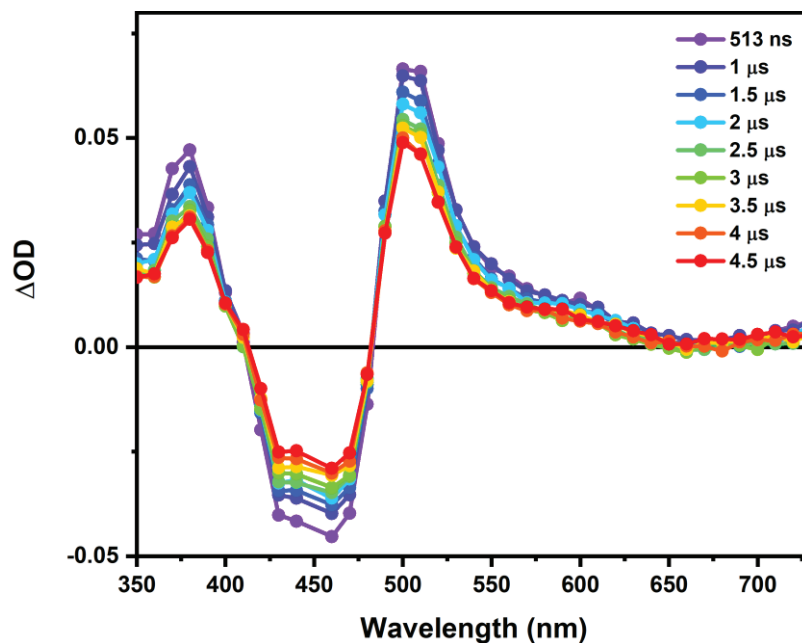


**Figure 3.30** nsTA spectrum of the excited-state proton transfer products for the reaction between  $[\text{Ru}(\text{bpy})_2(4,4'-(\text{OH})_2\text{bpy})]^{2+}$  and pyridine.

A discussion of the trends in free energy dependence for the rate constant for ESPT will be made in the following section. In addition, the relationship between the extracted hydrogen-bond equilibrium constant for the excited-state hydrogen-bond pair,  $K_{\text{HB}}$ , will be discussed in terms of free energy for proton transfer from the excited-state.

### 3.3.3 Back Proton Transfer Reaction Dynamics

Back reaction dynamics were preliminarily investigated using the hexafluorophosphate salt of the complex. Although this data is not comparable, per se, to the previous reported data for ESPT quenching (*vide supra*), it is still worthwhile to discuss the results, and what further exploratory experiments should be conducted to conclusively understand the nature of the back reaction kinetics.

Thermochemical analysis of the free energy for back proton transfer indicate that the reaction should be much more exergonic than the ESPT reaction. This is due to the fact

that the  $pK_a$  of the chromophore in its ground state is more basic than the excited state, making  $\Delta pK_a$  larger. For all models of excited-state proton transfer free energy relationships (vide infra), it should be noted that with increasingly negative free energy for reaction, an expected increase in rate constant should be observed. As such, one could expect that for the pyridines with more acidic conjugate acids, the rate constant for back proton transfer should be the greatest.

The kinetics for back proton transfer were investigated for several bases. The resulting data from fitting are shown in Table 3.3. Interestingly, the back reaction does not appear to occur via the anticipated equal-concentration second order kinetics pathway. Instead, on initial evaluation of the decay of the signal for the ESPT product measured at 510 nm (see figure 3.30), it appears that back reaction occurs much faster than second-order kinetics would predict. Upon evaluation of each base with both an equal concentration second-order kinetics fit and an exponential decay fit, the data appears to fit much better to the exponential decay. This suggests that there is a pseudo-first-order back reaction occurring. One explanation for this is the presence of water in solution. Although attempts were made to rid solutions of excess water, through distillation of the solvent and drying of the pyridine bases over molecular sieves, even a 0.1 mM concentration of water could make PT to water the dominant back reaction mechanism.

For some of the bases, back reaction seemed to have two competitive components, one for the pseudo-first-order PT to water, the other through a second-order back reaction with pyridinium. A simple model was developed based on the rate expression for the concomitant reactions and is shown as the integrated rate expression in equation 3.9. In this expression,  $[A]_t$  is the concentration of the deprotonated chromophore at time  $t$ ,  $P$  is a

pre-exponential factor defined by the initial concentration of deprotonated chromophore and the sum of the rate constants for each reaction path,  $k_1$  is the rate constant for the pseudo-first-order reaction, and  $k_2$  is the rate constant for the second-order reaction.

$$[A]_t = \frac{k_1}{(p * e^{k_1 t}) - k_2} \quad (3.9)$$

Figure 3.31 shows an example of the fitting of back reaction kinetics at 510 nm for the reaction between the deprotonated chromophore and benzo[h]quinoline.

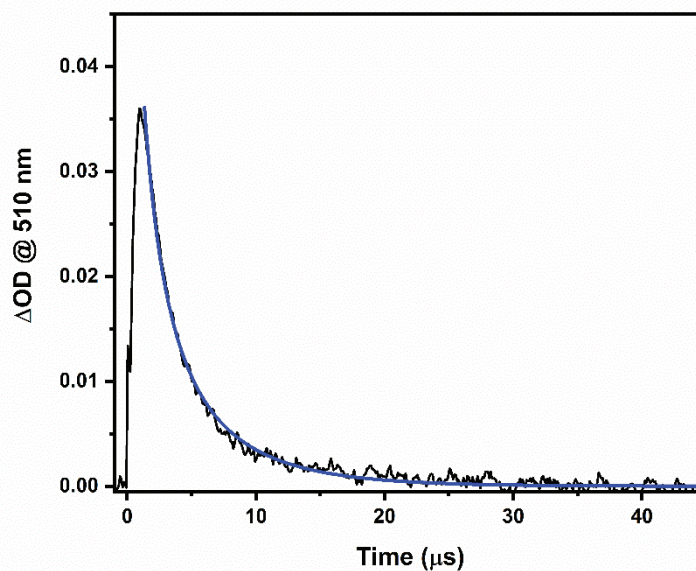


**Figure 3.31** Back proton transfer kinetics monitored at 510 nm for reaction between the deprotonated ruthenium complex and benzo[h]quinoline

In light of the back reaction data, it is important to note that removal of water is exceptionally difficult in the climate that these experiments were conducted in, such that, despite the best efforts to remove water and avoid reintroduction of water, water still remains a viable source of protonation of the complex.

In the future, studies using the BARF<sub>24</sub> salt of the complex conducted on solutions that are rigorously dried would need to be explored to gain a better understanding of the nature of back reaction kinetics. In addition, conducting an experiment where the concentration of water is varied would provide greater certainty in the presumption that water is an interfering component in re-protonation of the chromophore.

**Table 3.3** Table of Back Reaction Rate Constants for Selected Bases

	<b>Best Fitting Routine</b>	<b>k<sub>1</sub> (first-order rate constant) [M<sup>-1</sup>s<sup>-1</sup>]</b>	<b>k<sub>2</sub> (second-order rate constant) [M<sup>-1</sup>s<sup>-1</sup>]</b>
<i>pyridine</i>	Exponential Decay	4.2 x 10 <sup>5</sup>	
<i>2,4,6-collidine</i>	Exponential Decay	4.2 x 10 <sup>5</sup>	
<i>2,6-lutidine</i>	Exponential Decay	3.92 x 10 <sup>5</sup>	
<i>2-picoline</i>	Concomitant Fit	1.4 x 10 <sup>5</sup>	4.2 x 10 <sup>10</sup>
<i>quinoline</i>	Exponential Decay	3.65 x 10 <sup>5</sup>	
<i>benzo[h]quinoline</i>	Concomitant Fit	1.6 x 10 <sup>5</sup>	4.5 x 10 <sup>10</sup>

### 3.3.4 Free Energy Dependence for Proton Transfer Kinetics

Investigation of the free energy dependence for excited-state proton transfer reactions on driving force is made possible given the extracted rate constants for PT with various pyridine bases and [Ru(bpy)<sub>2</sub>(4,4'-(OH)<sub>2</sub>bpy)]<sup>2+</sup>. Understanding the nature of the kinetic dependence on the free energy for ESPT can allow for the evaluation of the intrinsic barrier to ESPT between the hydroxylated ruthenium complex and pyridine bases. Knowing what barriers exist for ESPT reactions can inform the design of systems for ESPCET.

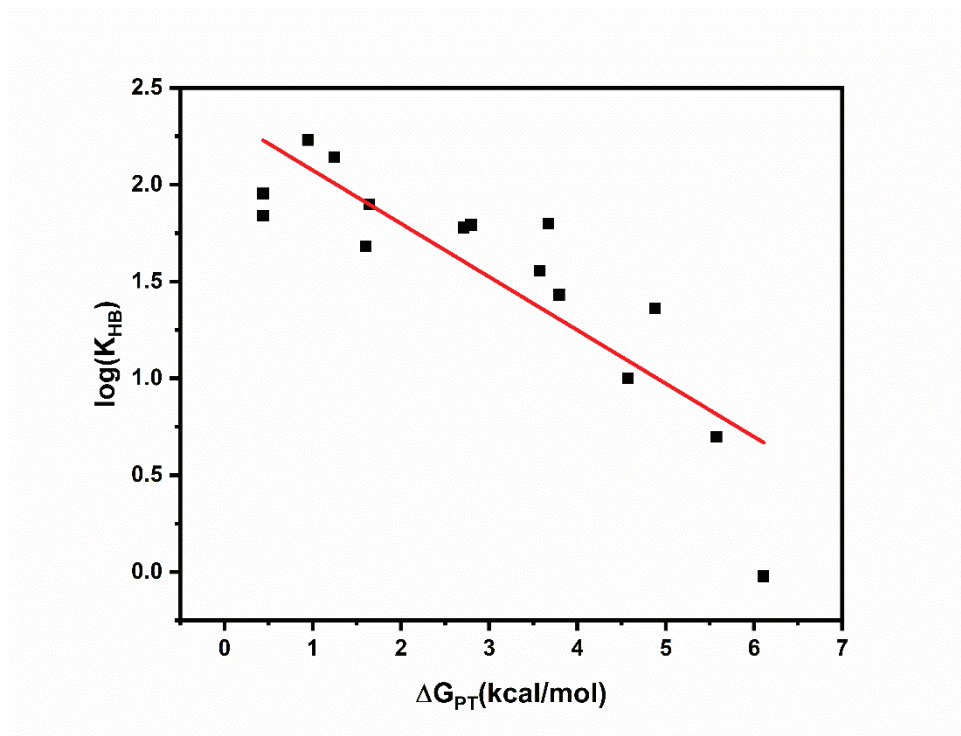


**Figure 3.32** Plot of the  $\log(K_{HB})$  vs.  $\Delta G_{PT^*}$

Before embarking on a discussion of the free energy relationship, there are a few trends in the data to discuss. The first is the relationship between the extracted hydrogen bond equilibrium constant,  $K_{HB}$ , and the free energy for ESPT. This is displayed in figure 3.31 as a  $\log(K)$  vs  $\Delta G_{PT^*}$  plot. There is a clear linear dependence of  $K_{HB}$  on the free energy for ESPT. As was noted earlier, there is a component for the chromophore hydrogen bonding to acetonitrile included in this equilibrium constant, but these values are still comparable, as this will be the same for any base used. The relationship between the free energy for excited-state proton transfer and the hydrogen bond equilibrium constant is anticipated as the factors that influence full proton transfer will also influence the ability of the base to form a hydrogen bond.

In figure 3.31, the last point at a  $\Delta G_{PT}^*$  value of 6 kcal/mol is for the ESPT between the chromophore and benzo[h]quinoline. With this base, steric effects may play an important role in the ability for the complex to hydrogen bond effectively to the base, yielding a very small value for the equilibrium constant for hydrogen bonding relative to other bases in this series.

Unfortunately, for this system, there remain constraints in developing a good fit of data for the free energy dependence of the kinetics for ESPT. The main issue with this system is that there are significant constraints on the free energy for the reaction. If bases with  $pK_a$ 's of the conjugate acid higher than 15 are used, then ground-state deprotonation becomes a concern, and if too much of the ground-state is deprotonated, the amount of protonated chromophore available for photoinduced proton transfer is diminished. In addition, slow kinetics for bases with  $pK_a$ 's of the conjugate acid lower than 11 create the issue of having inefficient quenching. This results in difficulty measuring the rate constant for ESPT without using large amounts of the base, possibly creating the added issue of altering the solvent environment, such that the data is no longer comparable between bases.

With that in mind, it is proposed that the ESPT reaction free energy relationship can be modeled with a classical equation for proton transfer. There is no reason to believe that higher vibronic states for either the reactant or product states are influential in this reaction. In addition, proton tunneling is not presumed to be a substantial factor in the transfer of a proton between  $[\text{Ru}(\text{bpy})_2(4,4'-(\text{OH})_2\text{bpy})]^{2+}$  and any of the substituted pyridines. As such, a linear regression was used to fit the data. A classical approach to fitting the linear free energy dependence was used. Figure 3.33 shows the free energy relationships for ESPT as a plot of the  $\log(k_q)$  vs.  $\Delta pK_a$ .

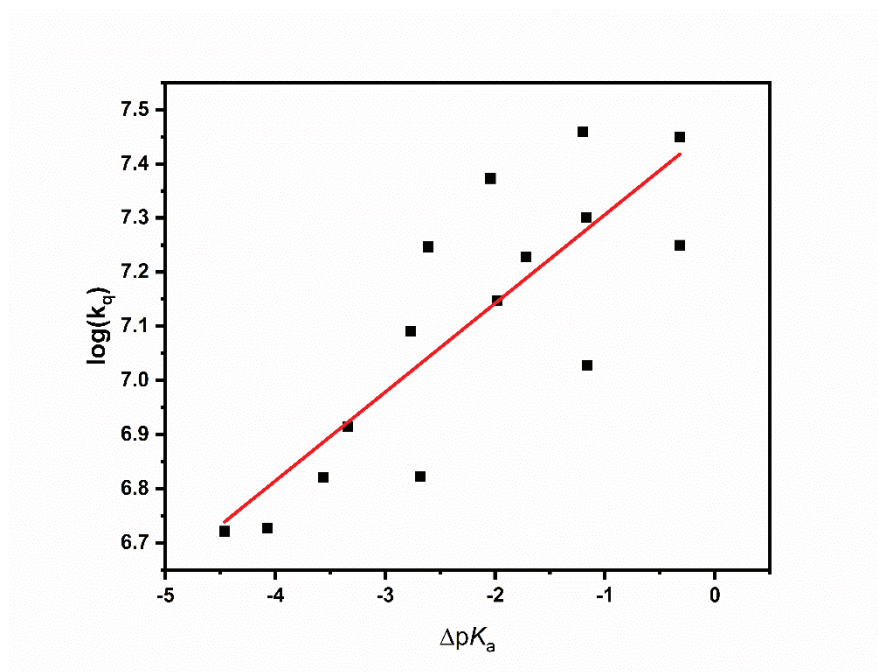


**Figure 3.33** Linear free energy relationship for the ESPT reaction between  $[\text{Ru}(\text{bpy})_2(4,4'-(\text{OH})_2\text{bpy})]^{2+}$  and substituted pyridine bases

The data was fit with a linear regression, for which the expression is shown in equation 3.10. This relationship is referred to as the Brønsted relation. Here, the slope is  $\alpha$ , commonly referred to as the Brønsted coefficient. This value ranges from 0 to 1 for proton transfer reactions. The value for  $\alpha$  from the linear fit is  $0.16 \pm 0.03$ . This value is reasonable, as  $\alpha$  is expected to range from 0 to 1.<sup>21</sup>

$$\log(k_q) = \alpha \log(\Delta pK_a) + c \quad (3.10)$$

Despite the limited range of free energies explored for the ESPT reaction, valuable insight is gained as to the nature of the rate constant dependence on driving force, and the identification of hydrogen bonding occurring in both the ground and excited-state for this complex.

### 3.4 Conclusion

Excited-state proton transfer reactions studied here were informative as to the effect of hydrogen bonding on the observed proton transfer reaction. Because an equilibrium exists for the ESPT reaction, it can be speculated that as the concentration of base is increased, the quenching processes reaches a plateau. This indicates a type of saturation kinetics that cannot be overcome for this reaction. Additionally, knowing that there is a static quenching component to the excited-state proton transfer mechanism, it can also be inferred that eventually the plateau will reach an asymptotic limit as the static quenching component dominates the dynamic component.

In evaluating these systems for excited-state proton-transfer, hydrogen bonding is a governing factor in ESPT. Knowing the relationship between the quenching rates and the degree of hydrogen bonding, further assists in the development of systems that exhibit ESPCET behavior, as pre-association of the donor and acceptor are influential factors in observing a concerted electron-proton transfer reaction (see Chapter 1). Analysis of the free energy dependence for excited-state proton transfer yielded the result that as the  $pK_a$  of the conjugate acid of the base increased (the base becomes more basic), the rate constant for ESPT also increased.

Given this information, Chapter 4 will cover the excited-state proton and electron transfer reactivity between a series of ruthenium complexes with hydroxy substituted diimine ligands and pyridinium quenchers. In Chapter 5, the impact of charge repulsion is explored in a system for which the electron and proton acceptor is a neutral species.

## CHAPTER 3 REFERENCES

- (1) Peterson, S. H.; Demas, J. N. Excited State Acid-Base Reactions of Transition Metal Complexes: Dicyanobis(2,2'-Bipyridine) Ruthenium(III) in Aqueous Acid. *J. Am. Chem. Soc.* **1976**, *98* (24), 7880–7881. <https://doi.org/10.1021/ja00440a100>.
- (2) Peterson, S. H.; Demas, J. N. Excited-State Acid-Base Reactions of Dicyanobis(2,2'-Bipyridine)Ruthenium(II) and Dicyanobis(1,10-Phenanthroline)Ruthenium(II). *J. Am. Chem. Soc.* **1979**, *101* (22), 6571–6577. <https://doi.org/10.1021/ja00516a015>.
- (3) O'Donnell, R. M.; Sampaio, R. N.; Li, G.; Johansson, P. G.; Ward, C. L.; Meyer, G. J. Photoacidic and Photobasic Behavior of Transition Metal Compounds with Carboxylic Acid Group(s). *J. Am. Chem. Soc.* **2016**, *138* (11), 3891–3903. <https://doi.org/10.1021/jacs.6b00454>.
- (4) Giordano, P. J.; Bock, C. R.; Wrighton, M. S.; Interrante, L. V.; Williams, R. F. X. Excited State Proton Transfer of a Metal Complex: Determination of the Acid Dissociation Constant for a Metal-to-Ligand Charge Transfer State of a Ruthenium(II) Complex. *J. Am. Chem. Soc.* **1977**, *99* (9), 3187–3189. <https://doi.org/10.1021/ja00451a066>.
- (5) Giordano, P. J.; Bock, C. R.; Wrighton, M. S. Excited State Proton Transfer of Ruthenium (II) Complexes of 4, 7-Dihydroxy-1, 10-Phenanthroline. Increased Acidity in the Excited State. *J. Am. Chem. Soc.* **1978**, *100* (22), 6960–6965.
- (6) Charboneau, D. J.; Piro, N. A.; Kassel, W. S.; Dudley, T. J.; Paul, J. J. Structural, Electronic and Acid/Base Properties of [Ru(Bpy)(Bpy(OH)<sub>2</sub>)<sub>2</sub>]<sup>2+</sup> (Bpy=2,2'-Bipyridine, Bpy(OH)<sub>2</sub>=4,4'-Dihydroxy-2,2'-Bipyridine). *Polyhedron* **2015**, *91*, 18–27. <https://doi.org/10.1016/j.poly.2015.02.001>.
- (7) Fuentes, M. J.; Bognanno, R. J.; Dougherty, W. G.; Boyko, W. J.; Scott Kassel, W.; Dudley, T. J.; Paul, J. J. Structural, Electronic and Acid/Base Properties of [Ru(Bpy(OH)<sub>2</sub>)<sub>3</sub>]<sup>2+</sup> (Bpy(OH)<sub>2</sub> = 4,4'-Dihydroxy-2,2'-Bipyridine). *Dalton Trans.* **2012**, *41* (40), 12514. <https://doi.org/10.1039/c2dt31706k>.
- (8) Klein, S.; Dougherty, W. G.; Kassel, W. S.; Dudley, T. J.; Paul, J. J. Structural, Electronic, and Acid/Base Properties of [Ru(Bpy)<sub>2</sub>(Bpy(OH)<sub>2</sub>)]<sup>2+</sup> (Bpy = 2,2'-Bipyridine, Bpy(OH)<sub>2</sub> = 4,4'-Dihydroxy-2,2'-Bipyridine). *Inorg. Chem.* **2011**, *50* (7), 2754–2763. <https://doi.org/10.1021/ic1017054>.
- (9) Martinez, K.; Stash, J.; Benson, K. R.; Paul, J. J.; Schmehl, R. H. Direct Observation of Sequential Electron and Proton Transfer in Excited-State ET/PT Reactions. *J. Phys. Chem. C* **2019**, *123* (5), 2728–2735.
- (10) Qu, F.; Martinez, K.; Arcidiacono, A. M.; Park, S.; Zeller, M.; Schmehl, R. H.; Paul, J. J.; Kim, Y.; Papish, E. T. Sterically Demanding Methoxy and Methyl Groups in

- Ruthenium Complexes Lead to Enhanced Quantum Yields for Blue Light Triggered Photodissociation. *Dalton Trans* **2018**, 47 (44), 15685–15693. <https://doi.org/10.1039/C8DT03295E>.
- (11) Viere, E. J.; Kuhn, A. E.; Roeder, M. H.; Piro, N. A.; Kassel, W. S.; Dudley, T. J.; Paul, J. J. Spectroelectrochemical Studies of a Ruthenium Complex Containing the PH Sensitive 4,4'-Dihydroxy-2,2'-Bipyridine Ligand. *Dalton Trans.* **2018**, 47 (12), 4149–4161. <https://doi.org/10.1039/C7DT04554A>.
- (12) Lymar, S. V.; Ertem, M. Z.; Lewandowska-Andralojc, A.; Polyansky, D. E. Role of Hydrogen Bonding in Photoinduced Electron–Proton Transfer from Phenols to a Polypyridine Ru Complex with a Proton-Accepting Ligand. *J. Phys. Chem. Lett.* **2017**, 8 (17), 4043–4048. <https://doi.org/10.1021/acs.jpcclett.7b01614>.
- (13) Lymar, S. V.; Ertem, M. Z.; Polyansky, D. E. Solvent-Dependent Transition from Concerted Electron–Proton to Proton Transfer in Photoinduced Reactions between Phenols and Polypyridine Ru Complexes with Proton-Accepting Sites. *Dalton Trans.* **2018**, 47 (44), 15917–15928. <https://doi.org/10.1039/C8DT03858A>.
- (14) Agmon, N. Elementary Steps in Excited-State Proton Transfer. *J. Phys. Chem. A* **2005**, 109 (1), 13–35. <https://doi.org/10.1021/jp047465m>.
- (15) Hynes, J. T.; Tran-Thi, T.-H.; Granucci, G. Intermolecular Photochemical Proton Transfer in Solution: New Insights and Perspectives. *J. Photochem. Photobiol. Chem.* **2002**, 154 (1), 3–11. [https://doi.org/10.1016/S1010-6030\(02\)00304-0](https://doi.org/10.1016/S1010-6030(02)00304-0).
- (16) Kiefer, P. M.; Hynes, J. T. Kinetic Isotope Effects for Nonadiabatic Proton Transfer Reactions in a Polar Environment. 2. Comparison with an Electronically Diabatic Description. *J. Phys. Chem. A* **2004**, 108 (52), 11809–11818. <https://doi.org/10.1021/jp040498h>.
- (17) Staib, A.; Borgis, D.; Hynes, J. T. Proton Transfer in Hydrogen-bonded Acid–Base Complexes in Polar Solvents. *J. Chem. Phys.* **1995**, 102 (6), 2487–2505. <https://doi.org/10.1063/1.468678>.
- (18) *Purification of Organic Chemicals*; Butterworth-Heinemann, 2009; pp 88–444. <https://doi.org/10.1016/B978-1-85617-567-8.50012-3>.
- (19) Yakelis, N. A.; Bergman, R. G. Safe Preparation and Purification of Sodium Tetrakis[(3,5-Trifluoromethyl)Phenyl]Borate (NaBArF<sub>24</sub>): Reliable and Sensitive Analysis of Water in Solutions of Fluorinated Tetraarylborates. *Organometallics* **2005**, 24 (14), 3579–3581. <https://doi.org/10.1021/om0501428>.
- (20) Kaljurand, I.; Kütt, A.; Sooväli, L.; Rodima, T.; Mäemets, V.; Leito, I.; Koppel, I. A. Extension of the Self-Consistent Spectrophotometric Basicity Scale in Acetonitrile to a Full Span of 28 pK<sub>a</sub> Units: Unification of Different Basicity Scales. *J. Org. Chem.* **2005**, 70 (3), 1019–1028. <https://doi.org/10.1021/jo048252w>.

- (21) Arnaut, L. G.; Formosinho, S. J. Excited-State Proton Transfer Reactions I. Fundamentals and Intermolecular Reactions. *J. Photochem. Photobiol. Chem.* **1993**, *75* (1), 1–20. [https://doi.org/10.1016/1010-6030\(93\)80157-5](https://doi.org/10.1016/1010-6030(93)80157-5).
- (22) Lõkov, M.; Tshepelevitsh, S.; Heering, A.; Plieger, P. G.; Vianello, R.; Leito, I. On the Basicity of Conjugated Nitrogen Heterocycles in Different Media: On the Basicity of Conjugated Nitrogen Heterocycles in Different Media. *Eur. J. Org. Chem.* **2017**, *2017* (30), 4475–4489. <https://doi.org/10.1002/ejoc.201700749>.
- (23) Pannwitz, A.; Wenger, O. S. Photoinduced Electron Transfer Coupled to Donor Deprotonation and Acceptor Protonation in a Molecular Triad Mimicking Photosystem II. *J. Am. Chem. Soc.* **2017**, *139* (38), 13308–13311. <https://doi.org/10.1021/jacs.7b08761>.
- (24) Demas, J. N. *Excited State Lifetime Measurements*; Academic Press, 1983.

## Chapter 4: Excited-State Reactions with 4,4'-bipyridinium Quenchers

Portions of this work were reprinted (adapted) with permission from Kristina Martinez, Jacqueline Stash, Kaitlyn R. Benson, Jared J. Paul, and Russell H. Schmehl *J. Phys. Chem. C*, **2019**, *123* (5), 2728-2735 DOI: 10.1021/acs.jpcc.8b09268 Copyright 2019 American Chemical Society.

### 4.1 Introduction

The utilization of solar energy to drive chemical reactions is of increasing value. While fundamental industrial chemical processes involve energy-intensive reactions, light-driven transformations have the advantage of using the abundance of solar energy available to drive forward chemical processes.<sup>1</sup> Current work in the field of light-to-chemical conversion is in pursuit of generating viable storable fuels from abundant substrates such as CO<sub>2</sub> and H<sub>2</sub>O.<sup>2</sup> Reactions such as the reduction of carbon dioxide require multiple electron and proton transfer events. Such multielectron, multi-proton reactions are facilitated by proton-coupled electron transfer (PCET) in natural systems such as the water oxidation reaction of photosynthesis.<sup>3</sup> The advantage of PCET over sequential redox and acid-base (electron transfer- proton transfer or proton transfer- electron transfer), is that it is always more thermodynamically favored over the stepwise reaction pathway.<sup>4</sup>

Incorporating light absorption into this reaction scheme creates a system poised to take light energy and transform it into new chemical bonds. The inclusion of light into these reaction schemes has been done in one of two ways, either through direct involvement of the excited state in the PCET reaction or the use of the light absorber to initiate electron transfer (ET) reactions through an oxidative or reductive quenching pathway. In a reaction where the excited state is involved directly in PCET, the light

absorber can act as either a proton and electron donor or acceptor. A recent review of such reactions was compiled by Dempsey and coworkers.<sup>5</sup>

Focusing on reactions that involve light absorbers that act as both proton and electron donors, systems that have been investigated to date often involve the use of covalently linked chromophores and substrates, or the use of preformed hydrogen-bond bridged donor and acceptor complexes.<sup>6-8</sup> One example of a such a system is the cyclometalated Ir complex incorporating a biimidazole ligand as a proton donor studied by Wenger.<sup>9</sup> In this work, the biimidazole ligand forms a salt bridge to the electron acceptor, dinitrobenzoate. The work uncovered that through tethering the donor and acceptor together via hydrogen bonds, the rate of ET was enhanced when compared to the *N*-methylated biimidazole complex. Additional examples of excited-state proton and electron donors can be seen in work done by Nocera and coworkers studying systems involving ruthenium diimine complexes and porphyrins as light absorbing molecules with the ability to partake in electron and proton transfer reactions. Though this work has been pivotal in understanding the factors that influence excited-state proton-coupled electron transfer reactions, they have disadvantages in the areas of ease of preparation and separation of photoproducts from the encounter complex. Without photoproduct separation, the system will inevitably be primed to undergo back reaction rapidly, as opposed to the slower kinetics of the diffusional back reaction.

In this chapter, a series of ruthenium complexes with hydroxylated 2,2'-bipyridine ligands and their reaction with monoquaternerized 4,4'-bipyridinium quenchers will be explored. Transient absorption spectroscopy will serve to detail the kinetics of the photoinduced reaction and help to distinguish between excited state electron transfer,

excited state proton transfer, and excited state proton-coupled electron transfer reactions. In addition, a detailed thermochemical analysis will help to guide the understanding the difference in reactivity among the chromophores explored.

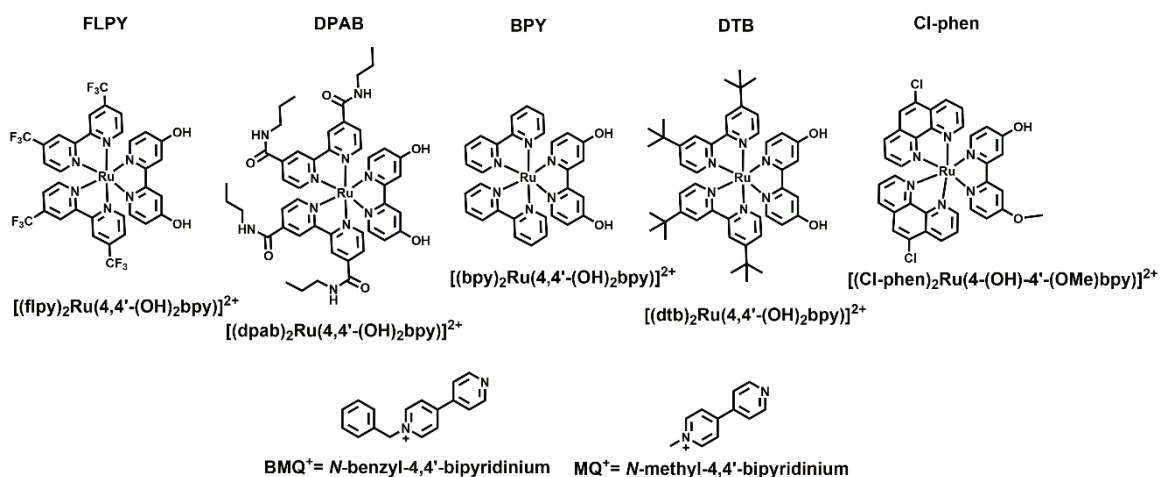


**Figure 4.1** Hydroxylated complexes and bipyridinium quenchers

A portion of this work was first published in a *Journal of Physical Chemistry C* article in 2019, it outlined the reaction of  $[\text{Ru}(\text{bpy})_2(4,4'\text{-(OH)}_2\text{bpy})]^{2+}$  with *N*-methyl-4,4'-bipyridinium ( $\text{MQ}^+$ ). The work will be revisited in the context of a series of chromophores of  $[\text{Ru}(\text{LL})_2(4,4'\text{-(OH)}_2\text{bpy})]^{2+}$  (LL= bpy, 4,4'-di-propylamido-2,2'-bipyridine, 4,4'-bis(trifluoromethyl)-2,2'-bipyridine, 4,4'-bis(di-tert-butyl)-2,2'-bipyridine) and mixed isomers of  $[\text{Ru}(\text{Cl-phen})_2(4\text{-(OH)-}4'\text{-(OMe)bpy})]^{2+}$  (Cl-phen= 5-chloro-1,10-phenanthroline) and their excited state reactions with both  $\text{MQ}^+$  and *N*-benzyl-4,4'-bipyridinium ( $\text{BMQ}^+$ ).<sup>10</sup> The goal of this work is to try to understand what thermodynamic factors are most influential in determining the mechanism for excited state quenching as one of three possibilities: proton transfer, proton-coupled electron transfer or electron transfer. In exploring this series of chromophores ESET, ESPT, and ESPCET were all

observed reactions, exemplifying the value of simple synthetic modification of ancillary ligands in directing excited state reactivity.

## 4.2 Experimental

For information on the synthesis of complexes, ligands, and their characterization please refer to chapter 2.

### 4.2.1 Materials

4-bromobenzenediazonium tetrafluoroborate (Alfa) was purified by rinsing with diethyl ether. Pyridine (Sigma Aldrich) was dried over 3 Å molecular sieves prior to use. Acetonitrile was distilled from  $\text{CaH}_2$  prior to use. Tetrabutylammonium hexafluorophosphate ( $\text{TBAPF}_6$ ) (TCI America) was recrystallized from hot ethanol, filtered and dried in vacuo prior to use. Deuterated solvents (methanol- $d_4$  and acetonitrile- $d_3$ ) were purchased from Cambridge Isotope Laboratories (CIL).  $\text{CD}_3\text{CN}$  was dried over 3 Å molecular sieves prior to use in kinetic isotope studies.  $\text{NaBARF}_{24}$  was prepared as reported in the literature.<sup>11</sup>

### 4.2.2 nsTA Spectroscopy

Nanosecond transient absorption measurements were done on an Applied Photophysics LKS 60 Laser Flash Photolysis system with laser excitation from a Quantel Brilliant B Q-switched laser with second and third harmonic attachments and an OPO (OPOTEK) for visible light generation, and data recorded using an Agilent Infinium digitizer. Laser excitation of the sample was from OPO at 450 nm for all measurements reported here, with a typical power output of 12 mJ/pulse. In order to maintain constant

ionic strength in quenching experiments, tetrabutylammonium hexafluorophosphate was added to all samples studied by transient absorption.

#### **4.2.3 Electrochemistry**

Electrochemical and spectroelectrochemical measurements were carried out using a CH Instruments 630E Electrochemical Analyzer/Workstation. All measurements were done in acetonitrile dried over  $\text{CaH}_2$  and distilled before use. Unless otherwise stated, cyclic voltammetric measurements were done using a glassy carbon working electrode, a platinum wire counter electrode, and an Ag/AgCl reference electrode. Spectroelectrochemical measurements were carried using an Ocean Optics HR2000 spectrophotometer along with a Pine Research Instruments platinum honeycomb working electrode, a Pt wire counter electrode and a Ag/AgCl reference electrode.

#### **4.2.4 $^1\text{H}$ NMR Spectroscopy**

$^1\text{H}$  NMR studies were conducted on a Varian 400 MHz NMR.

#### **4.2.5 UV-Vis Absorption Spectroscopy and Emission Spectroscopy**

Absorption spectra were collected using an Ocean Optics UV-visible source and HR2000 spectrometer. Emission spectra were collected on a PTI Quantamaster with a photomultiplier detector.

Photooxidation of the ruthenium complexes with hydroxylated bipyridine ligands was done using 0.2 M 4-bromobenzenediazonium tetrafluoroborate with and without 10 mM pyridine in acetonitrile solution. The concentration of chromophore in solution was kept between 30-60  $\mu\text{M}$ . The solutions were degassed with nitrogen for 15 minutes prior to irradiation under 460 nm light (supplied by Solid Apollo, 24 W). For each complex, four

solutions were prepared, a control solution with only chromophore, a solution with chromophore and pyridine, a solution with chromophore and 4-bromobenzenediazonium tetrafluoroborate, and a solution with chromophore, pyridine and 4-bromobenzenediazonium tetrafluoroborate. The absorbance was measured periodically during irradiation. When no further change in absorption was detectable, it is assumed that the reaction was complete.

#### 4.2.6 Preparation of Samples for KIE Studies

Deuteration of the complexes  $[(LL)_2Ru(4,4'-(OH)_2bpy)]^{2+}$  was accomplished by first exchanging the  $PF_6^-$  counterion for  $[BArF_{24}]^-$  (using sodium tetrakis[3,5-bis(trifluoromethyl)phenyl]borate) and then washing the complex in methanol- $d_4$  (CIL) under  $N_2$  gas three times. Synthesis of  $Na[BArF_{24}]$  is described elsewhere.<sup>24</sup> The complex was rinsed with chloroform- $d$ . The dry, deuterated complex was immediately transferred into a glovebox for sample preparation. Tetrabutylammonium hexafluorophosphate was used as electrolyte in solution for constant ionic strength. All materials were placed in the glove box and samples prepared and placed in sealed cuvettes prior to removal from glovebox. Upon removal, the samples were kept in a desiccator with a constant positive pressure of  $N_2$  gas supplied. Measurements were made immediately upon removal from the desiccator and were typically completed with 30 minutes of removal from the glovebox.

### 4.3 Results and Discussion

#### 4.3.1 Acid-Base and Redox Chemistry of Ruthenium Complexes

Ruthenium complexes with hydroxy-substituted diimine complexes have been investigated in the past for their excited-state proton transfer reactivity and some of the complexes reported in this chapter were discussed in detail in chapter 3. However, such

studies are not new. In the 1970's Giordano and coworkers investigated the complex  $[(\text{bpy})_2\text{Ru}(4,7\text{-(OH)}_2\text{phen})]^{2+}$  in aqueous solution and showed that, upon photoexcitation, the complex becomes more acidic than its ground state.<sup>12</sup> This can be rationalized by the fact that photoexcitation yields a charge transfer state to the 2,2'-bipyridine ligands, which would reduce the electron density on the metal complex, pi-donation of electron density from the hydroxylated ligand would thereby increase, causing an inductive effect, rendering the proton on the -OH more acidic.

In a Coordination Chemistry Review paper from 2011, Meyer and coworkers detailed the use of complexes with hydroxylated phenanthroline ligands as participants in a photoinduced proton-coupled electron transfer reaction with *N*-methyl-4,4'-bipyridinium.<sup>1</sup> The work speculated that the chromophore would act as both an electron donor and proton donor from its excited state to both reduce and protonate the bipyridinium compound. This reaction would be considered a proton-coupled electron transfer, not an H-atom transfer because the transferring electron and proton originates from the metal center and the proton comes from the hydroxyl substituent on the phenanthroline. The work claimed, without detail, that the reaction proceeded in a concerted fashion, where both electron and proton would be effectively transferred at the same time. No work was done to follow-up on these claims, and no analytical data was provided to justify the conjecture.

Work on this project has been inspired by the work of Meyer and colleagues to understand the utility of ruthenium complexes with hydroxylated diimine ligands to act as effective electron and proton donors from their excited states. In order to understand

reaction mechanisms in a meaningful way, careful mapping of the thermodynamics for independent reaction paths, ESET, ESPT, and ESPCET must be undertaken.

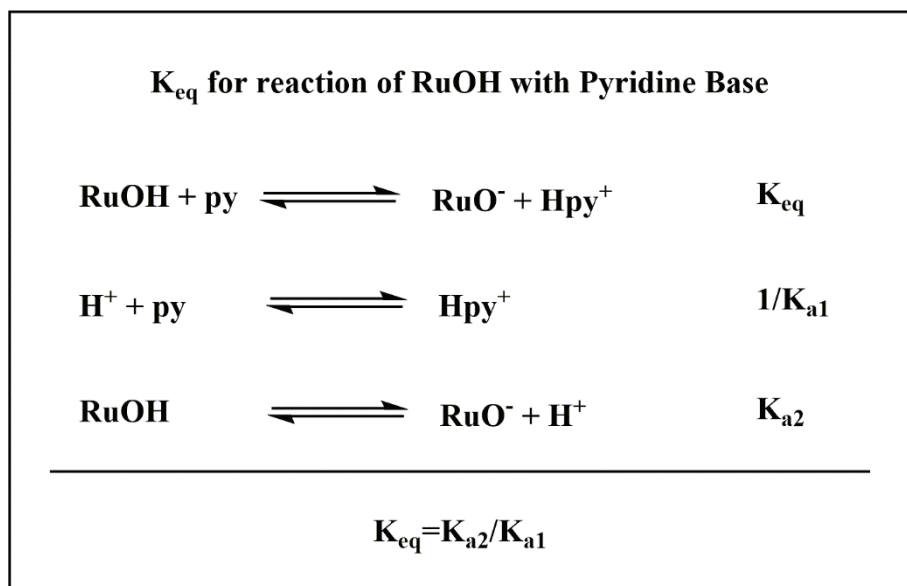


**Figure 4.2** Reactions used to calculate the equilibrium constant for the acid-base reaction between ruthenium complexes and pyridine/amine bases

A starting point for this analysis will be assessing the acid-base chemistry of the complexes. In addition to defining the acid-base chemistry of the complexes, the redox properties must also be considered. Analysis of the voltammetric data was conducted in Chapter 2, and thus the resulting redox potential will only be discussed in reference to the computation of the free energy for electron transfer and proton coupled electron transfer, and the computation of the excited-state redox potential for the complexes.

For all complexes in the series, the  $pK_a$  of the ground state was assessed using a photometric titration. Because the absorption spectra are known for both the protonated and deprotonated complex, measurement of the concentration of both species in the presence of a base with known  $pK_a$  allows for the assessment of the equilibrium constant for the proton transfer reaction. Figure 4.2 shows the reactions that are used to determine

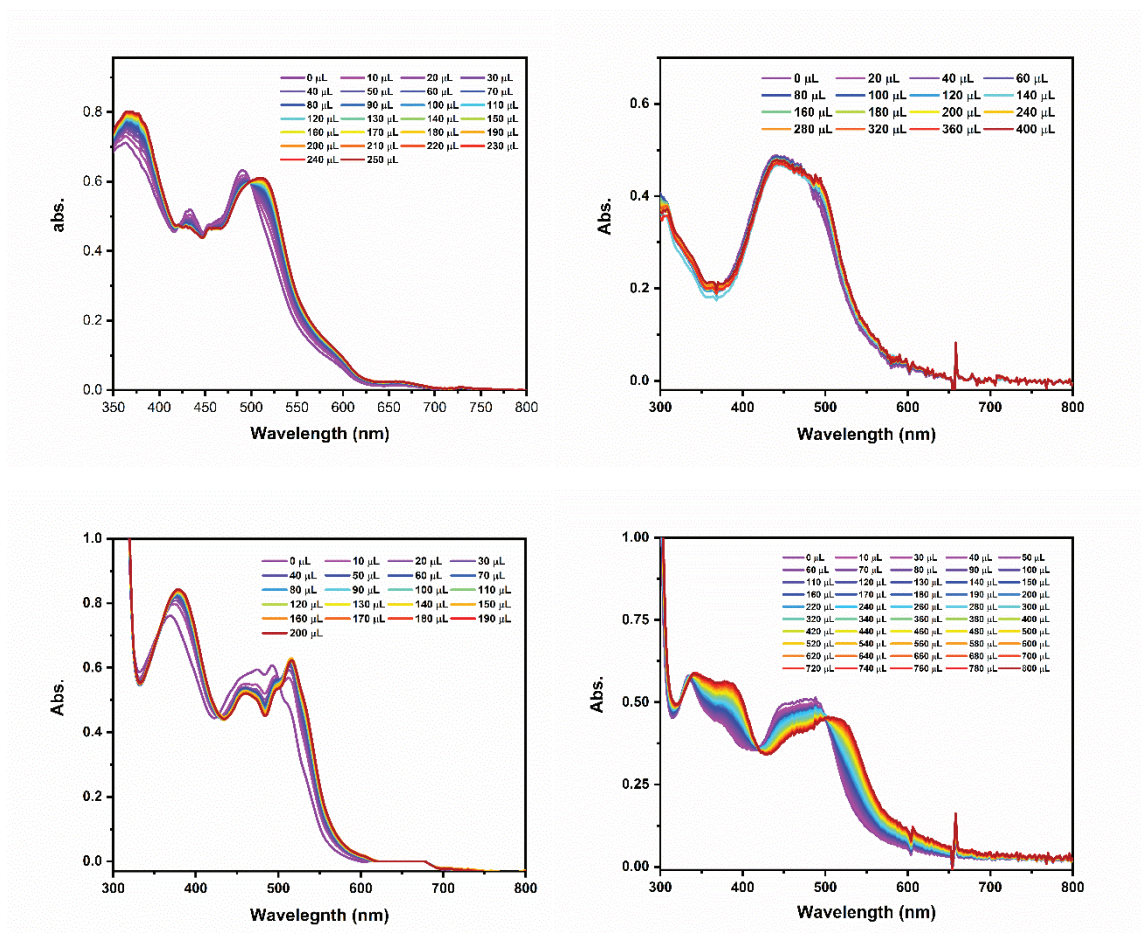


**Figure 4.3** UV-Vis spectrophotometric titration spectra for  $[(\text{Ru}(\text{flpy})_2(4,4'-(\text{OH})_2\text{bpy}))]^{2+}$  (top left),  $[\text{Ru}(\text{Cl-phen})_2(4\text{-OH-4'-OMebpy})]^{2+}$  (top right),  $[\text{Ru}(\text{dpab})_2(4,4'-(\text{OH})_2\text{bpy})]^{2+}$  (bottom left), and  $[\text{Ru}(\text{dtb})_2(4,4'-(\text{OH})_2\text{bpy})]^{2+}$  (bottom right).

the  $pK_a$  for the ruthenium complexes. For these studies, a solution with a known concentration of complex was used, and a base with a previously evaluated  $pK_a$  in acetonitrile was used as the titrant. The absorbance spectra for each complex titration are shown in figure 4.3. The titration is not shown for the complex  $[\text{Ru}(\text{bpy})_2(4,4'-(\text{OH})_2\text{bpy})]^{2+}$  because it was covered in Chapter 3 in the discussion of excited-state proton transfer. The  $pK_a$  and  $pK_a^*$  values are summarized in table 4.1. The linear plots from which the equilibrium constant for the acid-base reaction between each complex and the respective reference base are shown in figure 4.4.

Fortunately for the series of complexes, only  $[\text{Ru}(\text{bpy})_2(4,4'-(\text{OH})_2\text{bpy})]^{2+}$  showed involvement of the second acidic proton in the titration to determine the acid-base reaction equilibrium constant. There is an expected trend in acidity for the series. As the inductive withdrawing effect becomes stronger, the complex becomes more acidic. The  $\text{p}K_{\text{a}}$ 's are arranged as follows in order of most acidic to least acidic: flpy>dpab>Cl-phen>bpy>dtb.

In order to determine the excited-state acidity, a Förster thermodynamic cycle was used. For all but  $[\text{Ru}(\text{dtb})_2(4,4'-(\text{OH})_2\text{bpy})]^{2+}$  the deprotonated complex is not emissive in solution at room temperature.<sup>13</sup> Further work is being undertaken to establish why the dtb complex exhibits room temperature emission from the deprotonated complex in

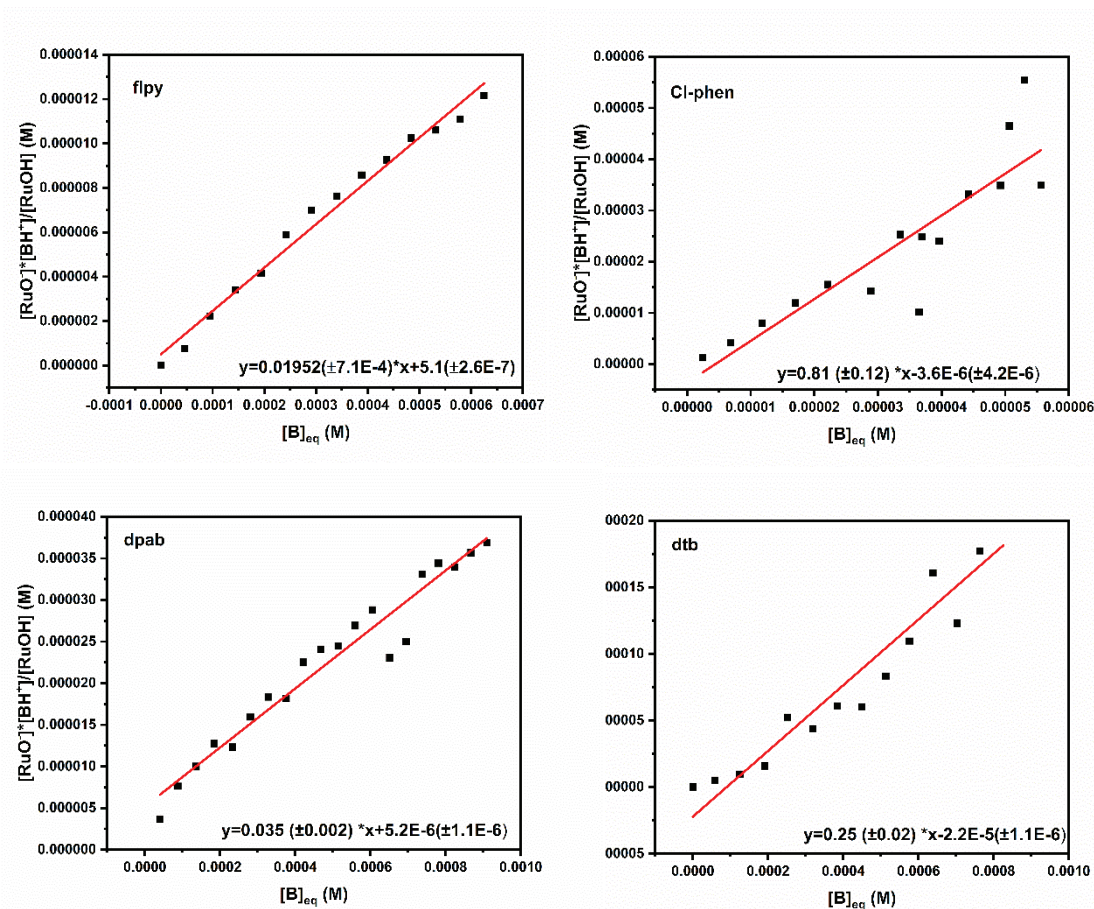


**Figure 4.4** Linear fit of  $[\text{RuO}^*][\text{BH}^+]/[\text{RuOH}]$  vs.  $[\text{B}]_{\text{eq}}$  to determine  $K_{\text{eq}}$  for acid-base reaction.

acetonitrile, but none of the other complexes in the series do. As such, low temperature emission measurements were used to calculate the excited state  $pK_a$ , as previously outlined in Chapter 3. The emission spectra of the protonated and deprotonated complexes are shown in figure 4.7. For all of the complexes, low temperature emission spectra were measured in acetonitrile solutions at a temperature slightly above the freezing point of acetonitrile ( $-42\text{ }^\circ\text{C}$ ). Deprotonation of the complexes was achieved by addition of one stoichiometric equivalent of tetrabutylammonium hydroxide. For the emission spectrum of the deprotonated flpy complex, the emission was very weak, despite using a high concentration of complex and increasing the integration time for collection. The spectrum

was treated using Origin Pro 2020 software's built in adjacent-averaging smoothing routine with 15 points averaged to help smooth the curve. The smoothing routine did not cause any change in the maximum of the emission spectrum but presents with significantly reduced noise.

When considering the reactions that can occur between the quat quenchers and the chromophores studied, the reaction of the Ru(III) complex with the reduced quat must be considered. To calculate the equilibrium constant, and thereby the free energy for this reaction, the  $pK_a$  of the Ru(III) was assessed. Using the Ru(III/II) reduction potentials for both the protonated and deprotonated complexes (see Chapter 2), a thermodynamic cycle can be used to determine the  $pK_a$  of the Ru(III) complexes. A schematic representation of the thermodynamic cycle used to make this calculation is shown in figure 4.5.<sup>4</sup>

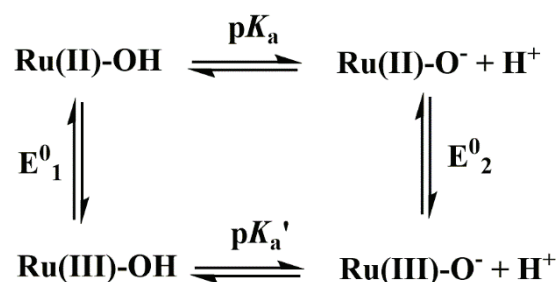


**Figure 4.5** Thermodynamic cycle for oxidation and deprotonation of ruthenium complexes. In this figure, the horizontal reactions are acid-base reactions, and the vertical reactions are redox reactions. Because the free energy for reaction is independent of the path of the reaction, the sum of the free energy for oxidation followed by deprotonation is equal to the free energy for deprotonation followed by oxidation. The  $pK'_a$ , or acidity of the Ru(III) complex, can thus be calculated with equation 4.1, where  $E^0_2$  is the Ru(III/II) potential of the deprotonated complex, or in the case of irreversible oxidation the cathodic peak potential,  $E^0_1$  is the Ru(III/II) potential for the protonated complex,  $R$  is the ideal gas

constant,  $T$  is temperature, and  $F$  is the Faraday constant. The calculated values for the  $pK_a'$  are also summarized in Table 4.1.

$$pK_a' = (2.303RTpK_a + FE_2^0 - FE_1^0)/2.303RT \quad (4.1)$$

As expected, oxidizing the complex makes it much more acidic. The rationale behind this increase in acidity is that upon oxidation to the Ru(III), the hydroxylated pyridine rings become strong pi-donors to offset the reduction in electron density on the metal, this results in an inductive effect that renders the hydroxy proton more acidic in the excited state than in the ground state. Figure 4.6 shows the relationship between the measured  $pK_a$  of the complexes in the ground state and the difference in energy between the oxidation and first reduction potentials as reported in Chapter 2. It is clear that as the difference in energy between the metal centered oxidation and ligand centered reduction increases, so to does the  $pK_a$ . The energy difference between the first reduction and metal centered oxidation correlates the energy of the metal-to-ligand charge transfer excited state. As inductive withdrawing by the ancillary ligands increases, the gap between the HOMO and LUMO likewise decreases. As the energy gap decreases, the  $pK_a$  lowers as the pi-donation from the hydroxylated pyridine rings becomes stronger, making the proton more acidic. This correlation between acid-base chemistry and redox chemistry is a well-known effect. In aqueous solution, reduction potentials decrease as a function of decreasing pH of

the solution when the pH is below the  $pK_a$  of the complex at a rate of 59 mV/pH unit for a single electron/proton transfer event.<sup>3</sup>

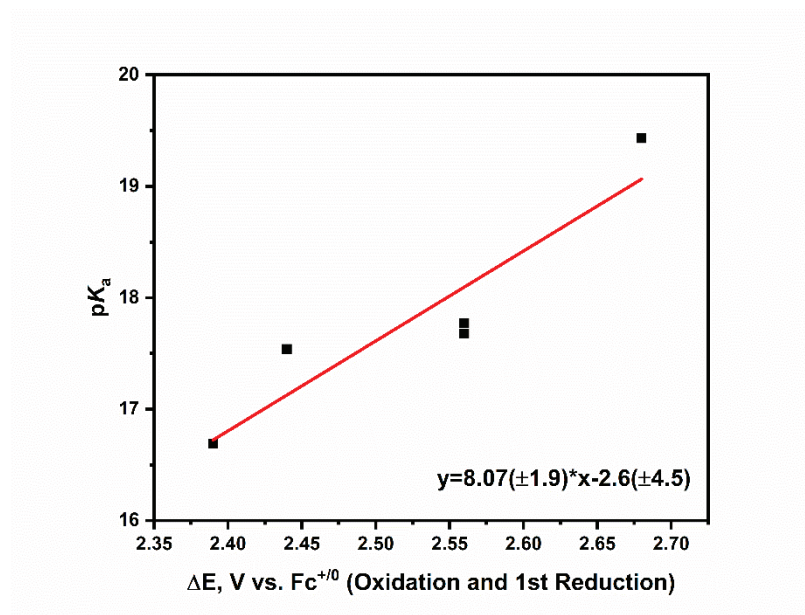


**Figure 4.6** Plot of the difference in energy between the first reduction and oxidation potentials of complexes vs.  $pK_a$

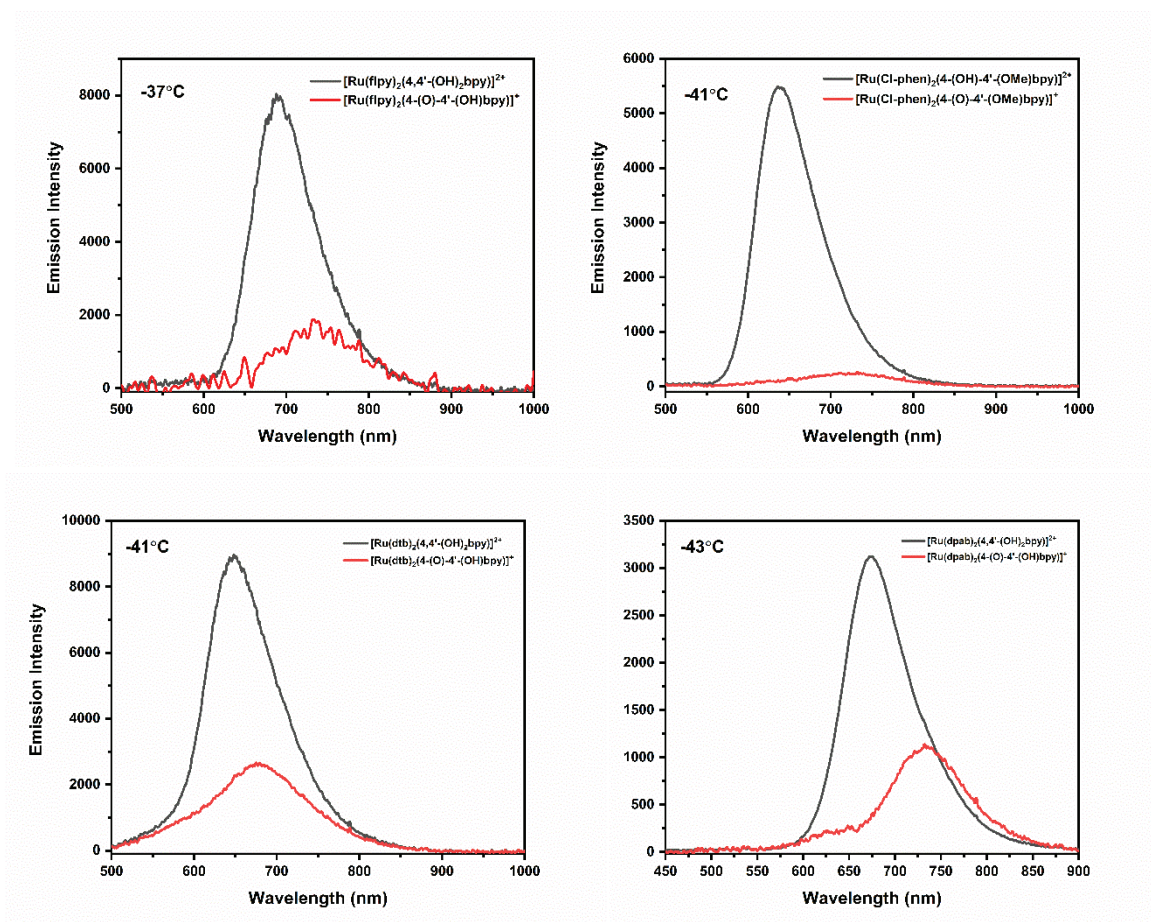


**Figure 4.7** Low temperature emission spectra of protonated and deprotonated ruthenium complexes in acetonitrile solution

**Table 4.1** Summary of  $pK_a$  for the ground state, excited state, and one-electron oxidized states. Reference compound  $pK_a$  values are from ref. 14.

	Reference Compound ( $pK_a$ ) <sup>14</sup>	$K_{eq}$	$pK_a$	$pK_a^*$	$pK_a'$
$[Ru(flpy)_2(4,4'-(OH)_2bpy)]^{2+}$	2,4,6-collidine (14.98)	0.0195 $\pm 7E-4$	16.7 $\pm$ 0.02	14.1	10.1
$[Ru(dpab)_2(4,4'-(OH)_2bpy)]^{2+}$	2-aminobenzimidazole (16.08)	0.035 $\pm 0.002$	17.5 $\pm$ 0.02	14.2	12.5
$[Ru(bpy)_2(4,4'-(OH)_2bpy)]^{2+}$	4-aminopyridine (17.63)	0.84 $\pm$ 0.04	17.710.02	15.2	7.7
$[Ru(Cl-phen)_2(4-(OH)-4'-(OMe)bpy)]^{2+}$	4-aminopyridine (17.63)	0.81 $\pm$ 0.12	17.7 $\pm$ 0.07	12.6	9.9
$[Ru(dtb)_2(4,4'-(OH)_2bpy)]^{2+}$	triethylamine (18.82)	0.25 $\pm 0.02$	19.4 $\pm$ 0.04	16.4	17.9

The excited-state redox potential were calculated using the relationship shown in figure 4.8. For the protonated complexes and control complexes, the values displayed for the emission energy were taken from room temperature emission spectra, while the values of the emission energy for the deprotonated complexes were taken from the low temperature emission spectra in acetonitrile that are shown in figure 4.7.

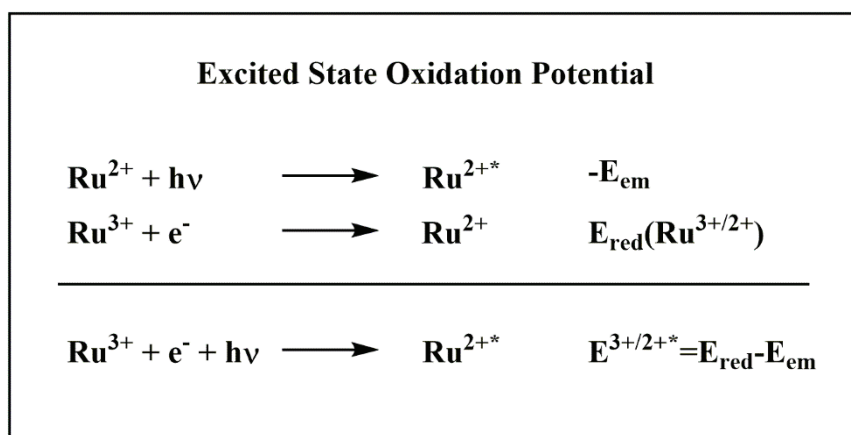


**Figure 4.8** Calculation of the excited state oxidation potential of ruthenium(II) complexes

**Table 4.2** Summary of redox potentials, excited state energies and excited state redox potentials

	$\text{Ru}^{\text{III/II}}$ ( $E_{1/2}$ ) (V vs. $\text{Fc}^{+/0}$ ) (-OH)	$\text{Ru}^{\text{III/II}}$ ( $E_{p,a}$ ) (V vs. $\text{Fc}^{+/0}$ ) (-O <sup>-</sup> )	$E_{\text{em}}$ (eV)	$E_{\text{em}}$ (eV) (-O <sup>-</sup> )	$\text{Ru}^{\text{III/II}^*}$ (V) (V vs. $\text{Fc}^{+/0}$ ) (-OH)	$\text{Ru}^{\text{III/II}^*}$ (V) (V vs. $\text{Fc}^{+/0}$ ) (-O <sup>-</sup> )
$[\text{Ru}(\text{bpy})_2(4,4'-(\text{OH})_2\text{bpy})]^{2+}$	0.85	0.26	1.93	1.82	-1.08	-1.56
$[\text{Ru}(\text{dpab})_2(4,4'-(\text{OH})_2\text{bpy})]^{2+}$	0.93	0.63	1.87	1.69	-0.94	-1.06
$[\text{Ru}(\text{flpy})_2(4,4'-(\text{OH})_2\text{bpy})]^{2+}$	1.05	0.66	1.83	1.68	-0.78	-1.02
$[\text{Ru}(\text{Cl-phen})_2(4-(\text{OH})-4'-(\text{OMe})\text{bpy})]^{2+}$	0.85	.38	1.97	1.71	-1.12	-1.33
$[\text{Ru}(\text{dtb})_2(4,4'-(\text{OH})_2\text{bpy})]^{2+}$	0.65	0.55	1.96	1.82	-1.31	-1.27
$[\text{Ru}(\text{bpy})_2(4,4'-(\text{OMe})_2\text{bpy})]^{2+}$	0.87		1.96		-1.09	
$[\text{Ru}(\text{dpab})_2(\text{bpy})]^{2+}$	1.02		1.95		-0.93	
$[\text{Ru}(\text{flpy})_2(\text{bpy})]^{2+}$	1.19		1.91		-0.72	
$[\text{Ru}(\text{Cl-phen})_2(\text{bpy})]^{2+}$	0.96		2.05		-1.09	
$[\text{Ru}(\text{dtb})_2(\text{bpy})]^{2+}$	0.79		1.99		-1.2	

Evaluation of the  $\text{pK}_a$ 's for the ground state, excited state, and one electron oxidized state of the chromophores in conjunction with the measured redox potentials for the complexes in both the protonated and deprotonated states along with the relevant  $\text{pK}_a$  and redox potentials of the bipyridinium quenchers allows for the computation of the free energy for the ET, PT, and PCET reactions in both the ground and excited state for the complexes. Table 4.2 summarizes the excited-state energies and redox potentials for each of the chromophores, including the control complexes used for mechanistic analysis.

### 4.3.2 Redox and Acid-Base Behavior of 4,4'-bipyridinium Quenchers

4,4'-bipyridinium salts have been used as oxidative quenchers in photochemical studies for decades. Perhaps the most well-known of such compounds is methyl viologen, or *N,N'*-dimethyl-4,4'-bipyridinium.<sup>14-17</sup> The compound has been known to effectively quench the excited state of ruthenium (II) diimine complexes through electron transfer. An advantage of using this compound as a quencher is that it does not absorb in the visible region, so there is no concern for co-absorption with the chromophore, but once it is reduced by one-electron, it exhibits strong absorbance in the 350-700 nm region of the spectrum and takes on a deep blue hue. This makes it ideal for quantifying the efficiency of charge separation from the geminate pair formed as a part of the overall excited state electron transfer process.

Mono-alkylated bipyridinium salts behave similarly to di-alkylated viologens when they are protonated at the tertiary nitrogen.<sup>1,18,19</sup> The advantage in using such a compound is that, before protonation, the reduction of these mono-quaternized bipyridines occurs at potentials up to 500 mV more negative than the protonated compound. This means that in order for reduction to occur, it must happen subsequent to or in concert with protonation, making these compounds of great utility for the analysis of proton-coupled electron transfer reactions.

In addition to the favorable redox and acid-base behavior of these compounds, they also exhibit unique absorbance for the protonated, reduced, and protonated/reduced states. This is of great advantage when using visible transient absorption to study reaction mechanisms, as the products of the photoreaction are easily discernable from one another for the ET, PT and PCET processes. *N*-methyl-4,4'-bipyridinium (MQ<sup>+</sup>) has been used in

previous studies of photoinduced proton-coupled electron transfer with transition metal complexes. In work by Wenger, the reactivity of the complex  $[\text{Ru}(\text{bpy})_2(\text{pyimH})]^{2+}$  (pyimH = 2-(20-pyridyl)imidazole) in the presence of  $\text{MQ}^+$  was evaluated in 1:1 water/acetonitrile solvent over the pH range of 3 to 10.<sup>18</sup> The unique absorbance features of the  $\text{MQ}^+$  quencher when it is reduced or reduced and protonated aided in the determination of the pH dependent reaction mechanism.

Two mono-quaternerized 4,4'-bipyridinium salts were used to study PCET reactivity of the hydroxylated ruthenium complexes, *N*-benzyl-4,4'-bipyridinium ( $\text{BMQ}^+$ ) and *N*-methyl-4,4'-bipyridinium ( $\text{MQ}^+$ ). Both compounds were prepared as outlined in Chapter 2 and were used as the  $\text{PF}_6$  salts for studies in acetonitrile.

The  $\text{pK}_a$  of each of these compounds was measured by  $^1\text{H}$  NMR analysis in the presence of trichloroacetic acid ( $\text{pK}_a=10.75$ ), as it contains no acidic protons in the aromatic region of the  $^1\text{H}$  NMR spectrum.<sup>21</sup> Figure 4.10 shows the  $^1\text{H}$  NMR spectra of the compounds in the presence of increasing concentration of  $\text{Cl}_3\text{CCOOH}$ . The equilibrium for this process is defined by the reactions in figure 4.9.

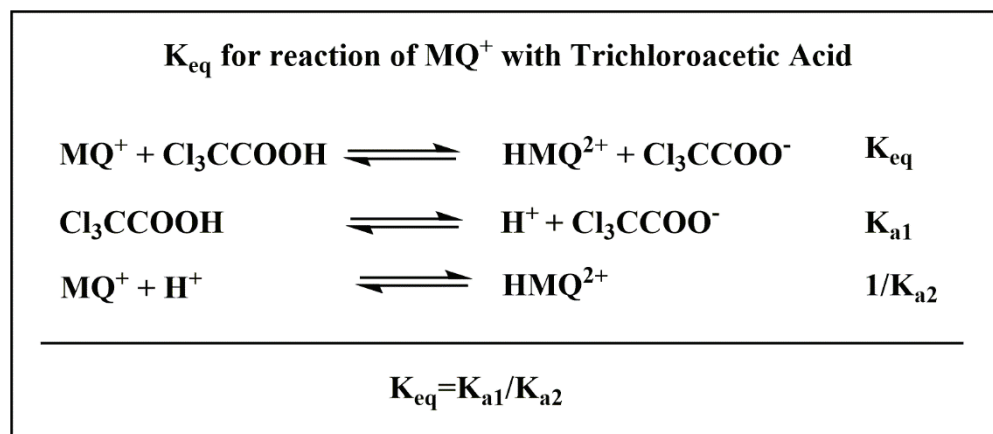


**Figure 4.9** Reactions for determining the  $\text{pK}_a$  of bipyridinium quenchers

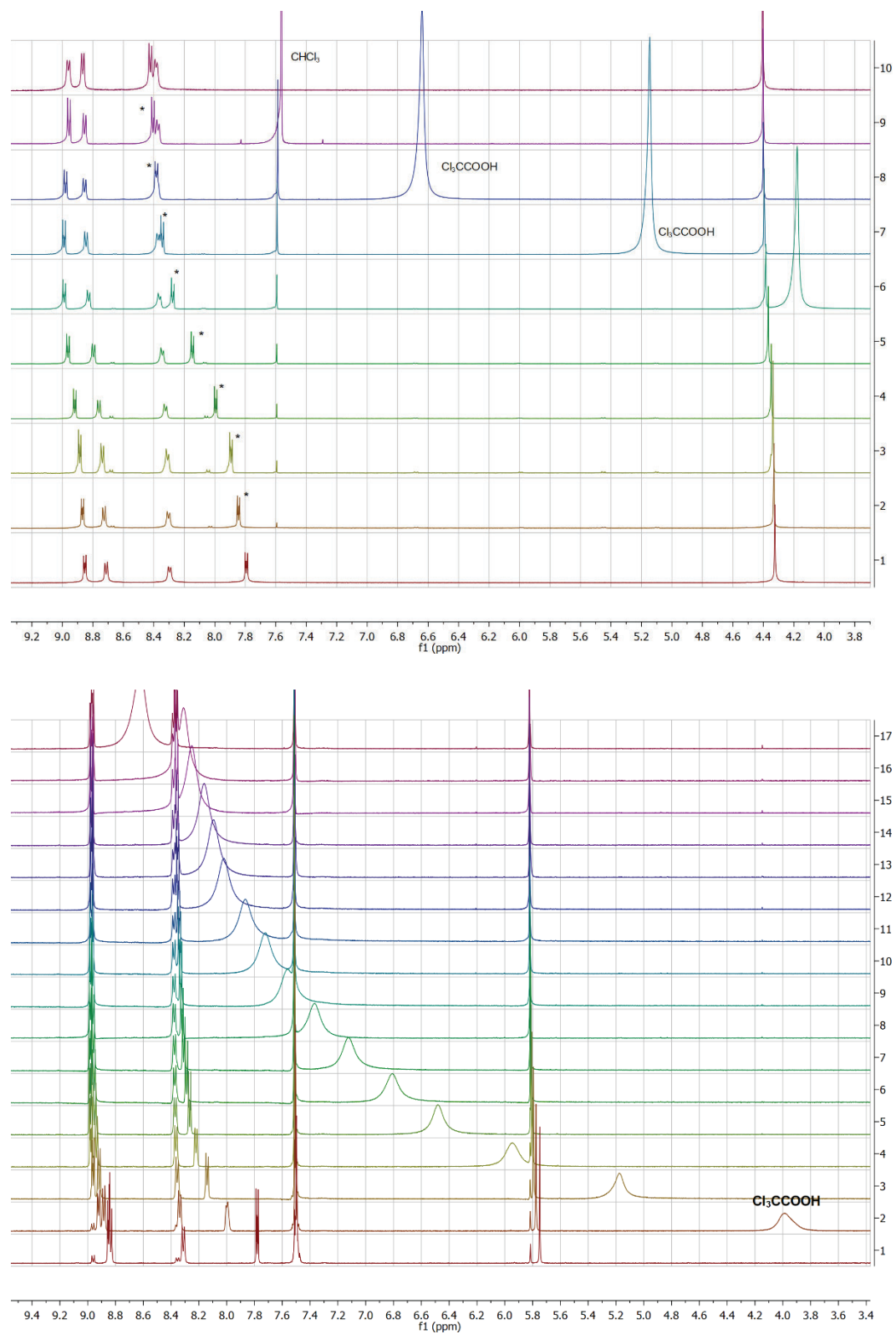


**Figure 4.10**  $^1\text{H}$  NMR spectra of  $\text{MQ}^+$  (top) and  $\text{BMQ}^+$  (bottom) with increasing concentration of  $\text{Cl}_3\text{CCOOH}$  going from bottom to top of spectra in  $\text{CD}_3\text{CN}$

The  $^1\text{H}$  NMR chemical shift change can be seen as a corresponding to the concentration of  $\text{HMQ}^{2+}$ . The relationship between the chemical shift and the concentration of  $\text{HMQ}^+$  is shown in equations 4.2 through 4.4 below. In this set of equations,  $x_{\text{HMQ}}$  is the mole fraction of  $\text{HMQ}^{2+}$ ,  $\delta_{\text{MQ}}$  is the chemical shift of  $\text{MQ}^+$  in the absence of acid,  $\delta_{\text{HMQ}}$  is the chemical shift of  $\text{HMQ}^{2+}$ , and  $\delta_{\text{obs}}$  is the observed chemical shift at any given concentration of added  $\text{Cl}_3\text{CCOOH}$ . Using this relationship, the equilibrium expression for the acid-base reaction between  $\text{MQ}^+$  and  $\text{Cl}_3\text{CCOOH}$  can be solved for the concentration of  $\text{HMQ}^{2+}$  and expression 4.4 can be substituted in for  $[\text{HMQ}^{2+}]$ , such that the expression is now in terms of the chemical shifts. This expression is shown in equation 4.5 and 4.6.

$$x_{\text{HMQ}} = [\text{HMQ}^{2+}]/[\text{MQ}^+]_0 \quad (4.2)$$

$$x_{\text{HMQ}} = \frac{|\delta_{\text{MQ}} - \delta_{\text{obs}}|}{|\delta_{\text{HMQ}} - \delta_{\text{MQ}}|} \quad (4.3)$$

$$[\text{HMQ}^{2+}] = [\text{MQ}^+]_0 \frac{|\delta_{\text{MQ}} - \delta_{\text{obs}}|}{|\delta_{\text{HMQ}} - \delta_{\text{MQ}}|} \quad (4.4)$$

$$\delta_{\text{obs}} = \delta_{\text{MQ}} + \frac{(|\delta_{\text{HMQ}} - \delta_{\text{MQ}}| * (K_{\text{eq}}([\text{Cl}_3\text{CCOOH}]_0 + [\text{MQ}^+]_0) + [\text{MQ}^+]_0) + b}{2(K_{\text{eq}} - 1)[\text{MQ}^+]_0} \quad (4.5)$$

$$b = \sqrt{(-K_{\text{eq}}([\text{Cl}_3\text{CCOOH}]_0 + [\text{MQ}^+]_0)^2 - 4(K_{\text{eq}} - 1)K_{\text{eq}}[\text{Cl}_3\text{CCOOH}]_0[\text{MQ}^+]_0)} \quad (4.6)$$

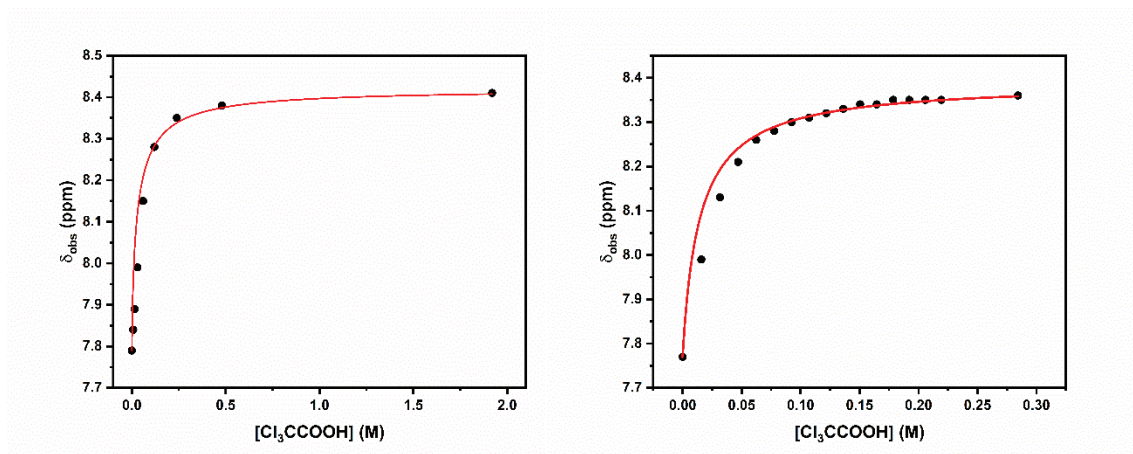


**Figure 4.11** Fit of  $^1\text{H}$  NMR titration data with  $\text{Cl}_3\text{CCOOH}$  to determine the  $\text{p}K_{\text{a}}$  of quenchers  $\text{MQ}^+$  (left) and  $\text{BMQ}^+$  (right)

Equations 4.5 and 4.6 were used to fit the data in the plot of  $[\text{Cl}_3\text{CCOOH}]$  vs.  $\delta_{\text{obs}}$ . The resulting data and fit are shown in figure 4.11. From the fit of the data, the  $\text{p}K_{\text{a}}$  can be calculated from  $K_{\text{eq}}$  (see figure 4.9).

In addition to establishing the  $\text{p}K_{\text{a}}$  of the quenchers, the  $\text{p}K_{\text{a}}$  of the reduced quencher is also a necessary value to obtain to calculate free energies for reaction. To do this, much like calculating the  $\text{p}K_{\text{a}}$  of the  $\text{Ru}(\text{III})$  complexes above, a thermodynamic cycle can be used. This cycle is shown in figure 4.14. In order to make this calculation, the redox potential for both the protonated and deprotonated quenchers must be analyzed. Cyclic voltammetry was used to measure the reduction potential of  $\text{MQ}^+$  and  $\text{BMQ}^+$  in the absence and presence of a strong acid, trifluoromethylsulfonic (triflic) acid. The samples were prepared with an excess (2 mM) of triflic acid present, and the solutions were degassed with argon to prevent reduction of dissolved oxygen. The cyclic voltammograms are shown in figures 4.12 and 4.13.

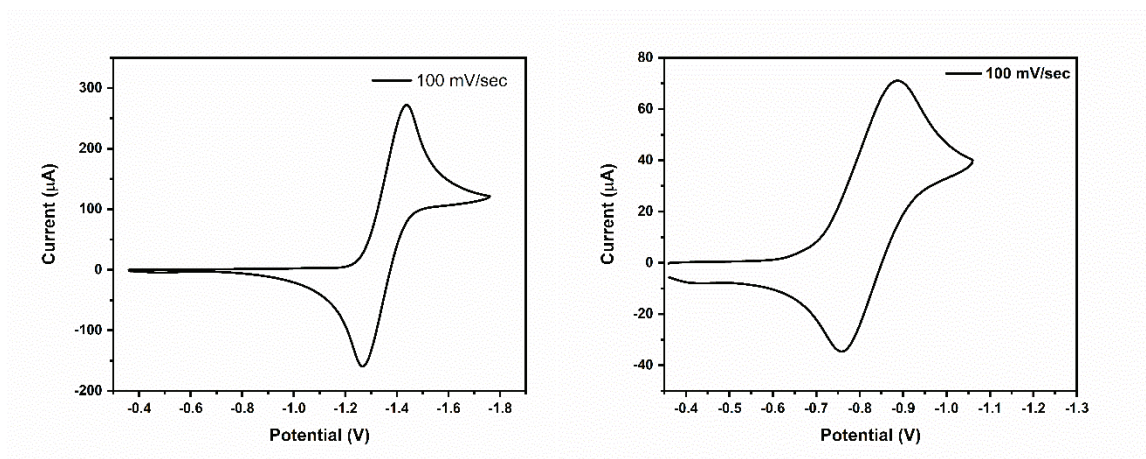


**Figure 4.12** Cathodic voltammograms of  $\text{MQ}^+$  (left) and  $\text{HMQ}^{2+}$  (right) vs.  $\text{Fc}^{+/0}$

From the voltammograms, it is clear that upon protonation, the reduction of  $\text{MQ}^+$  shifts 530 mV more positive, making it easier to reduce by over half of a volt. The same can be observed for  $\text{BMQ}^+$ , with change in the reduction potential of 490 mV upon protonation. A summary of the redox potentials and  $\text{p}K_a$  values can be found in Table 4.3.

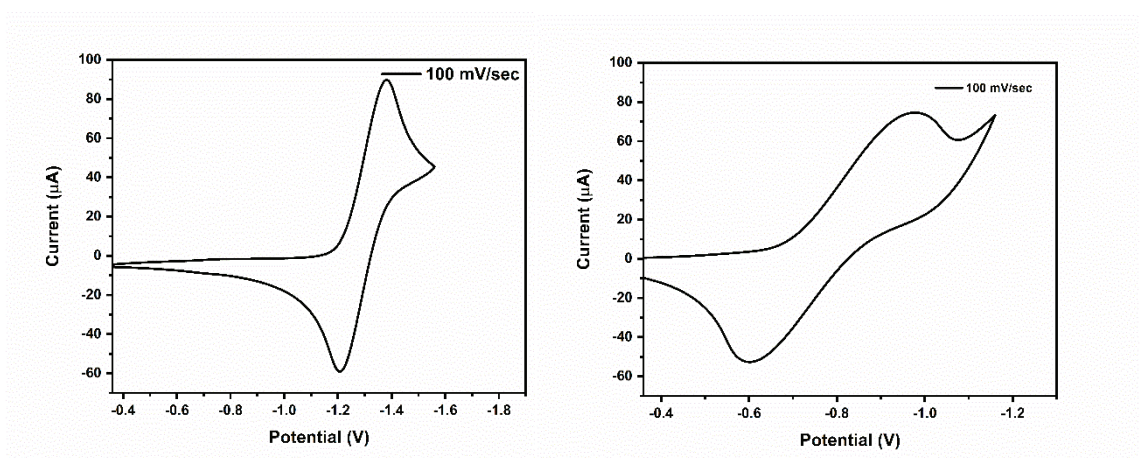


**Figure 4.13** Cathodic voltammograms of  $\text{BMQ}^+$  (left) and  $\text{HBMQ}^{2+}$  (right) vs.  $\text{Fc}^{+/0}$

Combining the electrochemical potentials with the acid dissociation constants, it is possible to calculate the  $\text{p}K_a$  of the reduced, protonated quenchers. The thermodynamic cycle relating these values is shown in figure 4.14.

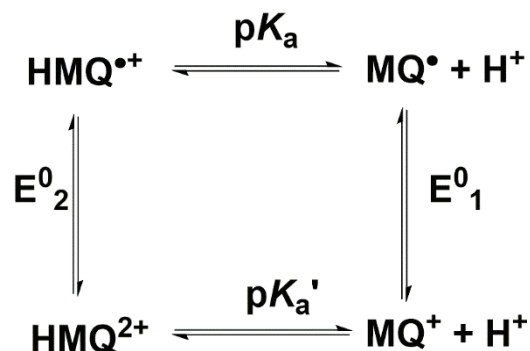


**Figure 4.14** Cathodic voltammograms of  $\text{BMQ}^+$  (left) and  $\text{HBMQ}^{2+}$  (right) vs.  $\text{Fc}^{+/0}$

Overall, the analysis of the redox potentials and  $\text{p}K_a$ 's of these quenchers revealed that upon protonation, the reduction potential for both  $\text{BMQ}^+$  and  $\text{MQ}^+$  shifted to nearly 500 mV more positive. In addition, upon reduction of  $\text{BMQ}^+$  and  $\text{MQ}^+$ , the conjugate acid became nearly 9 orders of magnitude more basic! These observed changes in the  $\text{p}K_a$  coupled to changes in redox potential help to highlight the thermodynamic advantage of coupling proton transfer with redox chemistry.

**Table 4.3** Summary of redox potentials and  $\text{p}K_a$ 's of quenchers

	$E_1^0$ (V. vs. $\text{Fc}^{+/0}$ )	$E_2^0$ (V. vs. $\text{Fc}^{+/0}$ )	$\text{p}K_a$	$\text{p}K_a'$
<i>N</i> -methyl-4,4'-bipyridinium	-1.35	-0.82	$10.3 \pm 0.1$	$19.2 \pm 0.2$
<i>N</i> -benzyl-4,4'-bipyridinium	-1.27	-0.78	$10.87 \pm 0.02$	$19.1 \pm 0.2$

### 4.3.3 Thermochemical Analysis of ESPT, ESET, and ESPCET Reactions

In analysis of reactions with multiple competitive reaction pathways, understanding the thermodynamic landscape prior to embarking on mechanistic studies is useful in guiding the analysis of reaction dynamics. Although the values presented are neglectful of activation barriers, they remain informative as to the reaction dynamics and for comparison

of reactivity of different chromophores with the same quencher. Many papers and review articles exist on the importance of establishing the thermochemical values for PT, ET, and PCET reactions.<sup>3,4,20</sup> An elegant example of the implementation of thermochemical analysis which informed the mechanistic assignment of the photoinduced reaction is the reaction between the triplet state of acridine orange (<sup>3</sup>AO) and tri-*tert*-butylphenol (<sup>ttb</sup>PhOH).<sup>21</sup> This work from the Dempsey group shows the value of understanding the thermochemical terrain for all possible reactions between <sup>3</sup>AO and <sup>ttb</sup>PhOH. Here, Eisenhart and Dempsey were able to conclude that the excited-state of <sup>3</sup>AO was able to react via a concerted electron-proton transfer pathway with <sup>ttb</sup>PhOH based upon both transient absorption studies and thermochemical analysis.

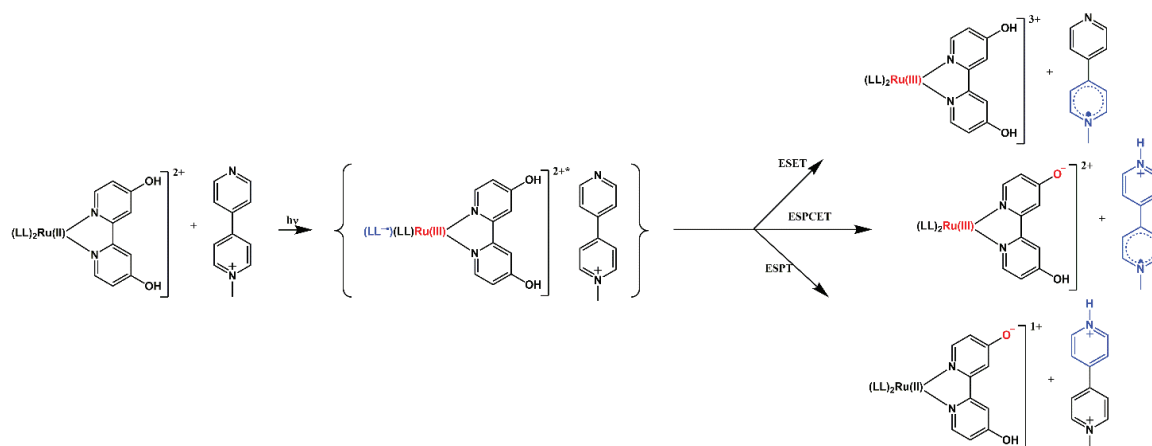


**Figure 4.15** Possible reactions between  $[\text{Ru}(\text{LL})_2(4,4'-(\text{OH})_2\text{bpy})]^{2+*}$  and  $\text{MQ}^+$

For the excited state reactions explored here, there are three possibilities, either electron transfer, proton transfer, or proton-coupled electron transfer. Figure 4.15 shows a generalized reaction between a ruthenium complex with a hydroxylated bipyridine ligand and  $\text{MQ}^+$ . For each case, the products that emerge from the cage will have different respective charges, which are pertinent to the discussion below.

For each complex reported here, the relevant free energies for ground and excited state PT, ET, and PCET were calculated using the previously established  $pK_a$ 's and redox potentials of each complex and the respective quenchers. Table 4.4 and 4.5 provide a summary of the calculated free energies for each reaction.

For calculating the free energy for proton transfer, the calculation is made by taking the difference in  $pK_a$  value between the chromophore and the base, this gives the equilibrium constant for the proton transfer reaction, which can then be used to calculate the Gibbs free energy for proton transfer. This can be done for the ground state, excited state, and the one-electron oxidized state of the chromophore. For the proton transfer reaction, the work term for bringing the two charged species will be zero. Equations 4.7-4.9 show the calculation of the free energy for proton transfer including the reactant and product work terms. In these equations,  $R$  is the ideal gas constant,  $T$  is the temperature,  $\Delta pK_a$  is the difference in  $pK_a$  between the chromophore in quencher,  $N_A$  is Avogadro's number,  $W_P$  is the work terms for product separation,  $W_R$  is the work term for bringing together the reactants,  $\epsilon_0$  is the permittivity of vacuum constant,  $a$  is the distance between the two species,  $z$  is the charge on each compound, and  $e$  is the elementary charge.<sup>22</sup>

$$\Delta G_{PT} = -2.303RT \ln(\Delta pK_a) + N_A(W_P - W_R) \quad (4.7)$$

$$W_P = \frac{z(A^-)z(BH^+)e^2}{4\pi\epsilon_0\epsilon_R a} \quad (4.8)$$

$$W_R = \frac{z(AH)z(B)e^2}{4\pi\epsilon_0\epsilon_R a} \quad (4.9)$$

Because the reactants will go from a 2+/1+ combination to products with a 1+/2+ charge combination for the pure proton transfer in either the ground or excited state, the

work term will end up being zero. For proton transfer following electron transfer, the work term cannot be omitted, as  $W_p$  will be nonzero, while  $W_r$  will be zero, assuming the separation distance remains constant. The same equations for work can be applied to the electron transfer reaction and proton coupled electron transfer reactions, as will be discussed further below.

The free energy for the electron transfer can likewise be calculated using the redox potentials for the complexes and the quenchers.  $\Delta G_{ET}$  can be calculated for the ground state and excited state electron transfer reactions using equation 4.10. This again includes the work term for bringing the charged species together along with the work required for charge separation. The pair will go from 2+/1+ for the charge combinations to 3+/0 following electron transfer. The distance between the complex and the quencher has been estimated using a value of 6 Å for the ruthenium complex (ref) based on  $[\text{Ru}(\text{bpy})_3]^{2+}$  and the collision radius for the molecular mechanics optimized structure of the quenchers. From gas phase molecular mechanics calculations, the collision radii of  $\text{MQ}^+$  and  $\text{BMQ}^+$  were found to be 3.5 Å and 4.5 Å, respectively. In equation 4.10,  $F$  is the Faraday constant,  $n$  is the number of electrons being transfer, and  $E(\text{Ru}^{\text{III/II}})$  and  $E(\text{MQ}^{+/0})$  are the reduction potentials for the ruthenium(III) complex and bipyridinium quencher.<sup>23</sup>

$$\Delta G_{ET} = -nF(E(\text{Ru}^{\text{III/II}}) - E(\text{MQ}^{+/0})) + N_A(W_P - W_R) \quad (4.10)$$

For calculation of the free energy for excited state electron transfer, the oxidation potential of the excited state of the ruthenium complex is substituted in for  $E(\text{Ru}^{\text{III/II}})$ . The values for the free energy of reaction for ESET are listed in Table 4.5.

For calculation of the free energy for proton-coupled electron transfer, two methods can be used, and should yield the same result within a margin of error attributable to the error associated with individual experimental values. The first method involves taking the sum of the free energy for ESPT, followed by ESET from the deprotonated complex to the protonated quencher. The second method is using the sum of free energies for ESET and ground state proton transfer from the Ru(III) to the reduced quencher. The reason for this is that excited state electron transfer deactivates the excited state, such that any proton transfer subsequently should occur from the ground state potential surface. Again, these values are summarized in Table 4.5.

**Table 4.4** Calculated Gibbs free energy for ground state reactions given in kcal/mol

	MQ <sup>+</sup>			BMQ <sup>+</sup>		
	$\Delta G_{ET}$	$\Delta G_{PT}$	$\Delta G_{PCET}$	$\Delta G_{ET}$	$\Delta G_{PT}$	$\Delta G_{PCET}$
$[Ru(bpy)_2(4,4'-(OH)_2bpy)]^{2+}$	52.6	12.0	35.0	50.8	11.4	33.3
$[Ru(dpab)_2(4,4'-(OH)_2bpy)]^{2+}$	54.5	11.8	43.4	52.6	11.2	41.7
$[Ru(flpy)_2(4,4'-(OH)_2bpy)]^{2+}$	57.3	10.7	42.9	55.4	10.0	41.2
$[Ru(Cl-phen)_2(4-(OH)-4'-(OMe)bpy)]^{2+}$	52.6	12.1	37.9	50.8	11.5	36.2
$[Ru(dtb)_2(4,4'-(OH)_2bpy)]^{2+}$	48.0	16.9	44.8	46.2	16.3	43.1
$[Ru(bpy)_2(4,4'-(OMe)_2bpy)]^{2+}$	53.1			51.2		
$[Ru(dpab)_2(bpy)]^{2+}$	56.6			54.7		
$[Ru(flpy)_2(bpy)]^{2+}$	60.5			58.6		
$[Ru(Cl-phen)_2(bpy)]^{2+}$	55.2			53.3		
$[Ru(dtb)_2(bpy)]^{2+}$	51.2			49.4		

**Table 4.5** Calculated Gibbs free energy for excited state reactions given in kcal/mol

	MQ <sup>+</sup>			BMQ <sup>+</sup>		
	$\Delta G_{ET}^*$	$\Delta G_{PT}^*$	$\Delta G_{PCET}^*$	$\Delta G_{ET}^*$	$\Delta G_{PT}^*$	$\Delta G_{PCET}^*$
$[Ru(bpy)_2(4,4'-(OH)_2bpy)]^{2+}$	8.14	6.85	-10.2	6.29	6.07	-10.0
$[Ru(dpab)_2(4,4'-(OH)_2bpy)]^{2+}$	11.4	5.34	-0.191	9.52	4.56	0.0153
$[Ru(flpy)_2(4,4'-(OH)_2bpy)]^{2+}$	15.1	5.21	0.594	13.2	4.43	0.801
$[Ru(Cl-phen)_2(4-(OH)-4'-(OMe)bpy)]^{2+}$	7.21	3.15	-8.6	5.37	2.37	-8.40
$[Ru(dtb)_2(4,4'-(OH)_2bpy)]^{2+}$	2.83	8.36	-2.02	0.988	7.58	-1.81
$[Ru(bpy)_2(4,4'-(OMe)_2bpy)]^{2+}$	7.91			6.06		
$[Ru(dpab)_2(bpy)]^{2+}$	11.6			9.75		
$[Ru(flpy)_2(bpy)]^{2+}$	16.4			14.6		
$[Ru(Cl-phen)_2(bpy)]^{2+}$	7.91			6.06		
$[Ru(dtb)_2(bpy)]^{2+}$	5.37			3.52		

Taking this into account, the free energy diagram in figure 4.16 shows the relative free energy of reaction for ESET, ESPT, and ESPCET for each of the complexes studied. This comparison between the free energies of the different reactions will serve to inform

the mechanistic analysis in the subsequent section. Upon initial inspection, one might expect that the system most amenable to ESPCET would be  $[\text{Ru}(\text{bpy})_2(4,4'-(\text{OH})_2\text{bpy})]^{2+}$  with either of the quenchers, but a thermochemical analysis provides only a limited depiction of the reaction, and neglects the additional features that may impact the observed reaction mechanism, including the interaction distance between the chromophore and quencher as well as the activation free energy for reaction, which could vary depending on the nature of the spectator ligands. Thus, further investigation of these reactions will be needed to make any determination of reaction mechanism.

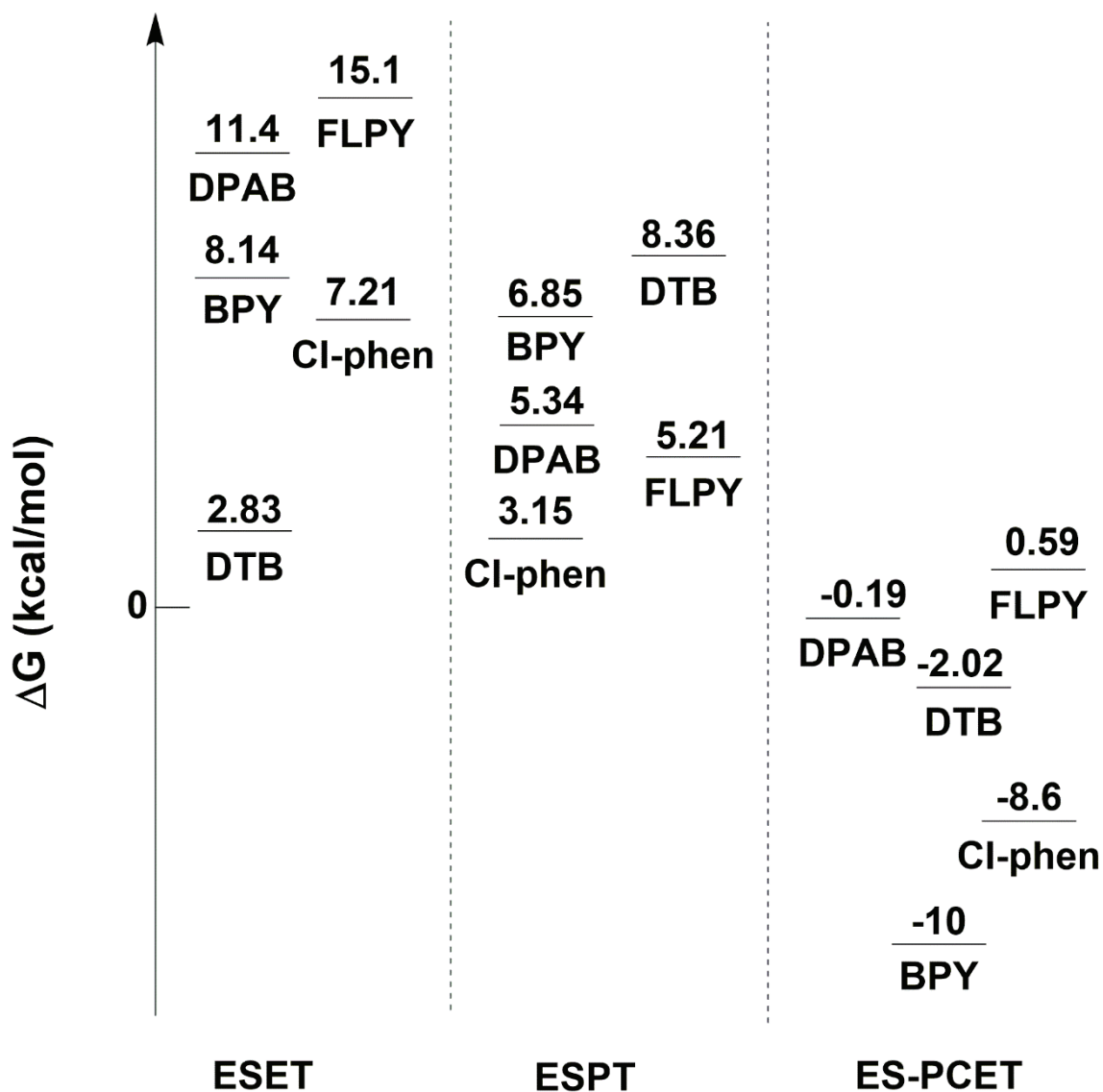


**Figure 4.16** Free energies of reaction for each complex, for ESET, ESPT, and ESPCET with  $\text{MQ}^+$

#### 4.3.4 Simulation of ET, PT, and PCET Product Spectra

In order to evaluate the reactivity between the bipyridinium quenchers and ruthenium chromophores, nanosecond transient absorption was used to assess the reaction dynamics. Interpretation of transient absorption spectra requires knowledge of the absorption features of anticipated reaction products. Because nanosecond transient

absorption is on a timescale longer than the lifetime of the encounter complex, what is observed in the spectrum will be the spectral signatures of the cage escape products.

Simulation of the cage escape products for ESET, ESPT, and ESPCET can be done using a variety of experimental techniques. For excited-state proton transfer, the expected products can be simulated by knowing that the protonated quencher does not have absorption in the visible region being probed in the TA experiment. The absorbance spectra for  $\text{MQ}^+$ /  $\text{HMQ}^{2+}$  and  $\text{BMQ}^+$ / $\text{BMQ}^{2+}$  are shown in figure 4.17. Knowing that  $\text{HMQ}^{2+}$  and  $\text{BMQ}^{2+}$  do not absorb in the range of the TA experiment, it is reasonable to state that any observed absorbance will come from the deprotonated ruthenium complex. Because transient absorption spectra are difference absorption spectra (discussed in

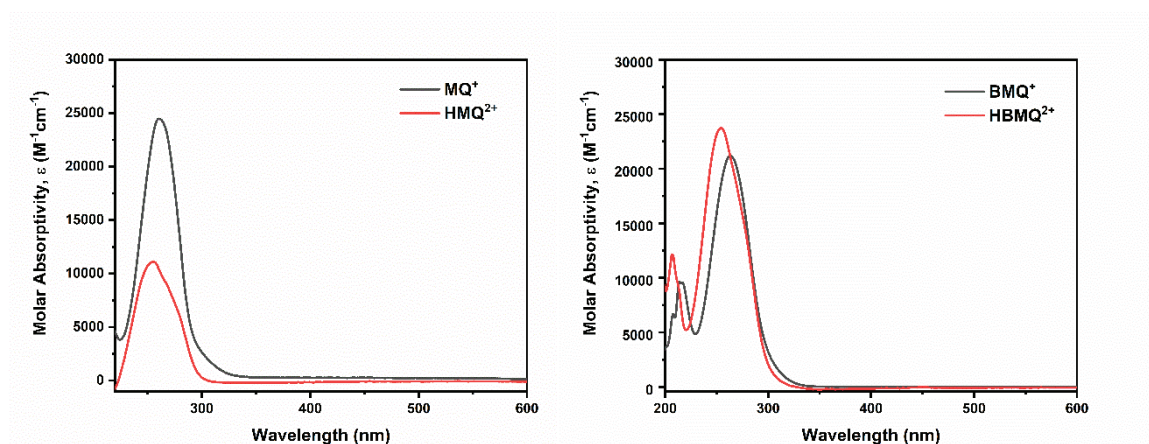


**Figure 4.17** Absorption spectra of  $\text{MQ}^+$ ,  $\text{HMQ}^{2+}$ ,  $\text{BMQ}^+$ , and  $\text{HBMQ}^{2+}$  in acetonitrile

further detail subsequently), taking the difference between the spectrum of the deprotonated complex and protonated complex, yields the expected spectrum of the ESPT products. Figure 4.18 shows the generated ESPT product spectra for each complex. Note, because ruthenium is the only absorbing species, the product spectra are the same for reaction with either  $\text{BMQ}^+$  or  $\text{MQ}^+$ . In the spectra shown in figure 4.18, there are three

main absorbance features for the simulated difference absorption spectra which include a positive absorbance between 350-400 nm, the bleach of the ground state between 400-500 nm, and a positive absorbance between 500-600 nm. Table 4.6 tabulates the values for the two positive ( $\lambda_{1PT}$  and  $\lambda_{2PT}$ ) absorbance features for each complex and their respective molar extinction coefficients.

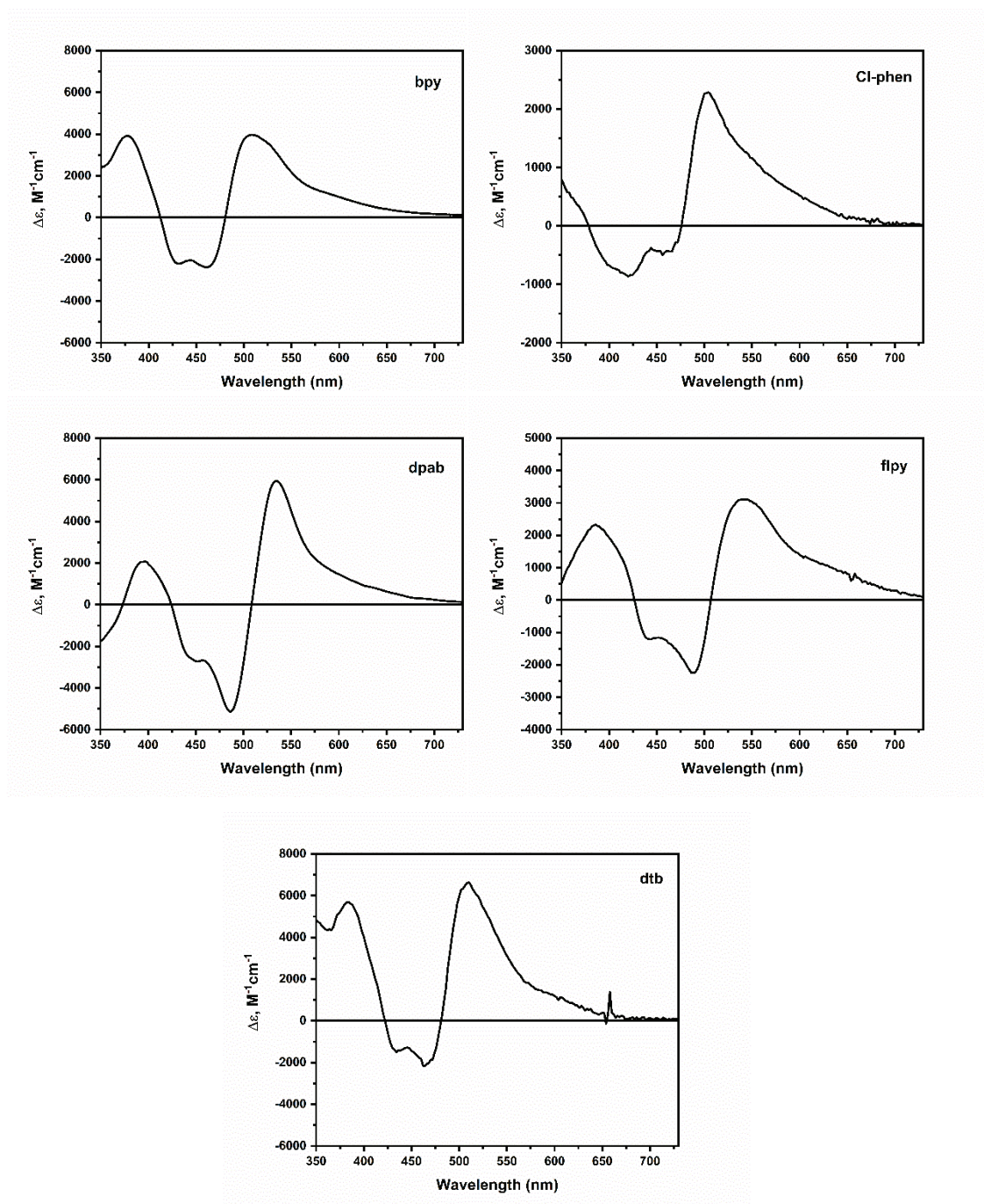


**Figure 4.18** Simulated spectra for ESPT for ruthenium complexes in acetonitrile

**Table 4.6** Summary of absorbance features for simulated ESPT products

	$\lambda_{1PT}$ , nm ( $\epsilon$ , $M^{-1}cm^{-1}$ )	$\lambda_{2PT}$ , nm ( $\epsilon$ , $M^{-1}cm^{-1}$ )
$[Ru(bpy)_2(4,4'-(OH)_2bpy)]^{2+}$	377 (3900)	508 (3970)
$[Ru(dpab)_2(4,4'-(OH)_2bpy)]^{2+}$	395 (2100)	535 (5900)
$[Ru(flpy)_2(4,4'-(OH)_2bpy)]^{2+}$	386 (2300)	542 (3100)
$[Ru(Cl-phen)_2(4-(OH)-4'-(OMe)bpy)]^{2+}$	350 (730)	502 (2270)
$[Ru(dtb)_2(4,4'-(OH)_2bpy)]^{2+}$	384 (5700)	508 (6600)

Spectroelectrochemistry is a technique that has wide versatility. The technique involves coupling electrochemical methods with spectroscopy. It has been applied to a variety of spectroscopic techniques, including infrared spectroscopy and UV-Visible spectroscopy. For our studies, UV-Visible spectroelectrochemistry was used to simulate the product spectra for excited state electron transfer between the quenchers  $BMQ^+$  and  $MQ^+$  and the ruthenium complexes.

First, reductive spectroelectrochemistry is used to generate the spectrum of the reduced quencher. Knowing the concentration of the solution allows for determination of the molar extinction coefficient of each absorbance feature in the spectrum. Spectroelectrochemistry is also used to generate the spectrum of the one-electron oxidized ruthenium complex. Taking the sum of the spectra of the reduced quencher and oxidized ruthenium complex less the spectrum of the ruthenium (II) spectrum yields the expected absorbance spectrum of the electron transfer products. The ESET product spectra for both the hydroxy-bipyridine complexes and the control complexes reacting with  $MQ^+$  and

BMQ<sup>+</sup> are shown in figures 4.19-4.22. For both the control complexes and hydroxylated complexes, the simulated ESET product spectra show three absorbance features similar to that of the ESPT products, with positive absorption between 350-400 nm, ground state bleaching between 400-500 nm, and positive absorption between 500-600 nm. The absorption feature between 500-600 nm is due to the reduced bipyridinium quencher, as such the maximum is roughly the same despite the nature of the complex. Table 4.7 provides a summary of the absorbance features for both the control and hydroxylated complexes with  $\lambda_{1ET}$  and  $\lambda_{2ET}$  indicating the two positive absorption features.

The difference in absorption features between the ESET and ESPT products is subtle, however the magnitude of the respective positive absorbance features in the ESET and ESPT spectra help to distinguish the cage escape products. For ESET, the first positive absorption between 350-400 nm has two-fold greater absorption than the peak between 500-600 nm. With ESPT, the two peaks between 350-400 nm and 500-600 nm have approximately equivalent extinction coefficients.

**Table 4.7** Summary of absorbance features for simulated ESET products

	MQ <sup>+</sup>		BMQ <sup>+</sup>	
	$\lambda_{1ET}, \text{nm} (\epsilon, \text{M}^{-1}\text{cm}^{-1})$	$\lambda_{2ET}, \text{nm} (\epsilon, \text{M}^{-1}\text{cm}^{-1})$	$\lambda_{1ET}, \text{nm} (\epsilon, \text{M}^{-1}\text{cm}^{-1})$	$\lambda_{2ET}, \text{nm} (\epsilon, \text{M}^{-1}\text{cm}^{-1})$
$[Ru(bpy)_2(4,4'-(OH)_2bpy)]^{2+}$	365 (25,500)	532 (12,000)	368 (15,000)	534 (7200)
$[Ru(dpab)_2(4,4'-(OH)_2bpy)]^{2+}$	366 (14,600)	542 (8500)	350 (6600)	548 (4700)
$[Ru(flpy)_2(4,4'-(OH)_2bpy)]^{2+}$	367 (23,000)	537 (11,800)	373 (13,000)	542 (7200)
$[Ru(Cl-phen)_2(4-(OH)-4'-(OMe)bpy)]^{2+}$	366 (31,300)	537 (12,500)	366 (20,600)	542 (7920)
$[Ru(dtb)_2(4,4'-(OH)_2bpy)]^{2+}$	367 (20,800)	538 (9800)	372 (10,000)	542 (5300)
$[Ru(bpy)_2(4,4'-(OMe)_2bpy)]^{2+}$	367 (22,300)	537 (12,100)	372 (12,100)	538 (7400)
$[Ru(dpab)_2(bpy)]^{2+}$	367 (24,900)	537 (11,500)	372 (14,500)	542 (6900)
$[Ru(flpy)_2(bpy)]^{2+}$	368 (21,600)	536 (9700)	372 (11,500)	540 (5100)
$[Ru(Cl-phen)_2(bpy)]^{2+}$	367 (26,800)	537 (10,500)	367 (16,000)	541 (5800)
$[Ru(dtb)_2(bpy)]^{2+}$	368 (21,600)	536 (9900)	372 (11,600)	540 (5300)

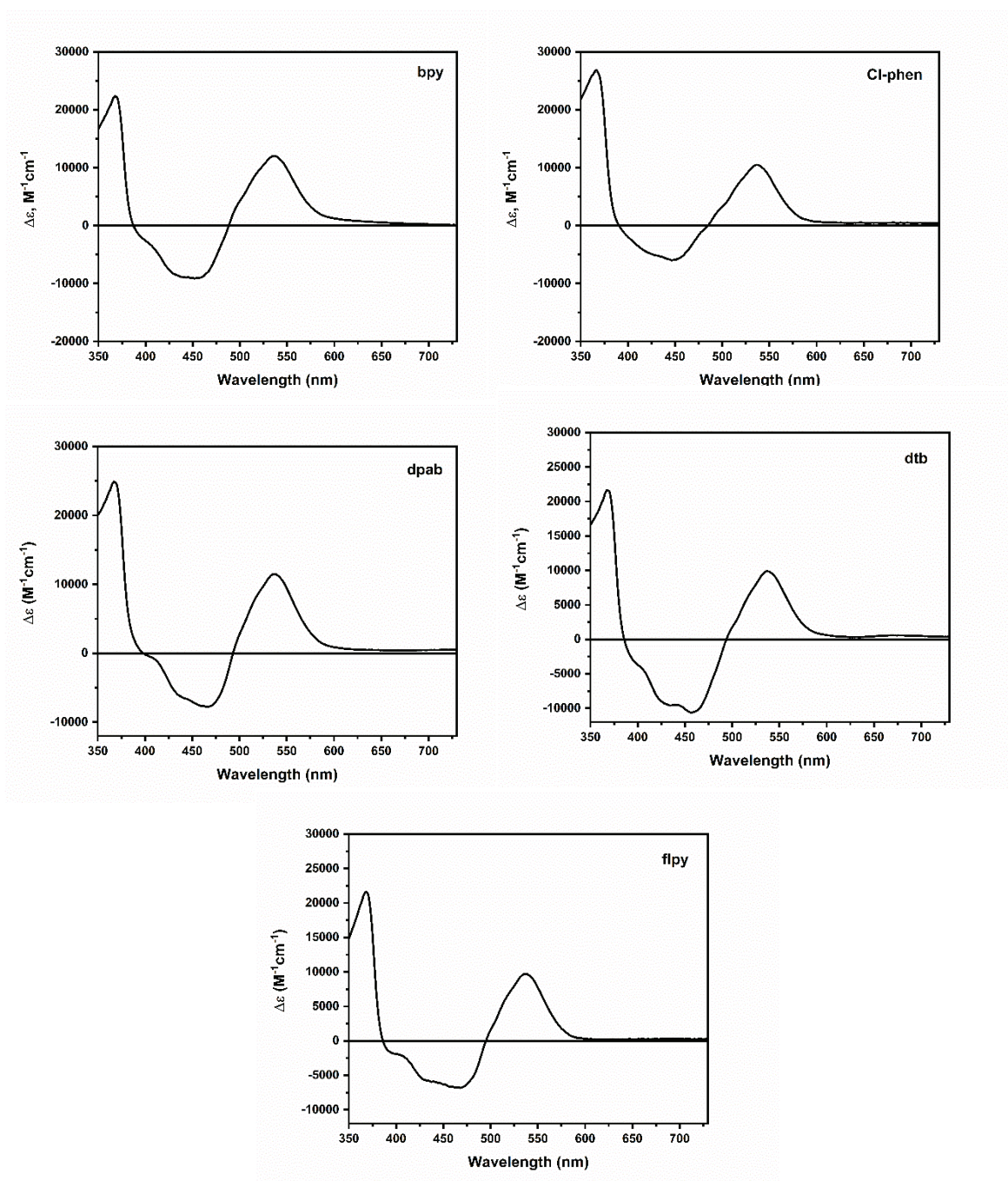


**Figure 4.19** Simulated spectra for ESET products for control complexes and their reaction with  $MQ^+$

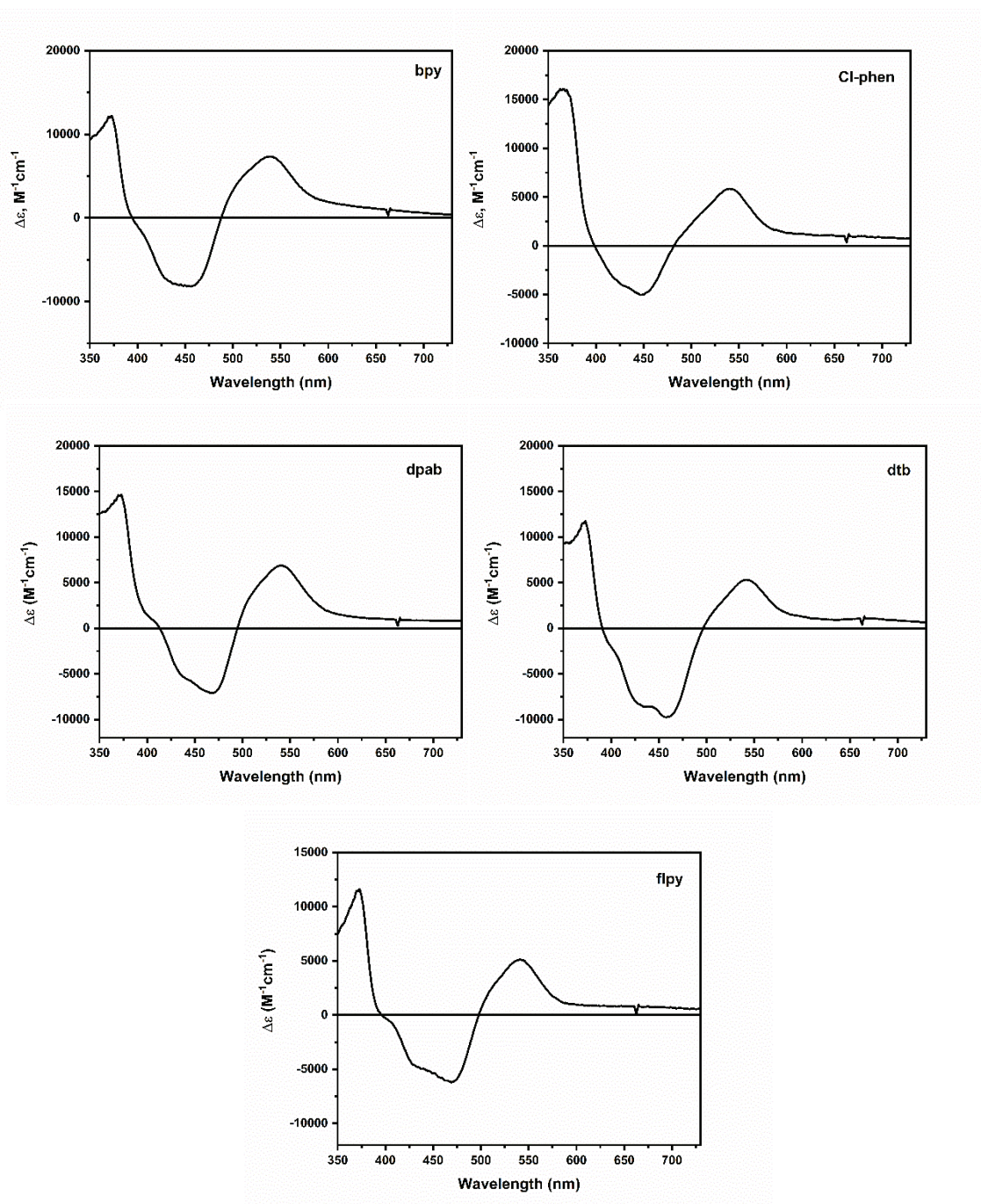


**Figure 4.20** Simulated spectra for ESET products for control complexes and their reaction with  $BMQ^+$

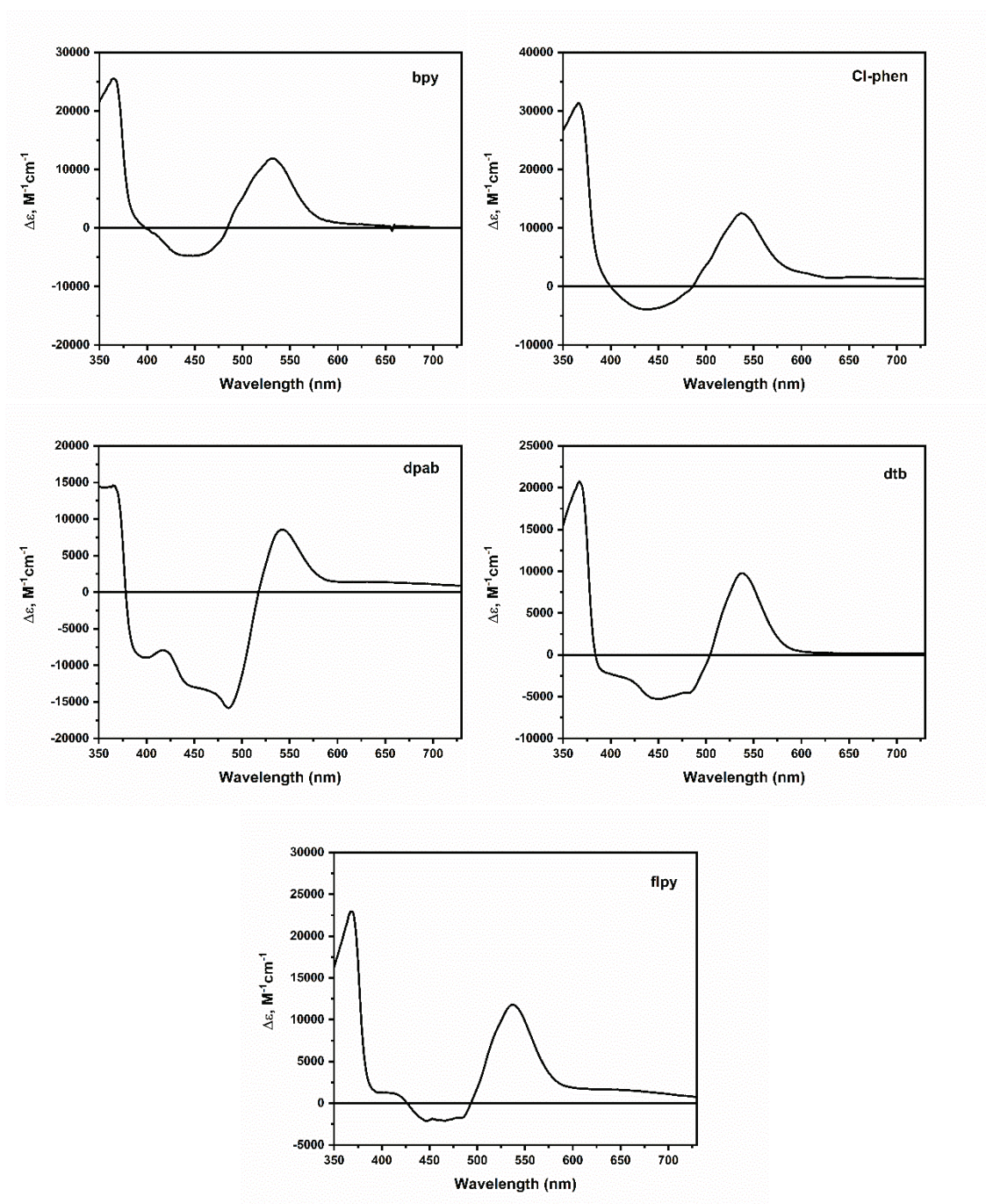


**Figure 4.21** Simulated spectra for ESET products for hydroxylated complexes and their reaction with  $MQ^+$

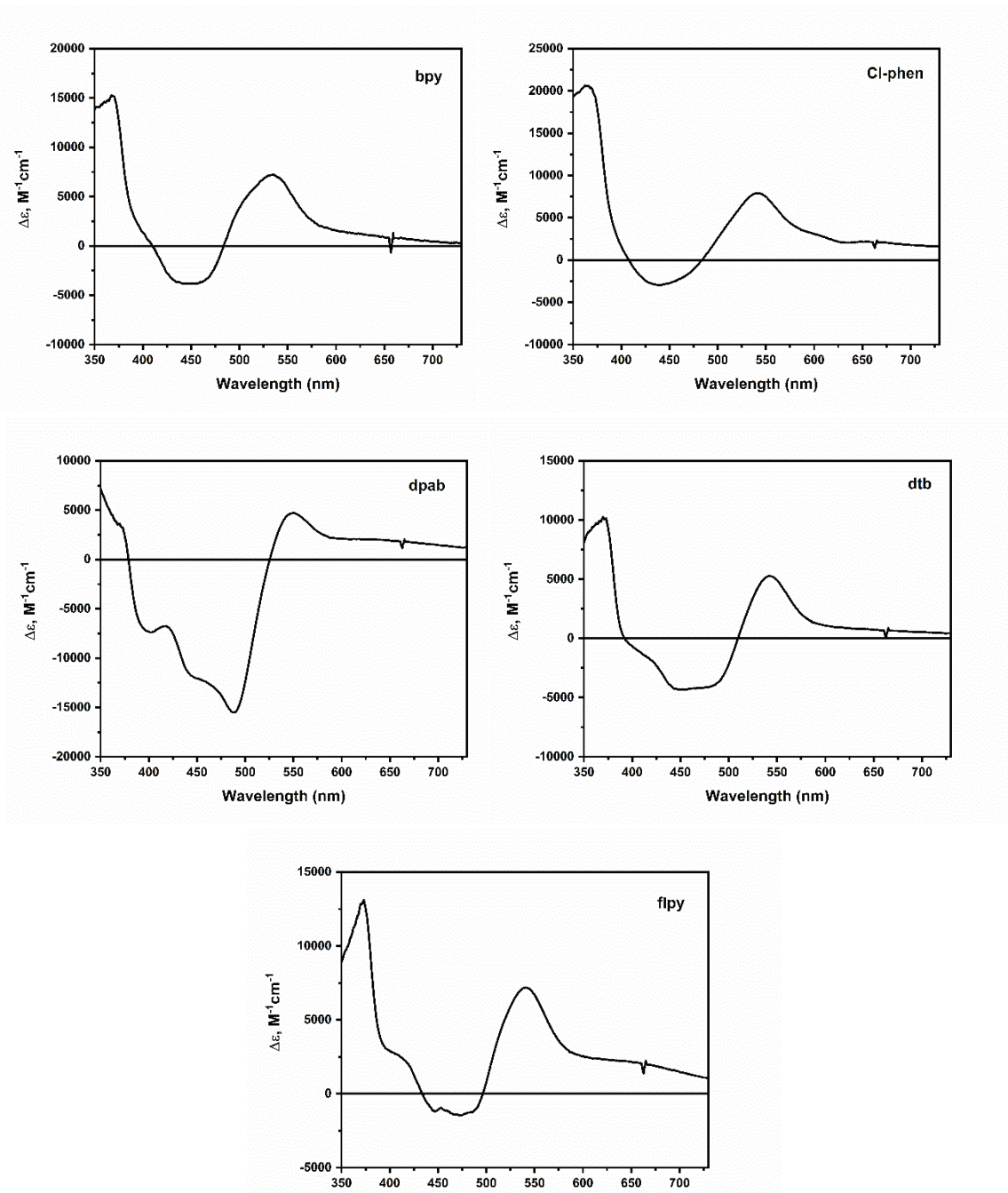


**Figure 4.22** Simulated spectra for ESET products for hydroxylated complexes and their reaction with  $\text{BMQ}^+$

For generation of the spectra for the excited state proton coupled electron transfer products, the spectra of the protonated reduced quenchers,  $\text{HMQ}^+$  and  $\text{HBMQ}^+$  must be generated. This was done using spectroelectrochemistry and the addition of strong acid to

protonate the reduced bipyridinium compound. For generation of the spectrum of the one-electron oxidized, deprotonated ruthenium complexes, spectroelectrochemistry in the presence of base yielded only the spectrum of the protonated, oxidized complex. Instead of using spectroelectrochemistry, reaction of the complex with an irreversible oxidative quencher, 4-bromobenzenediazonium tetrafluoroborate, in the presence of pyridine yielded the spectrum of the oxidized deprotonated complex. 4-bromobenzenediazonium was chosen as an irreversible oxidative quencher because it does not absorb past 350 nm and has a low reduction potential ( $E_{p,c} = -0.4$  V vs.  $Fc^{+/0}$ ), making the free energy for oxidative quenching of the excited state very favorable, even for the fppy complex.<sup>24,25</sup> In addition, back electron transfer will not occur because the kinetics are slower than the kinetics for loss of dinitrogen from the compound.

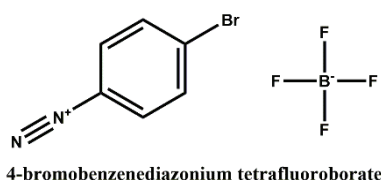


**Figure 4.23** Structure of 4-bromobenzenediazonium tetrafluoroborate

This reaction was carried out over the course of several hours of irradiation of the solution, until no further change in the spectrum could be detected. To confirm that the spectrum was indeed that of the oxidized deprotonated complex, solutions with only chromophore, chromophore and pyridine, and chromophore and 4-bromobenzenediazonium tetrafluoroborate were irradiated under the same conditions as the solution with oxidant and base. The spectrum with just 4-bromobenzene diazonium tetrafluoroborate and chromophore matched the spectrum produced by spectroelectrochemistry for the Ru(III) complex. With only chromophore, no detectable change upon irradiation was present. With

base and chromophore, again, no detectable change was observed. Taking the spectra produced via oxidation by 4-bromobenzendiazonium tetrafluoroborate in the presence of pyridine along with the spectra of  $\text{HMQ}^+$  and  $\text{HBMQ}^+$  allows for the generation of the spectrum of the ESPCET products. As the control complexes do not partake in proton transfer, the only spectra generated are for the hydroxy-bipyridine complexes. The spectra are shown in figures 4.24 and 4.25.

It is clear from figures 4.24 and 4.25 that absorbance for the PCET products is dominated by absorbance of the reduced and protonated bipyridinium quencher. As such, the important absorbance features are the strong absorbance at 390 nm for the reduced and protonated bipyridinium with an extinction coefficient of approximately  $60,000 \text{ M}^{-1}\text{cm}^{-1}$  for  $\text{HMQ}^+$  and  $40,000 \text{ M}^{-1}\text{cm}^{-1}$  for  $\text{HBMQ}^+$ , and a broad absorption between 550 nm and 700 nm. These are the spectral features that truly distinguish the presence of PCET products from ET and PT products.

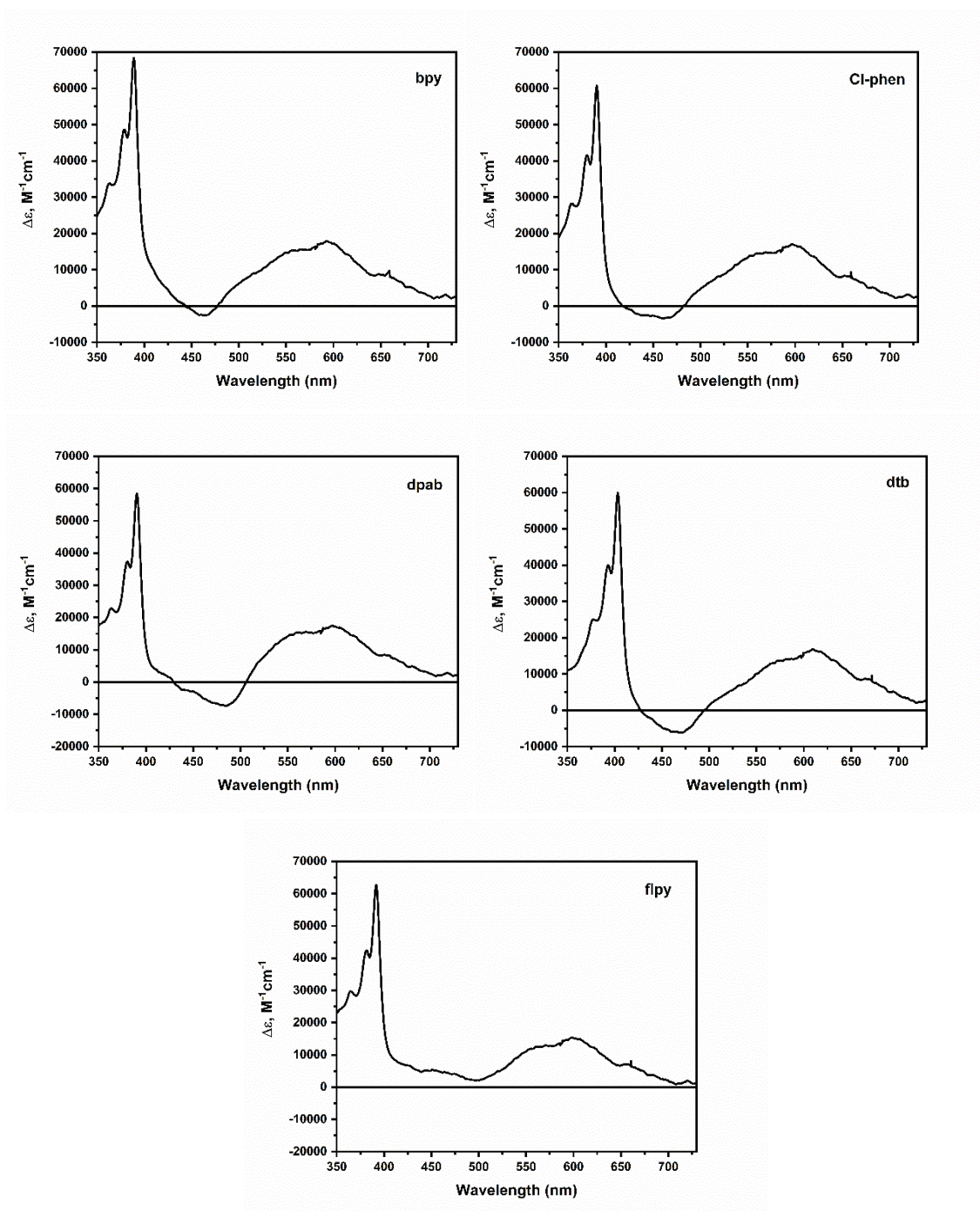


**Figure 4.24** Simulated spectra for ESPCET products for hydroxylated complexes and their reaction with  $MQ^+$

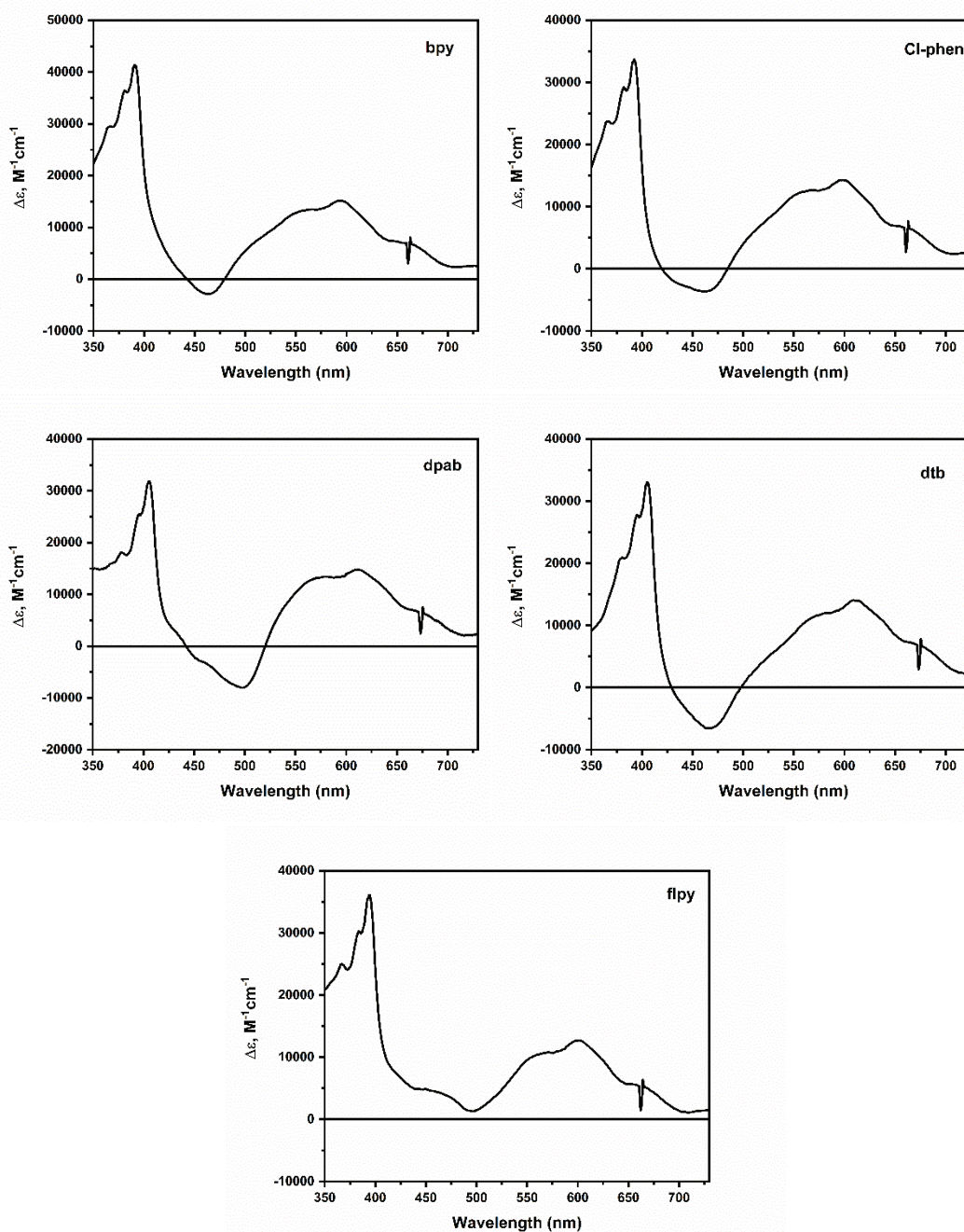


**Figure 4.25** Simulated spectra for ESPCET products for hydroxylated complexes and their reaction with  $\text{BMQ}^+$

With both knowledge of the thermodynamics for individual reactions and of the spectra of possible products from the photoinduced reaction between the bipyridinium

quenchers and the ruthenium complexes, it is possible to interpret the mechanism by which the photoreaction occurs. The subsequent section will discuss the photoinduced reaction between the bipyridinium quenchers and the series of ruthenium complexes.

#### 4.3.5 ET, PT and PCET Quenching

Using transient absorption spectroscopy, the reaction between  $[\text{Ru}(\text{LL})_2(4,4'-(\text{OH})_2\text{bpy})]^{2+}$  and the quenchers  $\text{MQ}^+$  and  $\text{BMQ}^+$  was examined. For determination of the rate constant for excited state quenching, Stern-Volmer analysis of the luminescence lifetimes as a function of the concentration of quencher was used. The Stern-Volmer equation was previously defined in chapter 3. Figures 4.26-4.44 show the exponential decays of the excited states and the Stern-Volmer plots for the excited state reaction between control complex, hydroxylated complex and  $\text{MQ}^+$  and  $\text{BMQ}^+$ . The  $K_{\text{SV}}$  values,  $k_{\text{q}}$ , and  $\tau_0$  for each quencher and complex combination are shown in table 4.8.

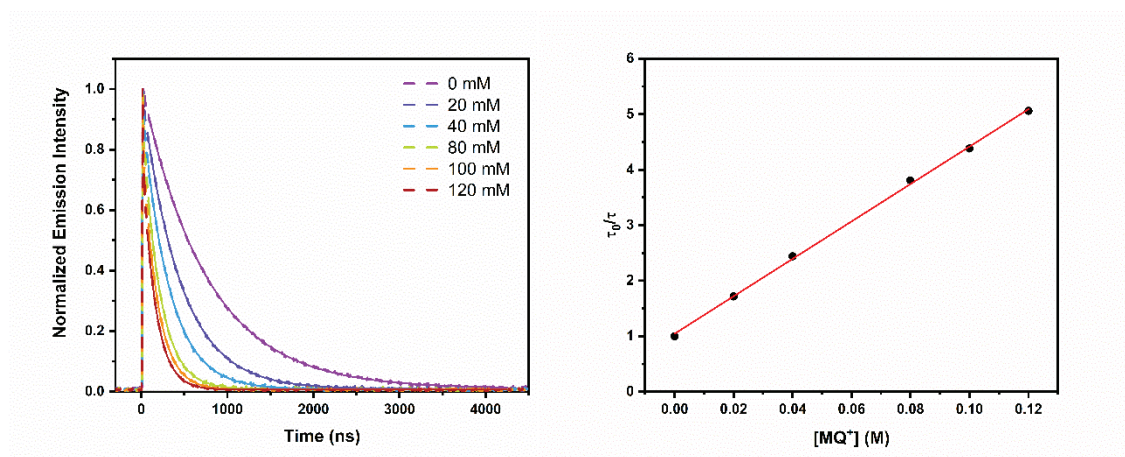


**Figure 4.26** Luminescence lifetime quenching of  $[\text{Ru}(\text{bpy})_2(4,4'-(\text{OMe})_2\text{bpy})]^{2+}$  by  $\text{MQ}^+$  (left) and the resulting Stern-Volmer plot (right)

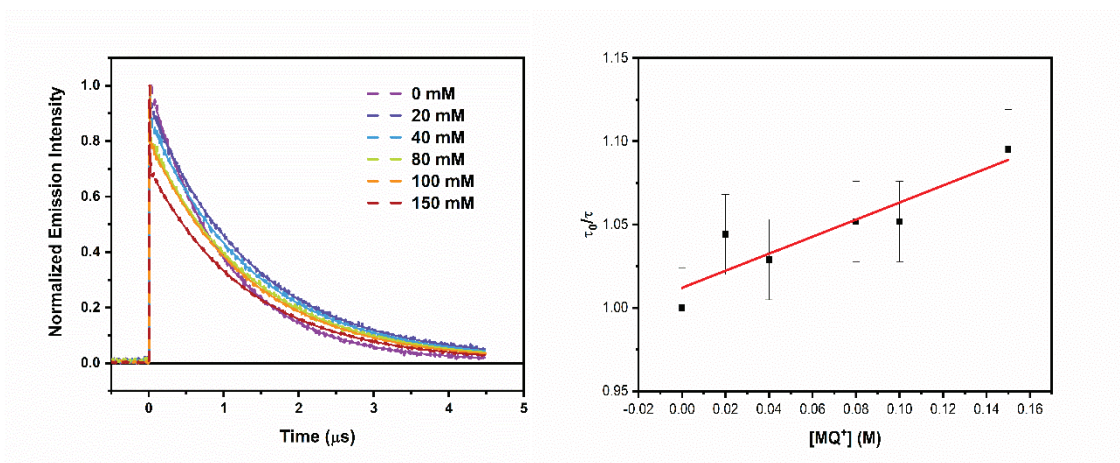


**Figure 4.27** Luminescence lifetime quenching of [Ru(dpab)<sub>2</sub>(bpy)]<sup>2+</sup> by MQ<sup>+</sup> (left) and the resulting Stern-Volmer plot (right)

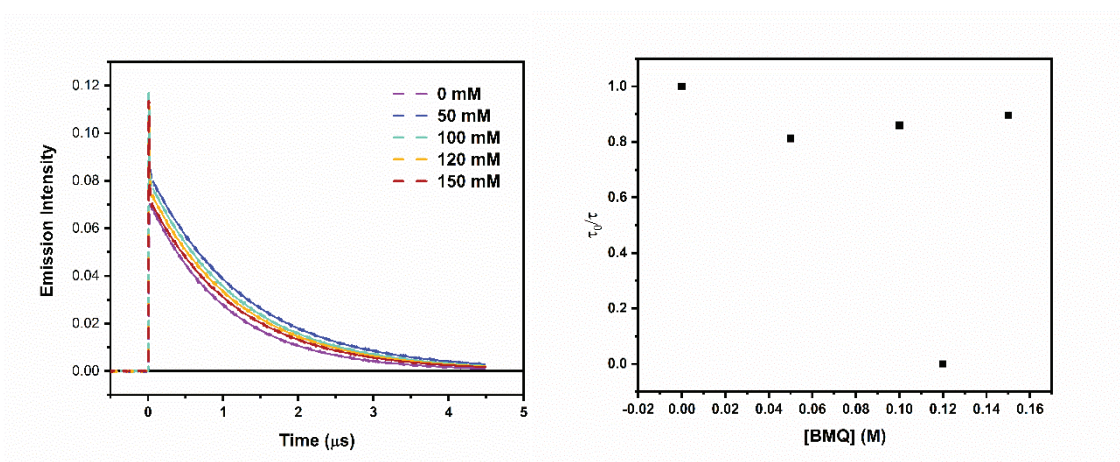


**Figure 4.28** Luminescence lifetime quenching of [Ru(dpab)<sub>2</sub>(bpy)]<sup>2+</sup> by BMQ<sup>+</sup> (left) and the resulting Stern-Volmer plot (right)

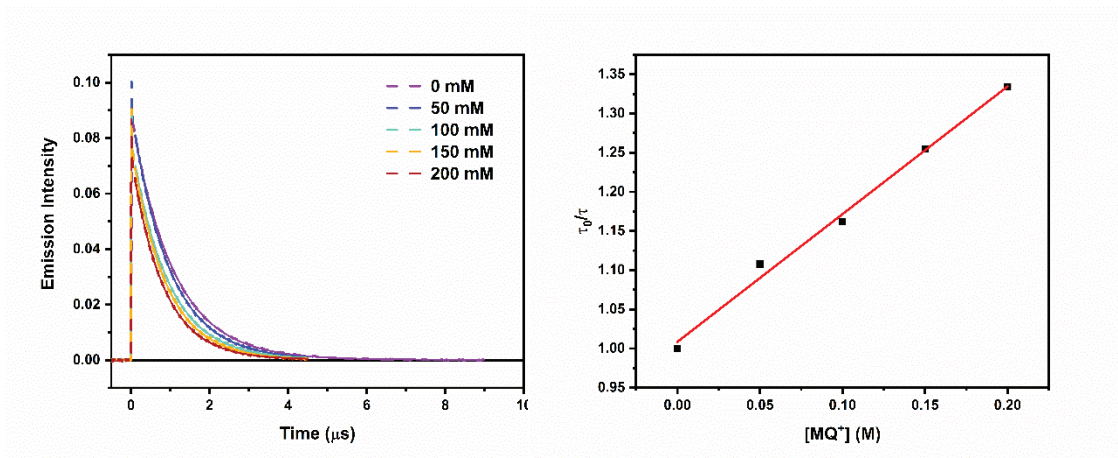


**Figure 4.29** Luminescence lifetime quenching of  $[\text{Ru}(\text{Cl-phen})_2(\text{bpy})]^{2+}$  by  $\text{MQ}^+$  (left) and the resulting Stern-Volmer plot (right)

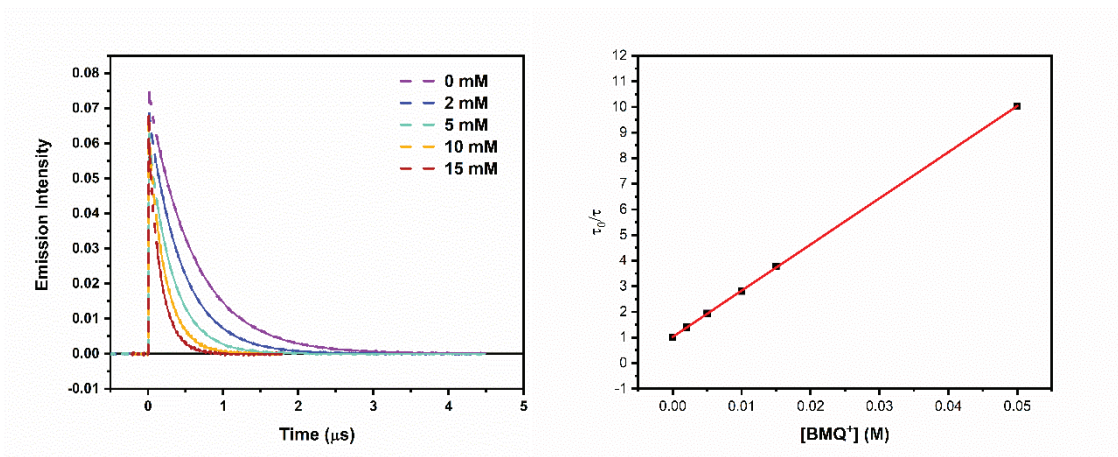


**Figure 4.30** Luminescence lifetime quenching of  $[\text{Ru}(\text{Cl-phen})_2(\text{bpy})]^{2+}$  by  $\text{BMQ}^+$  (left) and the resulting Stern-Volmer plot (right)

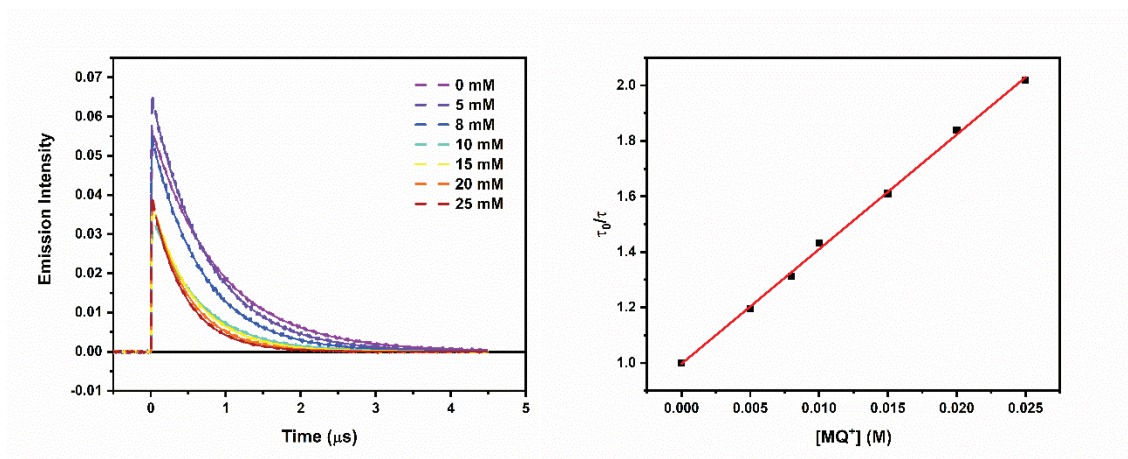


**Figure 4.31** Luminescence lifetime quenching of  $[\text{Ru}(\text{dtb})_2(\text{bpy})]^{2+}$  by  $\text{MQ}^+$  (left) and the resulting Stern-Volmer plot (right)

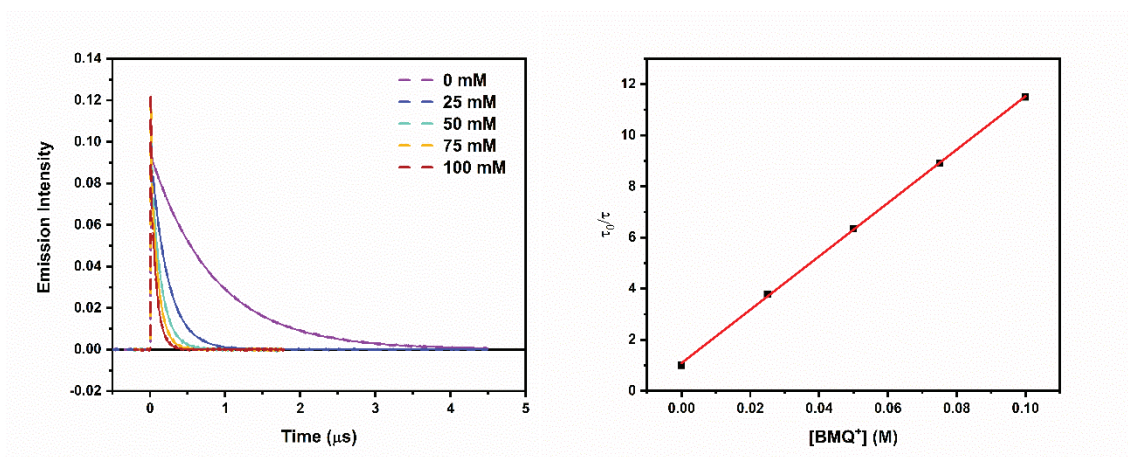


**Figure 4.32** Luminescence lifetime quenching of  $[\text{Ru}(\text{dtb})_2(\text{bpy})]^{2+}$  by  $\text{BMQ}^+$  (left) and the resulting Stern-Volmer plot (right)

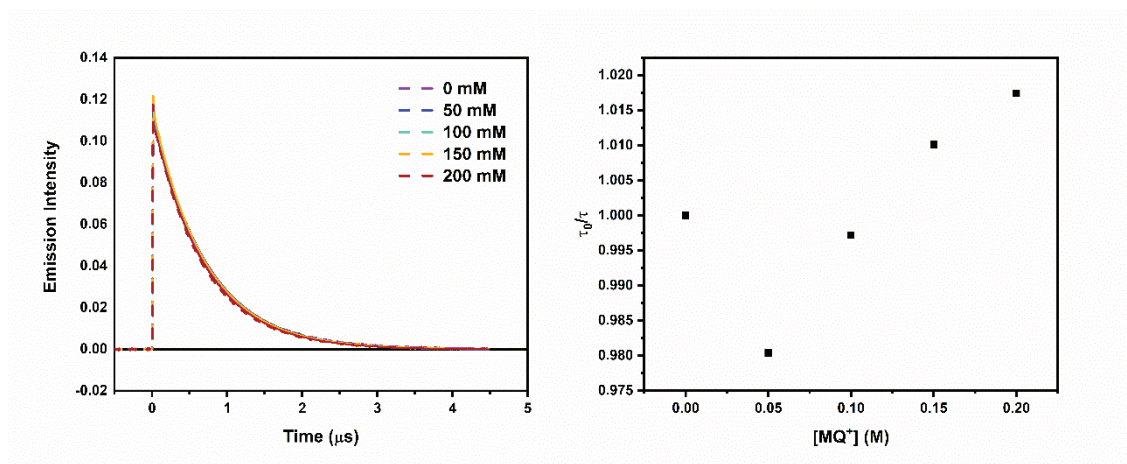


**Figure 4.33** Luminescence lifetime quenching of  $[\text{Ru}(\text{flpy})_2(\text{bpy})]^{2+}$  by  $\text{MQ}^+$  (left) and the resulting Stern-Volmer plot (right)

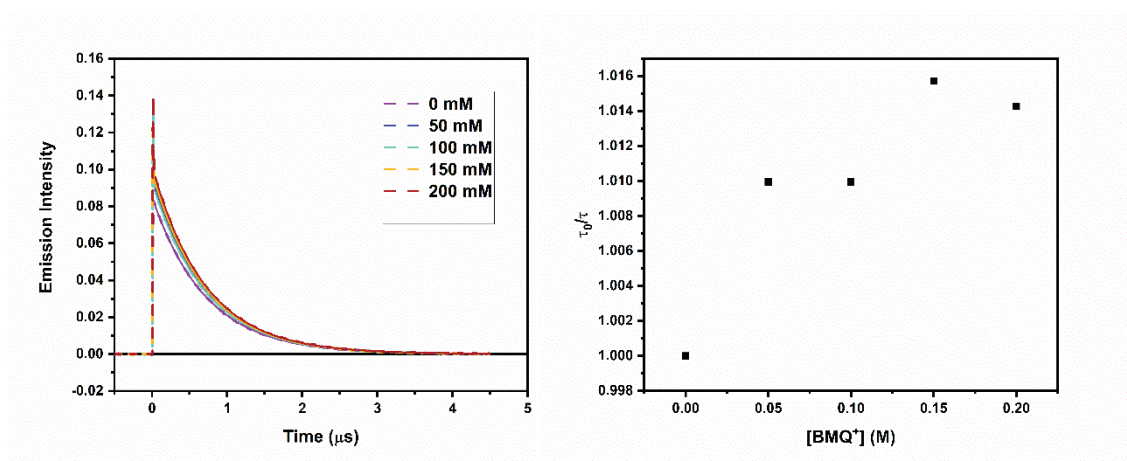


**Figure 4.34** Luminescence lifetime quenching of  $[\text{Ru}(\text{flpy})_2(\text{bpy})]^{2+}$  by  $\text{BMQ}^+$  (left) and the resulting Stern-Volmer plot (right)

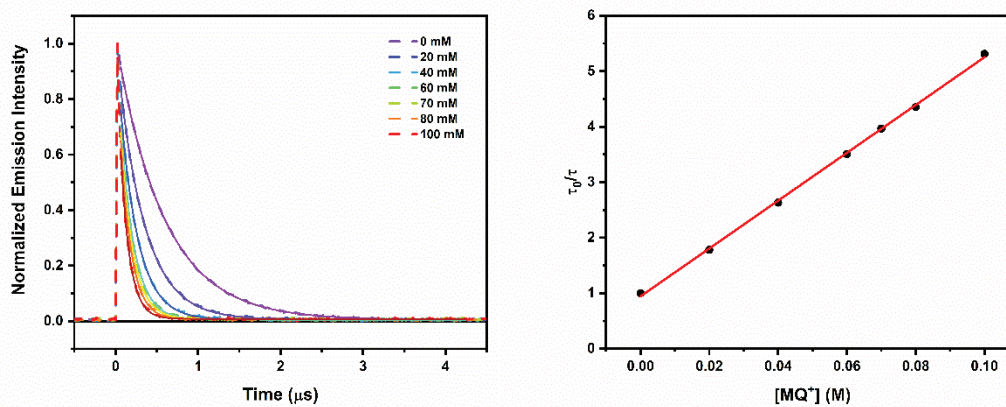


**Figure 4.35** Luminescence lifetime quenching of  $[\text{Ru}(\text{bpy})_2(4,4'-(\text{OH})_2\text{bpy})]^{2+}$  by  $\text{MQ}^+$  (left) and the resulting Stern-Volmer plot (right)

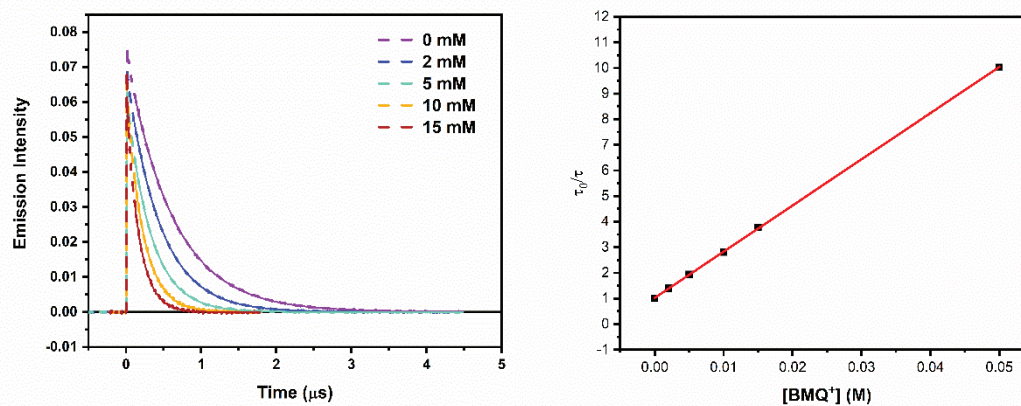


**Figure 4.36** Luminescence lifetime quenching of  $[\text{Ru}(\text{bpy})_2(4,4'-(\text{OH})_2\text{bpy})]^{2+}$  by  $\text{BMQ}^+$  (left) and the resulting Stern-Volmer plot (right)

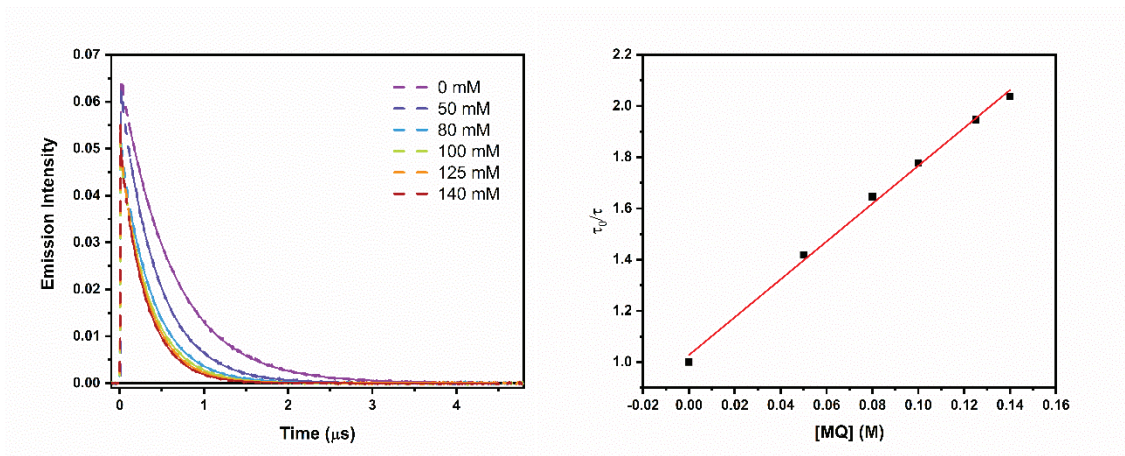


**Figure 4.37** Luminescence lifetime quenching of [Ru(dpab)<sub>2</sub>(4,4'-(OH)<sub>2</sub>bpy)]<sup>2+</sup> by MQ<sup>+</sup> (left) and the resulting Stern-Volmer plot (right)

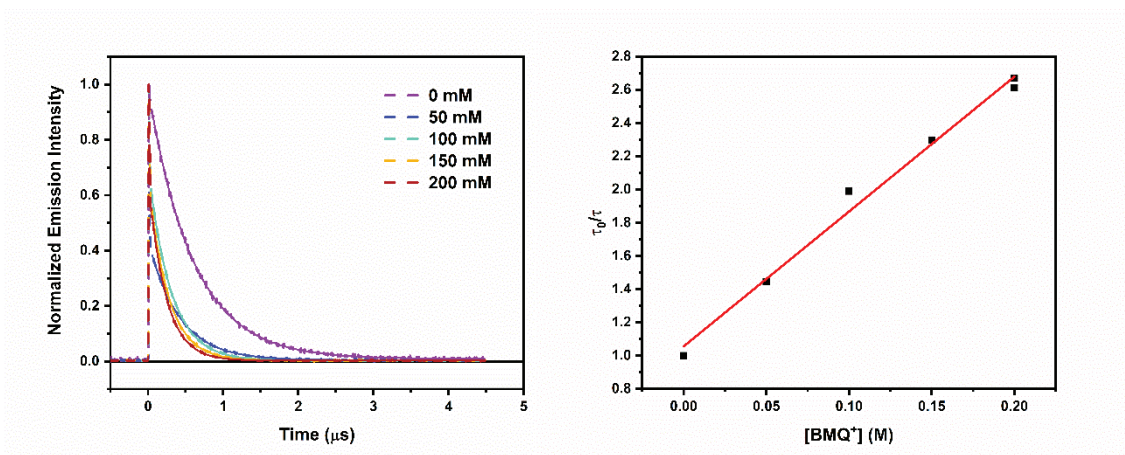


**Figure 4.38** Luminescence lifetime quenching of [Ru(dpab)<sub>2</sub>(4,4'-(OH)<sub>2</sub>bpy)]<sup>2+</sup> by BMQ<sup>+</sup> (left) and the resulting Stern-Volmer plot (right)

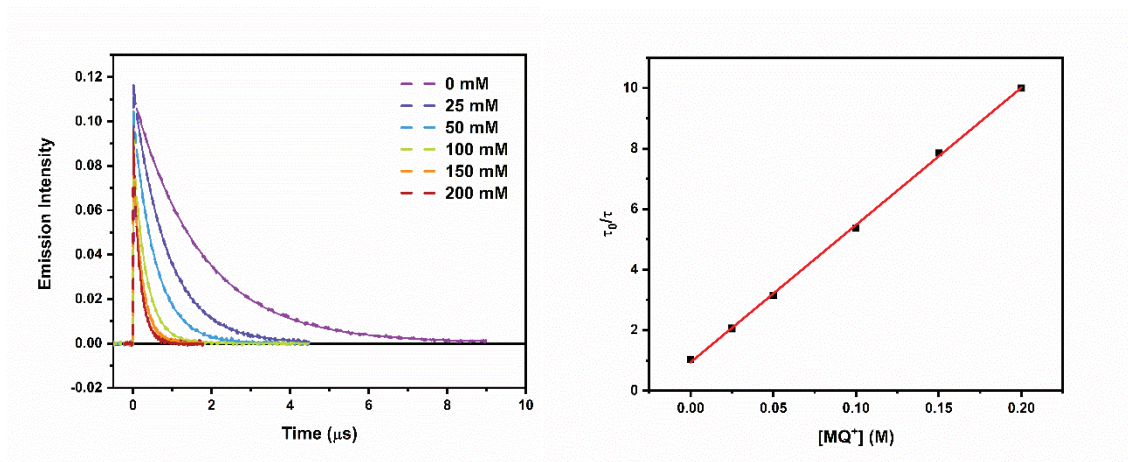


**Figure 4.39** Luminescence lifetime quenching of [Ru(Cl-phen)<sub>2</sub>(4-(OH)-4'-(OMe)bpy)]<sup>2+</sup> by MQ<sup>+</sup> (left) and the resulting Stern-Volmer plot (right)

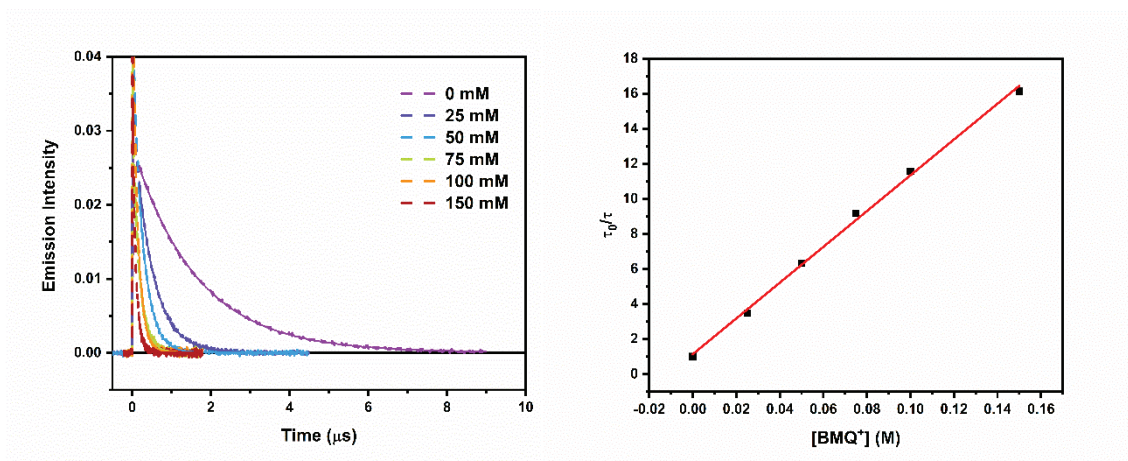


**Figure 4.40** Luminescence lifetime quenching of [Ru(Cl-phen)<sub>2</sub>(4-(OH)-4'-(OMe)bpy)]<sup>2+</sup> by BMQ<sup>+</sup> (left) and the resulting Stern-Volmer plot (right)

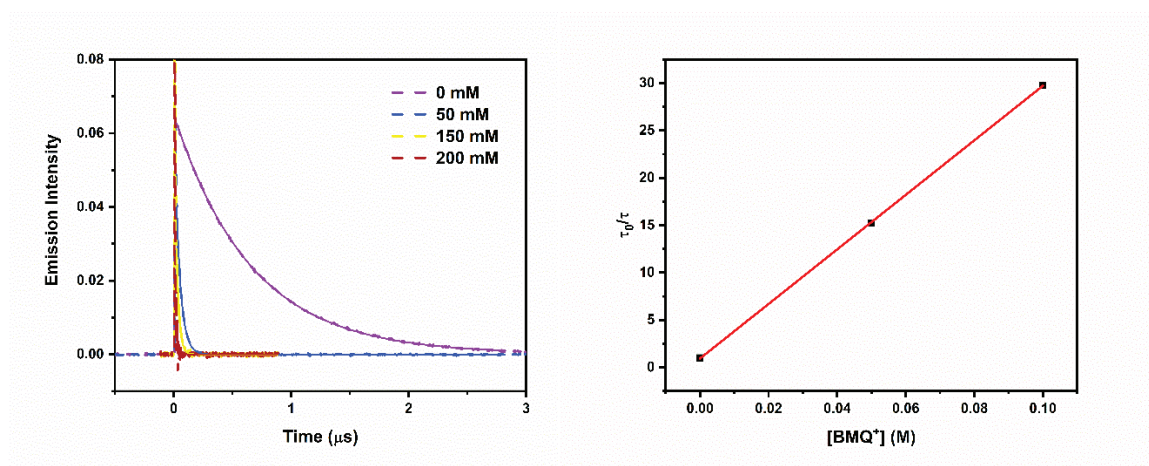


**Figure 4.41** Luminescence lifetime quenching of  $[\text{Ru}(\text{dtb})_2(4,4'-(\text{OH})_2\text{bpy})]^{2+}$  by  $\text{BMQ}^+$  (left) and the resulting Stern-Volmer plot (right)

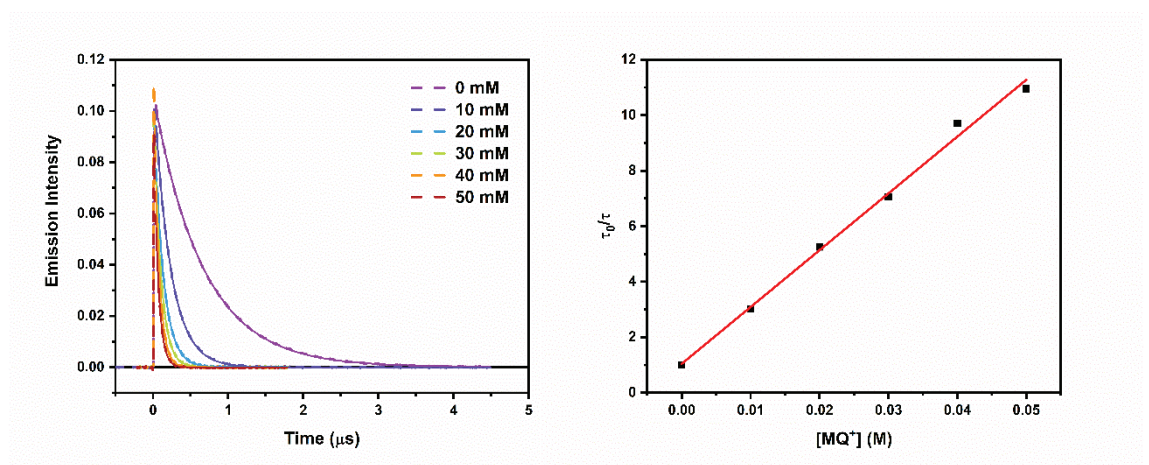


**Figure 4.42** Luminescence lifetime quenching of  $[\text{Ru}(\text{dtb})_2(4,4'-(\text{OH})_2\text{bpy})]^{2+}$  by  $\text{MQ}^+$  (left) and the resulting Stern-Volmer plot (right)

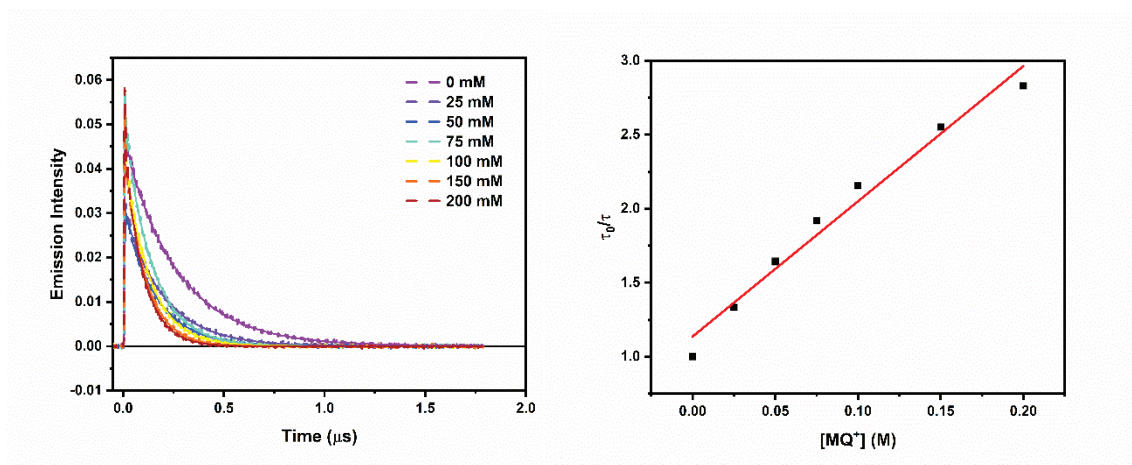


**Figure 4.43** Luminescence lifetime quenching of  $[\text{Ru}(\text{flpy})_2(4,4'-(\text{OH})_2\text{bpy})]^{2+}$  by  $\text{MQ}^+$  (left) and the resulting Stern-Volmer plot (right)

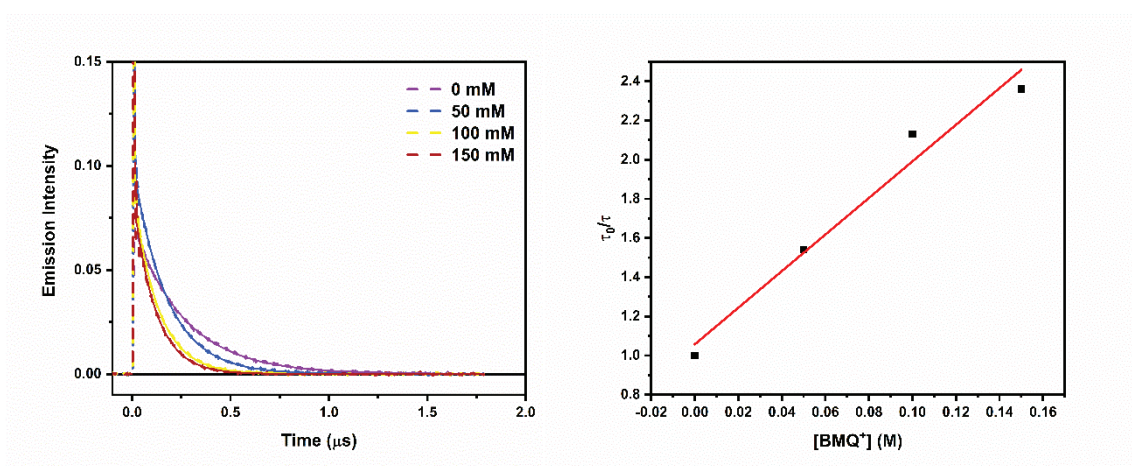


**Figure 4.44** Luminescence lifetime quenching of  $[\text{Ru}(\text{flpy})_2(4,4'-(\text{OH})_2\text{bpy})]^{2+}$  by  $\text{BMQ}^+$  (left) and the resulting Stern-Volmer plot (right)

**Table 4.8** Summary of quenching rate constants

	$\tau_0$ (ns)	MQ <sup>+</sup>		BMQ <sup>+</sup>	
		K <sub>SV</sub>	k <sub>q</sub> (M <sup>-1</sup> s <sup>-1</sup> )	K <sub>SV</sub>	k <sub>q</sub> (M <sup>-1</sup> s <sup>-1</sup> )
$[Ru(bpy)_2(4,4'-(OH)_2bpy)]^{2+}$	640	43.1	6.73E+07	180	2.81E+08
$[Ru(dpab)_2(4,4'-(OH)_2bpy)]^{2+}$	615	7.39	1.20E+07	8.12	1.32E+07
$[Ru(flpy)_2(4,4'-(OH)_2bpy)]^{2+}$	256	9.14	3.57E+07	9.34	3.65E+07
$[Ru(Cl-phen)_2(4-(OH)-4'-(OMe)bpy)]^{2+}$	1900	45.4	2.39E+07	102	5.37E+07
$[Ru(dtb)_2(4,4'-(OH)_2bpy)]^{2+}$	660	205	3.11E+08	288	4.36E+08
$[Ru(bpy)_2(4,4'-(OMe)_2bpy)]^{2+}$	750	33.7	4.49E+07		
$[Ru(dpab)_2(bpy)]^{2+}$	1040	0	0	0	0
$[Ru(flpy)_2(bpy)]^{2+}$	629	0	0	0	0
$[Ru(Cl-phen)_2(bpy)]^{2+}$	1000	1.63	1.63E+06	10	1.00E+07
$[Ru(dtb)_2(bpy)]^{2+}$	790	41.3	5.23E+07	104	1.32E+08

Transient absorption (TA) spectra for the reaction of the control complexes and hydroxylated complexes with bipyridinium quenchers are shown in figures 4.45-4.52. For each TA spectrum of the hydroxylated complexes, the corresponding control complex spectrum is shown by its side to help highlight the differences in reactivity with the bipyridinium quenchers. For the complex  $[\text{Ru}(\text{bpy})_2(4,4'-(\text{OH})_2\text{bpy})]^{2+}$  and its reaction with  $\text{BMQ}^+$ , no control study was done, as the outcome of such a study is presumed to be the same as for the  $\text{MQ}^+$  studies.

For control complexes, it was determined based on the spectroscopic features of the TA spectra in conjunction with the simulated spectra (*vide supra*) that reaction with the bipyridinium salts proceeds through an outer sphere electron transfer mechanism. This is evident for the complexes  $[\text{Ru}(\text{bpy})_2(4,4'-(\text{OMe})_2\text{bpy})]^{2+}$ ,  $[\text{Ru}(\text{dtb})_2(\text{bpy})]^{2+}$ , and  $[\text{Ru}(\text{Cl-phen})_2(\text{bpy})]^{2+}$ . With the control complexes  $[\text{Ru}(\text{dpab})_2(\text{bpy})]^{2+}$  and  $[\text{Ru}(\text{flpy})_2(\text{bpy})]^{2+}$ , there was no observed excited state quenching by the bipyridinium compounds. The lack of excited state quenching for the flpy and dpab controls can be rationalized from a thermodynamic perspective. The free energy for ET is simply too endergonic for these processes to be observed, given the excited state decay rate constants of the complexes. In analysis of the reaction of the analogous hydroxylated complexes, this observation will aid in the assignment of the reaction mechanisms which is to follow.

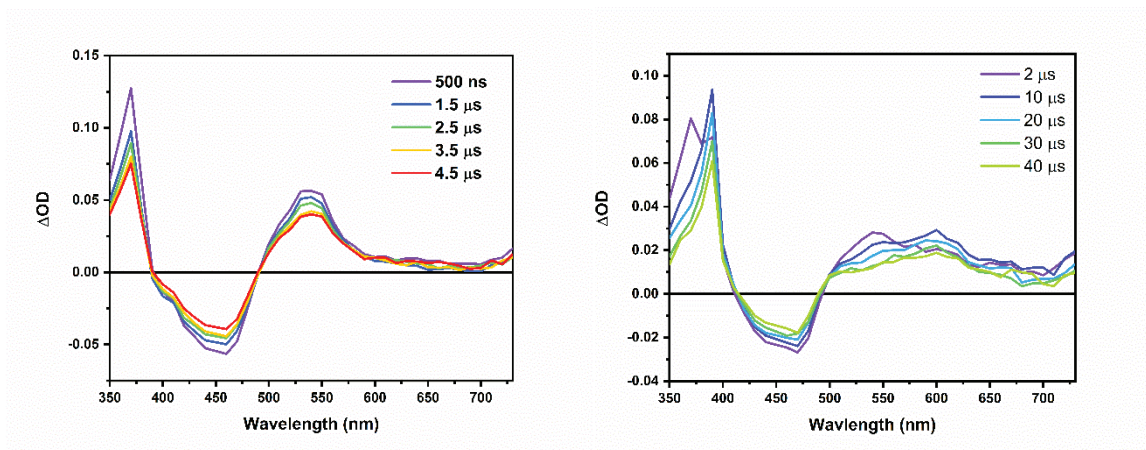


**Figure 4.45** nsTA spectra of  $[\text{Ru}(\text{bpy})_2(4,4'\text{-(OMe)}_2\text{bpy})]^{2+}$  in the presence of 120 mM

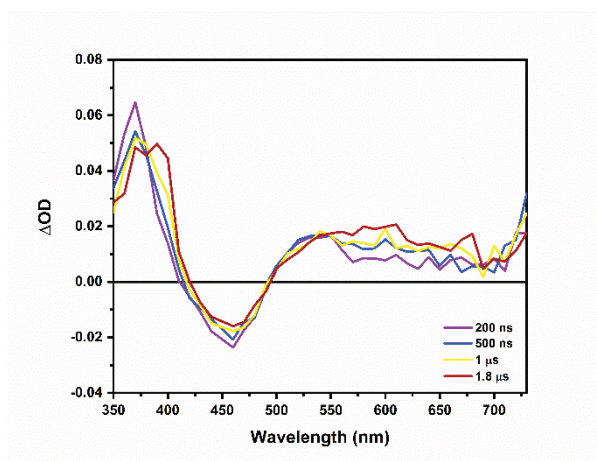


**Figure 4.46** nsTA spectra  $[\text{Ru}(\text{bpy})_2(4,4'\text{-(OH)}_2\text{bpy})]^{2+}$  in the presence of 15 mM  $\text{BMQ}^+$

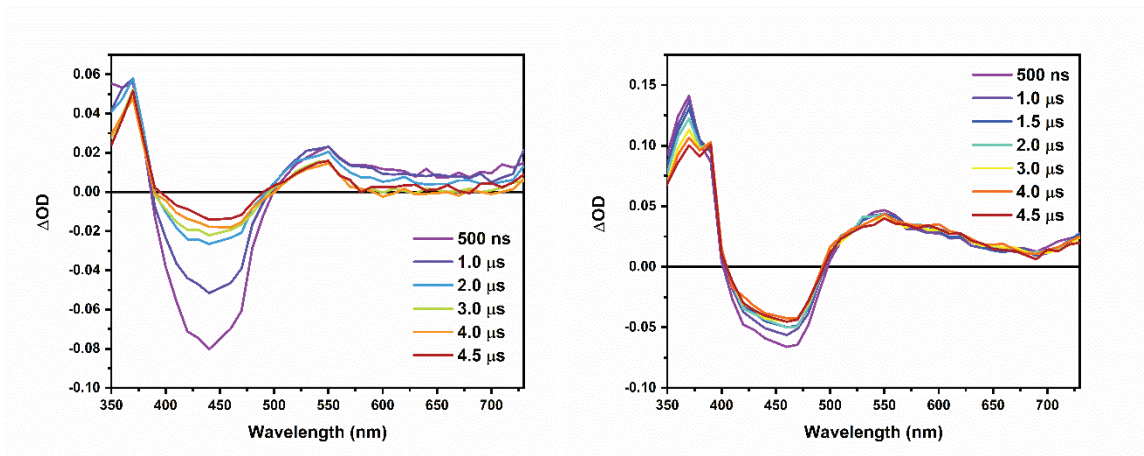


**Figure 4.47** nsTA spectra of  $\text{Ru}(\text{Cl-phen})_2(\text{bpy})]^{2+}$  in the presence of 200 mM  $\text{MQ}^+$  (left) and  $[\text{Ru}(\text{Cl-phen})_2(4-(\text{OH})-4'-(\text{OMe})\text{bpy})]^{2+}$  in the presence of 200 mM  $\text{MQ}^+$  (right)

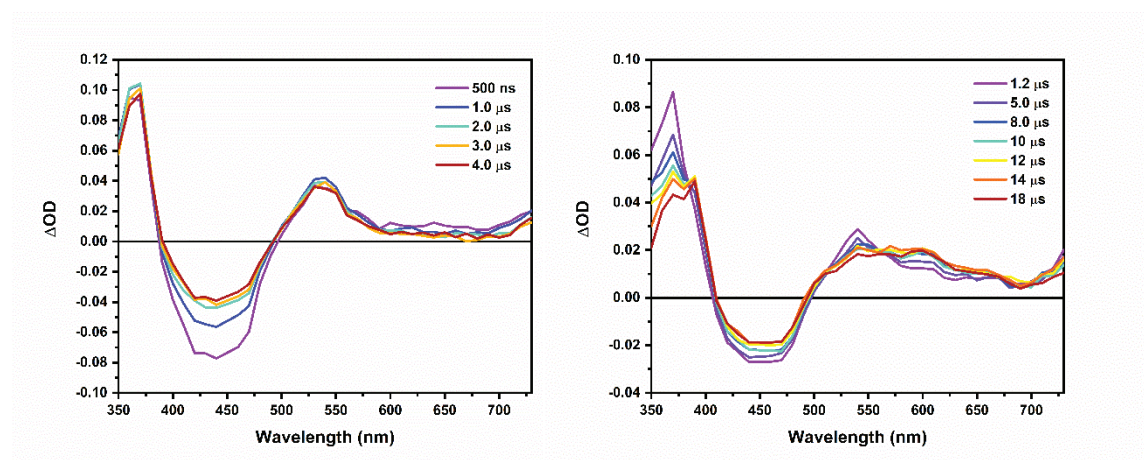


**Figure 4.48** nsTA spectra of  $\text{Ru}(\text{Cl-phen})_2(\text{bpy})]^{2+}$  in the presence of 15 mM  $\text{BMQ}^+$  (left) and  $[\text{Ru}(\text{Cl-phen})_2(4-(\text{OH})-4'-(\text{OMe})\text{bpy})]^{2+}$  in the presence of 15 mM  $\text{BMQ}^+$  (right)

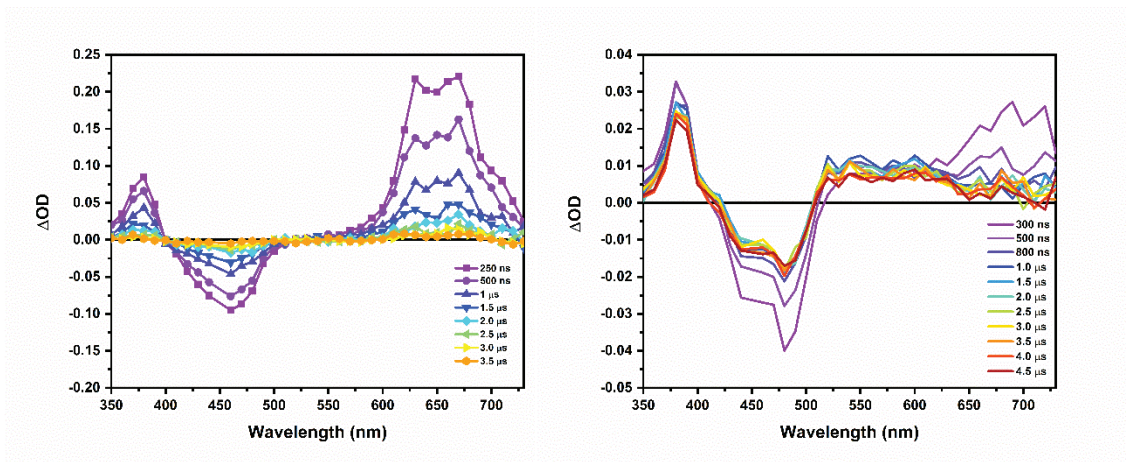


**Figure 4.49** nsTA spectra of Ru(dpab)<sub>2</sub>(bpy)]<sup>2+</sup> in the presence of 150 mM MQ<sup>+</sup> (left) and [Ru(dpab)<sub>2</sub>(4,4'-(OH)<sub>2</sub>bpy)]<sup>2+</sup> in the presence of 140 mM MQ<sup>+</sup> (right)

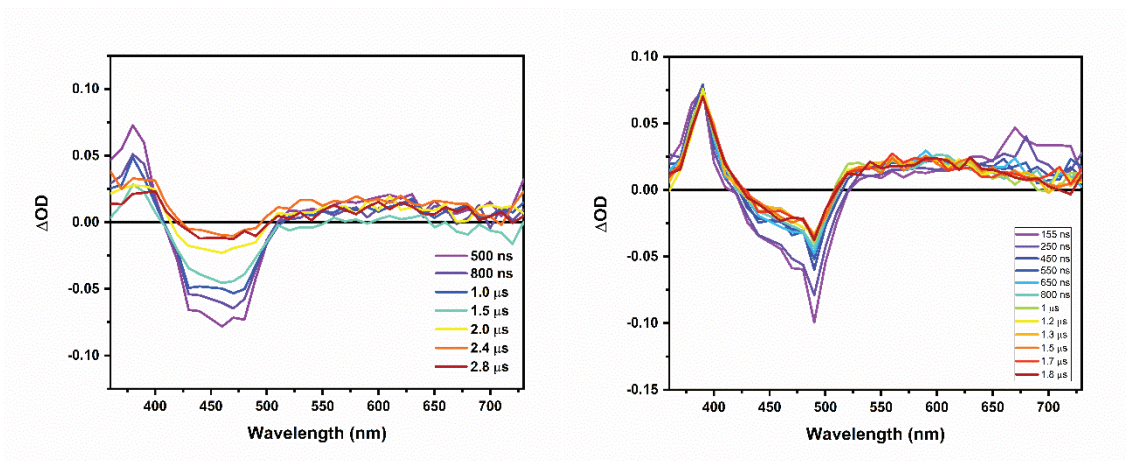


**Figure 4.50** nsTA spectra of Ru(dpab)<sub>2</sub>(bpy)]<sup>2+</sup> in the presence of 150 mM BMQ<sup>+</sup> (left) and [Ru(dpab)<sub>2</sub>(4,4'-(OH)<sub>2</sub>bpy)]<sup>2+</sup> in the presence of 200 mM BMQ<sup>+</sup> (right)

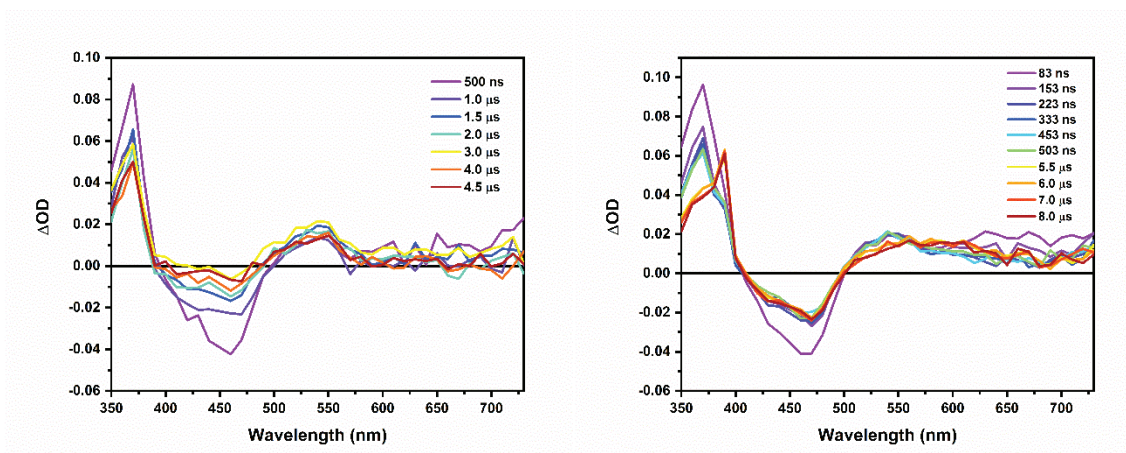


**Figure 4.51** nsTA spectra of  $\text{Ru(dtb)}_2(\text{bpy})]^{2+}$  in the presence of 25 mM  $\text{MQ}^+$  (left) and  $[\text{Ru(dtb)}_2(4,4'-(\text{OH})_2\text{bpy})]^{2+}$  in the presence of 50 mM  $\text{MQ}^+$  (right)

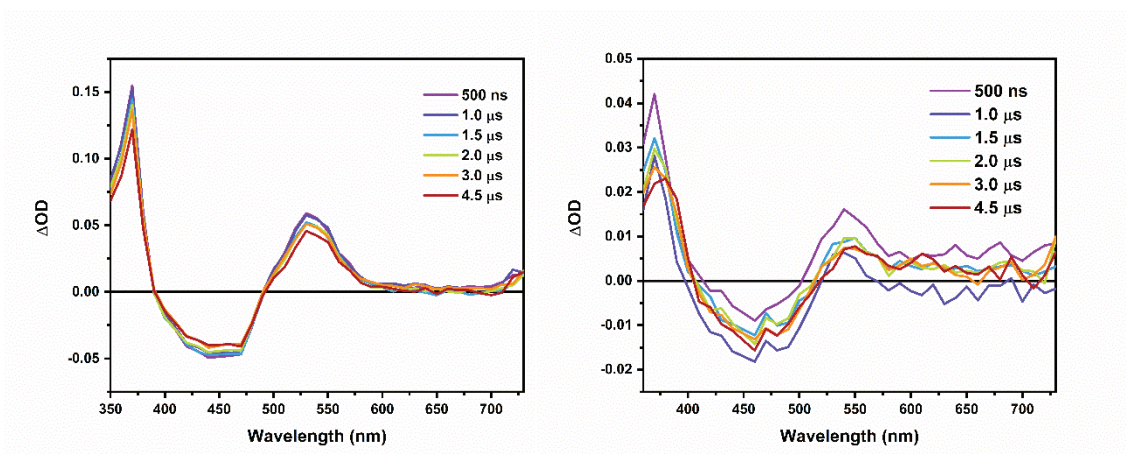


**Figure 4.52** nsTA spectra of  $\text{Ru(dtb)}_2(\text{bpy})]^{2+}$  in the presence of 100 mM  $\text{BMQ}^+$  (left) and  $[\text{Ru(dtb)}_2(4,4'-(\text{OH})_2\text{bpy})]^{2+}$  in the presence of 200 mM  $\text{BMQ}^+$  (right)

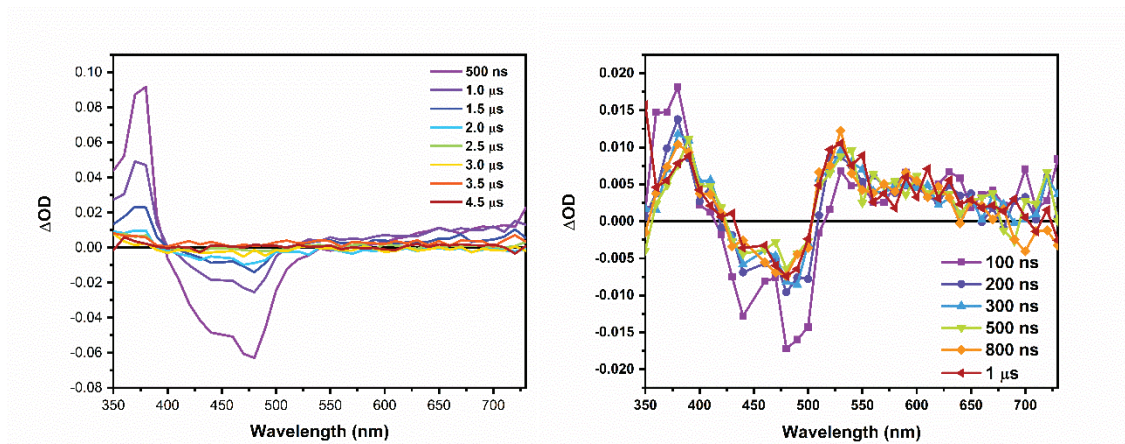


**Figure 4.53** nsTA spectra of Ru(flpy)<sub>2</sub>(bpy)]<sup>2+</sup> in the presence of 200 mM MQ<sup>+</sup> (left) and [Ru(flpy)<sub>2</sub>(4,4'-(OH)<sub>2</sub>bpy)]<sup>2+</sup> in the presence of 200 mM MQ<sup>+</sup> (right)

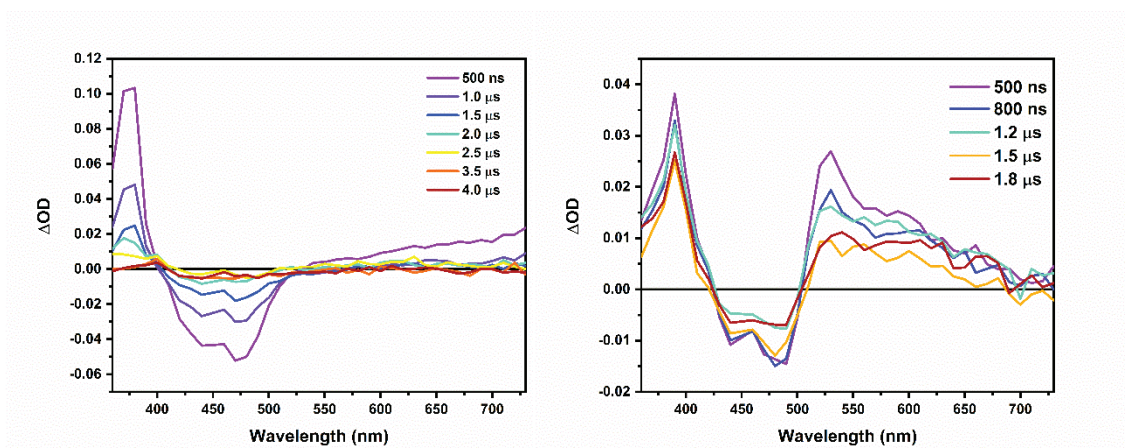


**Figure 4.54** nsTA spectra of Ru(flpy)<sub>2</sub>(bpy)]<sup>2+</sup> in the presence of 200 mM BMQ<sup>+</sup> (left) and [Ru(flpy)<sub>2</sub>(4,4'-(OH)<sub>2</sub>bpy)]<sup>2+</sup> in the presence of 150 mM MQ<sup>+</sup> (right)

For reaction with the hydroxylated complexes, observation of intermediate species in the TA spectra provide insight into the reaction mechanism. For complexes where electron transfer is more favorable, such as the bpy, dtb, and Cl-phen complexes, transient absorption spectra show spectroscopic signatures consistent with electron transfer products as evidenced by the peak maxima and relative intensity of the peaks. After a period of several microseconds, the spectrum evolves to reveal absorption consistent with the PCET

products. This indicates that reaction must occur through a sequential process, ESET-PT. The nature of the proton transfer step has been explored for  $[\text{Ru}(\text{bpy})_2(4,4'-(\text{OH})_2\text{bpy})]^{2+}$ , and it is probably safe to assume that the other complexes, dtb and Cl-phen, demonstrate similar PT mechanisms.

Because oxidative quenching of the excited state yields the ground state ruthenium(III) complex, proton transfer can only occur through a thermal pathway. Protonation of  $\text{MQ}^0$  or  $\text{BMQ}^0$  must occur via either the ruthenium(III) or ruthenium(II) in solution. From a thermodynamic perspective, the free energy for proton transfer from ruthenium(III) to  $\text{MQ}^0$  or  $\text{BMQ}^0$  is going to be more negative than for proton transfer from ruthenium(II) to  $\text{MQ}^0$  or  $\text{BMQ}^0$ . The free energy for this proton transfer step can be calculated by using the  $\text{p}K_a'$  values and the  $\text{p}K_a$  values for the conjugate acid of the reduced bipyridinium quenchers. Although protonation by the oxidized ruthenium complex is favored, the free energy for proton transfer from ruthenium(II) is close to zero for each complex. That being said, it becomes imperative to acknowledge the position of equilibrium for these reactions. Considering that the concentration of ruthenium(III) formed in the photoreaction is much less than the bulk ruthenium(II) present, the acid-base equilibrium for reaction between the ruthenium(II) complex and  $\text{MQ}^0$  or  $\text{BMQ}^0$  will be the dominate equilibrium, as the  $\text{MQ}^0$  is more likely to encounter a ruthenium(II) in solution than ruthenium(III).

Concentration dependence studies were undertaken to test this hypothesis. In figure 4.57, the plot of the rate constant for proton transfer versus the concentration of ruthenium(II) is shown, along with the monitored signal at 390 nm corresponding to the absorbance of  $\text{HMQ}^+$ . The rate constant for proton transfer was extracted from global

analysis of the full transient absorption spectra using LKS Pro-Kineticist software. The linear dependence of the rate of proton transfer on the concentration of ruthenium present indicates that the predominate means of protonation to form  $\text{HMQ}^+$  following photoinduced electron transfer to form  $\text{MQ}^0$  must be via protonation by ruthenium(II) in solution. The non-zero intercept of the fit is suggestive that the ruthenium(III) in solution also contributes to the protonation of  $\text{MQ}^0$ , but to a lesser extent. It is expected that if the intercept obtained from the linear fit of the plot in figure 4.57 is subtracted from the observed rate constants, then that rate should reflect the rate dependence on the concentration of ruthenium(II). In evaluating this data, when the intercept is subtracted, the rate constant obtained doubles when the concentration of ruthenium(II) doubles, indicated a first order dependence for the observed reaction. Table 4.9.

**Table 4.9** Rate Dependence on the Concentration of Ru(II) for PT

[Ruthenium (II)] (M)	$k_{\text{obs}}$ ( $\text{s}^{-1}$ ) (with y-intercept subtracted)	change in rate (change in concentration)
1.50E-04	331552	1.0 (1.0)
2.00E-04	451172	1.36 (1.33)
2.50E-04	569772	1.72 (1.67)
3.00E-04	665772	2.00 (2.00)

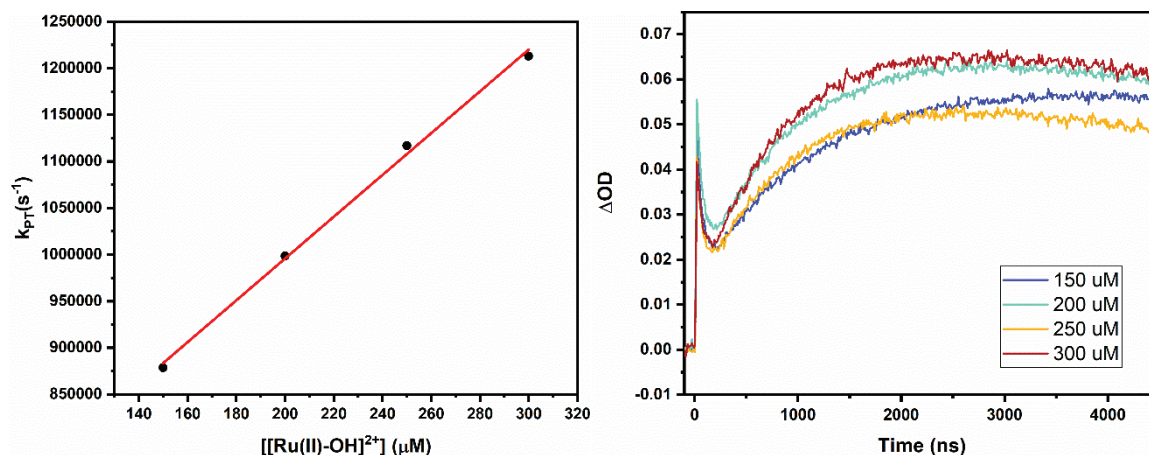


**Figure 4.55** Plot of the rate constant for PT vs. concentration of ruthenium(II) (left) and kinetics at 390 nm (right).

For complexes that undergo ESET-PT reaction with bipyridinium quenchers, the rate constant for proton transfer following ESET was assessed by global analysis as stated above. The second order rate constants for the thermal proton transfer are shown in table 4.10. Because proton transfer occurs from the bulk ruthenium(II) in solution, the rate constants that are extracted from global analysis are pseudo-first order. Taking the first order rate constant and dividing it by the concentration of ruthenium calculated from the ground state absorbance spectra allows for the extraction of the second order rate constant for protonation. All rate constants appear to be within or close to the diffusion limited regime for bimolecular reactions in acetonitrile.

**Table 4.10** Summary of PT rate constants for reaction following ESET

	<b>MQ<sup>+</sup></b> <b>k<sub>PT</sub> (M<sup>-1</sup>s<sup>-1</sup>)</b>	<b>BMQ<sup>+</sup></b> <b>k<sub>PT</sub> (M<sup>-1</sup>s<sup>-1</sup>)</b>
$[Ru(bpy)_2(4,4'-(OH)_2bpy)]^{2+}$	2.2E+09	1.4E+10
$[Ru(Cl-phen)_2(4-(OH)-4'-(OMe)bpy)]^{2+}$	3.3E+09	7.8E+09
$[Ru(dtb)_2(4,4'-(OH)_2bpy)]^{2+}$	3.5E+11	6.6E+11

The two complexes of the series that exhibit unique quenching dynamics are the dpab and flpy complexes. As mentioned previously, the control complexes were not quenched by the bipyridinium quenchers. The fact that electron transfer does not occur, and thermodynamics indicate that the free energy for the reaction of control complexes and hydroxylated complexes are within 1 kcal/mol, strongly suggests that excited state quenching of the hydroxylated complexes must occur via either ESPCET or ESPT.

One thing worth mentioning at this point is that in figure 4.46, the control reaction with BMQ<sup>+</sup> and  $[Ru(dpab)_2(bpy)]^{2+}$  appears to have some degree of change in absorbance consistent with the PCET products. This is in fact due to the presence of a trace amount (<1%) impurity of benzyl viologen from the synthesis of BMQ<sup>+</sup>. Unfortunately, the rate constant for oxidative quenching by benzyl viologen is orders of magnitude larger than BMQ<sup>+</sup>, and the molar extinction coefficient for the reduced viologen is also large, leading to a small amount of absorption present in the control spectrum. This was verified by subsequent electrochemical studies on the quencher that showed the presence benzyl viologen. The Stern-Volmer analysis still indicates that excited state quenching by BMQ<sup>+</sup> is not occurring, at least to any measurable extent.

For the  $[\text{Ru}(\text{flpy})_2(4,4'-(\text{OH})_2\text{bpy})]^{2+}$ , the transient absorption spectrum reveals two positive features, one at approximately 380 nm, the other at 530 nm. From the simulated spectra, the ET products should have peaks at 367 and 537 nm, while for PT they will appear at 385 and 542 nm. It is unlikely that ET is the cause of the transient absorption given the analogous control complex exhibits no ET in the presence of either bipyridinium quencher. The most likely explanation for the observation of peaks at 380 and 530 nm is that ESPT is occurring. Unfortunately, given the slow quenching kinetics, short lifetime of the chromophore, and solubility limit of the quencher, spectra with better signal-to-noise were unattainable. Additionally, the peak at 530 nm, could well actually be at 537 nm, however the resolution of the experiment was only 10 nm. Despite these experimental issues, it is most likely that the excited-state quenching of  $[\text{Ru}(\text{flpy})_2(4,4'-(\text{OH})_2\text{bpy})]^{2+}$  occurs via proton transfer. For reaction of flpy with  $\text{BMQ}^+$ , the TA spectrum is dominated by absorption features consistent with ESPT, much like with  $\text{MQ}^+$ , although it does appear that there may be a mix of absorption, perhaps from PCET is also occurring. Further studies need to be conducted to confirm this observation, as it could simply be the result of residual benzyl viologen present, or simply poor signal-to-noise in the data.

Changing the  $\pi^*$  level of the complexes through incorporation of functional groups on spectator ligands has provided the ability to see extremes of reactivity with the same set of quenchers. The challenge lies in finding the thermodynamic regime where ESPCET will likely occur. Unfortunately, observation of excited state proton-coupled electron transfer is not as common as proton and electron transfer. One reason for this is that the vibronic coupling between the reactant and product states is too small to facilitate PCET, allowing ET reactions to dominate. In the case where PT is observed over PCET, it is reasonable to

say that the driving force for ET, and also PCET is just not favorable enough to enable PCET.

In the final example of excited state reaction with bipyridinium quenchers is that of the complex  $[\text{Ru}(\text{dpab})_2(4,4'-(\text{OH})_2\text{bpy})]^{2+}$ . As mentioned before, control studies indicate that, like with the flpy complex, electron transfer should not occur. In examining the transient absorption spectra, it is clear that there is a broad absorbance feature in the region of 550-700 nm. This feature is perhaps consistent with the reduced protonated bipyridinium compound. Knowing that the only possible means of excited state quenching are either PT or PCET, comparison of the two spectra becomes imperative for interpretation of the reaction mechanism. From the simulated spectra, the PT products shown two positive absorbance features, with the peak at 386 nm being about 70% the intensity of the peak at 542 nm. This would be what is expected in the transient absorption spectrum if PT were the dominant quenching mechanism. In the TA spectrum, the peak around 390 nm is about three times that of the broad absorption between 550-700 nm. This is precisely the ratio of the peaks for the PCET products that is expected. Unfortunately, the quenching efficiency of this reaction is low, resulting in a small degree of charge separated species. This makes that transient signal for the PCET products small. Again, solubility limits for the quencher are prohibitive in enhancing the signal-to-noise for the spectrum. Despite this, it is evident that quenching of the excited state occurs via PCET.

#### 4.3.6 Back Reaction Kinetics

Back reaction kinetics were explored for selected complexes. Table 4.11 shows the second order rate constant for back electron/proton transfer ( $k_{BPCT}$ ) for reaction of  $[\text{Ru}(\text{dtb})_2(4,4'-(\text{OH})_2\text{bpy})]^{2+}$  and  $[\text{Ru}(\text{bpy})_2(4,4'-(\text{OH})_2\text{bpy})]^{2+}$  with  $\text{MQ}^+$ . Back reaction

kinetics were also assessed for reaction of  $[\text{Ru}(\text{dpab})_2(4,4'-(\text{OH})_2\text{bpy})]^{2+}$  with  $\text{BMQ}^+$ . Despite the nature of the forward reaction, back reaction does not appear to show signs of intermediate species formation. Further investigation of the back reaction would be needed to ascertain whether the reaction is sequential or concerted. Figures 4.58 and 4.59 show the kinetics of back reaction. For dtb and bpy, the bleach recovery signal at 460 nm was monitored. For dpab, the back reaction was monitored at 390 nm. Because the reaction follows the rate law for a second order reaction, it implies that back reaction occurs between the oxidized deprotonated complex and the reduced protonated bipyridinium.

**Table 4.11** Summary of selected rate constants for back PCET

	<b>Quencher</b>	<b><math>k_{\text{BPCET}} (\text{M}^{-1}\text{s}^{-1})</math></b>
$[\text{Ru}(\text{dpab})_2(4,4'-(\text{OH})_2\text{bpy})]^{2+}$	$\text{BMQ}^+$	1.74E+09
$[\text{Ru}(\text{bpy})_2(4,4'-(\text{OH})_2\text{bpy})]^{2+}$	$\text{MQ}^+$	3.21E+09
$[\text{Ru}(\text{dtb})_2(4,4'-(\text{OH})_2\text{bpy})]^{2+}$	$\text{MQ}^+$	5.11E+09

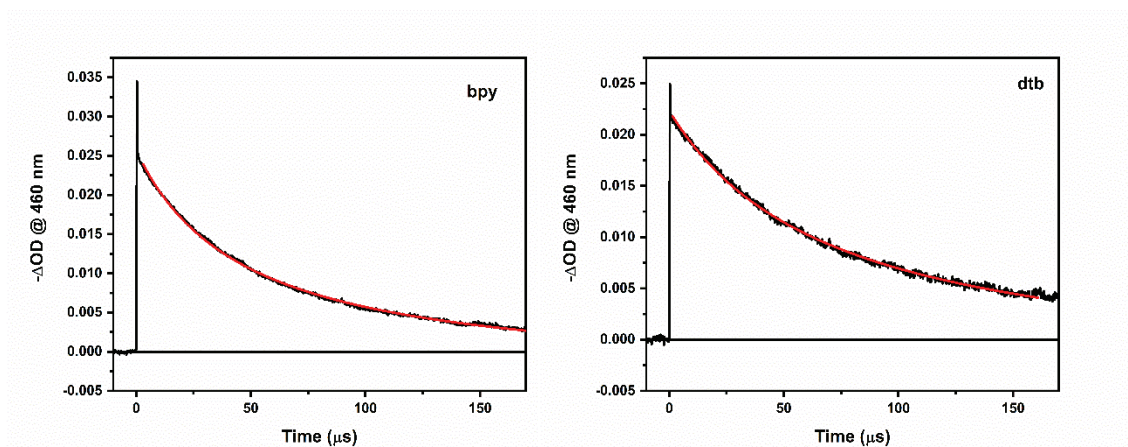


**Figure 4.56** Back reaction kinetics at 460 nm for  $[\text{Ru}(\text{bpy})_2(4,4'-(\text{OH})\text{bpy})]^{2+}$  (left) and  $[\text{Ru}(\text{dtb})_2(4,4'(\text{OH})_2\text{bpy})]^{2+}$  (right) in the presence of 200 mM  $\text{MQ}^+$

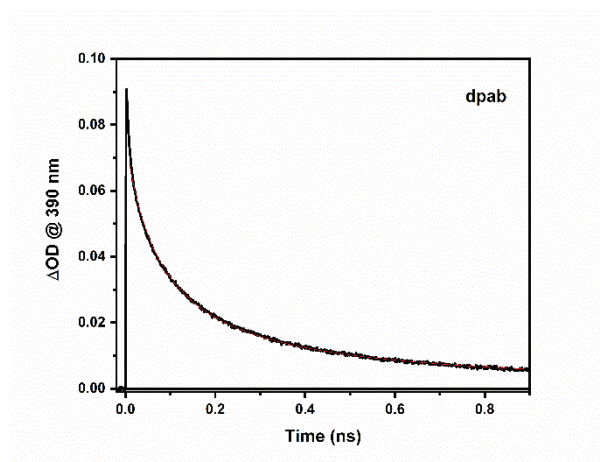


**Figure 4.57** Back reaction kinetics at 390 nm for  $[\text{Ru}(\text{dpab})_2(4,4'(\text{OH})_2\text{bpy})]^{2+}$  in the presence of 200 mM  $\text{BMQ}^+$

### 4.3.7 Kinetic Isotope Effect Studies

Kinetic deuterium isotope effect (KIE) studies can provide insight into reaction mechanism. For reactions involving the loss of a proton, a kinetic deuterium isotope effect can indicate whether or not deprotonation is a rate limiting step. This will be evidenced by a decrease in the rate constant for the reaction when deuterium is substituted for protium. The ratio of the rate constant for reaction of the proteo compound and rate constant for

reaction involving the deuterio compound is the (KIE) ratio. If the KIE ratio is greater than 1, it is described as having a primary kinetic isotope effect. The nature of the slower reaction kinetics has to do with the zero-point energy for the X-H bond (X=C, O, N, etc.). Zero-point energy is the lowest energy vibrational mode for bond stretching. The frequency of the zero-point energy is inversely proportional to the square root of the reduced mass of the atom forming the bond. Because deuterium is a heavier atom than protium, the zero-point energy will be lower. Because of the lower frequency for the X-D versus X-H bond, the activation energy for bond-breaking is larger for the X-D, and the larger barrier to reaction results in slower reaction kinetics.<sup>26</sup>

In studies of systems that are thought to occur via proton-coupled electron transfer, KIE studies are often conducted to shed light on the involvement of proton transfer in the reaction. If a primary kinetic isotope effect is observed, this is evidence that reaction occurs either via a PT-ET mechanism or a PCET mechanism. It is not a test to verify PCET over PT first reactivity, but rather a means of verifying that proton transfer is involved in the rate determining step of the reaction sequence. There are many reports of unexpectedly large KIE ratios in the PCET literature, theoretical work has posited that perhaps proton tunneling through the electronic barrier is responsible for such observation. There are also reports that show no KIE, inverse KIE, or small KIE ratios for reactions that occur via PCET.<sup>27-33</sup>

Kinetic deuterium isotope effects for the excited-state reactions between  $[(\text{dpab})_2\text{Ru}(4,4'-(\text{OH})_2\text{bpy})]^{2+}$  and the bipyridinium quenchers were probed. In order to measure the  $k_{\text{H}}/k_{\text{D}}$  values, the deuterio complex was prepared, and transient absorption experiments were conducted in deuterated acetonitrile. Table 4.12 shows the observed

$k_H/k_D$  for  $[(dpab)_2Ru(4,4'-(OH)_2bpy)]^{2+}$  as well as  $[(bpy)_2Ru(4,4'-(OH)_2bpy)]^{2+}$  and  $MQ^+$  and  $BMQ^+$ . Unfortunately, no substantial deuterium kinetic isotope effect could be measured by way of Stern-Volmer quenching. It is possible that the lack of KIE can be explained by the fact that there is a small degree of excited-state quenching for the reaction between  $[(dpab)_2Ru(4,4'-(OH)_2bpy)]^{2+}$  and the respective quenchers. Given the small absolute difference in excited-state lifetime that was measured, the error in such measurements can be large, making it difficult to observe  $k_H/k_D$  values that are between 1 and 2. Further studies would need to be conducted to verify that the value of 1.30 for  $k_H/k_D$  is a true kinetic isotope effect. It would not be unreasonable to assume that it is based on the fact that the transient absorption spectra indicate quenching with  $BMQ^+$  occurs via ESPCET.

**Table 4.12** Summary of KIE Ratios

	<u><math>k_H/k_D</math> <math>MQ^+</math></u>	<u><math>k_H/k_D</math> <math>BMQ^+</math></u>
$[Ru(dpab)_2(4,4'-(OH)_2bpy)]^{2+}$	0.92	1.30
$[Ru(bpy)_2(4,4'-(OH)_2bpy)]^{2+}$	0.90	1.04

For  $[Ru(bpy)_2(4,4'-(OH)_2bpy)]^{2+}$ , the lack of KIE for ESET, however, is not surprising since the ET process that deactivates the excited-state should only require outer sphere contributions from deuterium in the solvent. The global fit analysis also yields a rate constant for the first process (ESET) within the error of the rate constant obtained from the Stern-Volmer analysis of the luminescence lifetime quenching. The rate constant extracted for the second process (PT from a Ru(II) chromophore) is also nearly the same as the extracted rate constant for the pseudo-first-order PT process.

#### 4.3.8 Free Energy Relationship for ET, PT, and PCET Reactions

Free energy relationships can provide insight into reaction mechanisms, such as the nature of the transition state or the thermodynamic barrier to reaction, and in some cases the necessary reorganization for a nonadiabatic reaction. The ability to assess the relationship between the free energy for reaction and the rate reaction can provide mechanistic details about a reaction that could inform the design of molecular systems for unique purposes, including light-induced proton coupled electron transfer reactions. As mentioned in chapter 1, initiating a cascade of reactions with the aim of artificial photosynthesis by photoinduced PCET, or ESPCET, would be beneficial in reducing charge buildup in a system and avoiding high energy intermediate species. With that in mind, this work sought to explore the thermodynamic and kinetic parameters for a series of homologous chromophores and their reaction with bipyridinium quenchers.

Thermodynamics dictate the reaction mechanism observed. As such, a free energy diagram cannot be constructed for these reactions because they operate under different reaction mechanisms. Despite this, it is useful to point out that the kinetics for the PCET reactions observed for dpab and both bipyridinium quenchers are slower than either PT or ET with the other systems. This is potentially a result of the slow kinetics for the concerted reaction versus the transfer of a single proton or electron.

Using the thermodynamics data outlined above, along with the now known reaction mechanism a zone diagram can be constructed to help inform the  $pK_a$  and redox potential region where specific reactions are likely to occur. This type of diagram was recently detailed in an article by Tyburski and coworkers.<sup>34</sup> The article is also a good overview of PCET reactivity. Figure 4.60 shows the resulting zone diagram for the hydroxylated

complexes explored in this chapter.

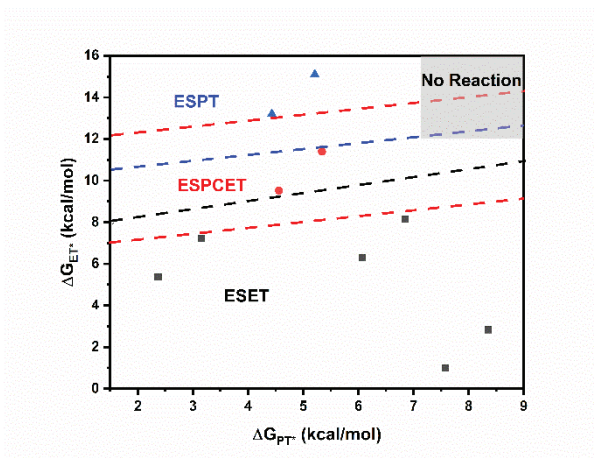


**Figure 4.58** Zone diagram relating the reaction mechanism to the free energy for PT and ET

In figure 4.60, the red lines indicate the broadest region that ESPCET can be expected to occur based on the highest free energies where ESET occurs and the lowest free energy where ESPT occurs. The blue line indicates the lowest expected region where ESPT is likely to become the dominant reaction mechanism, and the black line is where ESET is likely to occur. The slopes of the lines are arbitrary, as more data would be needed to truly distinguish the bounds for these regions. The gray square in the right corner represents where no reaction, ESET, ESPT, or ESPCET will occur based on data for ESET and ESPT that was previously collected. What is evident is that the region in which ESPCET is expected to occur for this system is relatively narrow. Truly the dominant mechanism for these reactions will be via electron transfer, until the free energy is too positive for ET to occur. When the free energy for electron transfer is large, but the free energy for proton transfer is still somewhat reasonable, then PT will be most likely to occur.

#### 4.4 Conclusions

The reactions explored in this chapter were conducted with the purpose of exploring the dominant factors governing whether ESPCET will occur over PT or ET for quenching of the excited state of ruthenium polypyridyl complexes with hopes of using this information to inform the rational design of systems for ESPCET. The thermodynamic parameters for ET, PT, and PCET in both the ground and excited state were measured experimentally and reported here. In addition, the kinetics of excited state quenching were assessed using time-resolved luminescence.

Transient absorption spectroscopy guided the assignment of the reaction mechanism, by allowing for the direct observation of intermediate species formed in sequential reactions. For most thermal proton-coupled electron transfer reactions, reactions occur upon mixing of the reagent and substrate and the ability to observe intermediate species during the course of the reaction is limited by the time resolution of techniques such as stopped-flow. For photoinduced processes, reaction between the substrate and reagent is controlled by the introduction of light. While techniques such as transient absorption spectroscopy are limited by the time resolution (here 10's of nanoseconds), it is still possible to observe intermediate species that are short-lived.

If this work were to be continued, it would be valuable to explore chromophore/quencher combinations that lie within the "PCET region" as depicted in figure 4.56. In addition, looking at the cage escape yields for PCET, ET, and PT reactions would be interesting to explore to compare the relative efficiency of charge separation from the geminate pair for the different reactions.

One roadblock to observing PCET for this system could be the electrostatic repulsion imparted by the positive charge on both the chromophore and quencher. This could limit the interaction distance between the charged species, and therefore make PCET less favorable. The following chapter will explore a system for which the quencher is a neutral species and how this influences excited state reactivity toward either ET, PT, or PCET.

## CHAPTER 4 REFERENCES

- (1) Gagliardi, C. J.; Westlake, B. C.; Kent, C. A.; Paul, J. J.; Papanikolas, J. M.; Meyer, T. J. Integrating Proton Coupled Electron Transfer (PCET) and Excited States. *Coord. Chem. Rev.* **2010**, *254* (21–22), 2459–2471. <https://doi.org/10.1016/j.ccr.2010.03.001>.
- (2) Gust, D.; Moore, T. A.; Moore, A. L. Solar Fuels via Artificial Photosynthesis. *Acc. Chem. Res.* **2009**, *42* (12), 1890–1898. <https://doi.org/10.1021/ar900209b>.
- (3) Weinberg, D. R.; Gagliardi, C. J.; Hull, J. F.; Murphy, C. F.; Kent, C. A.; Westlake, B. C.; Paul, A.; Ess, D. H.; McCafferty, D. G.; Meyer, T. J. Proton-Coupled Electron Transfer. *Chem. Rev.* **2012**, *112* (7), 4016–4093. <https://doi.org/10.1021/cr200177j>.
- (4) Mayer, J. M. PROTON-COUPLED ELECTRON TRANSFER: A Reaction Chemist's View. *Annu. Rev. Phys. Chem.* **2004**, *55* (1), 363–390. <https://doi.org/10.1146/annurev.physchem.55.091602.094446>.
- (5) Lennox, J. C.; Kurtz, D. A.; Huang, T.; Dempsey, J. L. Excited-State Proton-Coupled Electron Transfer: Different Avenues for Promoting Proton/Electron Movement with Solar Photons. *ACS Energy Lett.* **2017**, *2* (5), 1246–1256. <https://doi.org/10.1021/acsenerylett.7b00063>.
- (6) Pannwitz, A.; Wenger, O. S. Photoinduced Electron Transfer Coupled to Donor Deprotonation and Acceptor Protonation in a Molecular Triad Mimicking Photosystem II. *J. Am. Chem. Soc.* **2017**, *139* (38), 13308–13311. <https://doi.org/10.1021/jacs.7b08761>.
- (7) Kirby, J. P.; Roberts, J. A.; Nocera, D. G. Significant Effect of Salt Bridges on Electron Transfer. *7*.
- (8) Damrauer, N. H.; Hodgkiss, J. M.; Rosenthal, J.; Nocera, D. G. Observation of Proton-Coupled Electron Transfer by Transient Absorption Spectroscopy in a Hydrogen-Bonded, Porphyrin Donor–Acceptor Assembly. *J. Phys. Chem. B* **2004**, *108* (20), 6315–6321. <https://doi.org/10.1021/jp049296b>.
- (9) Freys, J. C.; Bernardinelli, G.; Wenger, O. S. Proton-Coupled Electron Transfer from a Luminescent Excited State. *Chem. Commun.* **2008**, No. 36, 4267. <https://doi.org/10.1039/b806175k>.
- (10) Martinez, K.; Stash, J.; Benson, K. R.; Paul, J. J.; Schmehl, R. H. Direct Observation of Sequential Electron and Proton Transfer in Excited-State ET/PT Reactions. *J. Phys. Chem. C* **2019**. <https://doi.org/10.1021/acs.jpcc.8b09268>.
- (11) Yakelis, N. A.; Bergman, R. G. Safe Preparation and Purification of Sodium Tetrakis[(3,5-Trifluoromethyl)Phenyl]Borate (NaBArF<sub>24</sub>): Reliable and Sensitive

- Analysis of Water in Solutions of Fluorinated Tetraarylborates. *Organometallics* **2005**, *24* (14), 3579–3581. <https://doi.org/10.1021/om0501428>.
- (12) Giordano, P. J.; Bock, C. R.; Wrighton, M. S. Excited State Proton Transfer of Ruthenium (II) Complexes of 4, 7-Dihydroxy-1, 10-Phenanthroline. Increased Acidity in the Excited State. *J. Am. Chem. Soc.* **1978**, *100* (22), 6960–6965.
- (13) Arnaut, L. G.; Formosinho, S. J. Excited-State Proton Transfer Reactions I. Fundamentals and Intermolecular Reactions. *J. Photochem. Photobiol. Chem.* **1993**, *75* (1), 1–20. [https://doi.org/10.1016/1010-6030\(93\)80157-5](https://doi.org/10.1016/1010-6030(93)80157-5).
- (14) Kaljurand, I.; Kütt, A.; Sooväli, L.; Rodima, T.; Mäemets, V.; Leito, I.; Koppel, I. A. Extension of the Self-Consistent Spectrophotometric Basicity Scale in Acetonitrile to a Full Span of 28 PKa Units: Unification of Different Basicity Scales. *J. Org. Chem.* **2005**, *70* (3), 1019–1028. <https://doi.org/10.1021/jo048252w>.
- (15) Bockman, T. M.; Kochi, J. K. Isolation and Oxidation-Reduction of Methylviologen Cation Radicals. Novel Disproportionation in Charge-Transfer Salts by x-Ray Crystallography. *J. Org. Chem.* **1990**, *55* (13), 4127–4135. <https://doi.org/10.1021/jo00300a033>.
- (16) Georgopoulos, M.; Hoffman, M. Z. Cage Escape Yields in the Quenching of Tris (2,2'-Bipyridine)Ruthenium(II) by Methylviologen: Presence of Triethanolamine as a Sacrificial Electron Donor. *J. Phys. Chem.* **1991**, *95* (20), 7717–7721. <https://doi.org/10.1021/j100173a031>.
- (17) KELLY, L.; RODGERS, M. INTERMOLECULAR AND INTRAMOLECULAR OXIDATIVE QUENCHING OF MIXED-LIGAND TRIS(BIPYRIDYL)RUTHENIUM(II) COMPLEXES BY METHYL VIOLOGEN. *J. Phys. Chem.* **1995**, *99* (35), 13132–13140. <https://doi.org/10.1021/j100035a015>.
- (18) Ohno, T.; Yoshimura, A.; Prasad, D. R.; Hoffman, M. Z. A Weak .DELTA.G.Degree. Dependence of Back Electron Transfer within the Geminate Redox Pairs Formed in the Quenching of Excited Ruthenium(II) Complexes by Methyl Viologen. *J. Phys. Chem.* **1991**, *95* (12), 4723–4728. <https://doi.org/10.1021/j100165a025>.
- (19) Pannwitz, A.; Wenger, O. S. Proton Coupled Electron Transfer from the Excited State of a Ruthenium(II) Pyridylimidazole Complex. *Phys. Chem. Chem. Phys.* **2016**, *18* (16), 11374–11382. <https://doi.org/10.1039/c6cp00437g>.
- (20) Tyburski, R.; Föhlinger, J.; Hammarström, L. Light Driven Electron Transfer in Methyl-Bipyridine Phenol Complexes Is Not Proton Coupled. *J. Phys. Chem. A* **2018**, *122* (18), 4425–4429. <https://doi.org/10.1021/acs.jpca.8b02221>.

- (21) Eckert, F.; Leito, I.; Kaljurand, I.; Kütt, A.; Klamt, A.; Diedenhofen, M. Prediction of Acidity in Acetonitrile Solution with COSMO-RS. *J. Comput. Chem.* **2009**, *30* (5), 799–810. <https://doi.org/10.1002/jcc.21103>.
- (22) Mayer, J. M.; Rhile, I. J. Thermodynamics and Kinetics of Proton-Coupled Electron Transfer: Stepwise vs. Concerted Pathways. *Biochim. Biophys. Acta BBA - Bioenerg.* **2004**, *1655*, 51–58. <https://doi.org/10.1016/j.bbabi.2003.07.002>.
- (23) Eisenhart, T. T.; Dempsey, J. L. Photo-Induced Proton-Coupled Electron Transfer Reactions of Acridine Orange: Comprehensive Spectral and Kinetics Analysis. *J. Am. Chem. Soc.* **2014**, *136* (35), 12221–12224. <https://doi.org/10.1021/ja505755k>.
- (24) Braslavsky, S. E. Glossary of Terms Used in Photochemistry, 3rd Edition (IUPAC Recommendations 2006). *Pure Appl. Chem.* **2007**, *79* (3), 293–465. <https://doi.org/10.1351/pac200779030293>.
- (25) Kavarnos, G. J.; Turro, N. J. Photosensitization by Reversible Electron Transfer: Theories, Experimental Evidence, and Examples. *Chem. Rev.* **1986**, *86* (2), 401–449.
- (26) Cano-Yelo, H.; Deronzier, A. Photo-Oxidation of Tris(2,2'-Bipyridine)Ruthenium(II) by Para-Substituted Benzene Diazonium Salts in Acetonitrile. Two-Compartment Photoelectrochemical Cell Applications. *J. Chem. Soc. Faraday Trans. 1 Phys. Chem. Condens. Phases* **1984**, *80* (11), 3011–3019. <https://doi.org/10.1039/F19848003011>.
- (27) Milanesi, S.; Fagnoni, M.; Albin, A. (Sensitized) Photolysis of Diazonium Salts as a Mild General Method for the Generation of Aryl Cations. Chemoselectivity of the Singlet and Triplet 4-Substituted Phenyl Cations. *J. Org. Chem.* **2005**, *70* (2), 603–610. <https://doi.org/10.1021/jo048413w>.
- (28) Modern Physical Organic Chemistry. *University Science Books*.
- (29) Bronner, C.; Wenger, O. S. Kinetic Isotope Effects in Reductive Excited-State Quenching of Ru(2,2'-Bipyrazine)<sub>3</sub><sup>2+</sup> by Phenols. *J. Phys. Chem. Lett.* **2012**, *3* (1), 70–74. <https://doi.org/10.1021/jz201494n>.
- (30) Edwards, S. J.; Soudackov, A. V.; Hammes-Schiffer, S. Analysis of Kinetic Isotope Effects for Proton-Coupled Electron Transfer Reactions<sup>†</sup>. *J. Phys. Chem. A* **2009**, *113* (10), 2117–2126. <https://doi.org/10.1021/jp809122y>.
- (31) Hammes-Schiffer, S. Theoretical Perspectives on Proton-Coupled Electron Transfer Reactions. *Acc. Chem. Res.* **2001**, *34* (4), 273–281. <https://doi.org/10.1021/ar9901117>.
- (32) Hammes-Schiffer, S. Proton-Coupled Electron Transfer: Moving Together and Charging Forward. *J. Am. Chem. Soc.* **2015**, *137* (28), 8860–8871. <https://doi.org/10.1021/jacs.5b04087>.

- (33) Kiefer, P. M.; Hynes, J. T. Kinetic Isotope Effects for Nonadiabatic Proton Transfer Reactions in a Polar Environment. 2. Comparison with an Electronically Diabatic Description. *J. Phys. Chem. A* **2004**, *108* (52), 11809–11818. <https://doi.org/10.1021/jp040498h>.
- (34) Kuss-Petermann, M.; Wenger, O. S. Photoacid Behavior versus Proton-Coupled Electron Transfer in Phenol–Ru(Bpy)<sub>3</sub><sup>2+</sup> Dyads. *J. Phys. Chem. A* **2013**, *117* (28), 5726–5733. <https://doi.org/10.1021/jp402567m>.
- (35) Ravensbergen, J.; Brown, C. L.; Moore, G. F.; Frese, R. N.; van Grondelle, R.; Gust, D.; Moore, T. A.; Moore, A. L.; Kennis, J. T. M. Kinetic Isotope Effect of Proton-Coupled Electron Transfer in a Hydrogen Bonded Phenol–Pyrrolidino[60]Fullerene. *Photochem. Photobiol. Sci.* **2015**, *14* (12), 2147–2150. <https://doi.org/10.1039/C5PP00259A>.
- (36) Tyburski, R.; Liu, T.; Glover, S. D.; Hammarström, L. Proton-Coupled Electron Transfer Guidelines, Fair and Square. *J. Am. Chem. Soc.* **2021**. <https://doi.org/10.1021/jacs.0c09106>.

## Chapter 5: Excited-State Proton-Coupled Electron Transfer with 9,10-Anthraquinone

*This work was done in collaboration with Jared Paul's group at Villanova. The physical measurements and syntheses were conducted by his student, Kaitlyn Benson working in the Schmehl lab for a summer under my supervision. I am profoundly grateful for Kaitlyn and her level of dedication to this project.*

### 5.1 Introduction

The previous chapters of this body of work indicate the utility of coupling proton transfer to electron transfer. Concerted proton and electron transfer reactions are well known to be more thermodynamically favorable than electron transfer only. Pourbaix ( $E^0$  vs pH) diagrams provide a schematic representation of the effect of protonation on the free energy for electron transfer.<sup>1,2</sup> For systems in which proton and electron transfer are possible mechanisms in addition to proton-coupled electron transfer, distinguishing between PCET and sequential processes is difficult because these reactions typically occur fast relative to electrochemical experiments. Detailed analysis of the activation parameters of electron transfer, proton transfer and the coupled electron/proton transfer are generally necessary to establish that the proton and electron transfer are indeed coupled in reactions between electron/proton donors and acceptors.<sup>3</sup>

Looking at reactions where ET, PT, and PCET can occur from the excited states of molecules, the electron and proton transfer reactions must compete kinetically with the relaxation of the excited state to the ground state. When considering the possibility of reactions that can occur from the excited-state, including PCET, ET-PT, and PT-ET, systems for which the products of individual reaction processes are readily distinguishable

by experimental techniques is imperative to making an assessment of the reaction dynamics.

In Chapter 4, a series of  $[(LL)_2Ru(4,4'-(OH)_2bpy)]^{2+}$  complexes and mono-quaternized 4,4'-bipyridines were investigated for PCET reactivity originating from the excited-state of the ruthenium chromophore. With this system, the bipyridinium quenchers provided a useful handle for assessing excited state reaction dynamics by visible nanosecond transient absorption spectroscopy. The quenchers allowed for ET, PT, and PCET products to be clearly distinguished from one another. In addition, the system was poised thermodynamically to undergo either ET, PT, or PCET with the ruthenium(II) excited state. A drawback of this system was the charge on the bipyridinium quencher. As mentioned in Chapter 1, donor-acceptor (D-A) distance is an important factor in facilitating concerted electron and proton transfer reactions. One could postulate that having a dicationic chromophore interacting with a cationic quencher may lead to electrostatic repulsion between the two species, increasing the D-A distance.<sup>4</sup>

In an effort to overcome this barrier, a new system was investigated. For the ease of characterization, 4-hydroxy-2,2'-bipyridine ligands were synthesized. Having one hydroxy group simplifies the characterization of the acid-base chemistry. As noted in Chapter 3, for the 4,4'-dihydroxy-2,2'-bipyridine having two acidic protons with  $pK_a$ 's closely spaced made assessing the acidity of the complex difficult. For the proton and electron acceptor, 9,10-anthraquinone was used, as it is a neutral substrate for PCET.

9,10-anthraquinone is not a unique molecule to the study of photoinduced electron transfer. There are many reports for which the complex is used as an oxidative quencher of ruthenium(II) <sup>3</sup>MLCT excited states.<sup>5,6</sup> Additionally, the compound has been incorporated

into a complex molecular triad by Wenger and coworkers, to facilitate the accumulation of multiple charges on a single compound.<sup>7</sup> Quinones are unique in their electron and proton transfer reactivity. In electrochemical studies, quinones are known to undergo electrochemical PCET in aqueous solution at reduced pH. Observation of intermediates is usually precluded by their lack of thermodynamic stability in solution, often semiquinone radical will undergo disproportionation events to generate more stable quinone and hydroquinone compounds. 1,4-dihydroxybenzene was explored by Concepcion and coworkers for its ability to reductively quenching the excited state of  $[(\text{bpy})_2\text{Ru}(\text{bpz})]^{2+}$  ( $\text{bpz}=2,2'$ -bipyrazine) via a photoinduced PCET reaction.<sup>8</sup> This work was substantiated by time resolved electron paramagnetic resonance studies to observe directly the semiquinone radical intermediate.<sup>9</sup>

In addition, quinones are of essential importance in the cascade of reactions that encompass photosynthesis. Their ability to store multiple charges, and the fact that reduction of the quinones to the respective hydroquinone compound occurs at lower potential than would ET only, makes them the ideal molecule for investigation of PCET reactivity.<sup>10</sup>

Explored in this chapter will be the thermodynamics and kinetics for reaction between  $[\text{Ru}(\text{bpy})_2(4\text{-(OH)bpy})]^{2+}$  and 9,10-anthraquinone. For control studies, the ET reaction between  $[\text{Ru}(\text{bpy})_2(4\text{-(OMe)bpy})]^{2+}$  was investigated. Time resolved luminescence was used to determine the rate constant for excited state quenching and transient absorption spectroscopy was used to observe the reaction evolution. A comparison of the reactivity in the presence and absence of added electrolyte was explored.

## 5.2 Experimental

### 5.2.1 Materials

9,10-anthraquinone was purchased from TCI Chemicals and purified as previously reported.<sup>11</sup> Tetrabutylammonium hexafluorophosphate (TBAPF<sub>6</sub>) was obtained from Alfa Aesar and was recrystallized from ethanol and dried *in vacuo*. Tetrabutylammonium hydroxide (TBAOH) was purchased from Alfa Aesar as a 40% solution in CH<sub>3</sub>OH and was used without further purification. 1,8-Diazabicyclo[5.4.0]-7-undecene (DBU) was purchased from TCI and used without further purification.

### 5.2.2 Electrochemical Measurements

Cyclic voltammetry, differential pulse voltammetry and spectroelectrochemical measurements were carried out using a CH Instruments 630 E Electrochemical Analyzer. Acetonitrile was dried over CaH<sub>2</sub> and distilled before use and TBAPF<sub>6</sub> was used as supporting electrolyte. Cyclic voltammetric measurements were done using a glassy carbon working electrode, a platinum wire counter electrode, and an Ag/AgCl pseudoreference electrode with an internal ferrocene standard. Spectroelectrochemical measurements were carried out using an Ocean Optics HR2000 spectrophotometer along with a Pine Research Instruments platinum honey-comb working electrode and a platinum wire counter electrode.

### 5.2.3 Nanosecond Transient Absorption Spectroscopy

Nanosecond transient absorption measurements were done on an Applied Photophysics LKS 60 Laser Flash Photolysis system with laser excitation from a Quantel Brilliant B Q-switched laser with second and third harmonic attachments and an OPO (OPOTEK) for visible light generation, and data recorded using an Agilent Infinium

digitizer. Laser excitation of the sample was typically done at 450 nm, unless otherwise stated.

#### 5.2.4 Steady-State Emission Spectroscopy

Steady state emission measurements were done on a PTI Quantamaster spectrophotometer fit with a Hamamatsu R928 PMT detector system. Sample excitation was done at 450 nm and the emission spectra were observed from 500 – 800 nm.

#### 5.2.5 UV-Visible Absorption Spectroscopy

UV-Visible absorption spectra were recorded on either a Hewlett-Packard 8452A diode array system or Ocean Optics HR2000+ spectrophotometer.

### 5.3 Results and Discussion

#### 5.3.1 Synthesis of Ligands and Complexes

The ligands 4-(OH)bpy and 4-(OMe)bpy were prepared by previously published literature methods. The complexes  $[(bpy)_2Ru(4-(OH)bpy)]^{2+}$  and  $[(bpy)_2Ru(4-(OMe)bpy)]^{2+}$  were prepared from  $[(bpy)_2RuCl_2]$  and each of the ligands as described in Chapter 2.

#### 5.3.2 Thermochemical Analysis

As previously demonstrated in Chapter 4, there is great value in knowing the thermochemical properties of reactants for PCET. The electrochemistry of the complexes  $[Ru(bpy)_2(4-(OH)bpy)]^{2+}$  and  $[Ru(bpy)_2(4-(OMe)bpy)]^{2+}$  were reported in Chapter 2, but are summarized again in table 5.1. The potential for the deprotonated complex was obtained by DPV following addition of DBU to solutions of the complex in  $CH_3CN$ . DBU was used because it is basic enough to react with the hydroxy complex ( $K_{eq} > 10^4$ ), but also

has a positive enough  $\text{DBU}^+/\text{DBU}$  potential that it will not undergo oxidation competitively with the hydroxy complex. Figure 5.1 shows the anodic voltammetry of the 4-(OH)bpy complex in  $\text{CH}_3\text{CN}$ , illustrating the fully reversible oxidation of the complex with no indication that the complex undergoes deprotonation following oxidation. The differential pulse voltammogram analysis in the presence of DBU (fig. 5.1b) shows that the Ru(III/II) potential maximum goes from 0.82 V vs.  $\text{Fc}^+/\text{Fc}$  to 0.55 V following addition of over 100 equivalents of DBU to the solution. Rather than observing a steady shift in the Ru(III/II) potential, the results illustrate two separate oxidation waves when sub-stoichiometric quantities of DBU are added. Addition of DBU results in no change to the Ru(III/II) potential for the methoxy complex.

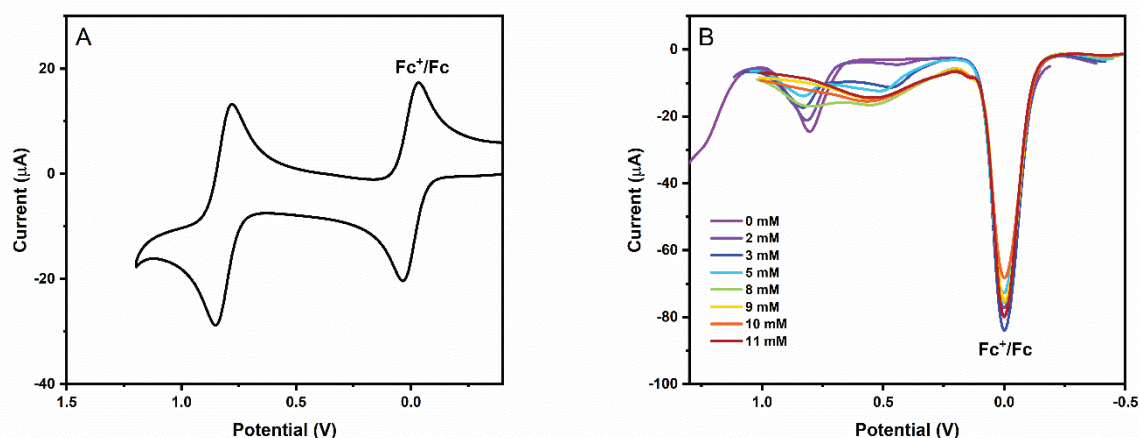


**Figure 5.1** (a) Cyclic voltammetry of  $[(\text{bpy})_2\text{Ru}(\text{OHbpy})]^{2+}$  in  $\text{CH}_3\text{CN}$  / 0.1 M  $\text{TBAPF}_6$  obtained at 0.1 V/s and (b) DPV of  $[(\text{bpy})_2\text{Ru}(\text{OHbpy})]^{2+}$  in the presence of 0 – 11 mM DBU. Potentials vs.  $\text{Fc}^+/\text{Fc}$ .

Although the voltammetry of AQ in  $\text{CH}_3\text{CN}$  has been reported earlier, the measurements were repeated for internal consistency. Figure 5.2 shows CV data for reduction of AQ in  $\text{CH}_3\text{CN}$  and reduction in  $\text{CH}_3\text{CN}$  containing triflic acid (HOTf). Two reversible reductions are observed in the absence of added HOTf, resulting in formation of

the 9,10-dihydroxyanthracene dianion ( $E_{\text{AQ}}^0(0/-) = -1.32 \text{ V vs. Fc}^+/\text{Fc}$ ). In the presence HOTf, a strong acid in  $\text{CH}_3\text{CN}$ , the voltammetry is considerably more complex. The first reduction is observed at much more positive potentials ( $E_{\text{HAQ}^+}^0(+/0) = -0.22 \text{ V vs Fc}^+/\text{Fc}$ ) and appears to be followed by a second reduction. An oxidation wave is observed as well, but with a large  $\Delta E_p$ ; this type of behavior is observed for quinone reduction in protic solvents and is the result of sequential reduction and protonation (or reduction, protonation and disproportionation) to yield the dihydroxyanthracene. According to literature reports, the reduction is likely a proton coupled electron transfer at the electrode as there is no direct evidence to suggest protonation precedes reduction.<sup>12</sup>

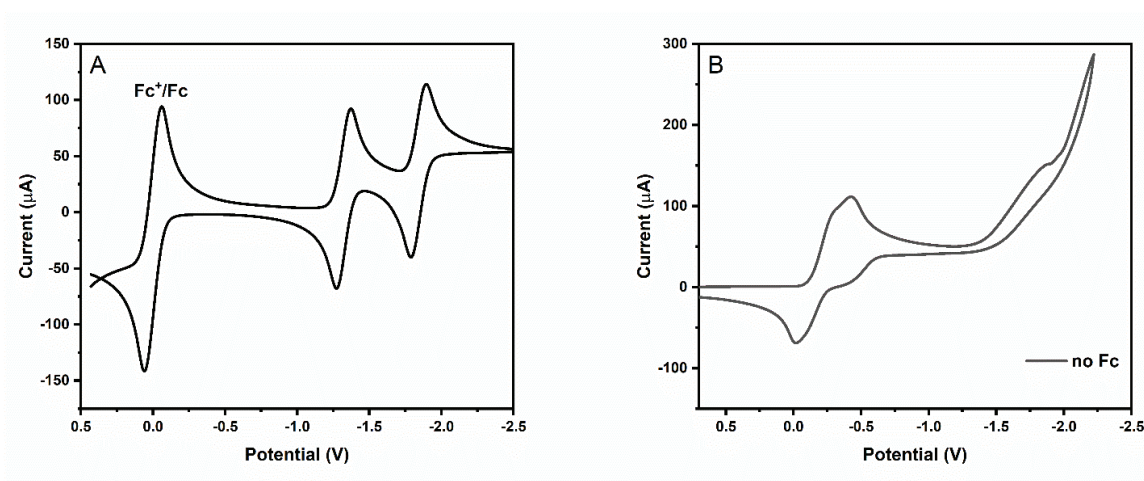


**Figure 5.2** Cyclic voltammetry of 3 mM AQ in  $\text{CH}_3\text{CN}$  / 0.1 M  $\text{TBAPF}_6$  obtained at 0.1 V/s in the presence of (a) 0 M and (b) 15 mM triflic acid). Potentials vs.  $\text{Fc}^+/\text{Fc}$ .

In order to determine the  $pK_a$  of the  $[\text{Ru}(\text{bpy})_2(4\text{-(OH)bpy})]^{2+}$ , a photometric titration was done, as with the previously evaluated hydroxy complexes. In order to evaluate the titration data, the spectra of both the protonated and deprotonated complexes must be known. The absorption spectra in acetonitrile were reported for both the protonated

and deprotonated forms, as well as for the control complex,  $[\text{Ru}(\text{bpy})_2(4\text{-(OMe)bpy})]^{2+}$  in Chapter 2, but are shown in figure 5.3 for convenience.

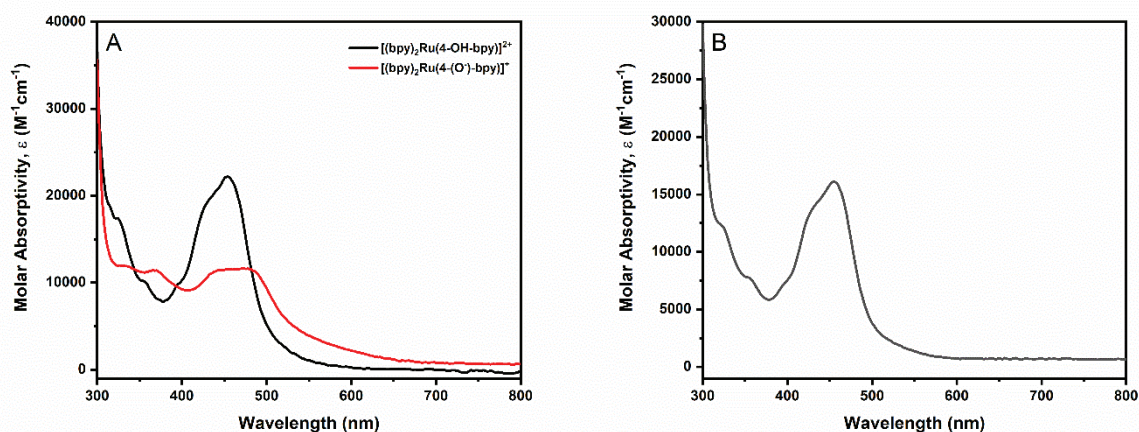


**Figure 5.3.** (a) UV-vis absorption spectrum of  $[(\text{bpy})_2\text{Ru}(\text{OHbpy})]^{2+}$  in  $\text{CH}_3\text{CN}$  (black) and in the presence of an excess of tetra-*n*-butylammonium hydroxide. (red) (b) the UV-vis absorption spectrum of  $[(\text{bpy})_2\text{Ru}(4\text{-(OMe)bpy})]^{2+}$  in  $\text{CH}_3\text{CN}$ .

The UV-vis absorption spectra of  $[(\text{bpy})_2\text{Ru}(4\text{-(OH)bpy})]^{2+}$  and  $[(\text{bpy})_2\text{Ru}(4\text{-(OMe)bpy})]^{2+}$  have spectral features in  $\text{CH}_3\text{CN}$  solution that are very similar to  $[(\text{bpy})_3\text{Ru}]^{2+}$ . Thus, the spectra have a bpy localized  $\pi \rightarrow \pi^*$  transition around 290 nm and two close lying  $d\pi \rightarrow \pi^*$  metal-to-ligand charge transfer transitions near 450 nm (table 5.1). Figure 5.3a shows absorption spectra of  $[(\text{bpy})_2\text{Ru}(4\text{-(OH)bpy})]^{2+}$  in  $\text{CH}_3\text{CN}$  as well as the complex in the presence of an 10x molar excess of  $\text{TBAPF}_6$ , yielding the spectrum of the deprotonated complex  $[(\text{bpy})_2\text{Ru}(\text{Obpy})]^{+}$ . Figure 5.3b shows the spectrum of  $[(\text{bpy})_2\text{Ru}(4\text{-(OMe)bpy})]^{2+}$  in  $\text{CH}_3\text{CN}$ . Maxima for the complexes are given in table 5.1; the maxima illustrate that the hydroxy and methoxy complexes have very similar spectra.

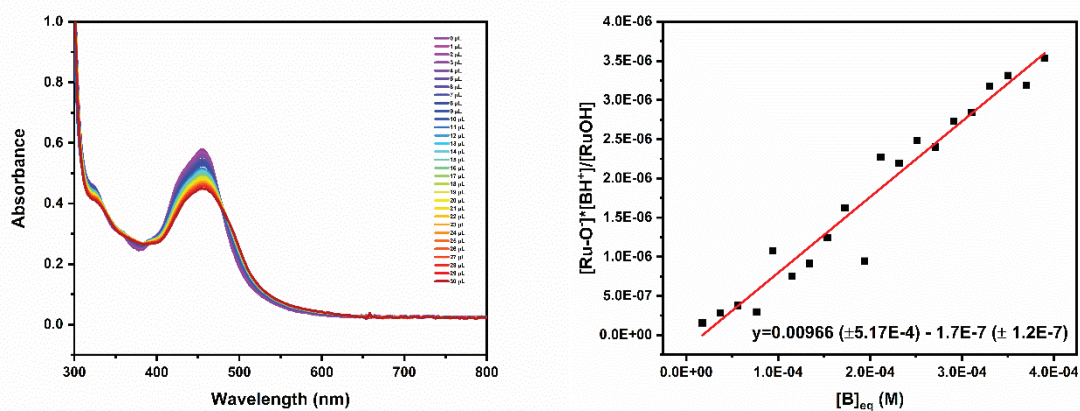


**Figure 5.4** Spectra from the titration of  $[\text{Ru}(\text{bpy})_2(4\text{-(OH)bpy})]^{2+}$  with 4-aminopyridine (left) and the linear fit of the concentrations calculated from the absorption spectra (right)

Titration of  $[(\text{bpy})_2\text{Ru}(4\text{-(OH)bpy})]^{2+}$  with the base 4-aminopyridine ( $\text{p}K_a=17.63$ ) in  $\text{CH}_3\text{CN}$  allowed determination of the  $\text{p}K_a$  of the hydroxy bipyridine; spectra from the titration as well as the linear fit to determine the equilibrium constant are shown in figure 5.4. Given the  $\text{p}K_a$  of 4-aminopyridine in  $\text{CH}_3\text{CN}$  and the spectral data, the  $\text{p}K_a$  of the hydroxy bipyridine coordinated to Ru was found to be 15.6, indicating that the ground state of the complex is a relatively weak acid.

The excited state acid dissociation constant is a function of the ground state  $\text{p}K_a$  for  $[\text{Ru}(\text{bpy})_2(4\text{-(OH)bpy})]^{2+}$  and the maximum emission energies for the protonated and deprotonated complexes (equation 5.1). Since the deprotonated

$$\text{p}K_a^* = \text{p}K_a - \frac{(E_{\text{em}}(\text{Ru(II)-OH}) - E_{\text{em}}(\text{Ru(II)-O}^-))}{2.303RT} \quad (5.1)$$

complex is nonluminescent at room temperature, an estimate of the room temperature emission energy was obtained from extrapolation from 77 K emission data (supplementary material). The resulting  $\text{p}K_a^*$  was 14.5, indicating that the MLCT state of  $[(\text{bpy})_2\text{Ru}(4-$

$[(\text{OH})\text{bpy}]^{2+}$  is slightly more acidic than the ground state; this suggests the MLCT state is largely  $\text{Ru}(d\pi) \rightarrow \text{bpy}(\pi^*)$  in character.

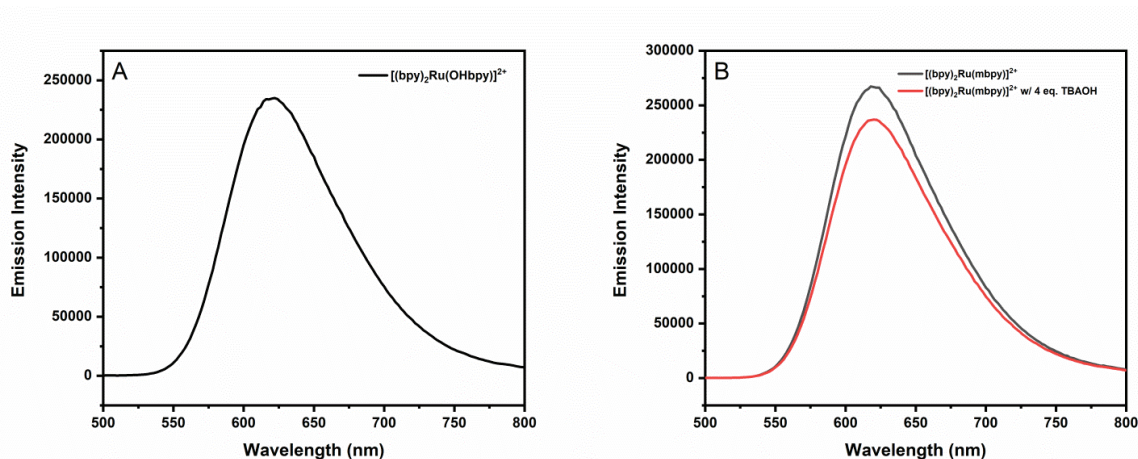


**Figure 5.5** (a) Luminescence spectra of  $[(\text{bpy})_2\text{Ru}(4\text{-OHbpy})]^{2+}$  in  $\text{CH}_3\text{CN}$  at room temperature. (b) Room temperature luminescence of  $[(\text{bpy})_2\text{Ru}(4\text{-(OMe)bpy})]^{2+}$  in  $\text{CH}_3\text{CN}$ . Excitation wavelength : 450 nm.

The excited state energy can be calculated from the emission maxima. Room temperature emission spectra of  $[(\text{bpy})_2\text{Ru}(4\text{-(OH)bpy})]^{2+}$  and of  $[(\text{bpy})_2\text{Ru}(4\text{-(OMe)bpy})]^{2+}$  in  $\text{CH}_3\text{CN}$  solutions are shown in figure 5.5. For  $[(\text{bpy})_2\text{Ru}(\text{OHbpy})]^{2+}$  no luminescence is observed upon the addition of a small molar excess of tetra-*n*-butylammonium hydroxide. The spectrum of  $[(\text{bpy})_2\text{Ru}(\text{O}^-\text{bpy})]^{2+}$  was obtained from 77 K luminescence observed for the complex in 1:1 methanol/ethanol. (figure 5.6).

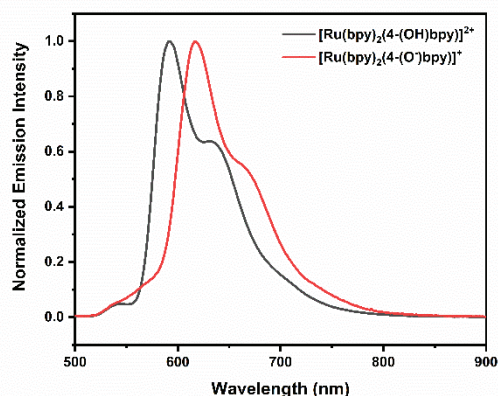


**Figure 5.6** 77 K emission spectra in 1:1 methanol/ethanol solution for  $[\text{Ru}(\text{bpy})_2(4\text{-(OH)bpy})]^{2+}$  and  $[\text{Ru}(\text{bpy})_2(4\text{-(O}^-\text{)bpy})]^+$

Correlation of the 77 K emission maxima with room temperature maxima for a series of hydroxy bipyridine Ru(II) complexes allowed estimation of the room temperature excited state energy of the nonluminescent deprotonated complex. The spectra were used to determine energies for the reactive MLCT ( $^*[\text{Ru}(\text{bpy})_2(4\text{-(OH)bpy})]^{2+}$  and  $^*\text{Ru}(\text{II})\text{-O}^-$ ) species.

**Table 5.1** Summary of redox and excited state energies

Complex $[(\text{bpy})_2\text{RuL}]^2+$	MLCT $\lambda_{\text{max}}$ , $\text{CH}_3\text{CN}$ , nm	$\lambda_{\text{max}}^{\text{em}}$ , RT $\text{CH}_3\text{CN}$ , nm	$\lambda_{\text{max}}^{\text{em}}$ , 77 K 1:1 $\text{MeOH}:\text{EtOH}$ , nm	$E_{\text{em}}$ , RT $\text{CH}_3\text{CN}$ , eV	$E^0$ ( $\text{Ru}(\text{III}/\text{II})$ ) V vs. $\text{Fc}^+/\text{Fc}$	$E^0$ ( $\text{Ru}(\text{III}/\text{II}^*)$ ) V vs. $\text{Fc}^+/\text{Fc}$
4-(OH)bpy	458	624	590	1.99	0.82	-1.17
4-(O <sup>-</sup> )bpy	472	--	617	~ 1.92*	0.55	~ -1.4
4-(OMe)bpy	460	620	--	2.0	0.83	-1.17

The emission maxima were used for the approximate excited state energies; thus, these energies are slightly lower than the  $E_{00}$  energies that might be obtained from a Franck-Condon fit of 77 K luminescence spectra.

The excited state singlet and triplet AQ are well established and were obtained from literature sources.<sup>13</sup> Most important to the discussion below is the triplet energy of AQ (<sup>3</sup>AQ), which, at 2.7 eV, is well above the energies of the triplet states of the two complexes used here as electron and/or proton donors. That being said, energy transfer is unlikely to occur from the [Ru(bpy)<sub>2</sub>(4-(OH)bpy)]<sup>2+</sup> excited state to form the <sup>3</sup>AQ.

To begin analysis of the free energy for ET, PT, and ESPCET, for [(bpy)<sub>2</sub>Ru(OHbpy)]<sup>2+</sup> (Ru(II)OH) and AQ, formation of the oxidized and deprotonated complex and the reduced and protonated AQ (the semiquinone radical) can occur via electron transfer followed by proton transfer or the converse, as shown in figure 5.6. The redox potentials for the Ru complex oxidation and the AQ reduction in CH<sub>3</sub>CN are well established and have small margins of error, thus ΔG<sub>ET</sub> is accurate. However, the associated pK<sub>a</sub> values for the Ru(III)-OH complex and AQ<sup>•</sup> species, and the associated ΔG<sub>PT</sub>, are much more difficult to determine.

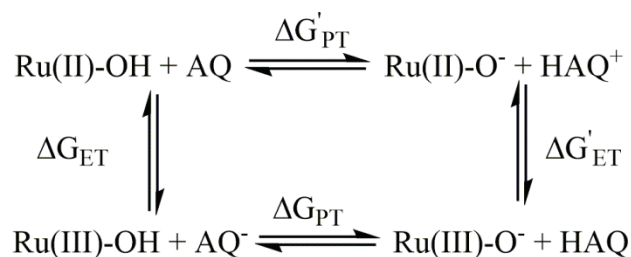


**Figure 5.7** Ground state reactions of Ru(bpy)<sub>2</sub>(4-(OH)bpy)]<sup>2+</sup> (Ru(II)-OH) and AQ.

As demonstrated above, the pK<sub>a</sub> of the Ru(II)OH can be determined accurately, however, the pK<sub>a</sub> of HAQ<sup>+</sup> is not known in CH<sub>3</sub>CN although it can be estimated to be lower than 2 (more likely <0). This estimate was made using a reported bond dissociation energy for the semiquinone radical obtained computationally.<sup>14</sup> Using this value and the measured redox potential for the semiquinone, the pK<sub>a</sub> of HAQ<sup>+</sup> can be calculated from a

thermodynamic cycle. The bond dissociation energy was converted to a bond dissociation free energy by incorporating a free energy term specific to acetonitrile solvent for H-atom transfer processes.<sup>12</sup> Thus, an estimate of the proton transfer equilibrium between Ru(II)OH and AQ can be made, yielding  $\Delta G'_{PT}$ . It is also possible to obtain an estimate of the potential for oxidation of Ru(II)O<sup>-</sup>,  $E^0_{RuO-(III/II)}$ , and the reduction potential for AQH<sup>+</sup>,  $E^0_{AQH(+/0)}$ , as shown by the DPV of Ru(II)OH in various concentrations of the base DBU (Fig. 3) and the CV of AQ in the presence of triflic acid (Fig. 4). With this information  $\Delta G'_{ET}$  ( $-nF(E^0_{AQH(+/0)} - E^0_{RuO-(III/II)})$ ) and  $\Delta G'_{PT}$  ( $2.3RT(pK_a(\text{Ru(II)OH}) - pK_a(\text{HAQ}^+))$ ) can be determined and the overall free energy for the ground state ET/PT process ( $\Delta G'_{PT} + \Delta G'_{ET}$ ) can be estimated to be +44 kcal/mol, and is therefore very endergonic. Thus, there is no concern about ground state proton transfer or electron transfer occurring to any extent upon mixing  $[\text{Ru}(\text{bpy})_2(4\text{-(OH)bpy})]^{2+}$  and AQ in any ratio.

The free energies for excited state electron transfer and proton transfer differ markedly since the excited state energy is approximately 2 eV above the ground state. Figure 5.7 shows the reactions associated with excited state electron and proton transfer. Of particular note is the fact that excited state proton transfer can result in either the ground

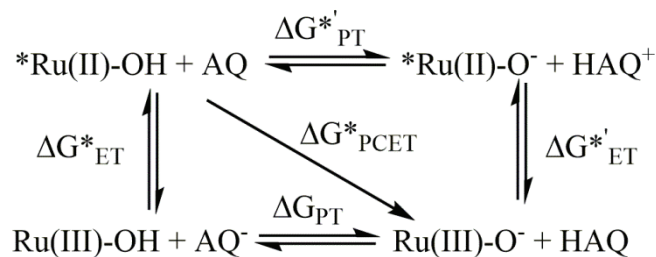


**Figure 5.8** Reactions of  $[\text{Ru}(\text{bpy})_2(4\text{-(OH)bpy})]^{2+}$  (Ru(II)-OH\*) (photoexcited) and AQ in CH<sub>3</sub>CN

state (figure 5.8, PT\*) or the excited state (figure 5.8, PT\*\*) of the deprotonated complex. Determination of the free energy of the PT\*/ET reaction can be approached by determining  $\Delta G^*_{PT}$  and  $\Delta G^*_{ET}$ . An good estimate of  $\Delta G^*_{PT}$  can be obtained using the approximate  $pK_a$  for  $HAQ^+$  discussed above and the  $pK_a$  for  $^*[\text{Ru}(\text{bpy})_2(4\text{-(OH)bpy})]^{2+}$ .

Combining this with the  $pK_a$  of  $HAQ^+$  (above), the  $\Delta G^*_{PT}$  value is + 19 kcal/mol. Thus, excited state proton transfer to form  $HAQ^+$  and the excited state of the deprotonated complex,  $[(\text{bpy})_2\text{Ru}(\text{O}^-\text{bpy})]^{2+*}$  is very endergonic.

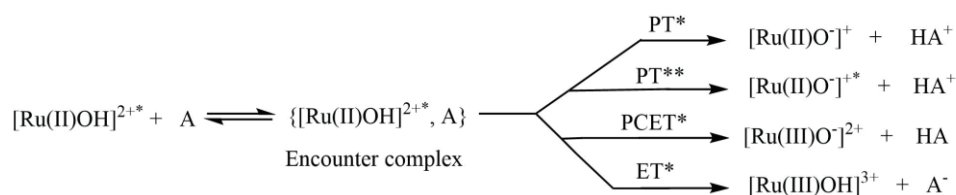


**Figure 5.9** Possible excited state reactions between  $[\text{Ru}(\text{bpy})_2(4\text{-(OH)bpy})]^{2+}$  (Ru(II)-OH) and AQ (A)

The excited state of  $[(\text{bpy})_2\text{Ru}(\text{O}^-\text{bpy})]^{2+}$  is 44 kcal/mol above the ground state and thus proton transfer to yield the ground state of the deprotonated complex (figure 5.8 PT\*) winds up being exergonic by over 25 kcal/mol. The free energy for excited state electron transfer from  $[(\text{bpy})_2\text{Ru}(\text{OHbpy})]^{2+*}$  to AQ is determined from  $E^0_{\text{RuOH(III/II)}}$  (0.82 V vs  $\text{Fc}^+/\text{Fc}$ ),  $E^0_{\text{AQ}(0/-)}$  (-1.32 V vs  $\text{Fc}^+/\text{Fc}$ ) and the excited state energy of  $[(\text{bpy})_2\text{Ru}(\text{OHbpy})]^{2+}$  (1.98 eV). This results in a  $\Delta G^*_{ET}$  of + 3.7 kcal/mol, much smaller than that for excited state proton transfer, but still endergonic.

**Table 5.2** Summary of Free Energies for ET, PT and PCET Reactions

$\Delta G$ (kcal/mol)	ET	PT	PCET	ET*	PT*	PCET*
$[Ru(bpy)_2(4-OH)bpy]^{2+}$	49.3	21	44	3.7	19	-7
$[Ru(bpy)_2(4-OMe)bpy]^{2+}$	49.6			3.5		

The free energy of the PCET\* reaction can most easily be obtained from the sum of  $\Delta G^*_{PT}$  (19 kcal/mol, above) and  $\Delta G^*_{ET}$ . The latter is the sum of  $E^0_{HAQ^+(+/0)}$  (-0.22 V vs.  $Fc^+/Fc$ ),  $-E^0_{RuO-(III/II)}$  (-0.55 V vs.  $Fc^+/Fc$ ) and the excited state energy of  $[(bpy)_2Ru(II)(4-(O^-)bpy)]^+$  (1.92 eV). This results in a  $\Delta G^*_{ET}$  of -26.5 kcal/mol and an overall  $\Delta G^*_{PCET}$  of approximately -7 kcal/mol or very nearly zero. The free energies of all the processes discussed above are summarized in table 5.2. From the diagram it is clear that, thermodynamically, the excited state of  $[(bpy)_2Ru(4-(OH)bpy)]^{2+}$  should react by PCET\*, however, the free energy for electron transfer (ET<sub>1</sub>\*) is only slightly endergonic and, in comparison to related systems evaluated in Chapter 4 of similar Ru(II) hydroxybipyridine chromophores and 4-(4'-pyridyl)-N-alkylpyridinium ions, electron transfer would be expected to be the kinetically favored process.

### 5.3.3 Simulation of ET, PT, and PCET Product Spectra

In order to spectroscopically evaluate the products of photoreactions between the photoexcited complexes and AQ, the absorption spectra of  $[(bpy)_2Ru(4-(OH)bpy)]^{3+}$  and  $[(bpy)_2Ru(4-(O^-)bpy)]^{2+}$  are required. For  $[(bpy)_2Ru(4-(OH)bpy)]^{3+}$  this was accomplished by spectroelectrochemistry. The oxidized species had a prominent absorption maximum at 340 nm and a much weaker, broad absorption with a maximum near 500 nm. Generation of the oxidized and deprotonated complex,  $[(bpy)_2Ru(4-(O^-)bpy)]^{2+}$ , required a different approach. The complex can be photochemically oxidized by one electron by irradiation

with visible light in the presence of 4-bromophenyl diazonium  $\text{BF}_4^-$  in the presence of a tenfold excess of pyridine. The spectral changes observed included a new maximum at 340 nm and broad, featureless absorption throughout the visible out to 650 nm. The absorption spectra of  $\text{AQ}^-$  and  $\text{HAQ}^\bullet$  in  $\text{CH}_3\text{CN}$  are also needed to generate the anticipated spectra for the  $\text{ET}^*$  and the  $\text{PCET}^*$  reactions, respectively (eq. 1). The  $\text{AQ}^-$  spectrum was obtained by spectroelectrochemistry of AQ in  $\text{CH}_3\text{CN}$ . The resulting difference spectra for ESET and ESPT are shown in figure 5.9.

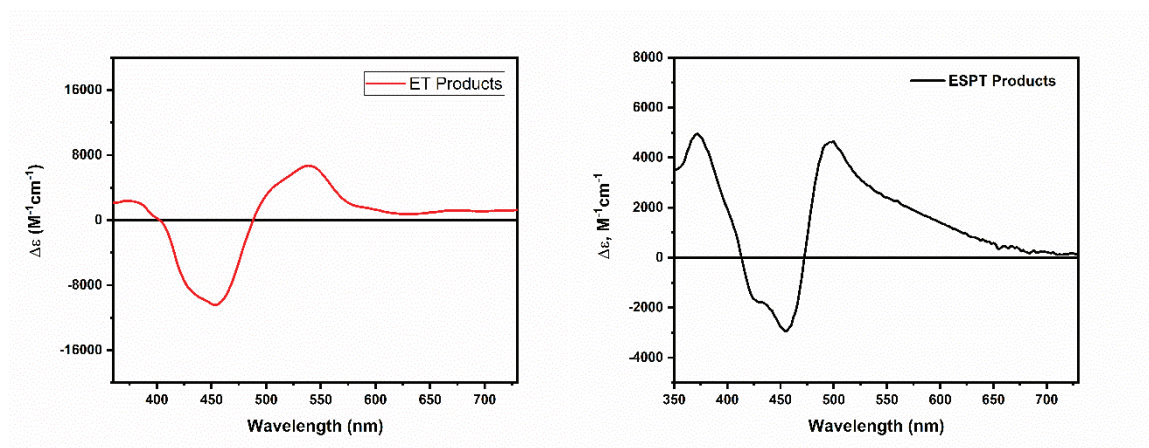


**Figure 5.10** The difference absorption spectra generated from UV-Vis spectra and spectroelectrochemistry for ESET (left) and ESPT (right) with AQ

In order to generate the spectrum for the ESPCET products, the spectrum of the semiquinone radical must be obtained. The  $\text{HAQ}^\bullet$  species readily disproportionates and the spectrum must be obtained by generating the transient species via pulsed laser excitation. The AQ triplet excited state reacts with 2-propanol via a H atom transfer process to yield the semiquinone radical (*vide infra*). Nanosecond time-resolved absorption spectroscopy was used for the determination of excited state lifetimes and also in the evaluation of radical ion products produced in bimolecular reactions of the excited states of complexes. The  $\text{HAQ}^\bullet$  was generated by 355 nm excitation (third harmonic output of a Nd: YAG laser) of

AQ in  $\text{CH}_3\text{CN}/2$ -propanol (0.1 M). The photoreaction involves H atom transfer from 2-propanol to the  $^3\text{AQ}$  to yield  $\text{HAQ}\cdot$  and the acetone ketyl radical (figure 5.10). Essentially the same spectrum has been reported in previously published work.<sup>5</sup>

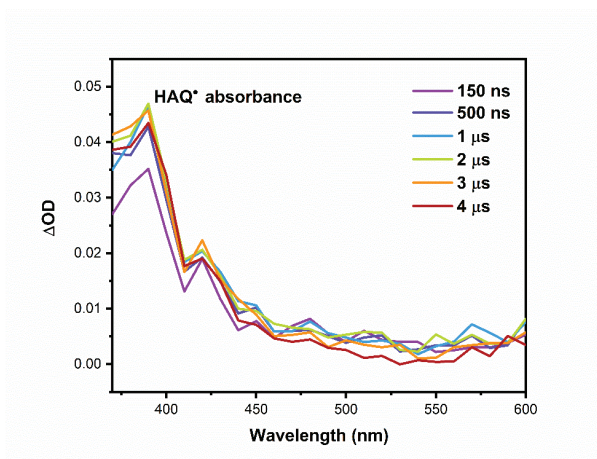


**Figure 5.11** TA of AQ in presence of *i*-prOH : spectrum of the HAQ radical.

The ESPCET product spectrum was generated using data from TA studies of AQ and the spectrum of the oxidized deprotonated ruthenium complex obtained by oxidative quenching of the ruthenium excited state by 4-bromobenzenediazonium tetrafluoroborate in the presence of pyridine. The resultant spectrum is shown in figure 5.11.

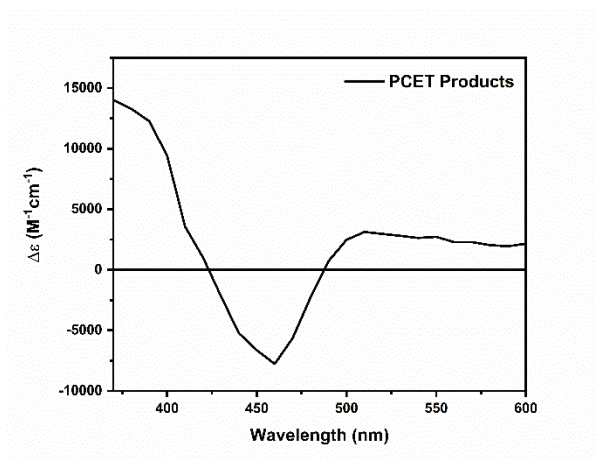


**Figure 5.12** Simulated PCET product spectrum for the reaction of  $[\text{Ru}(\text{bpy})_2(4\text{-(OH)bpy})]^{2+}$  with AQ

### 5.3.4 Quenching of Ruthenium(II) Excited States by AQ

Luminescence lifetime quenching of  $[(\text{bpy})_2\text{Ru}(\text{Xbpy})]^{2+}$  ( $\text{X} = \text{OH}$  or  $\text{OCH}_3$ ) by AQ in  $\text{N}_2$  degassed room temperature  $\text{CH}_3\text{CN}$  solution was examined and the Stern-Volmer Quenching kinetic plots are shown in figures 5.13 and 5.14. While the solubility limit of AQ in  $\text{CH}_3\text{CN}$  is less than 5 mM, at least 70% of the luminescence of each complex was quenched and quenching rate constants obtained were near  $10^9 \text{ M}^{-1}\text{s}^{-1}$ . Rate constants obtained were for either  $\text{ET}^*$ ,  $\text{PT}^{**}$  or  $\text{PCET}^*$  reaction of the excited state with AQ.

**Table 5.3** Lifetimes of Ru(II) complexes and quenching rate constants with AQ

	$\tau_0$ (ns)	$k_q$ ( $\text{M}^{-1}\text{s}^{-1}$ )
$[\text{Ru}(\text{bpy})_2(4\text{-OH)bpy}]^{2+}$	820	1.4 E-9
$[\text{Ru}(\text{bpy})_2(4\text{-OMe)bpy}]^{2+}$	912	7.8E-8

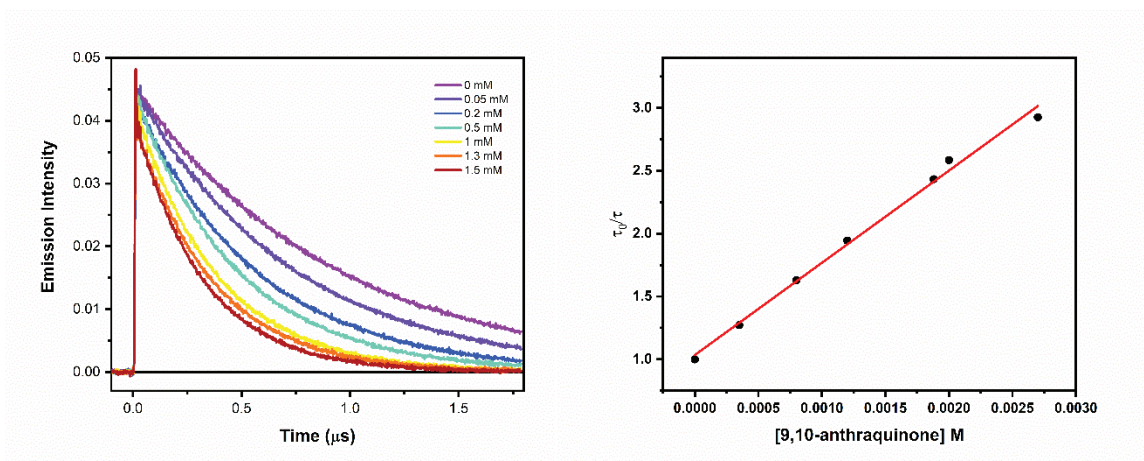


**Figure 5.13** Luminescence lifetime quenching of  $[\text{Ru}(\text{bpy})_2(4\text{-(OMe)bpy})]^{2+}$  by AQ in acetonitrile

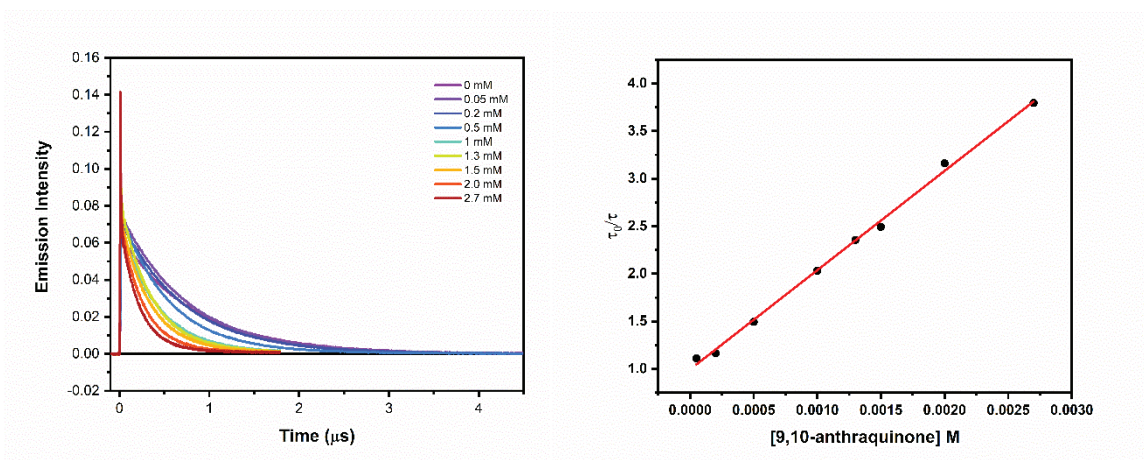


**Figure 5.14** Luminescence lifetime quenching of  $[\text{Ru}(\text{bpy})_2(4\text{-(OH)bpy})]^{2+}$  by AQ in acetonitrile

Transient absorption spectra of  $[\text{Ru}(\text{bpy})_2(4\text{-(OH)bpy})]^{2+}$  and  $[\text{Ru}(\text{bpy})_2(4\text{-(OMe)bpy})]^{2+}$  with and without AQ present were obtained. Both  $[(\text{bpy})_2\text{Ru}(4\text{-(OH)bpy})]^{2+}$  and  $[(\text{bpy})_2\text{Ru}(4\text{-(OMe)bpy})]^{2+}$  have excited state absorption features that are closely related to that of  $[(\text{bpy})_3\text{Ru}]^{2+}$ . Along with bleaching of the MLCT absorption in the 400 to 500 nm region, a strong excited state absorption is observed between 350 and 400 nm. This absorption has been attributed to a  $\pi_1^* \rightarrow \pi_2^*$  transition of the  $\text{bpy}^{\cdot-}$  like component of

the  $^3\text{MLCT}$  excited state. The spectra for the two complexes reported here are shown in figures 5.15a and 5.16a. Both complexes exhibit relatively strong luminescence in the absence of quenching species and the observed excited state absorption at wavelengths longer than  $\sim 575$  nm results from transient absorption measurements made that include correction for excited state emission. It is possible that the net excited state absorption observed may represent an overcorrection of the observed transient signal for the luminescence.

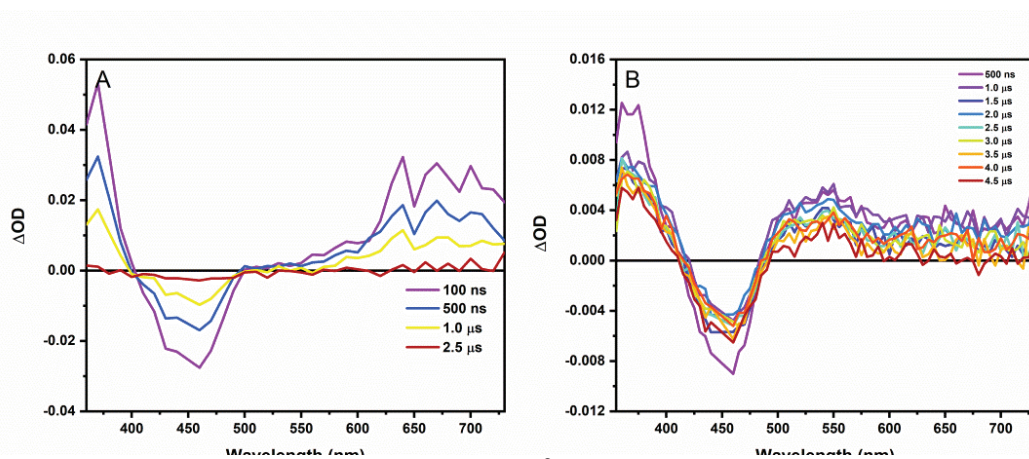


**Figure 5.15** TA spectra of  $[(\text{bpy})_2\text{Ru}(\text{OHbpy})]^{2+}$  in  $\text{CH}_3\text{CN}$  solution at room temperature in the presence of (a) 0 M and (b) 2.6 mM AQ and 20 mM  $\text{TBAPF}_6$ .

Initial studies in pure acetonitrile solution indicated that excited state quenching occurs, however transient absorption spectra show little absorption from any charge separated species. Earlier reports of photoinduced electron transfer involving electron donors and AQ and other substituted anthraquinone derivatives in nonaqueous solvents were observed to have higher charge separation yields in the presence of added electrolytes.

<sup>6</sup> When transient spectra were obtained for each of the Ru(II) complexes with AQ in  $\text{N}_2$  degassed  $\text{CH}_3\text{CN}$  in the presence of  $\text{TBAPF}_6$ , the resulting spectra are shown in Figures 5.15b and 5.16b. In each case the AQ concentration, 2.6 mM, was close to the saturation

concentration and resulted in quenching of between 65 and 75% of the excited chromophores. The magnitude of the transient signals at longer times were small for both complexes, indicating that only a small fraction of the radical ion species created escape the encounter complex. If the excited state reaction is ET\*, the encounter complex would consist of a 3+/1- radical ion pair, while PCET\* would yield a 2+/0 pair. Despite the low yield of radical ions, the spectral features are clearly defined for the species escaping the encounter complex. The recombination of the ions to return to starting materials, typically on the scale of hundreds of microseconds, is not shown and was not evaluated. However, no net products were formed upon prolonged photolysis of the reactants.

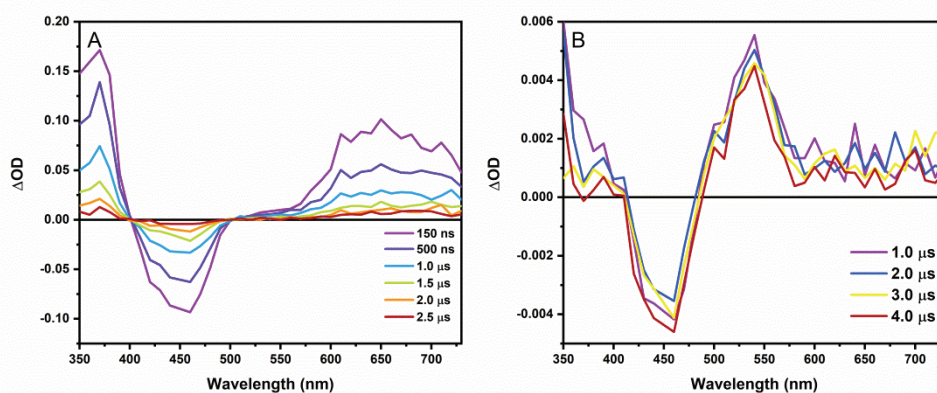


**Figure 5.16** TA spectra of  $[(\text{bpy})_2\text{Ru}(4\text{-(OMe)bpy})]^{2+}$  in  $\text{CH}_3\text{CN}$  at room temperature in the presence of (a) 0 and (b) 2.6 mM AQ and 20 mM  $\text{TBAPF}_6$ .

At this point it is necessary to comment on the observed behavior of  $[(\text{bpy})_2\text{Ru}(\text{OMe}\text{bpy})]^{2+}$ . The excited state of this complex does react with AQ and the only thermodynamically accessible path is ET\* to yield  $[(\text{bpy})_2\text{Ru}(4\text{-(OMe)bpy})]^{3+}$  and  $\text{AQ}^-$ . From figure 5.10 it is clear that  $\text{AQ}^-$  has a strong absorption at 550 nm and this would be expected to appear in the spectrum of the radical ions generated following charge separation of the electron transfer products. What is observed in the presence of added

electrolyte is relaxation of the excited state in the span of a few microseconds with *a small signal for radical ions*. As a result, it appears that, while excited state electron transfer is certainly the reaction between the photoexcited methoxy complex and AQ, the yield of radical ions from the encounter complex (a 3<sup>+</sup>/1<sup>-</sup> complex) is very small, but suggests the formation of AQ<sup>•-</sup>. In the absence of added electrolyte there is no measurable signal for radical ion products, only the excited state decay.

For [(bpy)<sub>2</sub>Ru(HObpy)]<sup>2+</sup>, the transient absorption spectrum of figure 5.15, obtained in the presence of added electrolyte, clearly illustrates the appearance of long lived radical ions. The spectrum exhibits features expected for ET<sub>1</sub>\* and for PCET\*. For PCET\* the spectrum would be expected to include absorption characteristics of [(bpy)<sub>2</sub>Ru(III)(O<sup>-</sup>bpy)]<sup>2+</sup> and HAQ<sup>0</sup>. The spectrum of HAQ<sup>0</sup>, shown in figure 5.11, has spectral features similar to that of figure 7, which also has a bleach in the 450-500 nm region that would be characteristic of the Ru(III) species. However, between a few hundred nanoseconds and 3 μs there is absorption between 500 and 550 nm that is not characteristic of the excited state or HAQ<sup>0</sup>, but would be expected for AQ<sup>•-</sup>, the ET\* product. The fact that this absorbance is gone after a little over 3 μs is the result of intermolecular protonation of AQ<sup>•-</sup> by the protonated complex.

#### 5.4 Conclusions

In summary, reaction of a Ru(II) 4-hydroxy-2,2'-bipyridine complex excited state with anthraquinone resulted in products emerging from the reaction cage that were consistent with a coupled electron transfer from the Ru(II) center and proton transfer from the hydroxy substituent to the anthraquinone acceptor. Related reaction of the <sup>3</sup>MLCT state

of a Ru(II) 4-methoxy-2,2'-bipyridine complex with AQ resulted in only electron transfer products out of the reaction cage. This system thus serves as an example of an excited state reaction where net products are observed following PCET between a photoexcited chromophore (a  $^3\text{MLCT}$  excited state) having both a metal center capable of being oxidized and a substituent  $-\text{OH}$  moiety that can serve as proton donor and a reactant capable of accepting both protons and electrons. Such reactions only occur when the excited state electron transfer is endergonic and the net PCET is exergonic. This result adds to the very limited number of bimolecular systems that definitively exhibit excited state proton coupled electron transfer within an encounter complex.<sup>15</sup>

## CHAPTER 5 REFERENCES

- (1) Rountree, E. S.; McCarthy, B. D.; Dempsey, J. L. Decoding Proton-Coupled Electron Transfer with Potential-PK(a) Diagrams: Applications to Catalysis. *Inorg. Chem.* **2019**, *58* (10), 6647–6658. <https://doi.org/10.1021/acs.inorgchem.8b03368>.
- (2) Huynh, M. H. V.; Meyer, T. J. Proton-Coupled Electron Transfer. *Chem. Rev.* **2007**, *107* (11), 5004–5064. <https://doi.org/10.1021/cr0500030>.
- (3) Mayer, J. M. PROTON-COUPLED ELECTRON TRANSFER: A Reaction Chemist's View. *Annu. Rev. Phys. Chem.* **2004**, *55* (1), 363–390. <https://doi.org/10.1146/annurev.physchem.55.091602.094446>.
- (4) Hammes-Schiffer, S. Theoretical Perspectives on Proton-Coupled Electron Transfer Reactions. *Acc. Chem. Res.* **2001**, *34* (4), 273–281.
- (5) Görner, H. Photoreduction of 9,10-Anthraquinone Derivatives: Transient Spectroscopy and Effects of Alcohols and Amines on Reactivity in Solution. *Photochem. Photobiol.* **2003**, *77* (2), 171–179. [https://doi.org/10.1562/0031-8655\(2003\)077<0171:POADTS>2.0.CO;2](https://doi.org/10.1562/0031-8655(2003)077<0171:POADTS>2.0.CO;2).
- (6) Frank, R.; Greiner, G.; Rau, H. Photoinduced Electron Transfer from Excited [Tris(2,2'-Bipyridine)Ruthenium(II)]<sup>2+</sup> to a Series of Anthraquinones with Small Positive or Negative Gibbs Energy of Reaction. Marcus Behavior and Negative Activation Enthalpies. *Phys. Chem. Chem. Phys.* **1999**, *1* (15), 3481–3490. <https://doi.org/10.1039/A902486G>.
- (7) Kuss-Petermann, M.; Oraziotti, M.; Neuburger, M.; Hamm, P.; Wenger, O. S. Intramolecular Light-Driven Accumulation of Reduction Equivalents by Proton-Coupled Electron Transfer. *J. Am. Chem. Soc.* **2017**, *139* (14), 5225–5232. <https://doi.org/10.1021/jacs.7b01605>.
- (8) Concepcion, J. J.; Brennaman, M. K.; Deyton, J. R.; Lebedeva, N. V.; Forbes, M. D. E.; Papanikolas, J. M.; Meyer, T. J. Excited-State Quenching by Proton-Coupled Electron Transfer. *J. Am. Chem. Soc.* **2007**, *129* (22), 6968–6969. <https://doi.org/10.1021/ja069049g>.
- (9) Lebedeva, N. V.; Schmidt, R. D.; Concepcion, J. J.; Brennaman, M. K.; Stanton, I. N.; Therien, M. J.; Meyer, T. J.; Forbes, M. D. E. Structural and PH Dependence of Excited State PCET Reactions Involving Reductive Quenching of the MLCT Excited State of [Ru<sup>II</sup>(Bpy)<sub>2</sub>(Bpz)]<sup>2+</sup> by Hydroquinones. *J. Phys. Chem. A* **2011**, *115* (15), 3346–3356. <https://doi.org/10.1021/jp200381n>.
- (10) Moore, G. F.; Brudvig, G. W. Energy Conversion in Photosynthesis: A Paradigm for Solar Fuel Production. *Annu. Rev. Condens. Matter Phys.* **2011**, *2* (1), 303–327. <https://doi.org/10.1146/annurev-conmatphys-062910-140503>.

- (11) *Purification of Organic Chemicals*; Butterworth-Heinemann, 2009; pp 88–444. <https://doi.org/10.1016/B978-1-85617-567-8.50012-3>.
- (12) Warren, J. J.; Tronic, T. A.; Mayer, J. M. Thermochemistry of Proton-Coupled Electron Transfer Reagents and Its Implications. *Chem. Rev.* **2010**, *110* (12), 6961–7001. <https://doi.org/10.1021/cr100085k>.
- (13) *Handbook of Photochemistry*, 3rd ed.; 2006.
- (14) Zhu, X.-Q.; Wang, C.-H.; Liang, H. Scales of Oxidation Potentials, PKa, and BDE of Various Hydroquinones and Catechols in DMSO. *J. Org. Chem.* **2010**, *75* (21), 7240–7257. <https://doi.org/10.1021/jo101455m>.
- (15) Lennox, J. C.; Kurtz, D. A.; Huang, T.; Dempsey, J. L. Excited-State Proton-Coupled Electron Transfer: Different Avenues for Promoting Proton/Electron Movement with Solar Photons. *ACS Energy Lett.* **2017**, *2* (5), 1246–1256. <https://doi.org/10.1021/acsenergylett.7b00063>.